Noise shaping for Antenna Beamforming

Shahin Sheikh

A Thesis

In the Department

of

Electrical and Computer Engineering

Presented in Partial Fulfillment of the

Requirements for the Degree of

Doctor of Philosophy (Electrical and Computer Engineering)

at Concordia University

Montreal, Quebec, Canada

December 2022

CONCORDIA UNIVERSITY

SCHOOL OF GRADUATE STUDIES

This is to certify that the thesis prepared

By: Shahin Sheikh

Entitled: Noise Shaping for Antenna Beamforming

and submitted in partial fulfillment of the requirements for the degree of

Doctor Of Philosophy Electrical and Computer Engineering

complies with the regulations of the University and meets the accepted standards with respect to originality and quality.

Signed by the final examining committee:

_____ Chair
Dr. Govind Gopakumar

_____ Thesis supervisor
Dr. Ahmed A. Kishk

_____ Examiner
Dr. Robert Paknys

_____ Examiner
Dr. Abdel Razik Sebak

_____ Examiner
Dr. Jamal Bentahar

_____ External Examiner
Dr. Nader Behdad

Aproved by:

_____
Dr. Jun Cai,
Graduate Program Coordinator

December 6, 2022 _____
Dr Mourad Debbabi, Dean

Abstract

Noise Shaping for Antenna Beamforming

Shahin Sheikh, Ph.D.

Concordia University, 2022

This thesis is an exhaustive investigation of a well-known signal processing approach called noise shaping for beamforming. We adopted the noise-shaping approach for phase-only and amplitude-phase synthesis for the first time. To do that, 1-D and 2-D, real- and complex-coefficient, minimum-phase digital finite impulse response filters are designed based on the discrete Hilbert transform method. It is shown for the first time that by pushing the error out of the so-called visible region, the decrease of antenna directivity due to the quantization can be compensated to some extent, which provides an advantage over the uniform distribution of error. In some cases, pushing the error out of the visible region might be impossible. For such cases, we proposed using the spaced-notches filter. Moreover, it has been shown that the method is of maximum efficacy when both the phase and amplitude of the excitation signal are controllable. Thus, complex-valued noise shaping can be exploited for the phase-amplitude synthesis of the phased array, showing quite promising performance. Furthermore, the superiority of noise shaping over conventional random methods for null restoration is brought to attention with several examples for the first time.

Also, the method is implemented at the sub-array layer. A concept study based on the noise shaping approach addressing the quantization error at the sub-array layer is presented for the first time. The noise shaping might be used for the last layer since it typically has enough elements. In this case, the noise shaping is exploited to push the distortion to where other layers' sub-array

factors have enough attenuation, which is supposed to alleviate the quantization lobe level to some extent. To do that, a novel approach is proposed in which the sub-array factor, or composite sub-array factor, should be tiled with the periodicity of the ultimate-layer array factor, and subsequently, a contribution of all tiles yields the digital filter layout.

Moreover, we have investigated the quantization issue incurred by the practical pixel in reflectarray. The quantization error has been treated by using signal statistics and the noise shaping approach, which is used for space-fed antennas for the first time. For the space-fed antenna, we used real-valued noise shaping to address the quantization issue. Nevertheless, it is shown that the local periodicity assumption is an important limitation since increasing the depth of the stopband filter for noise shaping inserts a considerable portion of noise into the phase arrangement on the reflective surface, which is problematic for antenna performance. Also, the filter stopband should be designed for all extreme beams, limiting noise-shaping effectiveness for mechanical steering. Then, a resonant type element based on the delay line is chosen for better control of phase delay arrangement. Two prototypes are fabricated, one based on conventional design and the other based on spectrally shaped noise. The performance of the two antennas is compared with each other. It is concluded that the noise shaping can somewhat relax the reflectarray sidelobe level.

Keywords: Noise shaping, dither, digital filter, phased array, reflectarray, multi-focal reflectarray, digital phase shifter, digital attenuator, quantization, sub-array, analog beamforming, hybrid beamforming, digital beamforming, quantization lobe, visible/invisible region.

Acknowledgment

I would like to express my gratitude to my supervisor, Prof. Ahmed A. Kishk, for his guidance, patience, and comments.

Moreover, I appreciate the committee members: Dr. Robert Paknys, Dr. Abdel Razik Sebak, and Dr. Jamal Bentahar, for their time devoted to serving on my examining committee.

I would also like to thank the external examiner, Dr. Nader Behdad, for serving on the examining committee.

Table of Contents

List of Figures

List of Tables

List of Acronyms

ABF	Analog beamforming
ASIC	Application-specific integrated circuit
APS	Analog phase shifter
BB	Base band
BSO	Brainstorm optimization
BOS	Border of symmetry
CF	Characteristics function
CBW	Complex beamforming weighting
C-SAF	Composite sub-array factor
CCI	Co-channel interference
CV-NS	Complex-valued noise shaping
CDF	Cumulative distribution function
CCDF	Complex coefficient digital filter
DA	Digital attenuators
DSP	Digital signal processor
DBF	Digital beamforming
DPS	Digital phase shifter
DHT	Discrete Hilbert transform
DFT	Discrete Fourier transform
DSFT	Discrete space Fourier transform
DTFT	Discrete-time Fourier transform
EM	Electromagnetic
EIRP	Effective isotropic radiated power
ERP	Effective radiated power

EOC	Edge of the coverage
ELL	Element location lattice
ESB	Even stopband
FDTD	Finite difference time domain
FL-SAF	First-layer sub-array factor
F/D	Focal-to-diameter
FIR	Finite impulse response
FPGA	Field-programmable gate array
FS	Fourier series
FT	Fourier transform
FLB	Filter layout background
GA	Genetic algorithm
GaAs	Gallium arsenide
GEO	Geostationary orbit
GPB	Geographical and political boundary
GPDF	Gaussian probability density function
HPBW	Half-power beamwidth
HBF	Hybrid beamforming
HPA	High-Power amplifier
HP	High precision
HT	Hilbert transform
IIR	Infinite impulse response
IF	Intermediate frequency
IDSFT	Inverse discrete space Fourier transform
IDTFT	Inverse discrete time Fourier transform

iid	Identically distributed
JN	Jammer null
LO	Local oscillator
LPA	Local periodicity assumption
LEO	Low earth orbit
LNA	Low noise amplifier
LSB	Least significant bit
LSI	Linear shift-invariant
LP	Linearly polarized
MEO	Medium earth orbit
MF-RA	Multi-focal reflectarray
MOBSO	Multi-objective brainstorm optimization
MPF	Minimum-phase filter
MPS	Minimum phase system
MIMO	Multiple-input multiple-output
MMIC	Monolithic microwave integrated circuit
NFR	Near field region
NSD	Non-subtractive dither
NSGA	Non-dominated sorting genetic algorithm
NTF	Noise transfer function
O-AF	Overall array factor
OS	Objective space
PA	Phased array
P/A-CC	Phase/amplitude control circuit
PL	Periodicity lattice

PTC	Phase transfer function
PSO	Particle swarm optimization
PDA	Phase delay arrangement
PDF	Probability density function
PBC	Periodic boundary condition
QL	Quantization lobe
QFN	Quad flat no-lead
RA	Reflectarray
Ra-NFR	Radiating near field region
RBR	Realized band rejection
RCDF	Real coefficient digital filter
RoC	Region of convergence
RV-NS	Real-valued noise shaping
RF	Radio frequency
Re-NFR	Reactive near field region
RN	Restoring null
RPDF	Rectangular probability density function
SAF	Sub-array factor
SatCom	Satellite communication
SL-SAF	Second-layer sub-array factor
SLL	Side lobe level
SD	Subtractive dither
SB	Shifted stopband
SQNT	Signal-to-quantization-noise ratio
SUQ	Simple uniform quantization

TA	Transmitarray
T/R	Transmit/receive
TSSB	Truncated shifted stopband
TRP	Total radiated power
TEN	Transverse equivalent network
TE	Transverse electric
TM	Transverse magnetic
TPDF	Triangular probability density function
UL-AF	Ultimate-layer array factor
VRT	Variable rotation technique
WIP	Wavefront interruption problem
ZT	*z*-transform

Chapter 1
Introduction

1.1 issue

Antenna arrays capable of electronic steering are called phased arrays (PA). Typically, PA includes several transmit/receive (T/R) modules terminated by radiators. Each T/R module includes several devices, such as a high-power and/or low-noise amplifier, channelizer/synthesizer, *etc*. There are several approaches for PA beamforming. One is analog beamforming (ABF), in which the complex beamforming weights (CBWs) are implemented in the analog domain, usually in radio frequency (RF) or local oscillator (LO) signal path. Due to some reasons, e.g., fewer down/up converter mixers, it is more common to implement the phase/amplitude control circuit (P/A-CC) in the RF signal path. Besides, the digital control mechanism is conventionally preferred for P/A-CC in which the digital attenuator (DA) [1]-[5] and digital phase shifter (DPS) [6]-[8] are recruited. However, one should consider that the DPSs and DAs are complex, expensive, and power-hungry devices. This problem shows itself in multiple simultaneous beam applications, such as massive multiple-input multiple-output (MIMO), since several sets of DPSs and DAs are needed. To decrease the costs, there are some solutions, for example, the design of an array with large element spacing, contiguous sub-array, and using smaller bits number for DPSs and DAs.

Nevertheless, discretization of the signal domain, sampling, and signal range, quantization, are integrated with corresponding distortions. The spatial discretization is implicit with the antenna array; thereby, the spatial aliasing depends on the lattice specifications, including the pitch (element spacing) and the lattice fashion, such as square or hexagonal lattice. Violating from Nyquist design of array leads to wavenumber aliasing. This happens when the visible region radius

is larger than the fundamental period of the array factor. Thereby, grating lobe(s) may appear for some steered array factors. On the other hand, quantization error typically shows itself as a harmonic distortion in the Fourier domain since the error is a deterministic function of the input. The CBW quantization due to the limited bits number of DAs and DPSs can cause quantization lobes (QLs), gain loss, and beam point deviation. The QLs imitate the main beam shape due to the coherency of error. The DA, DPSs, and RF beamforming ICs are introduced in Chapter 2.

The other possibility of beamforming is after converting intermediate frequency (IF) or baseband signals to digital ones, called digital beamforming (DBF). This approach provides a list of advantages over ABF. Nevertheless, DBF usually increases hardware complexity and cost by dedicating one RF chain per radiator. Moreover, it is much more computationally intensive than ABF. That can prohibitively increase by increasing the sample rate, aperture size/element spacing, and the number of independent beams. In DBF, the inner product of two vectors amounts to a sum-of-products, which can be performed in a fully parallel multiply-and-add configuration, which can be implemented in the FPGA hardware or sequentially using complex multiply-accumulators (CMAC), which should be implemented by the DSP. Although in many practical cases, designers use DSP for beamforming, the FPGA might be more efficient for this purpose in terms of speed, chip area, and power consumption. This is because the FPGA is a hardware circuitry that contributes to a faster binary multiplier.

The number of partial products depends on the number of bits quantifying the multiplicand, the multiplier and the scheme used. For sure, the greater the number of partial products, the more time delay and more circuit area to compute the multiplication. To show this, 8 by 4 bits and 8 by 8 bits booth multipliers are implemented and compared. The schematic of the synthesized gate level and waveforms are shown in Fig.1.1.

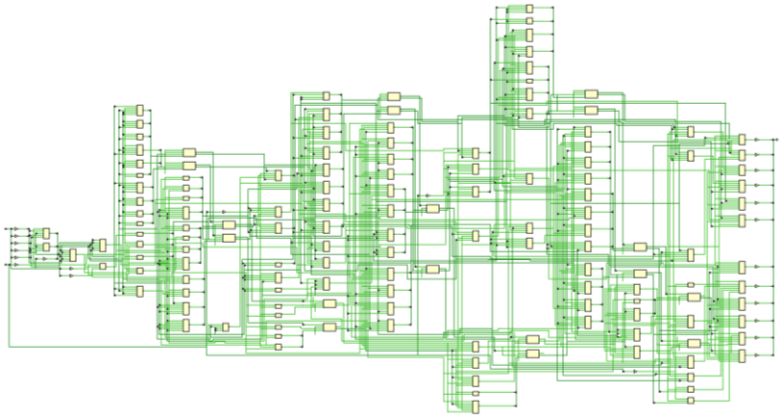

(a)

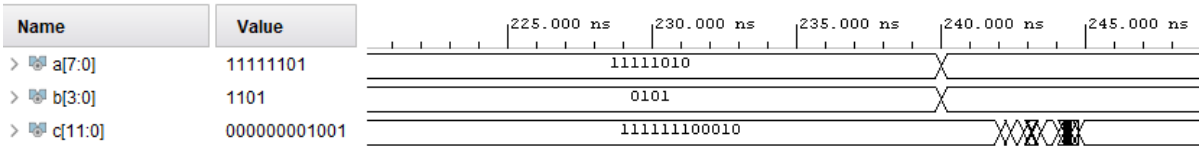

(b)

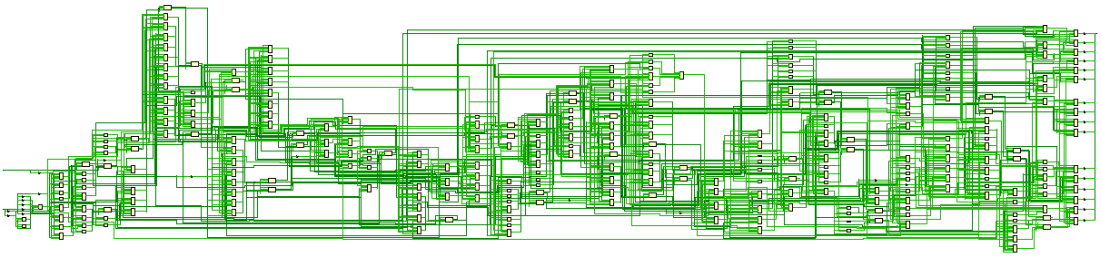

(c)

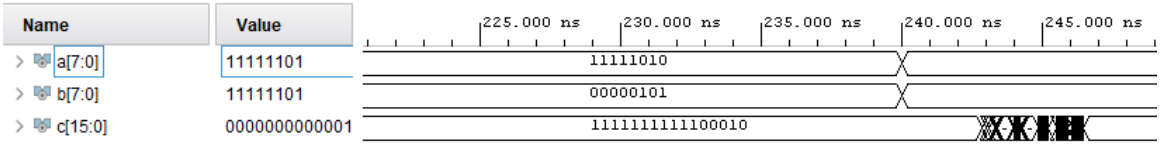

(d)

Fig. 1. 1 Schematic of synthesized booth algorithm (a) for 8 bits multiplicand and 4 bits multiplier, (b) the associated post-synthesis timing simulation. (c) Schematic of synthesized booth algorithm for 8 bits multiplicand and 8 bits multiplier, (d) the associated post-synthesis timing simulation.

The result of Fig. 1.1(a) includes 167 cells,12 I/O ports, and 271 nets, whereas the schematic of Fig. 1.1(c) comprises 323 cells, 32 I/O ports, and 551 nets. Comparing the two wave forms, one realizes the latter has about 2 ns more delay. Moreover, one should note that four multiplications are required per radiator and beam in DBF.

Accordingly, the major difficulty in DBF based on FPGA[1] is the gate propagation delay, which is more affected by multiplications. It should be noted that the number of independent beams can prohibitively increase the number of multiplications. This can be problematic for those applications needing multiple beams and high data rates, including radar, massive MIMO, and satellite communication (SatCom) implemented based on the DBF.

An alternate approach is Hybrid beamforming (HBF) [9]-[14], in which the array aperture is divided into some sub-arrays. Each output signal from sub-array combining is subsequently introduced to the digital platform after going through the RF chains and data converters; thus, the DBF is carried out on the array of analog sub-arrays. The lattice of the ultimate layer is usually much sparser than the first-layer lattice on which the radiators are located. Hence, the number of RF and digital chains becomes dramatically less than that of radiators, so the antenna can become cheaper and sizable data can be realized for DSP. However, the problem of multiple beams in the digital domain can still be drastically increased by increasing the sample rate, aperture size, and the number of beams.

Another cheap solution is a space-fed antenna such as reflectors and lenses. The discretized versions of space-fed antennas, such as transmitarray (TA) and reflectarray (RA), offer some further advantages, comprising better control over the aperture phase [15], cheap PCB fabrication, and lightweight, which makes them highly deployable. However, the cost is usually some inferior radiation characteristics such as narrower bandwidth, higher minor lobe level, and lower maximum gain. The RA and TA antennas also suffer from phase quantization. This is because the practical pixel provides a specific range of phases which can lead to coarse quantization at high frequency and for highly miniaturized pixel and reconfigurable types.

[1] Also, the application-specific integrated circuit (ASIC).

As stated, the quantization results in a signal-dependent error that manifests itself as a harmonic distortion inside the signal spectra. Strictly speaking, this statement, however, is incorrect. The quantization error is not a signal-dependent artifact if the input signal complies with some statistical specifications. In [16], the statistical condition of the (real) signal for the quantizer is provided with white quantization error and uniformly distributed. Although most practical signals do not comply with such a condition, it is possible to manipulate the original signal by adding an independent signal before the quantization process, satisfying the conditions provided in [16]. Such a signal is called dither [17]. It is typically but not necessarily, a random signal with specific statistical properties. The dithered quantization method is extensively utilized in many applications, such as audio signal processing, communication, control systems, and digital image halftoning [18]-[21].

The antenna community is familiar with the benefits of the dithered quantization. Several researchers have addressed the quantization issue in PA antenna [22]-[30]. A majority of such efforts are randomization-based methods (dither-based methods). It seems that earlier than all, it was Miller, in 1964, who tried to address the issue due to the quantization error periodicity of the PA [31]. Miller found the benefits of quadratic phase shift required for compensating the path length between the feed and elements in a space-fed antenna. In [24], one of the earliest ones, a random phasing approach, is proposed to break up the quantization error coherency in PA antenna, which is a dithering approach. There are, nevertheless, some problems with the dithering. Actually, the inserted noise deteriorates the antenna gain and is not optimal for QL level suppression. Also, the generated beam is not repeatable since, in general, the dither is a random signal. Moreover, for those applications, the null is embedded in the antenna pattern to cancel the interfering signal; random dither is ineffective since it contributes to a flat noise that simply fills up the nulls.

1.2 Motivation

As stated above, it was long believed that the error across the array aperture should be independent of the original signal with a uniform distribution, though there is no solid reason for the uniform distribution[2]. In fact, that might be a sub-optimal solution, which is also proved in other applications. For example, the human visual system discriminates between the spatial frequencies; therefore, it is more interesting to shape the noise and suppress it in those areas of the spectrum where the eye is more sensitive to them.

It is possible to control and shape the error signal spectra by using a filter in a feedback circuit of the quantizer system. This method is called noise shaping, a well-known and widely appreciated signal processing method. One of the earliest works back to Spang and Schultheiss [32]. Besides, earlier than all, Floyd and Steinberg exploited the benefits of noise shaping in digital image processing [33], although the method was used in audio signal processing a long time before that. Error diffusion is a popular name for noise shaping in the image processing community [34-36]. The method is also famous as $\Delta - \Sigma$ modulator/converter [37]. In Fig. 1.2, an image is quantized to 3 bits, and the performance of different schemes are compared. One can see the superiority of noise shaping over simple quantization and RPDF dithering. Floyd-Steinberg digital filter is used in Fig. 1.2(d). Therefore, it might be tempting to investigate whether noise shaping can be used to suppress the distortion due to the quantization in antenna design and what would be the challenges and possibilities. These are the prime motivations of the current research.

[2] Actually, there is a reason and that is for uniform distribution of phase error, the beam point deviation is zero. However, such a concern can also be addressed by spectrally shaped one.

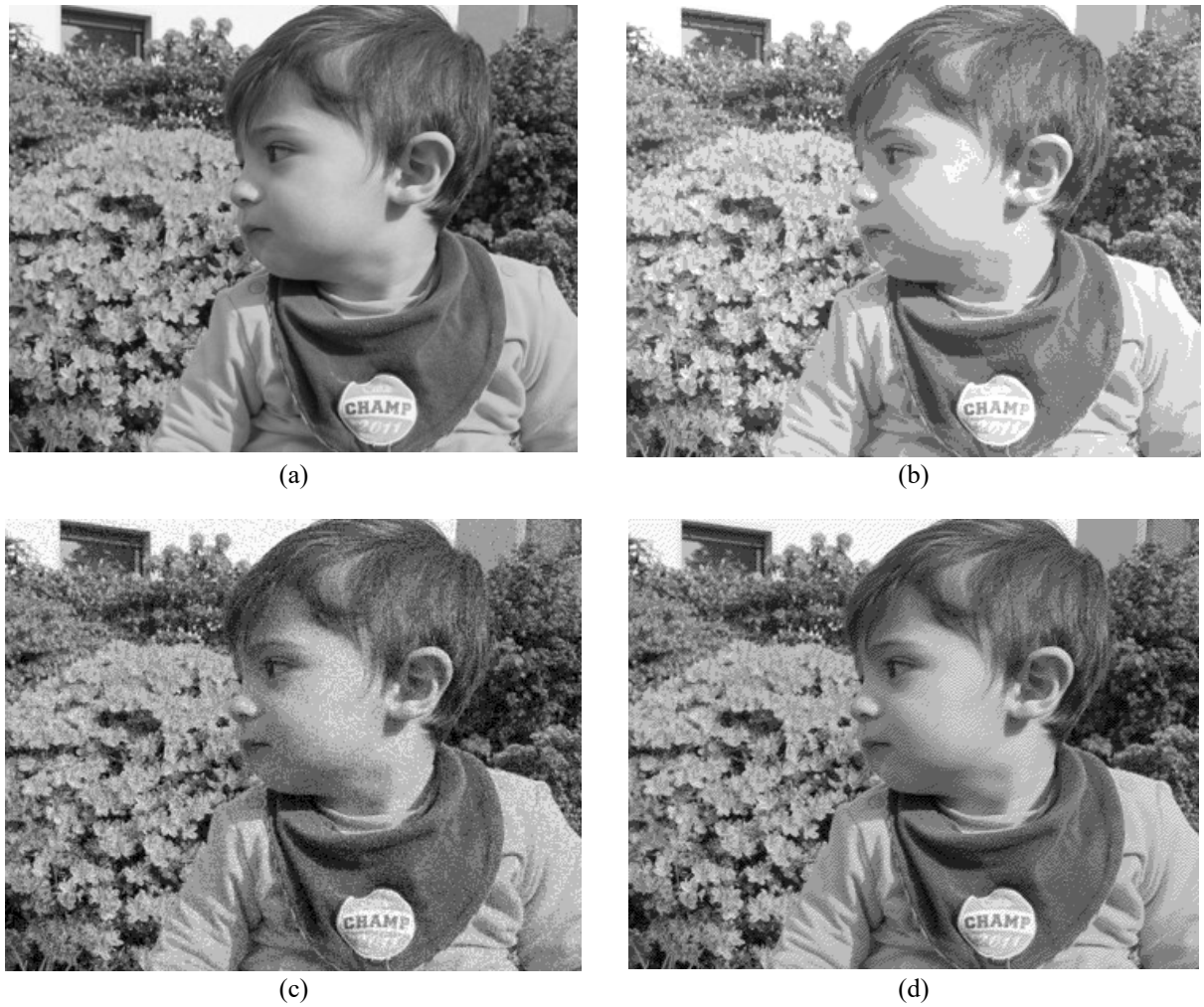

Fig. 1. 2 A photo with different quantization schemes. (a) Original picture, (b) 3-bit simple uniform quantization, (c) RPDF dithering response, and (d) spectrally shaped noise response.

1.3. Thesis contributions

We have proposed that the noise shaping can be recruited in ABF to address the distortion of antenna radiation patterns caused due to the limited number of bits of the DAs and DPSs. In contrast to dither, the spectrally shaped dither, which is the noise shaping approach, contributes to a repeatable solution. Moreover, the null retrieval problem can be conveniently treated with the spectrally shaped dither. We proposed for the first time that the jamming nulls (JNs) embedded in the radiation pattern should be addressed in the digital filter design; thus, the quantization error can be pumped out of those areas, and thereby, the nulls can be restored to some extent.

In DBF, as the number of beams increases, it becomes challenging to quantify the CBW with enough bits. In this regard, one may use a smaller bit number, e.g., 4 bits, to quantify the CBW and instead spectrally shape the excitation error signal to push the distortion out-of-band, which in this case might be the beamspace visible region or just an area of interest inside the visible region.

Moreover, we propose exploiting the noise shaping approach to address the quantization error at the sub-array layer. The method might be used for the last layer since it typically has enough elements. Nevertheless, in practice, the sub-array might be implemented with more than hundreds of elements; thus, it can also be utilized to shape the sub-array factor spectrally. The main discrepancy between the approach employed here and in the preceding paragraphs is that the signal set on the ultimate layer is typically much sparser than the first one; hence, the corresponding array factor fundamental period is smaller than the visible region, which makes it challenging to use the trick, pushing the quantization distortion directly to the so-called invisible region. Nevertheless, the noise shaping is exploited for the first time to push the distortion to where other layers' sub-array factors have enough attenuation, which is supposed to alleviate the QL level to some extent. To do that, a novel approach is proposed in which the sub-array factor (SAF), or composite sub-array factor (C-SAF), should be tiled with the periodicity of the ultimate-layer array factor, and subsequently, a contribution of all tiles yields the digital filter layout. This approach helps to pump the distortion to the area where the sub-array factor has enough attenuation; hence, the distortion can be mitigated in the overall array factor (O-AF).

We have also implemented some novel configurations of multi-layer contagious sub-array overlapping for the first time. It has been shown that very complicated sub-array overlapping can practically be realized in multi-layer architecture. This method is based on a multi-layer FIR filter, which is used to optimally design a contagious sub-array system as a cheap solution for a limited

scan range.

The optimizer engine is a multi-objective brainstorm optimizer (MOBSO) designed to search for decision variable space decimated by the orthogonal polynomial method. A multi-focal reflectarray (RA) is designed based on multi-objective optimization. In addition, we have investigated the quantization issue incurred by the practical pixel. This has been treated by using signal statistics and the noise shaping approach, which is used for space-fed antenna for the first time. This method can somehow mitigate the quantization issue due to practical pixel response.

1.4. Outline of the Thesis

The subsequent chapters in this thesis will be arranged as elaborated in the following paragraphs.

Chapter 2 includes a brief review of the fundamental concept of antenna. Then, a phased array antenna, different beamforming methods, and a literature review are presented. After that, space-fed antennas, including reflectors and RAs, are introduced. Some minor contributions comprising sub-wavelength pixel modeling are also presented.

Chapter 3 is devoted to quantization. In particular, the quantization issue in analog and digital beamforming is investigated. Then, the theory background of dithering is presented, and the method is theoretically investigated for PA based on ABF.

Chapter 4 discusses the theoretical background of spectrally shaped dither (noise shaping). In particular, Fourier analysis in 1D and 2D, digital filter design, discrete Hilbert transform method, sampling and lattice theory, and noise shaping approach are reviewed.

Chapter 5 is about the noise shaping approach in PA antenna based on ABF. The method is adapted for phase-only and amplitude-phase synthesis of PA. First, the method is implemented for a square lattice. Then, a hexagonal lattice is investigated, and the method is applied to pattern

synthesis and large element spacing problems.

Chapter 6 discusses the noise shaping approach at the sub-array layer. First, PA based on sub-array overlapping is introduced, and some complicated feeding network is implemented based on a multi-layer sub-array system. Then, the noise shaping approach is developed for the sub-array in which the periodicity of the penultimate layer tiles the sub-array factor. Then, all tiles are considered for the filter design used in the noise shaping approach at the sub-array layer.

Chapter 7 is about optimization. We have used multi-objective optimization for the design of the RA antenna. The detail of the optimization engine and the method to decimate the parameter space is detailed for the multibeam RA antenna. Then, as a single objective example, the digital filter layout is designed for large element spacing.

Chapter 8 is devoted to the RA antenna. The quantization issue is investigated for RA antenna, and several methods are discussed. Moreover, the measurement results for the RA antenna are presented and discussed. Finally, a conclusion is described in Chapter 9 with the main contributions and the future work of the research.

Chapter 2
Antenna fundamentals

In this chapter, first, fundamental antenna concepts are reviewed. Then, phased array and beamforming techniques are introduced. After that, a space-fed antenna including a reflector and reflectarray are presented. Finally, the sub-wavelength pixel is studied, and a simple analytical model is provided for fast analysis of the reflectarray (RA) antenna.

2.1. Radiation mechanism

An electric charge is associated with the electric field with an intensity of $\boldsymbol{E} = \frac{1}{4\pi\varepsilon}\frac{q}{r^2}\hat{r}$, which is initiated with q as the electric charge in coulomb (C), ε as the permittivity of surrounding space in Farad per meter (F/m), and r as radial distance in meter (m). A moving charge contributes to another field vector as well, called the magnetic field, with the intensity of $\boldsymbol{H} = \frac{1}{4\pi}\frac{q\boldsymbol{v}\times\hat{r}}{r^2}$, which is initiated with $\boldsymbol{v}$ as the electric charge velocity vector in meters per sec (m/sec). *These fields can only respond to events at the speed of light*. If an electric charge is accelerated, the electric field in the vicinity of the charge changes. As the field is required to be continuous, there would be a perturbation in field lines. As a matter of fact, alternating electric and magnetic fields are related based on Maxwell (curl) equations. The Maxwell curl equations are written in (2.1).

$$\nabla \times \boldsymbol{E} = -\frac{\partial \boldsymbol{B}}{\partial t} \tag{2.1a}$$

$$\nabla \times \boldsymbol{H} = \boldsymbol{J} + \frac{\partial \boldsymbol{D}}{\partial t} \tag{2.1b}$$

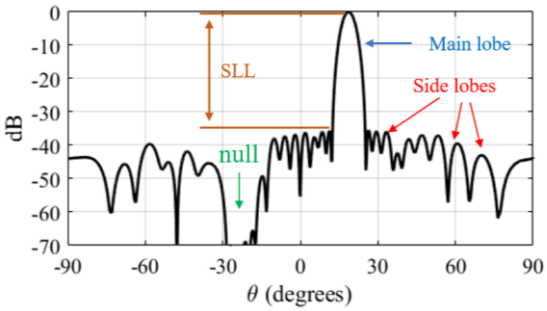

Fig. 2. 1. A one-dimensional normalized radiation pattern of a directive antenna with an embedded null.

in which ρ_v is the charge density, $\boldsymbol{J} = \sigma \boldsymbol{E}$ is the conduction current density vector, $\boldsymbol{D} = \varepsilon \boldsymbol{E}$ called displacement electric field or electric flux density, $\boldsymbol{B} = \mu \boldsymbol{H}$ where $\boldsymbol{B}$ is the magnetic flux density, and μ is the magnetic permeability of space in henry per meter (H/m). According to Maxwell curl equations in (2.1), the alternating electric field induces the magnetic one and vice versa. Thus, the electromagnetic (EM) perturbation (due to accelerated electric charge) must propagate in space with the speed of light, called EM wave. Hence, the antenna is an interface between the EM wave propagating in free space and the electric current at the antenna terminal. There are several antenna types, including wire antenna (such as dipole antenna), microstrip antenna, slot antenna, and leaky wave antenna. Each has its advantages and bottlenecks. In general, to have efficient radiation, the field should show up in phase on the "aperture," and the transmission line EM power should be acceptably delivered to the antenna.

2.2. Antenna definitions and concepts

A one-dimensional radiation pattern is shown in Fig. 2.1. The major lobe of the radiation pattern is called the main beam or, simply, beam. Other lobes, typically of smaller magnitudes than the main beam, are called minor lobes, including the side and the back lobe. The difference between the main lobe and the maximum sidelobes levels is called the sidelobe level (SLL). Occasionally, one sharp minimum might be embedded in the radiation pattern of the antenna for the purpose of direction-finding or interference cancellation in a specific direction called directional-null or

simply null, see Fig. 2.1.

Definition 2.1: The real power density (in watts per square meter) is defined by (averaged) *pointing vector* [38] as follows

$$\boldsymbol{P} = \frac{1}{2} Re(\boldsymbol{E} \times \boldsymbol{H}^*)$$

in which $\boldsymbol{E}$ and $\boldsymbol{H}$ are electric and magnetic vectors, respectively. ■

Therefore, the total radiated power (TRP) by the antenna can be computed as

$$P_{rad} = \int_0^{2\pi} \int_0^{\pi} \boldsymbol{P}\, r^2 \sin\theta \, d\theta d\varphi \tag{2.2}$$

Let $\boldsymbol{P} = p\hat{r}$, then the total power captured by the receiving antenna is

$$P_t = pA_e \tag{2.3}$$

where A_e is called the effective aperture.

Definition 2.2: Power radiated from an antenna per unit solid angle is defined as radiation intensity, U. Thus, one can write

$$P_{rad} = \int_{\Omega} U d\Omega = \int_0^{2\pi} \int_0^{\pi} U \sin\theta \, d\theta d\varphi$$ ■

$U = r^2 p$, which means that radiation intensity is independent of radial distance from the radiator. This is simply because an outward-traveling wave has to decay by r^{-1}; hence, the power density decays by r^{-2}. Moreover, it might be evident that the radiation intensity of an isotropic radiator is $U_0 = \frac{P_{rad}}{4\pi}$. Half-power beamwidth (HPBW) is the angle between the two directions in which the radiation intensity becomes half.

Definition 2.3: The ratio of radiation intensity in a specific direction to the average intensity in all directions is called antenna directivity.

$$D(\theta_0, \varphi_0) = \frac{U(\theta_0,\varphi_0)}{U_{av}}$$ ■

The directivity also can be computed by $D(\theta_0, \varphi_0) = 4\pi \frac{U(\theta_0,\varphi_0)}{P_{rad}}$, which means the radiation intensity in a specific direction to the radiation intensity of an isotropic radiator fed with the same amount of power.

Definition 2.4: The antenna gain is defined as the ratio of the radiation intensity in a specific direction to the radiation intensity that would be produced if the power *delivered* to the antenna were isotopically radiated. ■

The gain and directivity are related $G(\theta_0, \varphi_0) = \eta D(\theta_0, \varphi_0)$ where η is the radiation efficiency.

Definition 2.5: In a specific direction, the antenna gain (G) multiplied by the net power delivered to an antenna is called effective isotropic radiated power (EIRP), which can be computed (in dB) as follows:

$$EIRP = P - L + G$$

where L is the loss in the transmission line and P is the radiated power in a single direction.

2.3 Phased array antenna

2.3.1 Fundamental implications

Each radiator receives a signal replica in PA, depending on the antenna configuration and the element position. The received signals will be coherently combined yielding the "beam sum," as such, the whole assembly imitates a highly directive aperture. As stated before, spatial discretization is an inherent characteristic of an antenna array, as the name implies. In this regard, one may assume the PA is a spatial sampler of electromagnetic plane (EM) waves (more accurately, EM wave spatio-temporal sampler). On the other hand, an array of antennas provides spatial selectivity; therefore, PA precisely works like a spatial finite-impulse response (FIR) filter, finite because the physical aperture is limited to its active elements, which is reciprocal to a finite-

duration impulse response in digital filter theorem. In phased array terminology, combining complex weight multiplication and combining is called beamforming. This procedure might be realized in a physical circuitry contributing to ABF or implemented entirely in the digital domain, called DBF. Each approach has advantages and disadvantages. For example, ABF is sensitive to component tolerances and ambient medium parameters such as temperature and pressure. On the other hand, DBF is a much more accurate approach since it is realized in a digital platform; thus, the beamforming process is not a function of fabrication error, electromagnetic characteristics of materials, temperature, and pressure.

Moreover, it provides flexibility and superiority in design, including auto/self-calibration, and greater number of simulations beam, *etc*. Furthermore, implementing several blocks in a digital platform yields a more compact system than the analog counterpart. Besides, the digital array can easily be reconfigured by upgrading the software. However, DBF needs complete RF chains and a data converter per radiator which is expensive and complicated. As mentioned before, the compromised design is HBF, in which the array is partially implemented in the analog domain as an integration of several sub-arrays.

2.3.2 Analog Beamforming

As stated, the PA is an integration of several independent radiating elements connected to complicated multiple RF modules and feeding networks. So, each module should be designed and fabricated in a compact, multi-functional, low cost, and high-repeatability form. In the active PA, radiating elements are usually directly connected to amplifier chips comprising a high-power amplifier (HPA) for transmit mode, a low noise amplifier (LNA) for the received one, and some switches for signal duplexing. The main requirements of such monolithic microwave integrated

circuits (MMICs) are the power handling and low noise feature[3]. Several approaches control the amplitude and phase of the received signal replica. The signal conditioning can be realized in RF signal path (RF beamforming), IF path (IF beamforming), or LO signal path (LO beamforming).

The RF beamforming has the advantage of fewer supporting modules, including up/down converter mixers. This means that the beamforming is implemented after the upconversion in transmit mode and before the downconversion in receive mode. However, the signal must path through expensive, nonlinear, and dissipative components such as phase shifters and attenuators working at high frequencies. The MMICs needed for this task include several digital controls for the analog programmable phase shifter and attenuator[4] blocks. The current dominant technology for such ICs is gallium arsenide (GaAs). Compared to Silicon, GaAs provide better RF performance, including less noise and loss [39].

The IF beamforming is implemented after the down conversion for receive mode or before the upconversion for the transmitting one. Thus, the complex weight multiplication is realized at a lower frequency than RF, which relaxes the phase-amplitude control circuit complications. However, such an approach needs one up/down converter mixer per radiator, leading to an increase in cost and complexity.

The LO beamforming has the advantage of the least inserted noise and distortion to the original signal among all ABF approaches since the phase shifting is indirectly implemented during the frequency conversion. However, it has the same complication as the IF one and needs a high mixer dynamic range to stand against strong interferences.

[3] Specifically, the saturation power of HPA and noise figure of LNA.
[4] In some cases, variable amplifier might be used.

Overall, at the moment, RF beamforming is more common among ABF approaches mainly due to the smaller number of elements needed, which makes it a more viable candidate for at least large PA cheap solutions. However, as stated, RF beamforming has the difficulty of loss and high cost of constituting devices, phase shifters, and amplifiers/attenuators since they must work at high frequencies.

The main challenges of phase shifting in the analog domain includes non-linearity, limited bandwidth, insertion loss, and circuit complexity. The phase shifters can be categorized into analog phase shifters (APSs) and digital ones (DPSs). The APS provides continuous phase shift; however, the insertion loss is typically high and is somehow inaccurate in terms of phase delay and amplitude weighing due to massive variation of insertion loss for the phase shift range. Thus, it is not reliable to design of accurate PA antenna.

The DPS generates multi-stage constant phase shifts. Several stages might be cascaded or bypassed by the switches to obtain the desired phase. There are several possibilities for the DPS architecture, including the switched delay line, switched filter, *etc*. [7], [40]. Typically, the design is optimized to minimize the variation in attenuation for different phase shifts. This approach is more reliable than APS in generating a more accurate phase delay. However, the main challenges are the discrete phase shift and the significant number of switches and losses. By increasing the number of bits, the quantization error can be relaxed, but the device becomes more expensive, has a larger die[5] size, and is more dissipative. Two examples of DPSs are shown in Figs. 2.2 and 2.3. As can be seen, the DPS is a very power-hungry device. Typically, the price hugely increases by increasing the number of bits and the frequency of operation. The discrete phase shift is detrimental

[2] A small block of semiconductor material on which the main functional part of the device is implemented.

to antenna beamforming since it contributes to a periodic error in conventional array design. As the name implies, the DA switches in finite attenuation states. The discrete amplitude steps can be realized by exploiting semiconductor devices such as PIN diode and MESFET. The DAs supply the excitation magnitude control and are used along with the DPSs in the accurate amplitude-phase synthesis of PA antenna with uniform element spacing. Usually, the distortion due to discrete states of DAs is not severe as the one that DPSs yield but still can be detrimental for beamforming, specifically for SLL design and beam shaping. An exemplar broadband DA working up to 13 GHz is shown in Fig. 2.4. Indeed, it is more compact, so, preferable to implement both devices, DPS and DA, in one MMIC. In [39], the phase/amplitude control circuit is implemented in one MMIC. The block diagram and the phase/attenuation results are shown in Fig. 2.5. It comprises a 6-bit phase shifter and 6-bit attenuator, and six switches for transmitting, receiving, isolation, and calibration modes. To decrease the number of control lines, serial to the parallel interface is used.

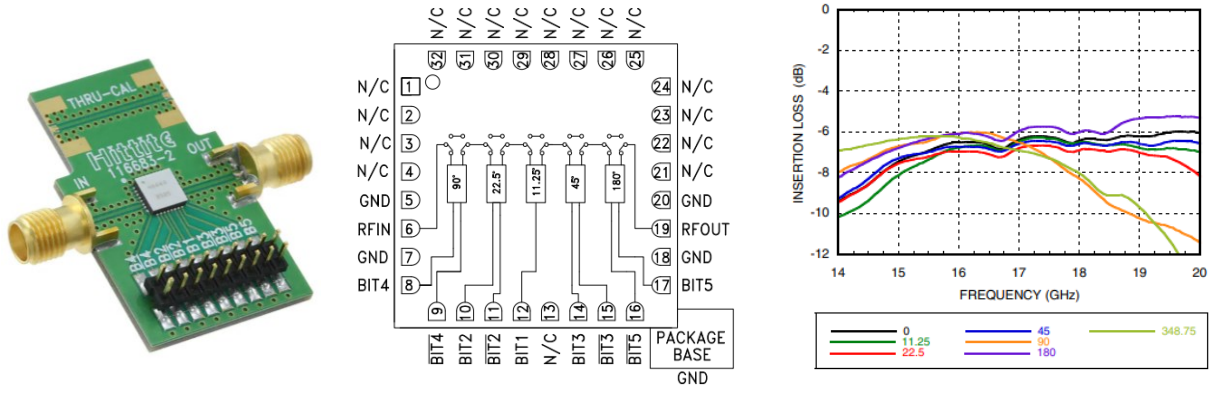

(a) (b) (c)

Fig. 2. 2. A 5-bit digital phase shifter. (a) Photo of a digital phase shifter, HMC644ALC5, on the evaluation board, working at 15-18.5 GHz, (b) functional diagram, and (c) insertion loss for major phase steps [41].

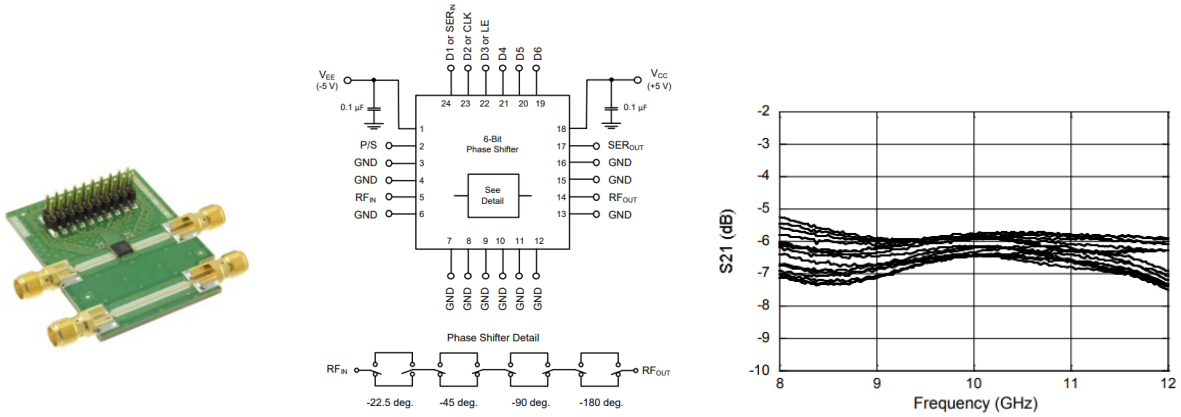

(a) (b) (c)

Fig. 2. 3. A 4-bit digital phase shifter. (a) Photo of the digital phase shifter, MAPS-010146, on evaluation board, working at 8-12 GHz, (b) functional diagram, and (c) insertion loss for all phase steps. [42]

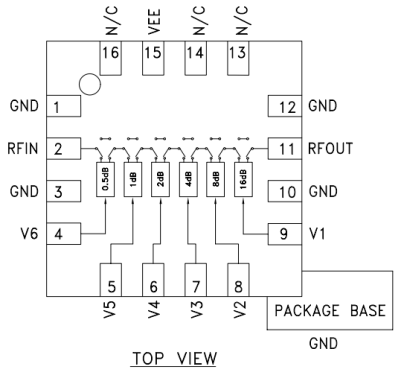

(a)

Control Voltage Input						Attenuation State RF1 - RF2
V1 16 dB	V2 8 dB	V3 4 dB	V4 2 dB	V5 1 dB	V6 0.5 dB	
Low	Low	Low	Low	Low	Low	Reference I.L.
Low	Low	Low	Low	Low	High	0.5 dB
Low	Low	Low	Low	High	Low	1 dB
Low	Low	Low	High	Low	Low	2 dB
Low	Low	High	Low	Low	Low	4 dB
Low	High	Low	Low	Low	Low	8 dB
High	Low	Low	Low	Low	Low	16 dB
High	High	High	High	High	High	31.5 dB

(b)

Fig. 2. 4. Example of broadband 6-bit GaAs digital attenuator, HMC424LP3E-AN, with 0.5 dB least significant bit and the most significant bit of 31.5 dB. (a) functional diagram and (b) truth table [43].

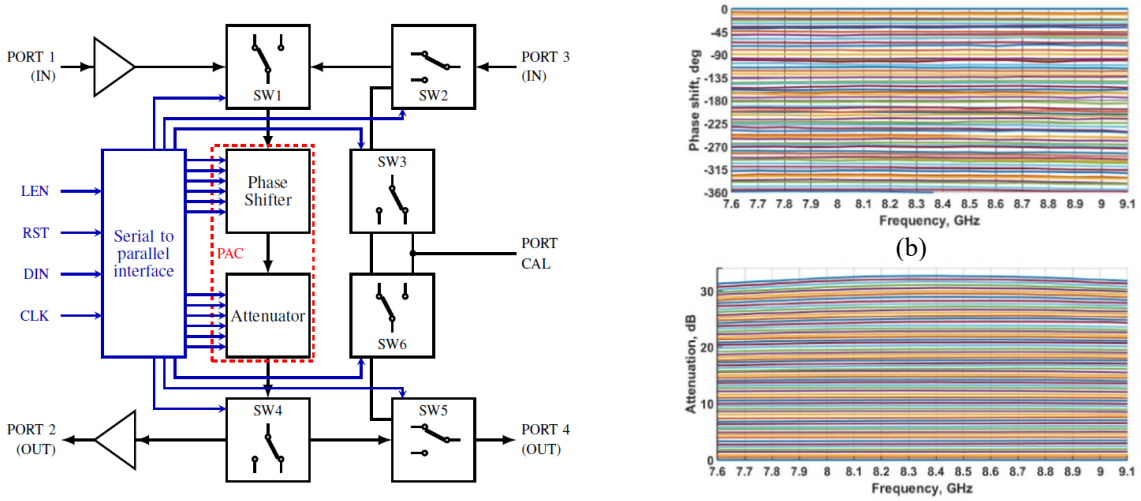

(a) (b) (c)

Fig. 2. 5. An exemplar beamforming IC. (a) Block diagram of the phase/amplitude control IC, the measured (b) phase shift, and (c) the attenuation in dB [39].

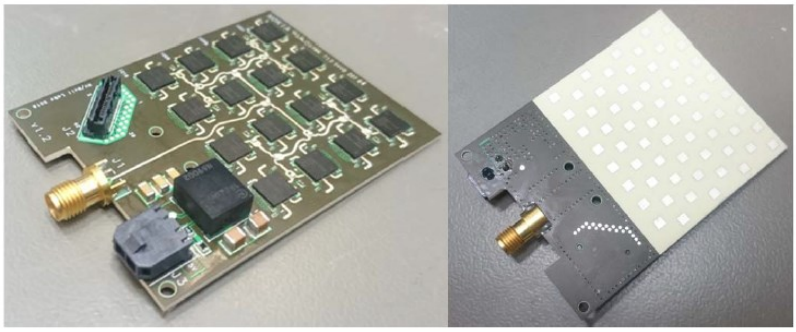

Fig. 2. 6. Two sides of phased array antenna, comprising 64 radiating elements and 16 commercial quad-core MMICs providing independent 5-bit phase and amplitude controls for each radiating element. Back side with ICs is shown on the left, and radiating patch side on the right [44].

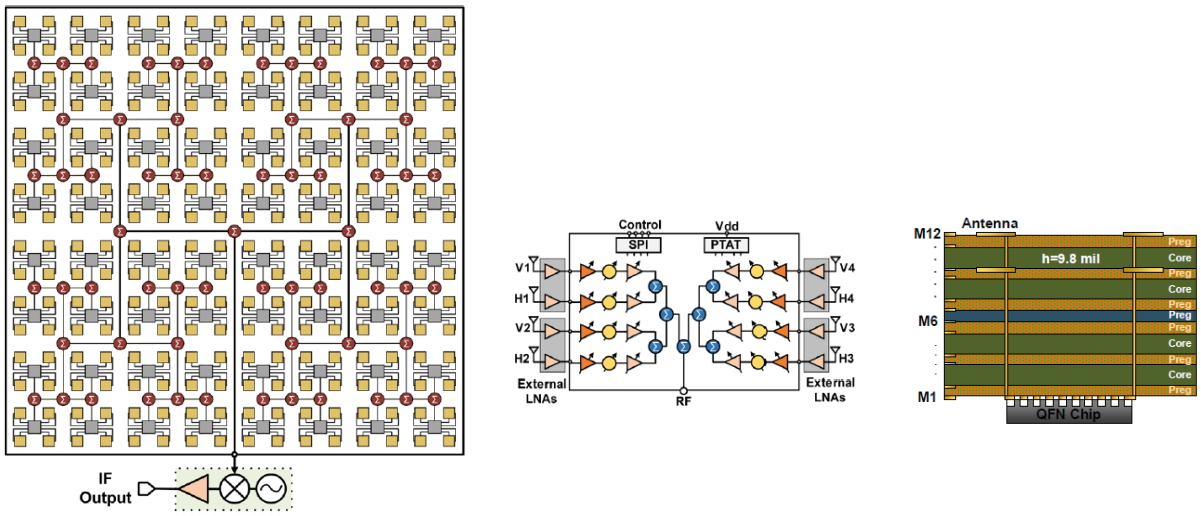

(a) (b) (c)

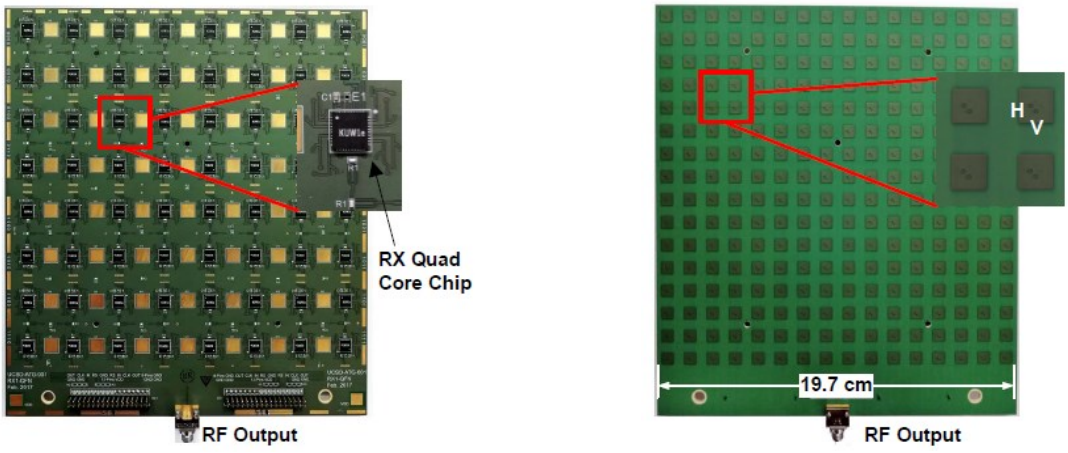

(d) (e)

Fig. 2. 7. Exemplar phased array receiver. (a) A schematic of a phased array receiver based on 64 beamformer chips, (b) Block diagram of the dual-polarized quad (2x2-elements) receive beamformer chip with external LNAs. (c) PCB cross-section. (d), Back view of the Ku-band phased array receiver shows 64 Rx chips. (e) Front view showing dual-polarized antennas [45].

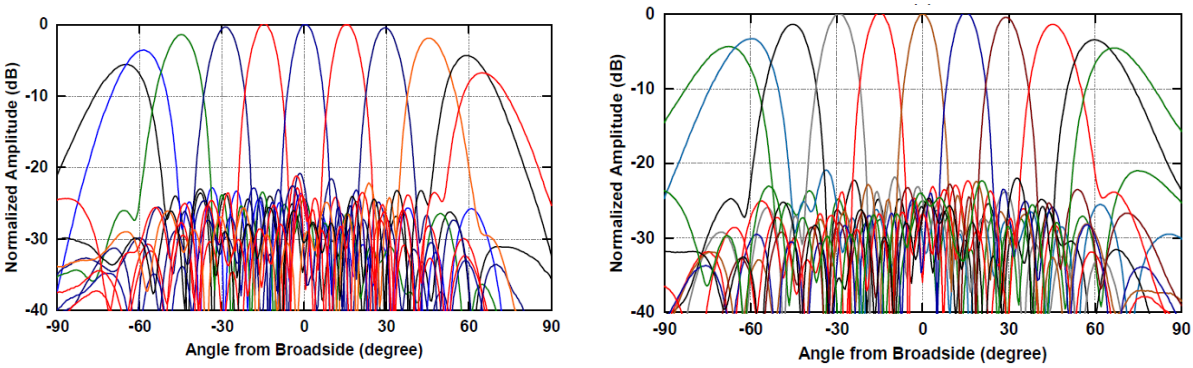

(a) (b)

Fig. 2. 8. Measured radiation pattern of phased array, shown in Fig. 2.7, on (a) E-plane and (b) H-plane [45].

Fig. 2.6 illustrates a fabricated electronically scanned PA antenna that uses Anokiwave quad-core RF beamforming MMIC, providing a 5-bit phase and amplitude-phase shift. Therefore, the RF beam forming MMICs generate 11.5° phase resolution and 1 dB for amplitude in the 31dB range. Also, the 1:16 Wilkinson power divider network is used for feeding the transceiver working at about 27.5 GHz.

Fig. 2.7 shows a Ku-band dual polarized electronically scanned square lattice PA (16 by 16). This PA uses quad-core silicon receive chips with 8 channels, as shown in Fig. 2.7(b). The array is designed for ±70° scan range on the E- and H-plane. Each channel provides 0.5 dB gain step control over a range of 21 dB and 6-bit phase resolution. The two sides of the fabricated antenna are shown in Figs. 2.7 (d) and 2.7(e). All power dividers are Wilkinson.

The receive QFN[6] chips are shown in Fig. 2.7(d) inset. The metallic rectangular patches are heat sinks to remove heat from the board. The measured radiation patterns are shown in Fig. 2.8.

[6] Quad flat no-lead (QFN) package makes it easy to assemble the chips on a PCB.

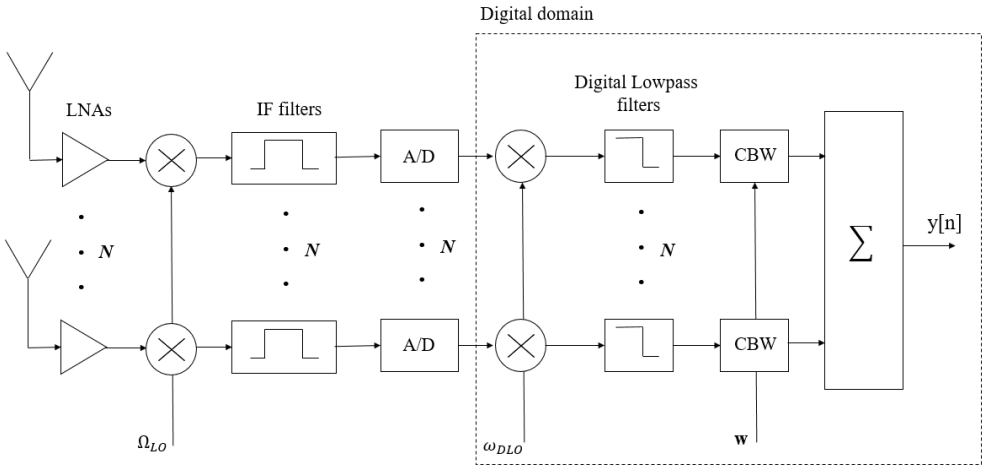

Fig. 2. 9. Schematic of simplified digital beamforming receiver.

2.3.3 Digital Beamforming

The other possibility of beamforming is after converting IF or baseband signals to digital ones, called digital beamforming (DBF). This approach provides a list of advantages over ABF, for example, superior interference cancellation, a more significant number of multiple simultaneous beams, and auto/self-calibration since the CBW is realized in the digital domain. Accordingly, the system can be more accurately implemented. Furthermore, implementing several blocks in a digital platform such as a digital signal processor (DSP), field-programmable gate array (FPGA), and application-specific integrated circuit (ASIC) usually yields a more compact system in comparison with the analog counterpart, which is somehow independent of ambient temperature, and pressure. Besides, the digital array can easily be reconfigured by upgrading the software. Nevertheless, DBF usually increases hardware complexity and cost by dedicating one RF chain per radiator. Moreover, it is much more computationally intensive than ABF. A block diagram of a simplified single-beam DBF receiver is shown in Fig. 2.9.

Evidently, for *M* independent beams, *M* sets of CBW vectors (of size *N*) and final summations are required for *N* radiators. Therefore, the computational burdens can be reduced by increasing the sample rate, aperture size/element spacing, the number of independent beams, and the number of

bits to quantify the data and complex multipliers.

2.3.4 Sub-array

There are verities of sub-array systems. One type of sub-array is just a matter of a feeding network. For example, in Fig. 2.7(a), a 2×2 sub-array is fed by a quad-core chip. This sub-array scheme which is just a matter of summation sense is out of interest here.

All sub-arrays are assumed with the same complex weights in one array architecture. Traditionally, it is implemented for HBF, but strictly speaking, it can be utilized purely for ABF and DBF. As stated, in HBF, the first-layer sub-array outputs are introduced to a digital platform or further tiled to a third layer, and so on. On the other hand, in ABF, all layers are implemented in physical circuitry, and overall array output will be introduced to a data converter. The underlying sub-array architecture partitions the full array aperture into some identical sub-arrays with the same complex weighting. In this configuration, the array is implemented like a multi-layer FIR filter. Besides, it might be realized in the overlapped sub-array configuration in which, by exploiting the spatial FIR filtering, sidelobes due to grating lobes or any other distortions can be considerably mitigated over a wide (temporal-) frequency band. Sub-array overlapping helps to increase the size of the fundamental period of the array factor at the sub-array layer, with the cost of considerable complexity of the feeding network, which facilitates the grating lobe cancelation to some extent. The beams can be steered at all layers comprising the element layer and/or sub-array layer(s). Steering at all layers is usually used in HBF for generating multiple simultaneous beams. In such a configuration, phase shifters might be used at the element layer, phase-steered sub-array, while at the sub-array layer, time-steered, for a wideband array, or phase-steered, as a narrowband solution, might be implemented digitally. An example is shown in Fig. 2.10 for a hexagonal sub-array overlapping seven elements. The beam is commanded at $[\theta, \varphi] = [20°, -90°]$. As seen in

Fig. 2.10(a), each element on the extreme of the sub-array is overlapped by three sub-arrays. Others do not overlap the elements at the center of sub-arrays. The hollow circles subsequently signify the sub-array output introduced to the digital platform. The steered sub-array factor (SAF) and ultimate layer array factor (UL-AF) are shown in Fig 2.10(b) and 2.10(c), respectively. Red lines show the periodicity of UL-AF. As seen in the overall array factor (O-AF), shown in Fig. 2.10(d), the grating lobes of UL-AF are suppressed by SAF. Thus, the ultimate layer becomes much sparser than the first-layer lattice, which relaxes the computational burdens. In addition, this approach generates low side lobe levels, as stated before.

Since the phase shifters are complex, expensive, and power-hungry devices, the sub-array might be designed in a static form which is so-called contiguous [46], without any programmable or variable phase-shifter, as an affordable solution for limited scan angle PA.

As stated before, the last layer might be implemented in the digital or analog domain, though the analog one might be more compatible with the problem since it typically offers a cheaper solution. However, the method has the disadvantage of limited scan angular range due to the un-steered sub-array factor. One conventional approach is to use a flat-top beam, which can acceptably solve the scan loss issue [47]. The scan range is a function of sub-array architecture, overlap efficiency, and sub-array coefficients (beamforming).

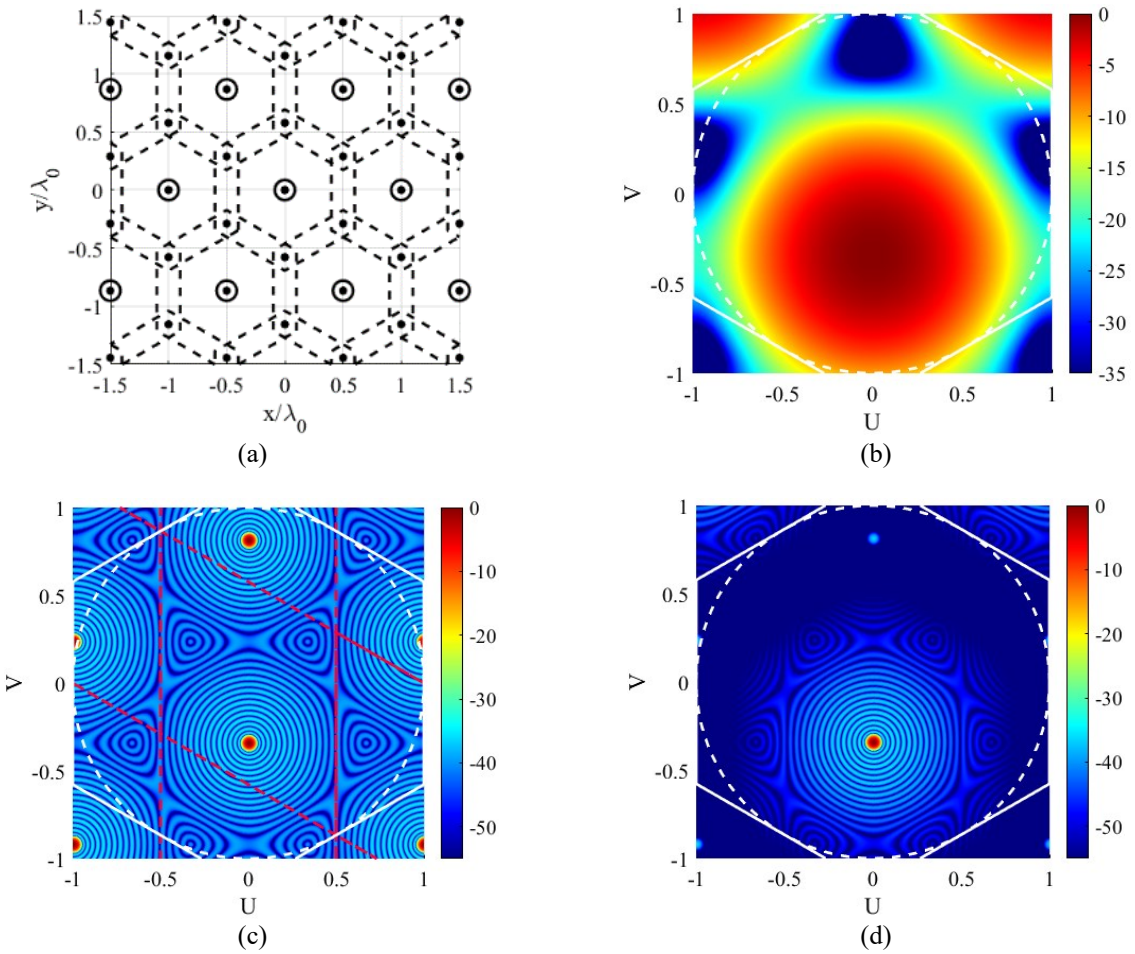

Fig. 2. 10 Example of sub-array overlapping. (a) schematic of element and overlapping sub-arrays, (b) sub-array factor, (c) ultimate-layer array factor, (d) overall array factor.

2.4. Space-fed Antenna

2.4.1 Reflector Antenna

The reflector antenna comprises a reflecting surface(s) and a feed system. The reflector may have different shapes, such as cylindrical and parabolic. The most common shape is parabolic. A center-fed paraboloid is a prime-focused reflector. In Fig. 2.11(a), some cross-section of the parabolic reflector is shown with different focal-diameter (F/D) ratios. For F/D = 0.25, the two reflector edges and focus are on the same line, meaning that the reflector encompasses its focus. For F/D = ∞, the reflector surface becomes flat. In Fig. 2.11(b), the relation between the main physical parameter of the reflector is as follows

$$D^2 = 16FH$$

Some options for the reflector feed include a horn, helix, and array antenna. Typically, a horn or system of horns, as the feed chain, is used. The physical dimension of the horn is of great importance for the performance of the system. The main problem of a prim-focus reflector is the feed blockage since, for a typical horn, the horn can block a majority of radiation intensity after reflection from the reflecting surface. One method to treat this issue is to use an offset-fed reflector, as shown in Fig. 2.11(c). Parameter *C*, called clearance, shows how much the feed is away from the reflecting surface. Sometimes the feed might be inside the aperture plane but farther from the maximum direction of radiation. In many applications, a system of feeds is required, such as multiple spot beams for satellite systems and contour beams. Such applications require offset fed reflectors since the feed chain makes a massive blockage. This approach increases the cross-polarization due to field projection on the aperture.

The power from the feed that is not intercepted by the reflecting surface is called spillover, see Fig. 2.11(c). The spillover is a prominent issue in multiple-beam reflectors since feeds are usually not optimal due to the small spacing available.

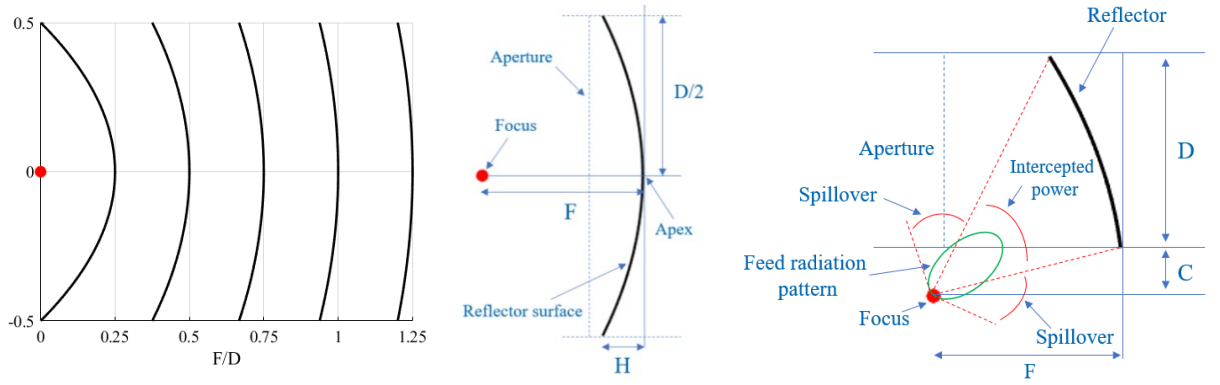

(a) (b) (c)

Fig. 2. 11 Reflector antenna schematic. (a) Cross section of the parabolic reflector with different F/D values, (b) Typical prime-focused reflector, and (c) Schema of an offset-fed reflector.

The spillover decreases as the feed becomes more directive or edge tapering increases. However, that increases the field tapering on the aperture, decreasing the reflector beam efficiency. Depending on the application, edge tapering might be chosen at about 10-15 dB. Usually, the offset-fed reflector has less noise temperature than the prim-focus one. This is because in receiving from satellite, the feed stands upward; hence, it receives a smaller portion of noise from the ground through the spill over radiation.

In some applications, a multi-reflector might be used in which there is typically one primary reflector and sub-reflector(s). The most famous architecture is Cassegrain and Gregorian [48], which are not treated here for brevity.

2.4.2. Reflectarray

One form of discretized reflector antenna is reflectarray (RA). The *IEEE* definition of RA is as follows [49]:

An antenna consisting of a feed and an array of reflecting elements arranged on a surface and adjusted so that the reflected waves from the individual elements combine to produce a prescribed secondary radiation pattern. Syn: reflective array antenna, reactive reflector antenna.

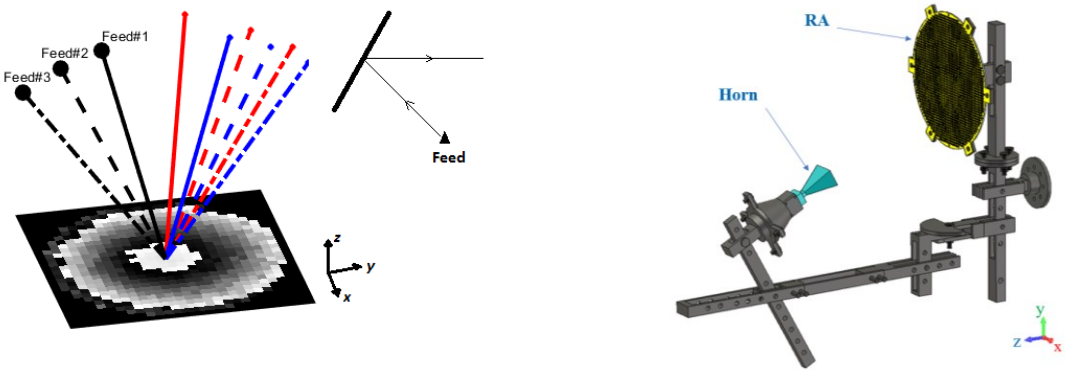

(a) (b)

Fig. 2. 12. reflectarray configuration. (a) Schema of reflectarray with three feed positions and (b) Visualization of reflectarray feed horn and struts system.

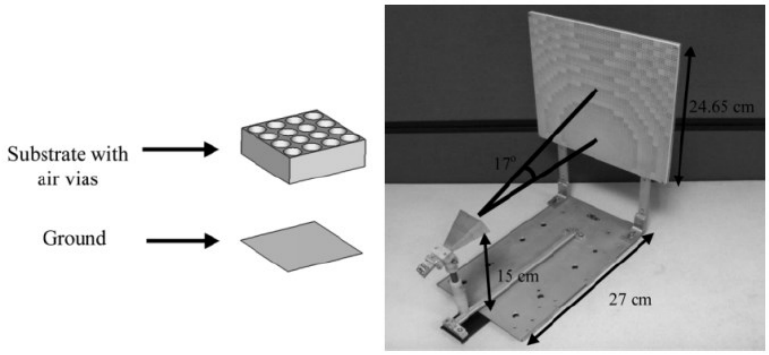

Fig. 2. 13. Ka-band reflectarray made of perforated dielectric substrate [71].

Typically, RA is a planar structure, but it can be implemented on a curved surface such as parabolic. Compared to the traditional reflector, the RA offers some further advantages, comprising better control over the aperture phase, cheap PCB fabrication, and lightweight, making them highly deployable. In addition, RA can manipulate two waves with orthogonal polarizations simultaneously. This can be realized by using pixels with different frequency responses for the two polarizations, see Fig. 2.12(a). A System of RA and feed is shown in Fig. 2.12(b). However, despite all advantages of RA over traditional reflectors, it usually has inferior radiation characteristics such as narrower bandwidth, higher minor lobe level, and lower maximum gain [50]-[77].

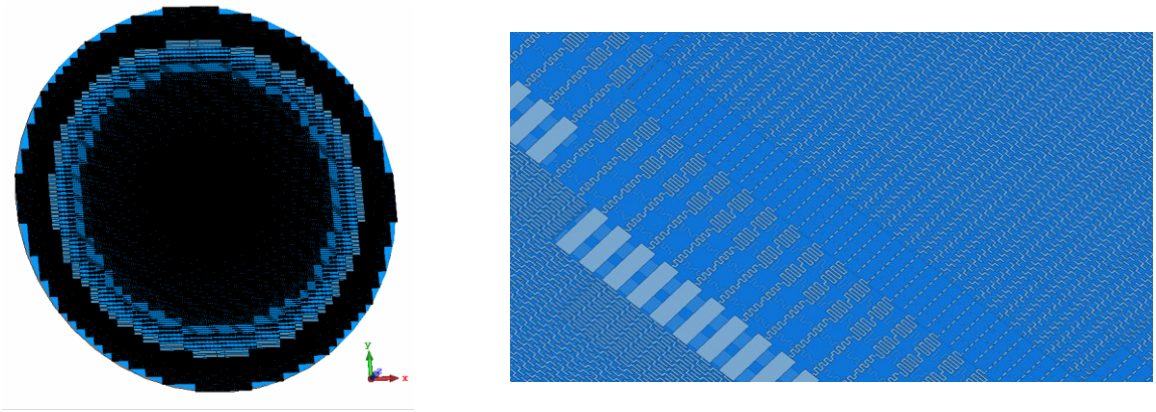

(a) (b)

Fig. 2. 14 An reflectarray based on interdigitated surface. (a) The whole aperture, (b) a closed view of the structure.

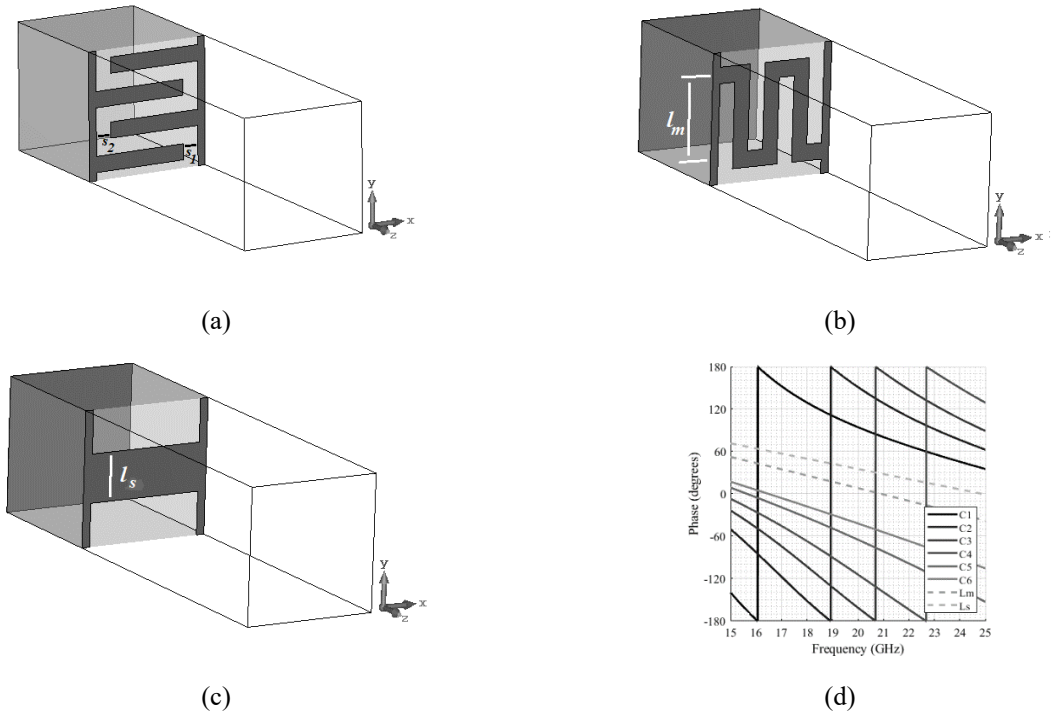

(a) (b)

(c) (d)

Fig. 2. 15. Schematic view of (a) capacitive pixels, (b) inductive pixels with the meandered line, (c) inductive pixels with a straight line, and (d) exact solution results (FDTD).

TABLE 2.1. THE PHYSICAL PIXELS IN FIG. 2.15D.

	Capacitors							Inductor		
		C_1	C_2	C_3	C_4	C_5	C_6		L_m	L_s
Physical_params (mm)	S_1	0.16	0.32	0.48	0.48	0.64	1.12	d_m	1	0.96
	S_2	0.16	0.32	0.32	0.48	0.64	1.12			

There are at least three types of pixels for a discretized space-fed antenna. One is the resonant element, like an array of resonant dipoles [55], microstrip patch [60], and antenna/phase-shifter/antenna configuration [67]. The second type is realized by manipulating the effective permittivity of dielectric material, as an example, by making use of perforation, as shown in Fig. 2.13. Such an approach requires a relatively thick and/or high permittivity dielectric.

The third type is the sub-wavelength pixel, which usually shows up in a smaller size than the types mentioned above. The sub-wavelength element can be designed based on the circuit concept, which is much easier to deal with than the field analysis [74]. Furthermore, it can resolve the bandwidth shortcoming of the resonant type pixel, although such an imperfection can be addressed by using multi-resonant structures, notably by exploiting the optimization techniques [55] [56]. Fig. 2.14 shows an RA based on the interdigitated surface. This configuration is a variant of a sub-wavelength unit cell. The unit cells are shown in Fig. 2.15. The frequency response of pixel for normal incidence is shown in Fig. 2.15(d). The physical parameters of capacitive and inductive cells are tabulated in Table 2.1.

High pixel resolution has some potential advantages for large aperture, tilted beams, and/or small focal-to-diameter ratio (F/D). The one with a smaller pixel size is less prone to quantization distortion since the quantization noise is, in general, a wideband signal; thus, more portion of noise power appears out of the (visible) band. Of far more significance is the violation of the local periodicity assumption (LPA) pertaining to the sharp variation of phase delay arrangement (PDA), in particular, close to the extreme of the aperture, which can limit the antenna bandwidth. Furthermore, miniaturizing the pixel size is, in general, beneficial for sub-wavelength pixel types since, typically, some spurious bands appear at some frequencies and/or happen at oblique incidences. By miniaturizing the pixel size, those spurious bands happen due to physical resonance

can be shifted to higher frequencies which would be out of the antenna bandwidth. The preceding statements, nevertheless, can be controversial since using tiny pixels puts lots of pressure on the system's performance. Specifically, miniaturizing the pixel size usually decreases the number of available phase states. Indeed, quantization distortion increases, in contrast to what was mentioned about the benefits of small pixels for circumventing that nonlinear distortion.

2.4.3 RA for Space Application

The Satellite has several applications in communication, so there are a variety of systems and custom designs. In this regard, the area of coverage and required channel capacity might be considered critical points, leading to different satellite classifications. Coverage may include wide continental contour coverage and/or spot beam. If the satellite footprint is subdivided into several radio cells, then an antenna capable of radiating multiple-beam might be favorable. During the past decades, there has been a continuous endeavor in satellite systems development using frequency-polarization reuse schemes in which the same bandwidth and/or polarization are allocated to some spatially isolated spot beams. The design of multibeam antennas for telecommunication satellites in the Ka-band must deal with challenging requirements, such as the generation of a large number of high-gain spot beams, the close separation between the beams, and the alternation of frequencies and/or polarizations for adjacent beams. A schema of 4-cell frequency-polarization reuse is shown in Fig. 2.16.

The main advantage of using a spot beam is increasing the satellite throughput as a frequency band and/or polarization can be reused in a regular pattern of radio cells in the coverage area, leading to more system capacity. However, there are some challenges. For example, co-channel interference (CCI) arises, and the payload and antenna system becomes complicated.

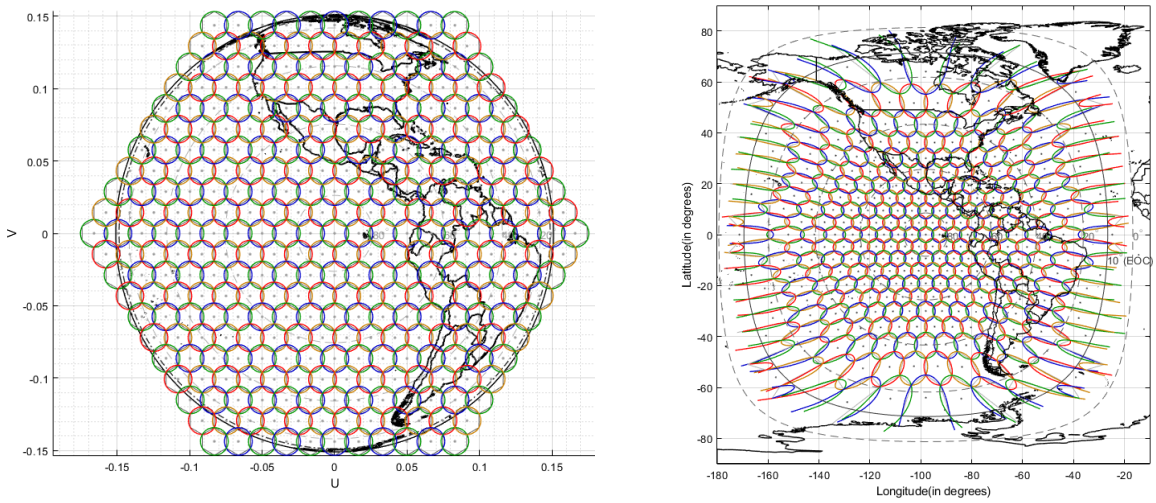

(a) (b)

Fig. 2. 16. Layout of the radio cells of 11 tiers with a 4-cell reuse scheme, the orbital position of the geostationary orbit satellite is considered at 98°W, (a) the layout of the radio cells from the antenna view angle, and (b) the projection of the radio cells on the earth.

Typically, ideal radio cells are defined in a hexagon shape to fill up the satellite footprint without overlapping radio cells, as every cell fits tight with the adjacent cells, making the analysis easier. In a bit more practical approach, the shape of the radio cells is inspired by the projection of a typical directive radiator (pencil beam) on the earth. Usually, 3- or 4-dB perfect circular spots with the same radii are considered the radio cells (see Figs. 1b), which are visualized from the antenna view angle (see Figs. 2.16). This means that the antenna is considered to have equal beamwidth for all cells. For a practical radiator, neither all spots have an exactly circular shape, nor do antenna gain and beamwidth remain constant as the beam is sweeping toward the edge of the coverage (EOC). Furthermore, the projection of the circular radio cells on the earth's surface is only circular for the cell generally illuminated by the satellite antenna, see Fig. 2.16(b).

The set of adjacent radio cells containing the total channels (C_t), the whole frequency and/or polarization assigned are called a cluster which will be repeated in the whole area of coverage. The size of the cell cluster, which is the number of beams inside a cluster, is called the reuse factor (k). Typically, it depends on the maximum amount of tolerable interference. Using a higher reuse factor

increases the distance between the co-channel spots, thus, improving the CCI. However, it simultaneously decreases the bandwidth per beam, leading to fewer users per beam. In other words, it decreases the number of channels per cell or capacity per spot ($C_c = {C_t}/{k}$). If clusters are replicated *N* times in a geographic area, then the whole system capacity reads:

$$SC = N \times C_t = N \times k \times C_c$$

Another major factor is the CCI, which is one of the most important parameters in every cellular network as there is a tendency to increase the whole system capacity by using higher coverage resolution, which decreases the physical distance between the co-channel spots.

As discussed in the previous section, the capability of RA to discriminate in frequency and/or polarization can be of particular interest for designing multibeam antennas in the Ka-band. In [78], the classic bifocal concept has been applied to the design of multibeam dual-reflectarray antennas in order to obtain better performance for the extreme beams while providing, at the same time, closer beams with non-overlapping feeds than those provided by a single-focus antenna. For the traditional design of the Multi-focal RA (MF-RA), the PDA might be written as

$$\varphi_{\boldsymbol{i}} = \left(\sum_{n=0}^{M-1} \alpha_n\right)^{-1} \sum_{n=0}^{M-1} \alpha_n \left(k\left\|\acute{\boldsymbol{r}}_{d_n,\boldsymbol{i}}\right\|_2 + \xi_{d_n,\boldsymbol{i}}\right) \tag{2.4}$$

where α_n is an arbitrary weighting, the subscript d_n signifies the n*th* design element, *e.g.,* assume $\boldsymbol{f}_{d_n}$ is the vector of the nth feed position associated with the nth beam direction, $\boldsymbol{p}_{d_n}$In the single-focus RA (SF-RA) sense, then $\acute{\boldsymbol{r}}_{d_n,\boldsymbol{i}} = \alpha \boldsymbol{L}\boldsymbol{i} - \boldsymbol{f}_{d_n}$, where $\boldsymbol{L}$ is the lattice matrix, α is the weighting factor, and $\boldsymbol{i}$ is an integer column vector. Besides, $\xi_{d_n,\boldsymbol{i}} = -k\left(\boldsymbol{r}_{\boldsymbol{i}} \odot \boldsymbol{p}_{d_n}\right)$. Accordingly, one may write

$$\Psi_{\boldsymbol{i}} = \langle \xi_{d_n,\boldsymbol{i}} \rangle_n + k\left[\langle \left\|\acute{\boldsymbol{r}}_{d_n,\boldsymbol{i}}\right\|_2 \rangle_n - \left\|\acute{\boldsymbol{r}}_{s,\boldsymbol{i}}\right\|_2\right] \tag{2.5}$$

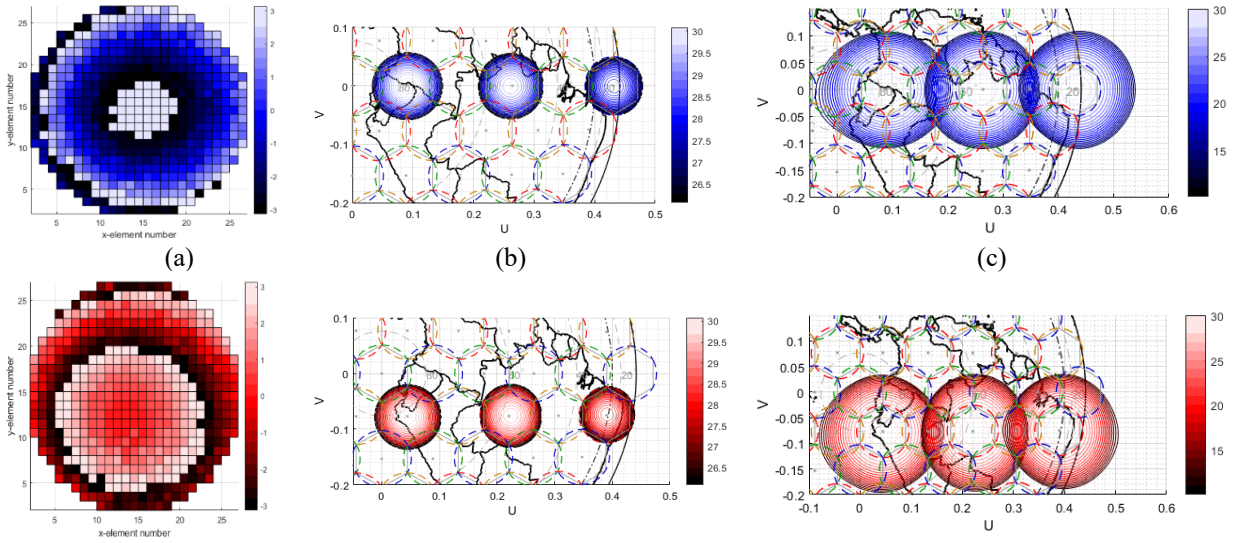

Fig. 2. 17. Optimized aperture phases with associated spots. (a) Optimized aperture phases for x-polarization at 18.9 GHz, (b) 4-dB spot beams for "blue cells," (c) 20-dB spot beams for blue cells, (d) optimized aperture phases for y-polarization at 18.9 GHz, (e) 4-dB spot beams for red cells, and (f) 20-dB spot beams for red cells.

where $\acute{\boldsymbol{r}}_{s,i} = \boldsymbol{r}_i - \boldsymbol{f}_s$ and $\boldsymbol{f}_s$ is an arbitrary feed position.

However, it can be shown that using the intuitive (2.4) does not contribute to the optimal solution. Besides, if one uses (2.4) to design the Multi-focal PDA for specific focuses and associated beam directions, the feed positions would not be precisely under control and should be specified for each vector $\boldsymbol{\alpha}$ chosen. This can be problematic for design, e.g., a feed position might not be practical due to the blockage it may cause. So, typically, an optimization scheme is required to be employed. In Figs 2.17, optimized aperture MF-RAs are designed for MEO satellites. The results of PDA for two channels and the associated spot beams are shown. The optimization algorithm is discussed in Chapter 8.

2.4.4 Sub-Wavelength Unit Cell

As stated, a sub-wavelength cell for RA is one type of unit cell. A prominent advantage of this type is that its frequency response can be modeled using lumped element, which facilitates the analysis. Here, we have modeled the pixel by using surface impedance which relates the surface

current to the tangential electric field; therefore, for the impedance boundary condition (IBC), we can write:

$$\bar{\bar{\mathbf{Z}}}_s \times \mathbf{J}_s = -\hat{n} \times \hat{n} \times \mathbf{E} \tag{2.6}$$

where $\mathbf{J}_s$ is the vector of surface current, $\bar{\bar{\mathbf{Z}}}_s$ is the tensor of the surface impedance, and $\mathbf{E}$ is the vector of the electric field and $\hat{n}$ is normal to the surface. We have the following equations on the boundary with respect to Fig. 2.18:

$$-\hat{z} \times (\mathbf{E}_2 \mid_{z=0^-} - \mathbf{E}_1 \mid_{z=0^+}) = 0 \tag{2.7.a}$$

$$-\hat{z} \times (\mathbf{H}_2 \mid_{z=0^-} - \mathbf{H}_1 \mid_{z=0^+}) = \mathbf{J}_s \tag{2.7.b}$$

where it is assumed that the impinging and reflected EM waves are in the first medium ($\mathbf{E}_1$, $\mathbf{H}_1$) on the positive side of the *z*-axis while the transmitted wave is supposed to be in the second medium (inside the substrate) on the negative side of the *z*-axis ($\mathbf{E}_2$, $\mathbf{H}_2$). Alternating (2.7.b) in (2.6) contributes to (2.8).

$$\hat{z} \times \bar{\bar{\mathbf{Z}}}_s \times \hat{z} \times (\mathbf{H}_2 \mid_{z=0^-} - \mathbf{H}_1 \mid_{z=0^+}) = -\hat{z} \times \mathbf{E} \mid_{z=0^+/0^-} \tag{2.8}$$

Then, we need to translate the coordinate system of the incoming wave from the feed coordinate system to the RA's coordinate system. This can be done by using a proper coordinate system rotation. Let us assume the incoming electric field in its coordinate system $\mathbf{E}'$ (see Fig. 2.18a); hence, the impinging field $\mathbf{E}$ in the coordinate system of the reflective surface can be written as (2.9), which is realized by proper rotation of the coordinate system.

$$\begin{bmatrix} E_x \\ E_y \\ E_z \end{bmatrix} = \begin{bmatrix} -\cos\varphi_i.\cos\theta_i & -\sin\varphi_i & \cos\varphi_i.\sin\theta_i \\ -\sin\varphi_i.\cos\theta & \cos\varphi_i & \sin\varphi_i.\sin\theta_i \\ -\sin\theta_i & 0 & -\cos\theta \end{bmatrix} \begin{bmatrix} E'_x \\ E'_y \\ E'_z \end{bmatrix} \tag{2.9}$$

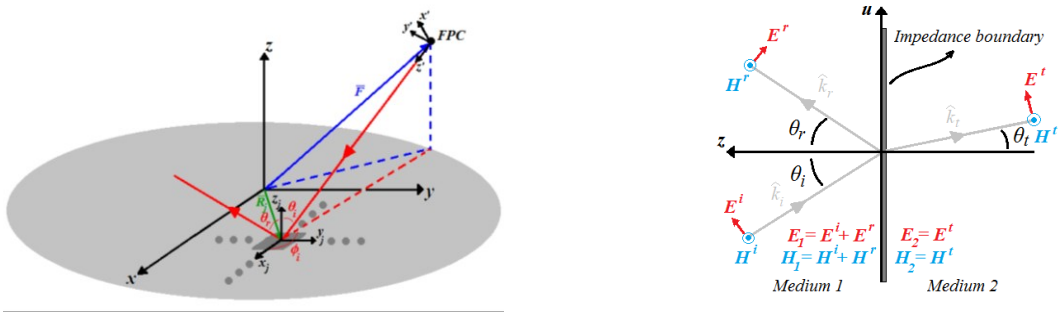

(a) (b)

Fig. 2. 18. Schematic view of the reflective surface. (a) Schematic view of arbitrary pixel and a feed at the focal point represented by the feed phase center (FPC) and (b) 2D schematic view of the impedance boundary condition for TE incidence.

Evidently, θ_i and φ_i are supposed to be known for each pixel, as the vectors $\vec{r}$ (feed position) and $\vec{\mathbf{k}}_j - \vec{\mathbf{k}}_{[m,n]}$ (the *j*th pixel position) are supposed to be known. For simplicity, we may consider a *y*-polarized wave. Also, we may assume that the pixel does not contribute to the aperture cross-polar content. Therefore, the surface impedance reflected and transmitted coefficients can be written as:

$$\bar{\bar{\mathbf{Z}}}_s = \begin{bmatrix} Z_{xx} & 0 \\ 0 & Z_{yy} \end{bmatrix} \tag{2.10.a}$$

$$\bar{\bar{\mathbf{\Gamma}}}_s = \begin{bmatrix} \Gamma_{xx} & 0 \\ 0 & \Gamma_{yy} \end{bmatrix} \tag{2.10.b}$$

$$\bar{\bar{\mathbf{T}}}_s = \begin{bmatrix} T_{xx} & 0 \\ 0 & T_{yy} \end{bmatrix} \tag{2.10.c}$$

The incident, reflected, and transmitted electric and magnetic fields on the impedance boundary (for *y*-polarized feed) are calculated as written in (2.11) in which θ_i', θ_r', and θ_t' are altitude angles of incoming and outgoing rays with respect to the positive direction of the *z*-axis and might be correspondingly written as $\theta_i' = \theta_i + \pi$, $\theta_t' = \theta_t + \pi$, $\theta_r' = -\theta_r$, $\boldsymbol{E}_0$ is the magnitude of the electric field

at the surface impedance boundary, k_1 and k_2 are the propagation constants in Medium 1 and 2, respectively.

$$\mathbf{E}^i|_{z=0^+} = E_0 \cdot (-\sin\varphi_i \hat{x} + \cos\varphi_i \hat{y}) \cdot \exp(j\psi_i) \tag{2.11.a}$$

$$\mathbf{E}^r|_{z=0^+} = E_0 \cdot (-\Gamma_{xx} \cdot \sin\varphi_r \hat{x} + \Gamma_{yy} \cdot \cos\varphi_r \hat{y}) \cdot \exp(j\psi_r) \tag{2.11.b}$$

$$\mathbf{E}^t|_{z=0^+} = E_0 \cdot (-T_{xx} \cdot \sin\varphi_t \hat{x} + T_{yy} \cdot \cos\varphi_t \hat{y}) \cdot \exp(j\psi_t) \tag{2.11.c}$$

$$\psi_i = -k_1 \cdot (x \cdot \cos\varphi_i \cdot \sin\theta_i' + y \cdot \sin\varphi_i \cdot \sin\theta_i') \tag{2.11.d}$$

$$\psi_r = -k_1 \cdot (x \cdot \cos\varphi_r \cdot \sin\theta_r' + y \cdot \sin\varphi_r \cdot \sin\theta_r') \tag{2.11.e}$$

$$\psi_t = -k_2 \cdot (x \cdot \cos\varphi_t \cdot \sin\theta_t' + y \cdot \sin\varphi_t \cdot \sin\theta_t') \tag{2.11.f}$$

Ignoring diffraction and scattering effects of the metallic layer and utilizing (2.7.a), (2.11), and the phase-matching condition [43], which implies that $\psi_i = \psi_r = \psi_t$. The boundary condition (2.8) contributes to (2.12):

$$T_{uu}\left(\frac{Z_{uu}\cos\theta_t}{\eta_2} + 1\right) = \frac{Z_{uu}\cos\theta_i}{\eta_1}(1 - \Gamma_{uu}) \tag{2.12}$$

where *u* might be alternated by *x* or *y*. Besides, the plane wave assumption ($\mathbf{H} = \frac{\vec{k}}{\eta} \times \mathbf{E}$) has been used in calculating the magnetic fields. Let us assume $Z_i = \frac{\cos\theta_i}{\eta_i}$ and $Z_t = \frac{\cos\theta_t}{\eta_t}$, then (2.12) can be simplified as follows:

$$\Gamma_{uu} = \frac{Z_t Z_{uu} - Z_i Z_{uu} - Z_i Z_t}{Z_t Z_{uu} + Z_i Z_{uu} + Z_i Z_t} \tag{2.13.a}$$

$$T_{uu} = \frac{2Z_t Z_{uu}}{Z_t Z_{uu} + Z_i Z_{uu} + Z_i Z_t} \tag{2.13.b}$$

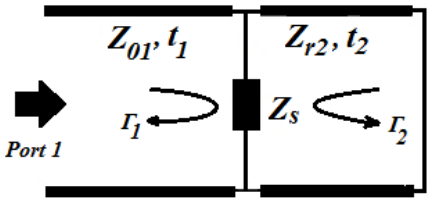

Fig. 2. 19. Simple equivalent circuit model of the RA pixel.

It can be shown that (2.13) is also correct for the *x*-polarized wave (TE incidence) by considering the $Z_i = \eta_i \cos\theta_i$ and $Z_t = \eta_t \cos\theta_t$. To find the total reflection from the pixel, we need to consider the simple equivalent circuit model presented in Fig. 2.19. It is possible to translate the oblique incidence of the plane wave to a transmission line model by considering the problem as a transverse equivalent network (TEN) [38]; therefore, the Z_{01} and Z_{r1} in Fig. 2.19 would be respectively equal to Z_i and Z_t for a wave propagating from the Medium 1 to 2. Moreover, the transverse propagation constants should be used $\beta_i = k_i \cos\theta_i$ and $\beta_t = k_t \cos\theta_t$ for both TE and TM incidences. Finally, by making use of the theory of small reflections [82], the total reflection coefficient can be written as:

$$\Gamma_{uu}^{t} = \left(\Gamma_{uu}^{11} + \frac{\Gamma_{uu}^{12} \cdot \Gamma_{uu}^{21} \cdot \Gamma_s \cdot e^{-2j \cdot k_2 \cdot t_2 \cdot \cos\theta_t}}{1 - \Gamma_{uu}^{22} \cdot \Gamma_s \cdot e^{-2j \cdot k_2 \cdot t_2 \cdot \cos\theta_t}} \right) \cdot e^{-2j \cdot k_1 \cdot t_1 \cdot \cos\theta_i} \tag{2.14}$$

where Γ_s is the reflection coefficient from the backscatterers. Hence, it might be considered as -1 for a solid PEC, Γ_{uu}^{11} and T_{uu}^{21} (Γ_{uu}^{22} and T_{uu}^{12}) can be calculated from (2.13) using Z_i and Z_t. As an example, for the TE incidence of a wave traveling from Medium 2 to Medium 1, the T_{uu}^{12} and Γ_{uu}^{22} can be calculated by considering $Z_i = \eta_2 \cos\theta_t$ and $Z_t = \eta_1 \cos\theta_i$. Note that (2.14) can be modified for several layers. The surface impedance can be determined by analytical calculation or

simply utilizing the curve fitting of the exact solution only for the normal incidence. If the cell is small enough, it acts like a lumped element; hence, the value of electrical parameters of the impedance boundary remains almost constant against the angle of incidence in an acceptable frequency band. There is necessary to note the prime assumptions made for the above calculations. Firstly, the pixel is considered infinitely periodic, which is not an accurate assumption for the modulated surface impedances. For a small enough variation of the surface impedance, for example, by gently changing the physical properties of the pixel, such as spacing or rotating the pixel, the above calculation remains almost accurate. However, there would be higher modes near the borders of the pixels due to discontinuities incurred for sharp variations. Reactive lumped elements can model the aforesaid evanescent modes as they are localized stored energies; thus, the effective value of the surface impedance deviates from the one assumed in the infinite periodic assumption introducing further error. Secondly, the pixels are assumed to be lossless and do not contribute to cross-polarization. The amount of this kind of error depends on the type of pixel and the material used. Finally, it has been assumed that the pixel is small enough. For the larger pixel sizes, the assumption of constant current might be undermined, and the higher orders of space harmonics start to be unleashed, contributing to the deviation of surface impedance values.

Fig. 2.20 compares the exact solution results (FDTD) and computed results of two arbitrary pixels in Fig. 2.15 for different frequencies and angles of incidence. The surface impedance matrix is extracted by curve fitting for the normal incidence. As can be seen, there is a very good agreement between the computed and exact solutions. In Fig. 2.21, the variation of transfer characteristics against the frequency and angle of incidence are analytically calculated and presented for TE incidence.

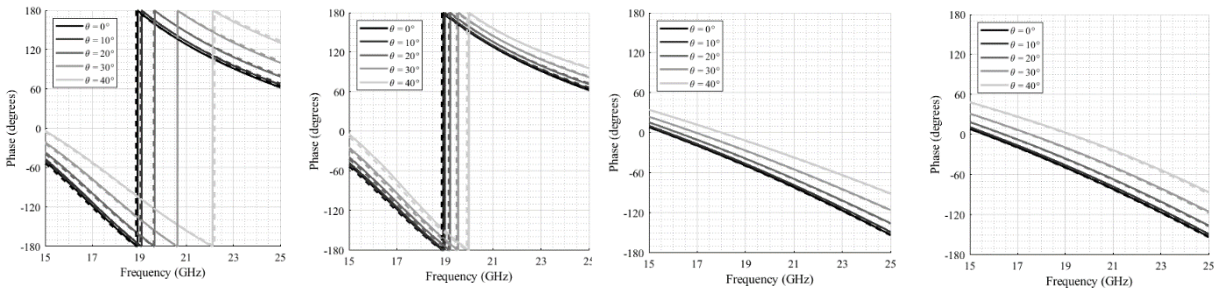

(a) (b) (c) (d)

Fig. 2. 20. Exact solutions (solid line) and proposed analytical method (dashed line) of (a) C2 (40 fF) in Fig. 2.15 for TE incidence, (b) C2 (40 fF) in Fig. 2.15 for TM incidence, (c) C5 (9.2 fF) in Fig. 2.15 for TE incidence, and (d) C5 (9.2fF) in Fig. 2.15 for TM incidence.

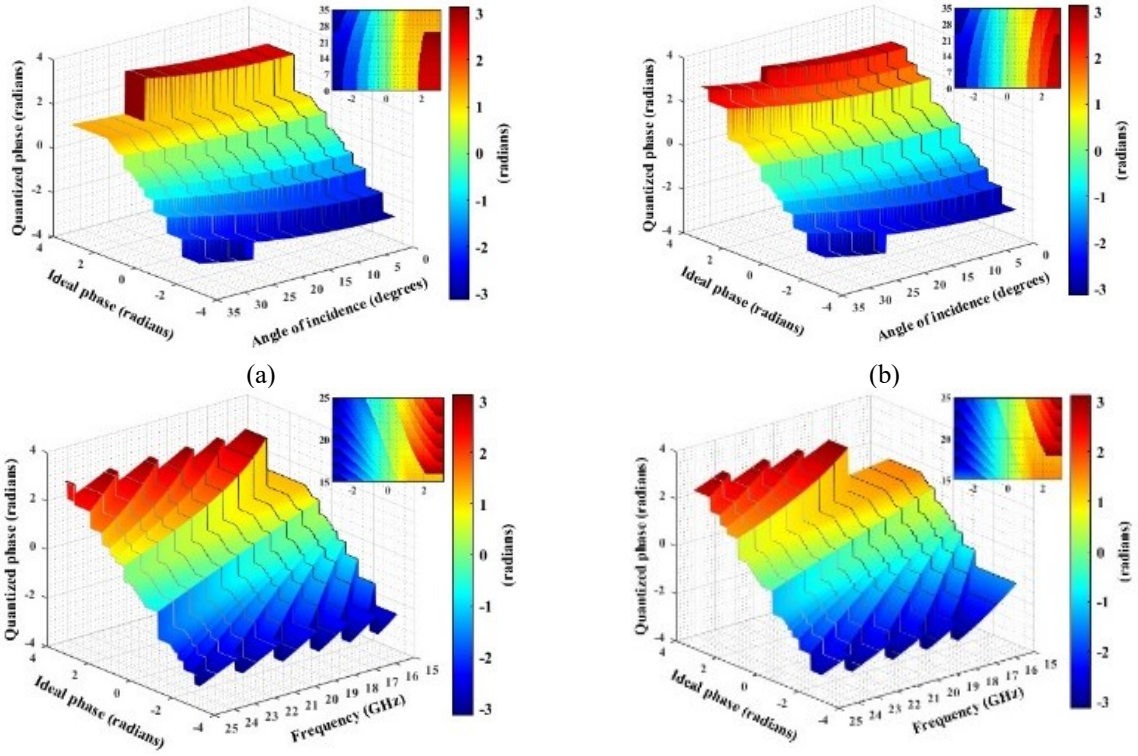

(a) (b)

(c) (d)

Fig. 2. 21. Variation of the transfer characteristics of the capacitive/inductive interdigitated pixels for TE incidences against frequency and angle of incidence, (a) at 17 GHz, (b) at 20 GHz, (c) for normal incidence (θ = 0°), and (d) for θ = 35°.

The solid lines show the exact solutions perfectly compatible with the analytical results. It can be seen that for the assumed distance of the port from the pixel (3 mm), the transfer characteristics have more significant jumps of phase states near the π for lower frequencies, whereas phase steps remain almost constant near $-\pi$ (compare Figs. 2.21 and 2.21). This also could be realized by noting Fig. 2.20. For higher frequency bands, the transfer characteristics seem less sensitive than the lower

frequency bands, but still, there are some deviations from the one for the center frequency. Also, it can be seen that the transfer characteristics are a nonlinear function of the incidence angle for parallel polarization (TE incidence). In particular, note that for a higher angle of incidence, the pixel has poorer transfer characteristics, especially at lower frequency bands. This may limit the antenna bandwidth.

Chapter 3
Quantization

3.1 Quantization in analog beamforming

As an example, for RA, let us assume one aperture-plane component of the reflected field as $E_C[\boldsymbol{i}] = jA_{\boldsymbol{i}}e^{j\Phi_i}$ where $\boldsymbol{i} \in \mathbb{Z}^2$. For high-precision PDA, let $\Phi_{\boldsymbol{i}} = \Psi_{\boldsymbol{i}}$ and for the quantized one, let $\Phi_{\boldsymbol{i}} = \Upsilon_{\boldsymbol{i}}$; thereby,

$$\Psi_{\boldsymbol{i}} = \varphi_{\boldsymbol{i}} - k\|\acute{\boldsymbol{r}}_{\boldsymbol{i}}\|_2, \qquad \Upsilon_{\boldsymbol{i}} = Q(\varphi_{\boldsymbol{i}}) - k\|\acute{\boldsymbol{r}}_{\boldsymbol{i}}\|_2$$

where $\varphi_{\boldsymbol{i}} = k\|\acute{\boldsymbol{r}}_{\boldsymbol{i}}\|_2 + \xi_{\boldsymbol{i}}, \acute{\boldsymbol{r}}_{\boldsymbol{i}} = \boldsymbol{r}_{\boldsymbol{i}} - \boldsymbol{f}_{\boldsymbol{d}}, \ \xi_{\boldsymbol{i}} = -k(\boldsymbol{r}_i \odot \boldsymbol{p}_{\boldsymbol{d}}), \boldsymbol{r}_{\boldsymbol{i}}$ is the i*th* pixel position vector, $\boldsymbol{f}_{\boldsymbol{d}}$ and $\boldsymbol{p}_{\boldsymbol{d}}$ are the vectors of feed position and beam direction, respectively. Accordingly, one may write the quantization error of the excitation signal as follows:

$$e_{E,C}[\boldsymbol{i}] = A_{\boldsymbol{i}}[\exp(j\Upsilon_{\boldsymbol{i}}) - \exp(j\Psi_{\boldsymbol{i}})] \tag{3.1}$$

by some trivial manipulations, it takes the following form:

$$e_{E,C}[\boldsymbol{i}] = -2A_{\boldsymbol{i}} \sin\frac{e_{\varphi,i}}{2} e^{j\left(\frac{e_{\varphi,i}}{2}+\Psi_i\right)} \tag{3.2}$$

where $e_{\varphi,\boldsymbol{i}} = \Upsilon_{\boldsymbol{i}} - \Psi_{\boldsymbol{i}}$ is the PDA error. One may simplify the equation for small quantization width by using the second-order approximation of the Taylor series, which reads (3.3).

$$e_{E,C}[\boldsymbol{i}] \approx -A_{\boldsymbol{i}}\, e_{\varphi,\boldsymbol{i}} e^{j\left(\frac{e_{\varphi,i}}{2}+\Psi_i\right)} \approx -A_{\boldsymbol{i}}\, e_{\varphi,\boldsymbol{i}} e^{j\Psi_i} \tag{3.3}.$$

For the argument of the complex exponential, half of the PDA error is not in the form of a progressive phase shift. Thus, the excitation error corresponds to the weighted PDA error steered to the beam point direction. In fact, (3.2) and (3.3) also work for the PA antenna by considering the phasor $jA_{\boldsymbol{i}}e^{j\Phi_i}$, as current excitation.

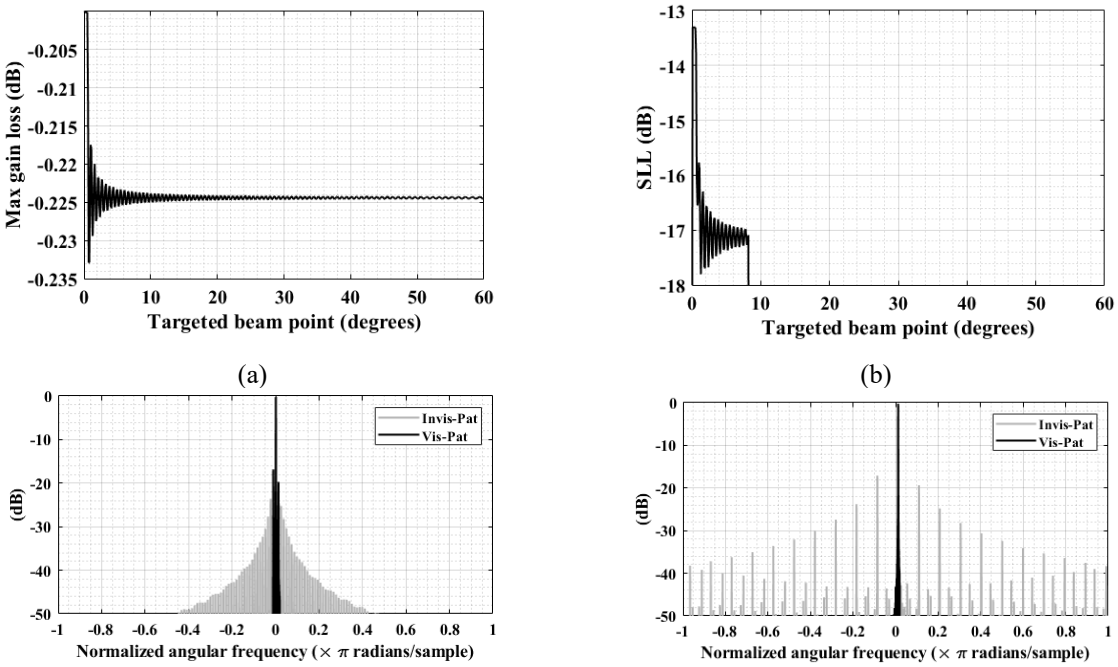

Fig. 3. 1 Computed results of exemplar phased array. (a) Maximum gain loss, (b) the first sidelobe level for linear "supersampled" array of length $25.5\lambda_0$. Computed array factor on one fundamental period of the beamspace for targeted beam point at (c) 4.4°, and (d) 38.6°.

Consider an equally spaced linear array with a simple cosine tapering as an illustrative example. The array length is assumed to be $25.5\lambda_0$. For now, we only consider phase quantization. In the current study, an ideal 3-*bit* digital phase shifter is assumed. Fig. 3.1 shows the result of beam steering up to 60° for a "supersampled" array, a quasi-continuous excitation. This is considered to discriminate between the effects of quantization and sampling errors. As seen in Fig. 3.1(a), the maximum gain loss hovers around a convergence level with an exponential envelope shape by increasing the steering angle. Also, it can be seen in Fig. 3.1(b) that the QL level drops after about 8.2°.

In fact, by increasing the steering angle, the period of quantization error decreases; thereby, the QLs shift to higher spatial frequencies, which are not inside the so-called "visible window" of the supersampled array. This has been shown in Figs. 3.1(c) and 3.1(d) for two exemplars commanded beam directions. Fig. 3.1(c) shows the pattern for a targeted point at 4.4° in one beamspace

fundamental period. As seen, the unperturbed radiation pattern is corrupted by at least two QLs inside the visible window, but there is no in-band QL for the one with the commanded beam at 38.6°, illustrated in Fig. 3.1(d). Finally, the harmonics become further separated by increasing the beam steering angle, making wider band excitation errors. This is simply because of the periodicity decrease of error signal by increasing the steering angle. In this regard, one may note the alias artifacts in Fig. 3.1(d).

Now, let us consider an array of the half-wavelength pitch. In this case, the array behavior changes to some extent. The signals illustrated in Figs. 3.2(a) and 3.2(b) are somehow the periodic versions of the ones illustrated in Figs. 3.1(a) and 3.1(b), respectively. However, each period shape is expanding as it approaches the 60° targeted point due to more severe aliasing. As stated before, by increasing the targeted beam point of the supersampled array, the QL harmonics become more separated; thereby, the error signal bandwidth gets wider, and the excitation error is more prone to spatial frequency aliasing.

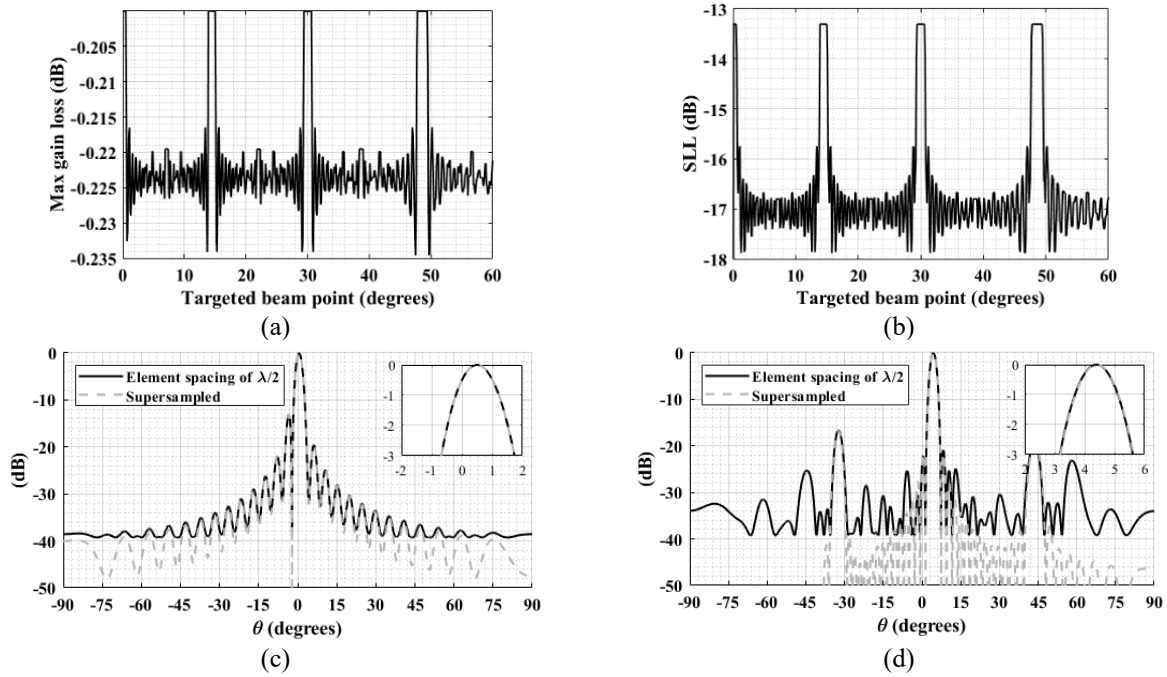

Fig. 3. 2. Computed results for exemplar linear array of length $25.5\lambda_0$ and $\lambda_0/2$ element spacing. (a) maximum gain loss, (b) the first sidelobe level. Computed array factor for targeted beam point at (c) 0.5°, and (d) 4.4°.

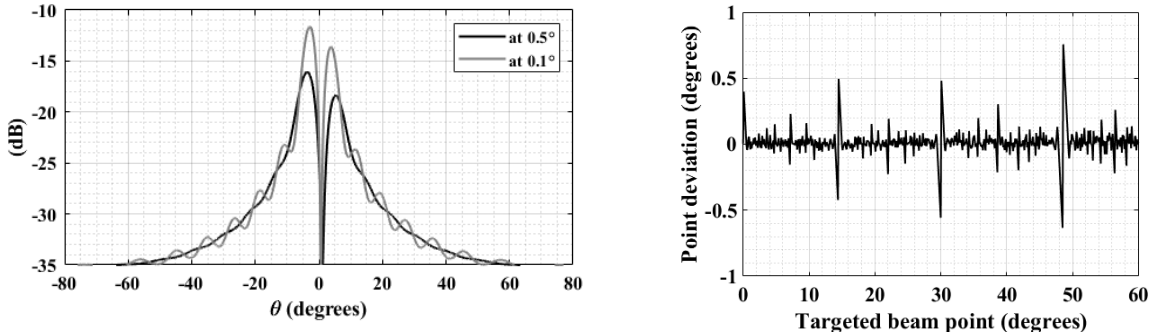

(a) (b)

Fig. 3. 3. Computed error pattern and point deviation for a linear array of length $25.5\lambda_0$ and $\lambda_0/2$ element spacing. (a) Error pattern for beam targeted at 0.1° and 0.5° and (b) Point deviation of linear array described in Fig. 2.2.

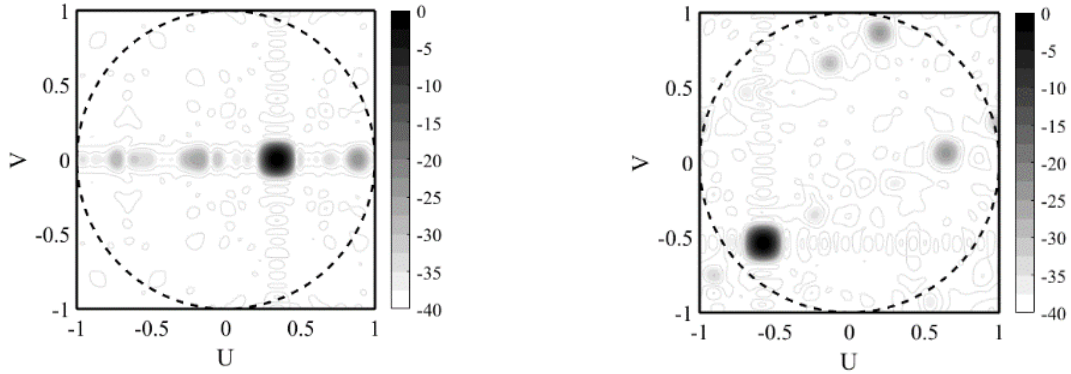

(a) (b)

Fig. 3. 4. Decibel array factors for 4-bit (a) $[\theta, \varphi]$ = [20°, 0°] and (b) $[\theta, \varphi]$ = [52°, 223°].

In Figs. 3.2(c) and 3.2(d), the phased array computed radiation patterns with a half-wavelength pitch are compared with their supersampled counterparts for the commanded beam points at 0.5° and 4.4°. It is well-known that the quantization noise is a wideband signal, but its manifestation is of harmonic form for a periodic signal. Therefore, several QLs appeared in the conventional array radiation pattern are, in fact, alias QLs.

The reason for point deviation is straightforward and well-understood. For example, for the linear array in example Fig. 3.2, the beam targeted at 0.1° collimates to 0.5° due to the phase ambiguity caused by the assumed 3-*bit* uniform quantizer. For 0.1°, the PDA signal has two quantized states. In other words, the quantizer simply rounds up all positive phases to a quantized

state, whereas all negative phases are rounded to the inferior quantized phase state; thereby, due to the low resolution of the quantizer, the system is unable to discriminate between the two commanded beam points which are 0.1° and 0.5°. This phenomenon shows itself in the beamspace domain, as the one illustrated in Fig 3. 3(a). In the case of a beam commanded at 0.5°, a broader null exists between two lobes of less magnitude than those commanded at 0.1°. Like SLL and gain loss, the point deviation shows up in a quasi-periodic fashion, with a seemingly exponential envelope, against the targeted beam point for an array with a half-wavelength pitch, as shown in Fig. 3. 3(b).

Finally, just as an example of a planar array, two steered array factors are shown in Fig. 3. 4. The array is of circular aperture with square lattice and half-wavelength pitch with a diameter of 13.5λ. Both phase and amplitude are quantized to 4 bits. As seen, it contributes to the appearance of QLs.

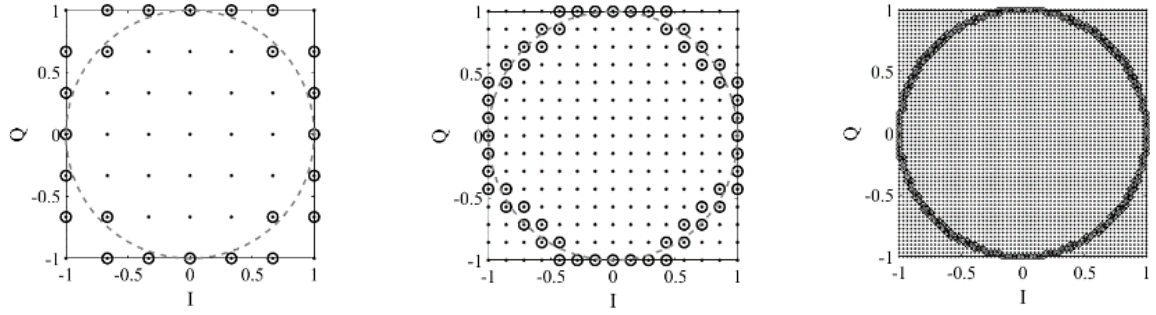

(a) (b) (c)

Fig. 3. 5. Complex beamforming weight with unity amplitude. The IQ plane is quantized to (a) 3, (b) 4, and (c) 6 bits.

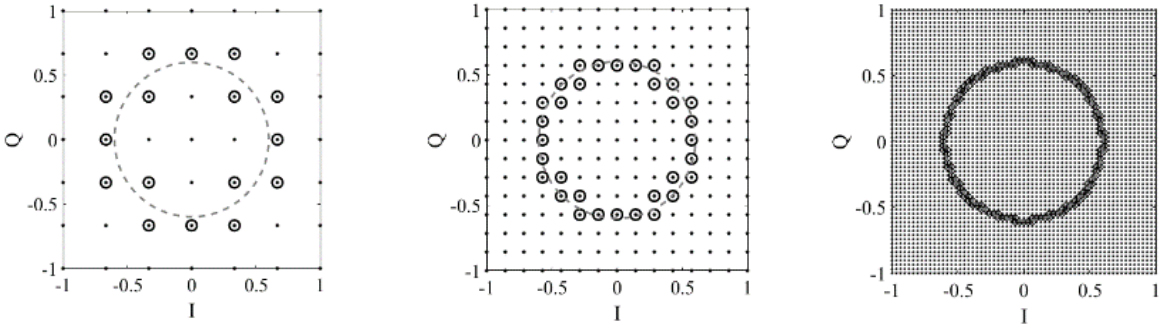

(a) (b) (c)

Fig. 3. 6. Complex beamforming weight with amplitude 0.6. The IQ plane is quantized to (a) 3, (b) 4, and (c) 6 bits.

3.2. Quantization in digital beamforming

In DBF, each antenna receives an RF signal replica which might be simply modeled as

$$f(t, \boldsymbol{k_i}) = x(t - \tau_i)\cos\left[w_{rf}(t - \tau_i)\right] \approx x(t)\cos(w_{rf}t - \varphi_i)$$

where $\boldsymbol{k_i}$ is element position vector and $\varphi_i = w_{rf}\tau_i$. Note that f is a function of $\boldsymbol{k_i}$ through the τ_i. The received RF signal is amplified, down-converted to IF or baseband (BB), and is subsequently digitized. Depending on the scheme used, digital down-conversion and filtering procedures would be used. Overall, the two I/Q components might be written

$$\mathcal{I}_i[m] = x[m]\cos\varphi_i,\ \mathcal{Q}_i[m] = x[m]\sin\varphi_i$$

where $\boldsymbol{i} \in A \subset \mathbb{Z}^2$ is the index number of the active elements in the spatial domain, and $m \in \mathbb{Z}$ counts the snapshots of the incident signal at a sampling rate acceptably above the Nyquist rate. The digital I/Q components might be multiplied by complex weights and subsequently combined. Accordingly, the ultimate sequence might be written as

$$s[m] = \frac{1}{|A|}\sum_{\boldsymbol{i}} \mathcal{I}_i[m]I_i + \mathcal{Q}_i[m]Q_i + \frac{j}{|A|}\sum_{\boldsymbol{i}} \mathcal{Q}_i[m]I_i - \mathcal{I}_i[m]Q_i$$

with $I_i = a_i\cos\varphi_i$, $Q_i = a_i\sin\varphi_i$, $w_i^* = I_i - jQ_i = a_i e^{-j\varphi_i}$ constituting the CBW matrix $\boldsymbol{W}^* = \boldsymbol{I} - j\boldsymbol{Q}$ and $|A|$ is the cardinality of set A, which is the set of active elements.

There might be two ways, at least, to quantify the complex exponent. One may consider N_φ and N_a bits for each I/Q component of complex exponent and amplitude components, a_i, or just $N_{I/Q}$ bits to quantify each I_i and Q_i. Therefore, the problem under study concerns the limited number of bits for complex weights in the digital domain.

Considering $w_i^* = a_i e^{-j\varphi_i}$, as stated, one may use N_a bits to quantify a_i and N_φ bits for each in-phase and quadrature component of $e^{-j\varphi_i}$. For now, let us assume a uniform amplitude of unity, a_i = 1. Fig. 3.5 shows the I/Q plane for 3-, 4- and 6-*bit* systems. For the 3-*bit* system, there are

seven quantization steps for each I and Q component; hence, the I/Q plane is resampled to a matrix of size 7×7 = 49, whose elements are shown by solid black circles. Each φ_i corresponds to a point on the unit circle shown by the dashed line. For such a case, those elements in the vicinity of the unit circle should be considered as available quantization steps, which are schematically illustrated by the hollow black circles. Clearly, this imposes phase and amplitude errors. Besides, if a specific array weighting is of interest, the amplitude coefficients, quantified by N_a bits should be multiplied by the results derived from the I/Q plane to realize the CBW matrix. On the other hand, as the second approach, one may quantify each I_i and Q_i by $N_{I/Q}$ bits. This approach imposes less computational burden; however, it incurs more severe distortion typically. The reason is that the amount of error somehow depends on amplitude. The perimeter of the high precision circle decreases for small magnitude, and less effective quantization steps would be available. This has been shown in Fig. 3.6 for a_i = 0.6. As seen, there are 16 phase quantization steps available for one cycle in Fig. 3.6(a), while there are 24 steps for the unit radii in Fig. 3.5(a); hence, the smaller the signal magnitude, the fewer quantization steps be available. The CBW quantization error can be written as follows:

$$e_i = \mathbb{Q}(c_i) - c_i = [\mathbb{Q}(I_i) - I_i] - j[\mathbb{Q}(Q_i) - Q_i] = e_{I,i} - je_{Q,i},$$

$$\varphi_{e,i} = -\tan^{-1}\left(\frac{e_{Q,i}}{e_{I,i}}\right) = -\tan^{-1}\left(\frac{\mathbb{Q}(Q_i) - Q_i}{\mathbb{Q}(I_i) - I_i}\right)$$

$$A_{e,i} = \sqrt{e_{I,i}^2 + e_{Q,i}^2}$$

The above statements provide some degrees of randomness for phase and amplitude errors which somehow helps to span the quantization error in the beamspace domain in contrast to harmonized error usually realized in ABF due to the direct quantization of phase and amplitude by DPSs, $\varphi_{e,i} = \mathbb{Q}(\varphi_i) - \varphi_i$, and DAs, $A_{e,i} = \mathbb{Q}(A_i) - A_i$.

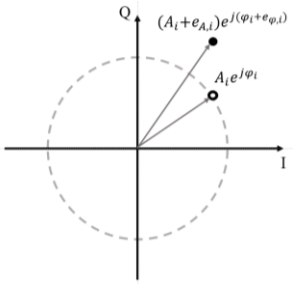

Fig. 3. 7. Schematic of an available quantized step, solid circle, for a high precision sample, hollow circle, in IQ plane.

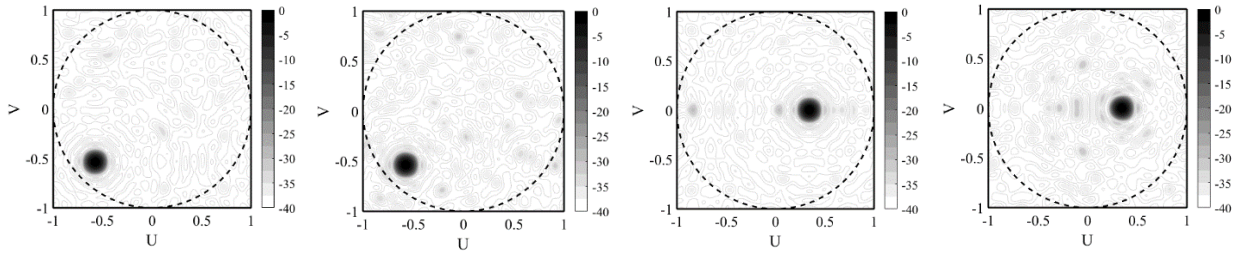

(a) (b) (c) (d)

Fig. 3. 8. Computed array factor for exemplar digital beamforming. Decibel array factor steered at $[\theta, \varphi]$ = [52°, 223°] for (a) $N_\theta = N_a = 4$, (b) $N_{I/Q} = 4$. Decibel array factor steered at $[\theta, \varphi]$ = [20°, 0°] for (c) $N_\theta = N_a = 4$, and (d) $N_{I/Q} = 4$.

Concerning Fig. 3.7, one may write the quantized signals and the associated error for the quantizer mentioned above as follows

$$\mathbb{Q}_1(c_i) = \left(A_i + e_{a,i}\right)\left(1 + e_{A1,i}\right)\exp\left[j\left(\varphi_i + e_{\varphi 1,i}\right)\right] \tag{3.4.a}$$

$$e_{1,i} \approx \mathbb{Q}_1(c_i) - c_i = j2A_i \exp(j\varphi_i)\exp\left(j\frac{e_{\varphi 1,i}}{2}\right)\sin\left(\frac{e_{\varphi 1,i}}{2}\right) + \left(e_{A1,i} + e_{a,i}\right)\exp\left[j\left(\varphi_i + e_{\varphi 1,i}\right)\right] \tag{3.4.b}$$

$$\mathbb{Q}_2(c_i) = \left(A_i + e_{A2,i}\right)\exp\left[j\left(\varphi_i + e_{\varphi 2,i}\right)\right] \tag{3.5.a}$$

$$e_{2,i} = \mathbb{Q}_2(c_i) - c_i = j2A_i \exp(j\varphi_i)\exp\left(j\frac{e_{\varphi 2,i}}{2}\right)\sin\left(\frac{e_{\varphi 2,i}}{2}\right) + e_{A2,i}\exp\left[j\left(\varphi_i + e_{\varphi 2,i}\right)\right] \tag{3.6.b}$$

where the first quantizer, $\mathbb{Q}_1$, is associated with the first quantizing approach and the second one, $\mathbb{Q}_2$, is defined for the second approach with $N_{I/Q}$ bits for quantifying the CBW components. The above results imply that the error array factor is steered to the commanded beam position in which the amplitude error contributes to the second term while the weighted phase error constitutes the first one. For enough bits, the $e_{a,i}$ can be neglected in (3.4. b); therefore, the two quantizer error can be written in a uniform formula, though that would be in form only. Accordingly, the baseband

error might be written as follows:

$$e_{\boldsymbol{i}} \approx e_{A,\boldsymbol{i}} + j2A_{\boldsymbol{i}} \sin\left(\frac{e_{\varphi,\boldsymbol{i}}}{2}\right) \approx e_{A,\boldsymbol{i}} + jA_{\boldsymbol{i}}\hat{e}_{\varphi,\boldsymbol{i}}$$

where $\hat{e}_{\varphi,\boldsymbol{i}}$ is the Tylor expansion of sine. For the $\mathbb{Q}_1$, the first term, the real part, may be neglected for enough bits; thus, only the phase error would be of significance, showing itself somehow in harmonized form. However, for the $\mathbb{Q}_2$, for an acceptably small amount of $A_{\boldsymbol{i}}$, the first term becomes considerable. The two methods of minor lobe performance for $N_\theta = N_a = N_{I/Q} = 4$ are shown in Fig. 3.8 for two different commanded beam directions. As expected, the second method generates more severe distortion and minor lobe increase.

3.3 Random dithered quantization

3.3.1 Statistics fundamentals

A stochastic process is a phenomenon evolving randomly. Mathematically, it is an integration of random variables. A random variable or vector can be characterized by its distribution and density functions.

Definition 3.1: The probability of event $\boldsymbol{u} < \boldsymbol{u}_0$ is defined as the cumulative distribution function (CDF),

$$F_{\boldsymbol{u}}(\boldsymbol{u}_0) = \mathbb{P}[\boldsymbol{u} \leq \boldsymbol{u}_0] \qquad \blacksquare$$

Definition 3.2: The probability density function (PDF) is defined as the derivative of CDF,

$$f_{\boldsymbol{u}}(\boldsymbol{u}_0) = \frac{\partial F_{\boldsymbol{u}}(\boldsymbol{u})}{\partial \boldsymbol{u}}\Big|_{\boldsymbol{u}=\boldsymbol{u}_0}$$

$\blacksquare$

Thus, one can write

$$F_{\boldsymbol{u}}(\boldsymbol{u}_0) = \int_{-\infty}^{\boldsymbol{u}_0} f_{\boldsymbol{u}}(\boldsymbol{u})d\boldsymbol{u} \tag{3.7}$$

If u_0 and v_0 are two events, then the conditional probability of u_0 given v_0 is as follows:

$$\mathbb{P}(u_0|v_0) = \frac{\mathbb{P}(u_0 \cap v_0)}{\mathbb{P}(v_0)} \quad .$$

Considering $\mathbb{P}(\boldsymbol{x}) = f_{\boldsymbol{x}}(\boldsymbol{x})\Delta\boldsymbol{x}$, one can write

$$f(u_0|v_0) = \frac{f_{u,v}(u_0, v_0)}{f_v(v_0)}$$

Definition 3.3: The conditional PDF of u given v is defined as

$$f(u|v) = \frac{f_{u,v}(u, v)}{f_v(v)} \quad \blacksquare$$

If the events u and v are statistically independent of each other, then

$$f_{u,v}(u, v) = f_u(u)f_v(v) \tag{3.8}$$

Also, it is possible to write

$$F_{u,v}(u, v) = F_u(u)F_v(v) \tag{3.9}$$

Definition 3.4: Let u be a random variable, then the expected value of $g(u)$ is

$$\underline{E}[g(u)] = \int_{-\infty}^{\infty} g(u)f_u(u)du \quad \blacksquare$$

Accordingly, the first moment (or mean) of random variable u is

$$m_u = \underline{E}[u] = \int_{-\infty}^{\infty} uf_u(u)du \tag{3.10}$$

The second moment (or mean) of random variable u is

$$r_u = \underline{E}[u^2] = \int_{-\infty}^{\infty} u^2 f_u(u) du \tag{3.11}$$

For a complex random variable, Equation (3.11) turns to $r_u = \underline{E}[uu^*]$. Just as a comment, the correlation matrix represents the complete set of second moments for a random vector $\boldsymbol{u}$, $\boldsymbol{R_u} = \underline{E}[\boldsymbol{u}\boldsymbol{u}^H]$ where H stands for Hermitian or conjugate transpose.

Definition 3.5: When $\underline{E}[|u|^n]$ exists, the *n*th moment of u is

$$\underline{E}[u^n] = \int_{-\infty}^{\infty} u^n f_u(u) du$$ ■

In statistics, the deflection of a random variable from the mean value is measured by variance.

Definition 3.6: The average of squared differences from the mean is variance,

$$var(u) = \underline{E}\{[u - m_u]^2\}$$ ■

It can be shown that

$$var(u) = \underline{E}(u^2) - \underline{E}^2(u) \tag{3.12}$$

Thus, if the mean of a random process becomes zero, the second moment and variance are equal. The square root of the variance is called standard deviation, $\sigma = \sqrt{var(u)}$.

The complete set of moment deviation for a complex random vector $\boldsymbol{u}$ is called the covariance matrix, $\boldsymbol{C_u} = \underline{E}[(\boldsymbol{u} - \boldsymbol{m_u})(\boldsymbol{u} - \boldsymbol{m_u})^H]$. The covariance and correlation matrices are related by

$$\boldsymbol{C_u} + \boldsymbol{m_u}\boldsymbol{m_u^H} = \boldsymbol{R_u} \tag{3.13}$$

Definition 3.7: The characteristics function (CF) of a random variable u is defined as

$$\mathbb{C}_u(w) = \underline{E}(e^{-j2\pi wu})$$ ■

Thus, the CF of a random variable is the Fourier transform of its PDF. Also, two random variables u and v are statistically independent if and only if

$$\mathbb{C}_{u,v}(w_u, w_v) = \mathbb{C}_u(w_u)\mathbb{C}_v(w_v) \tag{3.14}$$

3.3.2 Dithered system

As the previous section shows, the quantization error turns into a harmonic distortion. Nevertheless, that is not generally correct. It can be shown that under condition (3.15), the quantization error is uniformly distributed [83].

$$\mathbb{C}_x\left(\frac{k}{\Delta}\right) = 0, \qquad \forall k \in \mathbb{Z} \tag{3.15}$$

where Δ is the least significant bit (LSB). However, there are some important points to note. First, Equation (3.15) is defined for an infinite uniform quantizer. Secondly, condition (3.15) ensures the error would be uniformly distributed but not independent of the original signal. However, in many practical interests, that might be good enough. Overall, Equation (3.15) tells us that if the CF of a random variable becomes zero at specific points, there is a possibility that the error obeys a specific distribution.

It is possible to manipulate the original signal by adding an *independent* signal before the quantization process, satisfying the conditions provided in (3.15). Such a signal is called dither, typically but not necessarily, a random signal with some statistical properties. To develop the theory, consider a third random variable $z = x + y$, then the following relationship exists [84]

$$\mathbb{C}_z(w) = \mathbb{C}_x(w)\mathbb{C}_y(w) \tag{3.16}$$

This is reciprocal to $f_z(z) = f_x(x) * f_y(y)$. For an SD system, the quantization error is as follows

$$q_x^{SD} = \mathrm{Q}(x + \kappa) - \kappa - x = \mathrm{Q}(w) - \mathrm{w} \tag{3.17}$$

with $\mathrm{w} = x + \kappa$. Considering (3.15)-(3.17), the output error of the SD system would be at least uniformly distributed if (3.18) is complied. Nevertheless, it is possible to show with longer proof that the error becomes totally independent of the input and uniformly distributed [84].

$$\mathbb{C}_{\kappa}\left(\frac{k}{\Delta}\right) = 0, \qquad \forall k \in \mathbb{Z} \tag{3.18}$$

Now, one can easily realize that the space-fed antenna is naturally an SD system,

$$\Upsilon_{\boldsymbol{i}} = Q(k\|\acute{\boldsymbol{r}}_{\boldsymbol{i}}\|_2 + \xi_{\boldsymbol{i}}) - k\|\acute{\boldsymbol{r}}_i\|_2 \quad .$$

Although the quadratic phase shift $k\|\acute{\boldsymbol{r}}_{\boldsymbol{i}}\|_2$ does not comply with condition (3.18).

In an NSD system, it is not possible neither to make the total error independent of the input nor uniformly distributed, but making some moments of error, $\underline{E}(e_d^n)$, independent of the original signal by satisfying (3.19).

$$\mathbb{D}_{\kappa}^{(n)}\left(\frac{k}{\Delta}\right) = 0, \qquad \forall k \in \mathbb{Z} \tag{3.19.a}$$

$$\mathbb{D}_{\kappa}(f) \triangleq \mathrm{sinc}(f)\mathbb{C}_{\kappa}(f) \tag{3.19.b}$$

where $\mathrm{sinc}(f) \triangleq \sin \pi\Delta f / \pi\Delta f$ and $\mathbb{D}_{\kappa}^{(n)}$ signifies the nth derivative of $\mathbb{D}_{\kappa}$ [85]. For example, considering the CF of rectangular probability density function (RPDF), uniform distribution, is a Sinc function; then, for NSD-RPDF, the first moment of the error is statistically independent of the input, which is precisely zero, but a higher order of error moments are dependent on the original signal, contributing to noise modulation. For NSD with triangular probability density function (TPDF) of width 2Δ, the error's first- and second-moment are independent of the input. Among distributions complied with (3.19), the TPDF provides the minimum error variance, while the RPDF generates the lowest noise power that its m_e is zero.

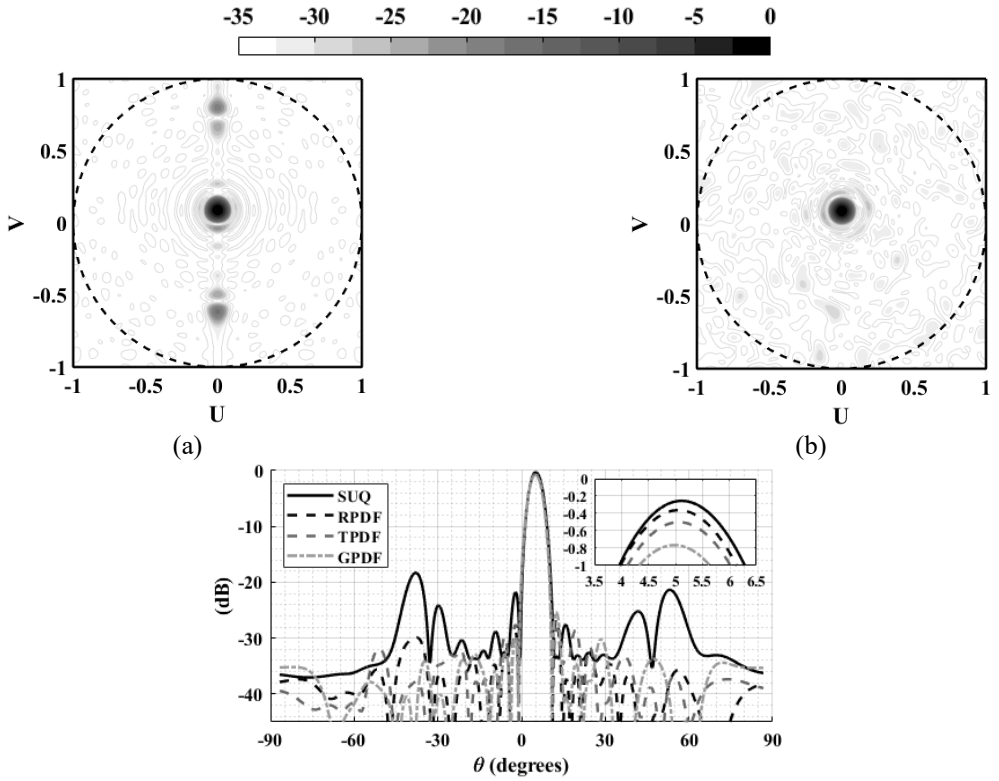

Fig. 3. 9. Decibel array-factor, normalized to the maximum of high precision aperture for 3-bit (a) simple uniform quantization, (b) non-subtractive dither with uniform distribution, and (c) The computed radiation patterns on φ = 90° plane for different non-subtractive dither methods.

A circular aperture PA with a diameter of about 15.5λ_0, with classic Nyquist design, ρ = 0.5, and Taylor weighting is considered with different dithering approaches, assuming the dither signal samples are independent and identically distributed (iid), iid NSD. In Figs. 3.9(a) and 3.9(b), the contour lines plotted faintly illustrate dB levels between -45 to -35.

The beam is assumed at $[\theta, \varphi]$ = [5°, 90°], where the z-axis is presumed as the boresight vector normal to the array surface. For Fig. 3.9(a), whose associated PDA is quantized to 3 bits by a simple uniform quantizer (SUQ), the array factor shows some high peak QLs. Fig. 3.9(b) illustrates the one in which the high-precision PDA is quantized by the RPDF-NSD scheme. The dither signal can disperse the QLs on the beamspace domain with considerably lower peak levels. Fig. 3.9(c) compares PA's radiation pattern designed by some exemplar NSD systems. The GPDF stands for

iid NSD with Gaussian density, $\sim\mathcal{N}(0, \frac{\pi}{8})$. As seen, by increasing the dither's power, the antenna directivity drops, which is the cost of inserted noise.

Chapter 4
Spectrally Shaped Dither (Noise Shaping)

4.1 Digital signal processing fundamentals

4.1.1 One-Dimensional digital signal processing

One may sample a continuous signal $x(t)$ by the sampling rate of $f_s = \frac{1}{T_s}$, generating a sequence of sampled values of $x(t)$ as written in (4.1).

$$x[n] = x(nT_s) = x(t) \sum_{n=-\infty}^{\infty} \delta(t - nT_s) \tag{4.1}$$

As a convention, we refer to the discrete-time/space signals as sequences. Also, as stated in (4.1), the sequence might be infinitely long. In practice, however, only finite sequences are computable; hence, the length of x[n] should be finite. Also, we introduce the 1-D unit sample sequence (or discrete time/space impulse or Dirac delta sequence) as

$$\delta[n] = \begin{cases} 0 & n \neq 0 \\ 1 & n = 0 \end{cases}$$

In this regard, any sequence can be defined as

$$x[n] = \sum_{m=-\infty}^{\infty} x[m]\delta[n - m]$$

For example, the unit step sequence u[n] = $\sum_{m=-\infty}^{\infty} \delta[m] = \sum_{m=0}^{\infty} \delta[n - m]$.

A linear shift-invariant (LSI) system *g* has the following property

$$y[n] = g\left\{\sum_{m=-\infty}^{\infty} x[m]\delta[n - m]\right\} = \sum_{m=-\infty}^{\infty} x[m]g\{\delta[n - m]\} = \sum_{m=-\infty}^{\infty} x[m]h[n - m]$$

where $h[n] = g\{\delta[n]\}$ is the system impulse response which means that the output of every LSI system can be predicted by its impulse response. Moreover, we recall the convolution operator as

$$x[n] * h[n] = \sum_{m=-\infty}^{\infty} x[m]h[n-m].$$

Thus, the LSI system output is the convolution of input and the impulse response.

Definition 4.1: A system is stable in the BIBO sense if and only if every bounded sequence as input produces a bounded sequence as output.

Corollary: An LSI system is stable if its impulse response is absolutely summable, $\sum_{m=-\infty}^{\infty}|h[m]| < \infty$.

Definition 4.2: The 1-D sequence x[n] is causal if x[n] = 0 for n < 0.

Many people have contributed to the Sampling theorem, which has many generalizations. The most significant point of this theorem is that sampling in time/space/frequency is commensurate to replication of the original signal spectrum in the Fourier domain. Shannon's version simply states that a sampled version of a signal band-limited to Ω_0 can perfectly be reconstructed as long as the (angular) sample rate is greater than $2\Omega_0$ which is famous as the Nyquist rate. To show that, one may substitute the Fourier series (FS) of the impulse train, $\frac{1}{T_s}\sum_k e^{\frac{j2\pi.k.t}{T_s}}$, in (4.1) and take a Fourier transform (FT) from both sides, contributing to:

$$Y(\Omega) = \frac{1}{T_s}\sum_{k=-\infty}^{\infty} X(\Omega - k\Omega_s) \tag{4.2}$$

where $\Omega_s = \frac{2\pi}{T_s}$. The equation (4.2) shows that the spectrum of the sampled signal is a periodic function of the spectrum of the original signal with period Ω_s. Therefore, if the original signal, $x(t)$, would be band-limited to Ω_m, the inequality $\Omega_0 < \Omega_s - \Omega_0$ is needed to be complied with to avoid the shifted copies in the spectral domain overlapping each other, which leads to the Nyquist rate, $\Omega_s > 2\Omega_0$. The main issue with the sampling theorem is that it is based on the concept

of band-limited signal, which is not practical (such signal must be infinitely extended in the time/spatial domain). Moreover, the condition of ideal sampling is implicit in the theorem, the infinite precision of the sample values. In practice, the exact value of samples cannot be held during the sampling procedure, introducing quantization noise. Therefore, there is always an amount of distortion in the spectral domain of the sampled signal.

Next, it is necessary to define digital frequency (more accurately, discrete or normalized frequency) because the time/space domain is discrete. This can be conveniently carried out by the following:

$$\omega = \Omega T_s = \frac{\Omega}{f_s} \tag{4.3}$$

where Ω is the continuous angular frequency. Note that the unit of the digital angular frequency, ω, is radians/sample since the sampling rate unit, f_s, is sample/sec (or sample/m) and the unit of the continuous angular frequency is radians/sec (or radians/m). Furthermore, digital frequency is a *continuous* parameter, although its name might be misleading. Thus, we will call it normalized frequency hereafter.

Definition 4.3: The discrete time/space Fourier transform (DTFT/DSFT) of a finite sequence of length *N* is defined as follows:

$$X(e^{j\omega}) = \sum_{n=0}^{N-1} x(nT_s)e^{-j\Omega nT_s} = \sum_{n=0}^{N-1} x[n]e^{-j\omega n} \quad ,$$

and the inverse operator (IDTFT/IDSFT) is:

$$x[n] = \frac{1}{2\pi}\int_{-\pi}^{\pi} X(e^{j\omega})e^{j\omega n}d\omega \qquad \blacksquare$$

Hence, it is impossible to calculate the DSFT since it is a continuous parameter having infinite values on a 2π period. To make it computable, it is necessary to sample the normalized frequency, providing finite samples. To this end, one method to approximately calculate the DSFT is to use *M* equally spaced samples on the unit circle (one fundamental period) as follows:

$$X\left(e^{j\omega_m}\right) = \sum_{n=0}^{N-1} x[n]e^{-j\omega_m n} \tag{4.4}$$

where $\omega_m = \frac{2\pi k}{K}, k = 0, 1, 2, \dots, K-1$, simply means *K* samples of ω on one fundamental period 2π. This has been schematically shown on the complex plane in Fig. 4.1. Accordingly, (4.4) can be written as the following definition, which is famous as discrete Fourier transform (DFT). The DFT and DSFT are defined on an infinite period, as the sequence can be infinitely long.

Definition 4.4: The DFT of a 1-D sequence x[n] is defined as

$$X[k] = \sum_{n=0}^{N-1} x[n]e^{-j\frac{2\pi k}{K}n}$$ ■

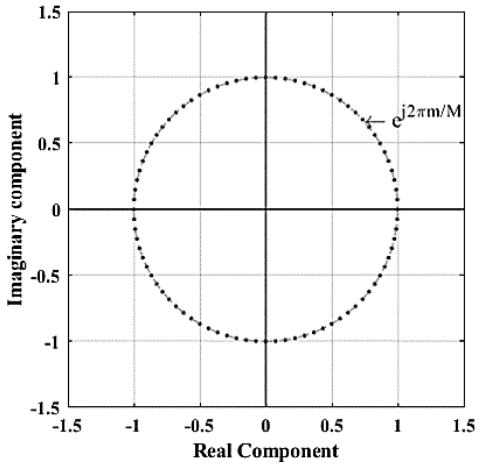

Fig. 4. 1. Schematic view of M samples of continuous frequency on the unit circle.

According to the Euler formula, $e^{-j\frac{2\pi m}{M}n} = \cos(\frac{2\pi m}{M}n) - j\sin(\frac{2\pi m}{M}n)$ and the Hermitian symmetry of a real signal, one may realize that the DFT (and DSFT) of a real and even (symmetric) sequence is real and even (symmetric). Similarly, the DFT (and DSFT) of a real and odd (anti-symmetric) sequence is purely imaginary and odd (anti-symmetric); thus, the DFT of a real signal is conjugate symmetric because it is always possible to decompose every sequence to even (symmetric) and odd (anti-symmetric) components. The above statement is equivalent to saying the magnitude of the DFT of the real signal is even while its phase is odd. Other important properties of DFT are tabulated in Table. 4.1.

Like the continuous case, the Laplace *s*-transform is used for analyzing the signal in the complex frequency domain, and the *z*-transform (ZT) can be used for signal processing in the digital complex frequency domain following definition 4.5.

Definition 4.5: The 1-D z-transform is defined as follows

$$X[z] = \sum_{n=0}^{N-1} x[n]z^{-n} \quad \blacksquare$$

Where $z = e^{sT_s} = e^{\sigma + j\omega}$. As stated before, the sigma is generally an infinite summation and might be defined as a one-sided or two-sided summation. The ZT is related to the DSFT as follows:

$$X[z] = \sum_{n=0}^{N-1} x[n]e^{-(\sigma+j\omega)n} = DSFT\{x[n]e^{-\sigma n}\} \tag{4.5}$$

TABLE 4.1. IMPORTANT PROPERTIES OF DFT.

DFT	$DFT\{x[n]\} = X(e^{j\omega})$
Linearity	$DFT\{ax[n] + by[n]\} = aX(e^{j\omega}) + bY(e^{j\omega})$
Spatial reversal	$DFT\{x[-n]\} = X(e^{-j\omega})$
Spatial shifting	$DFT\{x[n - n_0]\} = X(e^{j\omega})e^{-j\omega \cdot n_0}$
Frequency shifting	$DFT\{x[n]e^{j\omega_0 \cdot n}\} = X(e^{j\omega}e^{-j\omega_0})$
Spatial convolution	$DFT\{x[n] * y[n]\} = X(e^{j\omega})Y(e^{j\omega})$
Frequency convolution	$DFT\{x[n]y[n]\} = X(e^{j\omega}) * Y(e^{j\omega})$

Definition 4. 2, for a finite sequence, can be interpreted as a system with the impulse response, $h[n]$, of size *N*, *N* even, as $h[n] = 0$ for $\frac{N}{2} < n < N$, which comes from the periodicity assumption of the signal by the DFT operator, note that $h[0] = h[N]$.

Definition 4.6: A finite sequence $x[n]$, of size *N*, *N* even, is causal if $x[n] = 0$ for $\frac{N}{2} < n < N$.

Definition 4.7: An LSI system is stable if and only if all poles of its transfer function H(z) are located inside the unit circle |z| < 1.

Thus, the region of convergence (RoC) of the z-transform of the stable sequence includes the unit circle.

Definition 4.8: A minimum-phase system is an LSI system that is causal and stable with a causal and stable inverse system.

Definition 4.8 implies that all poles and zeros of a unidimensional minimum-phase system (MPS) are located inside the unit circle |z| < 1.

4.1.2 Multi-Dimensional digital signal processing

In general, Multi-dimensional signal processing is a generalization of the 1-D case. However, they differ in the number of samples to be processed and the fact that theorems and background math are less developed for Multi-dimensional cases compared to the 1-D counterpart. The other discrepancy is the lattice. In a unidimensional case, sampling is just a matter of scalar factor (sampling rate), but here, it is characterized by generating matrix; thus, it is not just a matter of spacing but also the lattice fashion, e.g., hexagonal, rectangular, square. Also, some fundamental concepts, such as causality, stability, *etc*., are somehow different to define or determine. For example, back to Definition 4.7, an LSI system with a 1-D impulse response is stable if all poles are located inside the unit circle. It is evident that this cannot be used for the *i*-D case since there would be at least two complex parameters, z_1 and z_2, which contribute to four real and imaginary components. Also, for time which is a unidimensional case, the definition of past and future is clear; thus, causality can be uniquely characterized, but that is not the case for 2-D one. It depends on the direction and reference sample chosen.

The 2-D unit sample or impulse can be written as

$$\delta[n_1, n_2] = \begin{cases} 1 & n_1, n_2 = 0 \\ 0 & otherwise \end{cases} .$$

Definition 4.9: The 2-D convolution operator is defined as

$$x[n_1, n_2] * h[n_1, n_2] = \sum_{m_2=-\infty}^{\infty} \sum_{m_1=-\infty}^{\infty} x[m_1, m_2]\, h[n_1 - m_1, n_2 - m_2\,] \quad ,$$

In a more compact form

$$x[\boldsymbol{n}] * h[\boldsymbol{n}] = \sum_{\boldsymbol{m}} x[\boldsymbol{m}] h[\boldsymbol{n} - \boldsymbol{m}] \quad \blacksquare$$

Definition 4.10: A 2D discrete space Fourier transform (2D-DSFT) of a 2D sequence of size $N_1 \times N_2$ might be defined as follows:

$$X\left(e^{j\omega_1}, e^{j\omega_2}\right) = \sum_{n_2=0}^{N_2-1} \sum_{n_1=0}^{N_1-1} x[n_1, n_2] e^{-j(\omega_1 n_1 + \omega_2 n_2)} \quad ,$$

more compact form written as

$$X\left(e^{j\boldsymbol{\omega}}\right) = \sum_{\boldsymbol{n}} x[n] e^{-j\boldsymbol{\omega n}} \quad \blacksquare$$

The same as the 1-D case, ω_1 and ω_2 are digital frequencies and are continuous parameters. As stated before, the above summation is impossible to be computed (and/or stored) as $X\left(e^{j\omega_1}, e^{j\omega_2}\right)$ is analog data; therefore, one may sample the digital frequencies making the above summation computable, contributing to 2-D discrete Fourier transform (2D-DFT) as written in (4.6).

$$X[k_1, k_2] = \sum_{n_2=0}^{N_2-1} \sum_{n_1=0}^{N_1-1} x[n_1, n_2] e^{-j2\pi\left(\frac{k_1}{K_1} n_1 + \frac{k_2}{K_2} n_2\right)} \tag{4.6}$$

The above summation means that ω_1 and ω_2 are sampled to K_1 and K_2 equally distant samples, respectively. Alternatively, one may say it is sampled on a square lattice. Note that $X[k_1, k_2]$ is supposed to be a periodic sequence with a period $[K_1, K_2]$, $X[k_1, k_2] = X[k_1 + K_1, k_2 + K_1]$. However, the DFT definition depends on how the discrete points are transformed.

Consider the span $\boldsymbol{L}\mathbb{R}^2$ on a plane and its sampled version, which contributes to a lattice $\boldsymbol{L}\mathbb{Z}^2$ initiated with $\boldsymbol{L} \triangleq [\boldsymbol{b_1}, \boldsymbol{b_2}]$ as the generating matrix, we call it lattice-matrix, including two basis vectors $\boldsymbol{b_1}$ and $\boldsymbol{b_2}$, which must not have a collinear relation with each other. Let us call the lattice $\boldsymbol{L}\mathbb{Z}^2$ as the element-location lattice (ELL). The reciprocal lattice of ELL is the periodicity lattice

(PL). If one resamples the lattice $\boldsymbol{L}\mathbb{Z}^2$ by a resampling or tiling matrix to generate a sparser lattice $\boldsymbol{LT}\mathbb{Z}^2$**,** which would associate with a reciprocal lattice which would be $|\boldsymbol{T}|$ times denser than PL. This reciprocal lattice might be called the steering lattice, defined by $\check{\boldsymbol{L}}_s = \boldsymbol{f}\boldsymbol{T}^{-1}\check{\boldsymbol{L}}$**,** which may or may not be in the same fashion as PL, $\boldsymbol{f}$ is an integer vector.

The lattice matrix is not unique. But the area of one period is unique, which is simply the determinant of the gram of PL matrix, $\boxtimes = \sqrt{\left|\mathbf{G}(\check{\boldsymbol{L}})\right|} = \sqrt{\left|\check{\boldsymbol{L}}^{\boldsymbol{t}}\check{\boldsymbol{L}}\right|}$ where $\boxtimes$ signifies the normalized area of the fundamental period with any shape.

Definition 4.11: A generalized form of 2D-DFT can be defined as follows:

$$X[\boldsymbol{k}] = \sum_{\boldsymbol{n}} x[\boldsymbol{n}] e^{-j2\pi(\boldsymbol{k}\boldsymbol{T}^{-1}\boldsymbol{n})} \qquad \blacksquare$$

In the above definition, $\boldsymbol{T}$ is an arbitrary resampling matrix, and $\boldsymbol{n}$ and $\boldsymbol{k}$ are integer vectors.

Definition 4.12: A 2D z-transform of a 2D sequence of size $N_1 \times N_2$ is defined as follows:

$$X(z_1, z_2) = \sum_{n_2=0}^{N_1-1} \sum_{n_1=0}^{N_2-1} x[n_1, n_2] z_1^{n_1} z_2^{n_2} \qquad \blacksquare$$

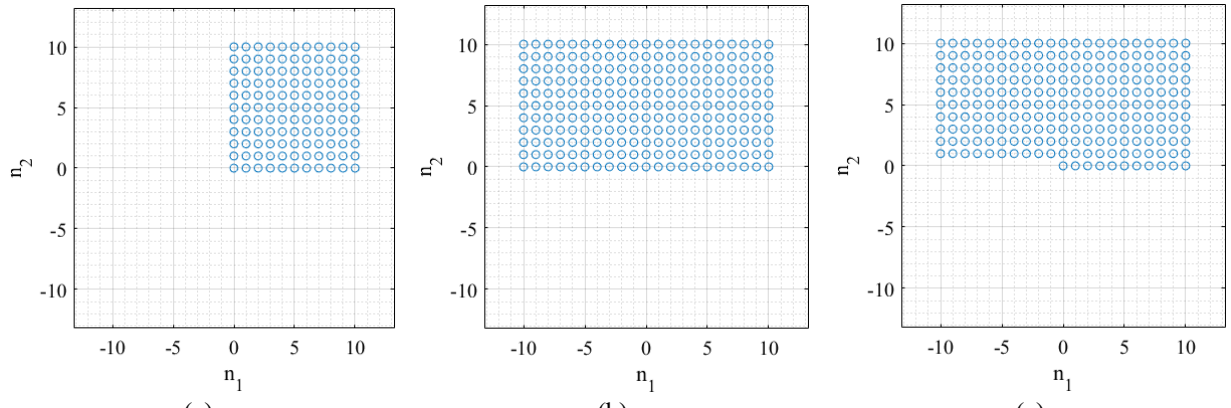

(a) (b) (c)

Fig. 4. 2. Different 2D systems. (a) First quadrant, (b) symmetric, and (c) asymmetric half-plane system.

Definition 4.13: A 2-D LSI system with non-zero impulse response in a particular plane region is called a special support system.

For example, the quadrant, symmetric and anti-symmetric half-plane systems are schematically shown in Fig. 4.2.

Definition 4.14: A 2-D system is casual if it is a one-sided special support system.

For example, the system of Fig. 4.2(c) is causal in asymmetric half-plane scenes.

Definition 4.15: A 2-D LSI system is stable if and only if its impulse response is absolutely summable.

In contrast to Definition 4.7 for a one-dimensional case, a similar approach cannot be applied to a 2-D counterpart. Nevertheless, there are some theorems for the stability tests of quadrant support systems.

Shank's theorem: For a first quadrant support system of form $H(z_1, z_2) = \frac{1}{A(z_1,z_2)}$, the system is stable if

$$\forall |z_1|, |z_2| \geq 1: \; A(z_1, z_2) \neq 0 \qquad \therefore$$

As seen, shank's theorem asks for a search in a 4-D space, which is a challenging task. A method with a smaller search space is Huang's theorem.

Huang's theorem: For a first quadrant support system of form $H(z_1, z_2) = \frac{1}{A(z_1,z_2)}$, the stability can be ensured if the following condition complies:

$$A(z_1, z_2) \neq 0, \qquad for \begin{cases} |z_1| = 1, & |z_2| \geq 1 \\ |z_2| = 1, & |z_1| \geq 1 \end{cases} \qquad \therefore$$

There are other methods for the 2-D system stability test, such as Decarlo and Strintzis's theorem [86], which are not discussed here for brevity. If the causality and the system's stability are secured, having proved the stability of the inverse system, the causality of that will be automatically insured, which means the 2-D system would be minimum-phase.

4.1.3 Digital filter introduction

Digital filters have been investigated and used in a variety and extensive applications comprising data communication [87]-[88], audio, image, and video processing [89]-[90]. One popular and simple type of digital filter is the LSI type, whose output is a linear combination of the input samples with constant coefficients (with respect to the position of samples). In general, this class of digital filters has two types, including infinite-duration impulse response (IIR) filters and finite-duration impulse response (FIR) filters; as their names imply, their impulse responses have infinite and finite durations, respectively. The main difference between the FIR and IIR filters is that an IIR filter provides the prescribed frequency response with a more compact structure. However, it is impossible to design a linear-phase IIR filter. To compromise that, a subsequent all-pass filter might be applied, complicating the system design.

On the other hand, the design of a linear-phase FIR filter is possible but at the expense of more computational complexity due to the higher number of coefficients required and more delay, which can be too large for some applications. Also, the FIR filter is inherently stable. The same is not applied to the IIR filter; hence, stability should be considered during the design procedure [91]. This might be why the 2-D FIR filters got more popularity in applications such as image processing. It should be noted that in the 2-D IIR filters case, the stability of the system (and sometimes the inverse system) might not be convenient to test as their 1-D counterparts. However,

a system using an FIR filter with a long impulse duration in its feedback circuit is also prone to instability. In the FIR filter, there is no feedback, which grants the finite impulse.

On the other hand, the IIR filters use feedback. However, it does not mean that if there is feedback, the impulse response would be infinite. An example is the moving average filter which uses feedback, but the output is finite.

From another perspective, the digital filter family may be categorized into two types: a real-coefficient digital filter (RCDF) and a complex-coefficient digital filter (CCDF). The CCDF has a one-sided frequency response; therefore, the asymmetric case entails a complex-coefficient impulse response.

4.2 Noise shaping fundamental implications

Noise shaping is a well-known signal processing approach. It is sometimes called “error diffusion,” in image processing in particular [92]-[93], and also $\Delta - \Sigma$ modulator/converter [94]-[95]. However, in traditional $\Delta - \Sigma$ noise shaping, the signal is oversampled and then quantized with the feedback noise shaper as a unit delay system, and then a decimation procedure is carried out, including lowpass filtering and subsequent downsampling. The nomenclature noise shaping describes the system performance from the spectral domain perspective, while the error diffusion points to the method systematic procedure in the signal domain, input space of Fourier transform. The $\Delta - \Sigma$ refers to the system block diagram.

The rationale behind the noise shaping is diffusing the current element's error to some neighboring elements. Each element error is diffused among the neighboring elements by specific weighting factors. Those diffused errors will be addressed later, so the name "error diffusion." It is the digital filter that governs the amounts of weighting.

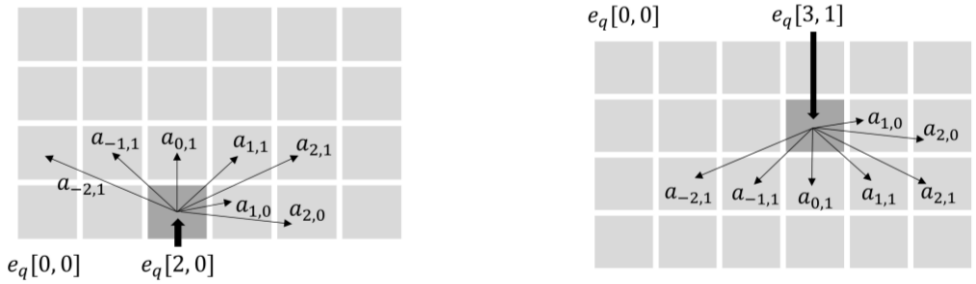

(a) (b)

Fig. 4. 3. Error diffusion for an exemplar system. Two wavefront traversals starting from (a) northeast and (b) southwest.

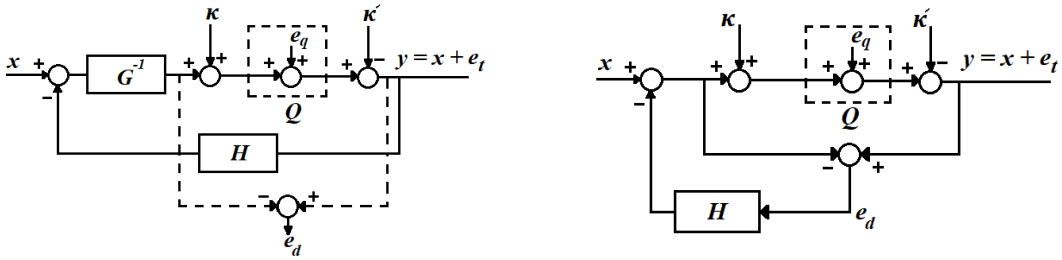

(a) (b)

Fig. 4. 4. Two possible structures of noise shaper.

In noise shaping, each element error is diffused among the neighboring elements by some specific weighting factors, $a_{n,m}$, which is determined by the digital filter. In Fig. 4.3, the error redistribution is shown in which the revised system is

$$H(z_1, z_2) = a_{1,0}z_1^{-1} + a_{2,0}z_1^{-2} + a_{-2,1}z_1^2 z_2^{-1} + a_{-1,1}z_1^1 z_2^{-1} + a_{0,1}z_2^{-1} + a_{1,1}z_1^{-1}z_2^{-1} + a_{2,1}z_1^{-2}z_2^{-1}$$

initiated with $\sum_{n,m} a_{n,m} = 1$. During the wavefront traversal, the noise shaper meets up with each sample once and diffuses the sample quantization error to the neighboring ones. For example, in Fig. 4.3(a), when the noise shaper meets the sample [3, 0], it finds the high precision value $\hat{x}[3,0] = x[3,0] - a_{1,0}e_q[2,0] - a_{2,0}e_q[1,0]$, where $x[3,0]$ represents the original high-precision sample value; thereby, the error would become $e_q[3,0] = Q\{\hat{x}[3,0]\} - \hat{x}[3,0]$.

As such, each time the noise shaper wavefront strikes a sample, several neighboring samples will be affected, depending on the size of the impulse response. In this regard, one may choose different wavefront traversals. For example, it may start from the southwest, Fig 4.3(a), or the

northwest, as shown in Fig. 4.3(b). Of course, the noise shaper wavefront finally strikes the last element: its error cannot be diffused to any other. However, that error is assumed to be negligible for enough samples and the number of array elements.

A schematic of a generic noise shaper is illustrated in Fig. 4.4(a), in which *x* is the input signal, κ and $\acute{\kappa}$ are the dither signals, *H* is the transfer function of the "revised" system, *G* is called noise transfer function (NTF) equal to 1-*H,* and *Q* signifies the quantizer. Fig. 4.4(b) illustrates the alternative error feedback structure. Let us consider e_t and e_d, respectively as total error and quantization error, and ϵ_t and ϵ_d as their z-transforms correspondingly. Indeed, if no dither is applied, then $e_q = e_d$. Analysis of the Figs. 4.4 yields

$$Y(z) = X(z) + \epsilon_t(z) \tag{4.7.a}$$

$$G(z) = 1 - H(z) = \frac{\epsilon_t(z)}{\epsilon_d(z)} \tag{4.7.b}.$$

Equation (4.7. b) states that if the quantization error spectrum is flat, the shape of total error spectra corresponds to $|G(z)|$. The distortion can be spectrally shaped by the transfer function $H(z)$ in the feedback loop. Considering a unit delay system, the inverse NTF works like an integrator, Σ. At the same time, the weighted quantization error of the current sample is fed back and subtracted from the subsequent sample of the original signal Δ, which clarifies the reason behind the nomenclature $\Delta - \Sigma$ modulator/converter. Note that (4.7) is independent of the quantization scheme used, including non-dithered or dithered and uniform or non-uniform schemes.

Applying dither in a noise shaping system increases the noise power leading to more antenna gain drop. Besides, the computation is not reproducible. Therefore, an un-dithered quantizing system is used in our noise-shaping approach. However, if the dither is not applied, meaning that

κ and $\acute{\kappa}$ are considered zero entries, some signal-dependent artifacts may appear inside the spectrum since the quantization error is generally not flat.

The quantizer is a non-linear system. A traditional approach considers the quantizer output as an input signal with additive white noise, see Figs. 4.4. This approximation sounds unorthodox because the quantization error is a complicated function of the input signal. Such an assumption, in practice, might be one of the reasons that the noise shaper stability and/or performance can be undermined. In particular, this happens for a higher-order filter design due to the saturation of the quantizer (signal clipping) [96]-[97], which can render the system unstable.

Of interest is the MPS, which refers to an LSI system that is causal and stable with a causal and stable inverse [98]. The MPS has the smallest group delay among all causal and stable *unidimensional* LSI systems, which meet the same magnitude specification. In other words, the MPS minimizes the delay of the impulse energy delivery, which means that its first sample has a higher magnitude than its other counterparts [99].

The amount of noise rejection is related to the position of the zeros of the transfer function. In general, the noise shaper decreases the SQNR. The optimum system is the one that effectively pushes the in-band noise out-of-band while it preserves the highest SQNR. For a causal and stable system of the form $G(z) = 1 - H(z)$, where $H(z)$ does not have a constant term, the following inequality can be written [84]:

$$\int_{-\pi}^{\pi} \log(\left|1 - H\left(e^{j\omega}\right)\right| d\omega \geq 0 \tag{4.8}$$

In (4.8), equality happens for an MPS. Accordingly, one may make the inference minimum-phase filter (MPF) is optimal for noise shaping since the integral has a positive value for other systems that are not MPS.

4.2.1 Discrete Hilbert transform method

Definition 4.16: The Hilbert transform (HT) of a 1-D signal $x(t)$ is defined as the convolution

$$HT[x(t)] = x(t) * \frac{-1}{\pi t} \qquad \blacksquare$$

Recall that the Fourier transform (FT) of the signum function, $sgn(t)$, is equal to

$$FT[sgn(t)] = \begin{cases} \frac{2}{j\omega} = \frac{1}{j\pi\upsilon} & \omega \neq 0 \\ 0 & \omega = 0 \end{cases} ,$$

The HT of function turns to a convolution with the signum spectrum. It is always possible to reconstruct a real and causal function $f(t)$ from its even component as

$$f(t) = f_e(t)[1 + sgn(t)]$$

where $f_e(t) = \frac{f(t)+f(-t)}{2}$. This will be explained more for discrete signals and sequences next. Thus, one may write

$$FT[f(t)] = FT[f_e(t)] + j.HT\{FT[f_e(t)]\}$$

that implies that the real and imaginary parts of FT of a causal function are related by the HT; note $FT[f_e(t)]$ is real.

A conjugate symmetric sequence is as $x_e[n] = x_e^*[-n]$. The same can be written for the conjugate anti-symmetric one $x_o[n] = -x_o^*[-n]$. Accordingly, any sequence can be expressed by conjugate and anti-conjugate components

$$\begin{cases} x[n] = x_e[n] + x_o[n] \\ x_e[n] = \frac{1}{2}\{x[n] + x^*[-n]\} \\ x_o[n] = \frac{1}{2}\{x[n] - x^*[-n]\} \end{cases} \tag{4.9}$$

This might be evident that for a real sequence, the conjugate symmetric one is an even sequence, and the conjugate anti-symmetric one is the odd one. As a Fourier transform property, $x_e[n]$ has a

real DSFT and $x_o[n]$ one is purely imaginary. Thus, one may write

$$\begin{cases} X(e^{j\omega}) = X_R(e^{j\omega}) + jX_I(e^{j\omega}) \\ X_R(e^{j\omega}) = \frac{1}{2}\{X(e^{j\omega}) + X^*(e^{j\omega})\} \\ X_I(e^{j\omega}) = \frac{-j}{2}\{X(e^{j\omega}) - X^*(e^{j\omega})\} \end{cases} \tag{4.10}$$

If x[n] would be a causal sequence, the even and odd components should cancel each other for n < 0, and that one may write

$$x[n] = 2x_e[n]u[n] - x^*[0]\delta[n].$$

The DSFT can be written as

$$X(e^{j\omega}) = \frac{1}{\pi}\int_{-\pi}^{\pi} X_R(e^{j\omega})\, U(e^{j(\omega-\theta)})d\theta - x^*[0]$$

Considering that

$$U(e^{j\omega}) = \frac{1}{2} - \frac{j}{2}\cot\frac{\omega}{2} \sum_{k=-\infty}^{\infty} \pi\delta(\omega - 2\pi k)$$

One can write

$$X(e^{j\omega}) = X_R(e^{j\omega}) + \frac{1}{2\pi}\int_{-\pi}^{\pi} X_R(e^{j\theta})d\theta$$

$$-\frac{j}{2\pi}\int_{-\pi}^{\pi} X_R(e^{j\theta})\cot\left(\frac{\omega-\theta}{2}\right)d\theta - Re\{x^*[0]\} - j\mathcal{Im}\{x^*[0]\}$$

And thereby,

$$X_I(e^{j\omega}) = -\frac{1}{2\pi}\int_{-\pi}^{\pi} X_R(e^{j\theta})\cot\left(\frac{\omega-\theta}{2}\right)d\theta - \mathcal{Im}\{x^*[0]\} \tag{4.11}$$

Equation (4.11) is a Hilbert transform (HT) relationship between real and imaginary parts of DTFT of complex causal sequence x[n].

Definition 4.17: The complex cepstrum of x[n] is defined as

$$\hat{x}[n] \triangleq IDSFT\{\log[X(e^{j\omega})]\} \qquad \blacksquare$$

Note that the complex cepstrum of a minimum-phase sequence is causal [17].

Considering that

$$log\{X(e^{j\omega})\} = log|X(e^{j\omega})| + j\measuredangle X(e^{j\omega}),$$

One may insert $\hat{x}[n]$ in (4.11) and find

$$\measuredangle X(e^{j\omega}) = \frac{-1}{2\pi}\int_{-\pi}^{\pi} \log|X(e^{j\theta})| \cot\left(\frac{\omega-\theta}{2}\right) d\theta - \mathcal{I}m\{\hat{x}^*[0]\} \qquad (4.12)$$

where the imaginary part of the reference sample vanishes for the minimum-phase case contributing to a uniform relationship between real and complex (causal) sequences. Thus, it is proved that HT relates log magnitude and phase of the spectrum of a minimum-phase sequence.

The same decomposition we did for continuous and infinite sequences can be applied to periodic sequence x[n], which has *N* samples per period

$$\begin{cases} x[n] = x_e[n] + x_o[n] \\ x_e[n] = \frac{1}{2}\{x[n] + x^*[N-n]\} \\ x_o[n] = \frac{1}{2}\{x[n] - x^*[N-n]\} \end{cases}, \quad for\ n = 1, 2, \dots N-1 \quad (4.13)$$

Note that $x[0] = x[N]$ and *N* is even. Thus, one may write $x_o[n] = sgn[n]x_e[n]$ for sequence x[n], which is causal on a period. In this regard, the 1-D periodic unit sample can be defined in the following definition.

Definition 4.18: One-dimensional periodic sequence unit sample is defined as

$$sgn[n] \triangleq \begin{cases} 1 & n = 1, \dots, \frac{N}{2} - 1 \\ 0 & n = 0, \frac{N}{2} \\ -1 & n = \frac{N}{2} + 1, \dots, N - 1 \end{cases} \quad \blacksquare$$

Thus, the same as the continuous case, the discrete Hilbert transform (DHT) is equivalent to convolution with a DFT of $sgn[n]$.

Definition 4.19: The DHT of periodic sequence x[n] is defined as

$$DHT\{X[k]\} \triangleq -jDFT\{sgn[n]x[n]\} \quad \blacksquare$$

The above definition might be generalized for the multi-dimensional case as the following definition.

Definition 4.20: The DHT of *i*-dimension sequence x[**n**] is defined as

$$DHT_i\{X[\boldsymbol{K}]\} = -jDFT_i\{sgn[\boldsymbol{n}]x[\boldsymbol{n}]\} \quad \blacksquare$$

In Definition 4.20, the $sgn[\boldsymbol{n}]$ might be written as written in Definition 4.21.

Definition 4.21: The 2-D periodic finite sequence unit sample is defined as

$$sgn[n_1, n_2] \triangleq \begin{cases} 1 & n_2 = 0, n_1 = 1, \dots, \frac{N}{2} - 1 \\ 1 & n_2 = 1, \dots, \frac{N}{2} - 1 \\ -1 & n_2 = 0, n_1 = \frac{N}{2} + 1, \dots, N - 1 \\ -1 & n_2 = \frac{N}{2} + 1, \dots, N - 1 \\ 0 & otherwise \end{cases} \quad \blacksquare$$

Accordingly, the minimum-phase impulse response can be numerically computed using (4.14).

$$h[n] = IDFT_i\{|H[\boldsymbol{k}]|e^{j\varphi_k}\} \tag{4.14a}$$

$$\varphi_{\boldsymbol{k}} = DHT_i\{\log|H[\boldsymbol{k}]|\} \tag{4.14b}$$

4.2.2 Design of minimum-phase digital filter for noise shaping

The noise shaper design can be accomplished by defining a digital filter $\widehat{H}(z)$ according to the spectrum of interest. Then it should be translated to the revised transfer function $H(z)$, used in the feedback noise shaper. Hence, $\widehat{H}(z)$ might be normalized to its unit term and subsequently excluded from the result, as in (4.15) for a unidimensional filter.

$$H(z) = \sum_{n=1}^{N} \frac{a_n}{a_0} z^{-n} \tag{4.15}$$

where a_0 is the unit term, $n = 0$, of $\widehat{H}(z)$. Normalizing the impulse response to its unit sample shifts the frequency response magnitude. This is easier to understand why MPF is optimal for noise shaping. Since MPF concentrates the impulse energy on the low-delay coefficients; thus, the up-shift is minimized.

As much as the filter cut-off frequency increases, the impulse energy-delivery delay increases, and the out-off band noise amplification increase so that the noise shaper loses its ability to push the in-band quantization noise out-of-band. As a comparative example, in Fig. 4. 5, two 21-tap MPFs have been designed with different cut-off frequencies. The root-loci diagrams show that both designed filters are MPF. As seen in Figs. 4. 5(e) and 4. 5(f), the amount of out-off band noise amplification is more for the filter having a higher cut-off frequency than that of the filter with a lower cut-off, which has impulse energy of smaller magnitude.

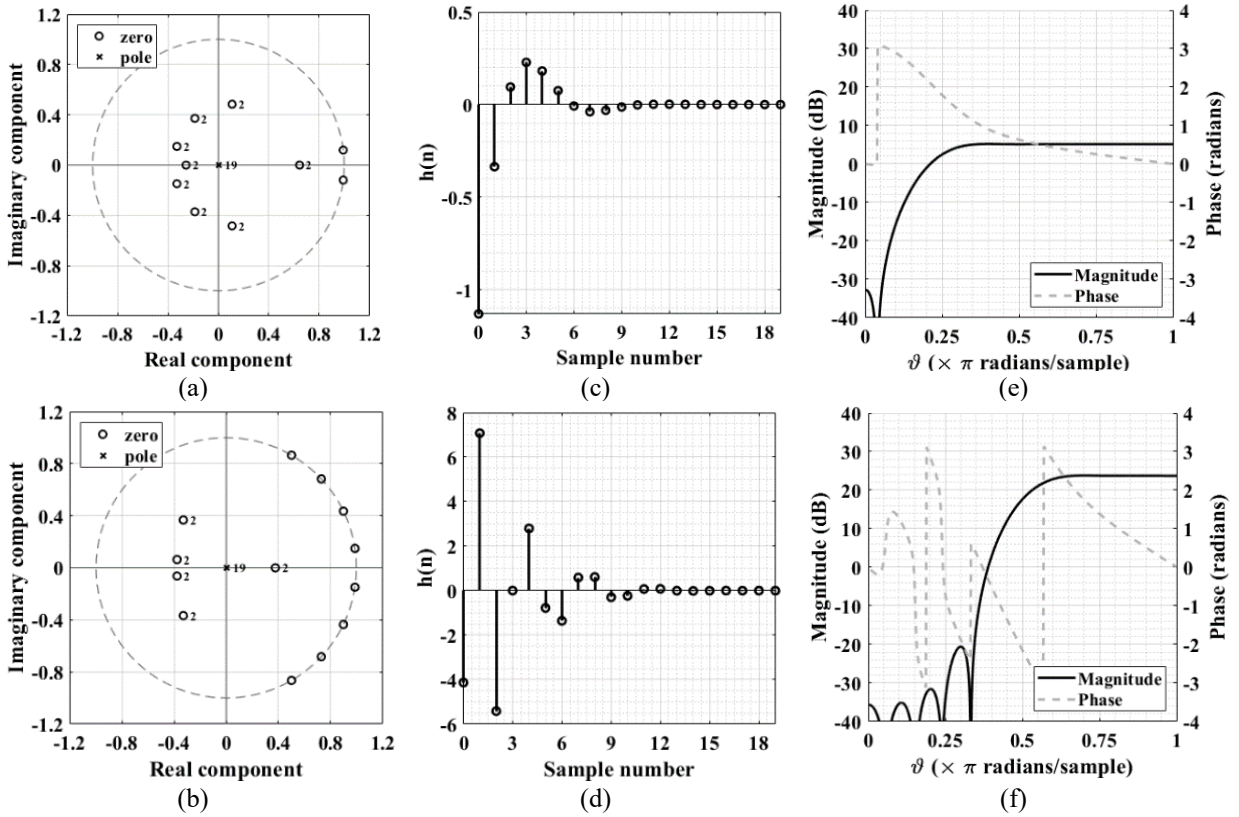

Fig. 4. 5. Two 1D minimum-phase filters with different stopbands. (a) and (b) illustrate the z-plane of the two filters transfer functions, $\widehat{H}(z)$, with different cut-off frequencies, (c) and (d) are the revised impulse responses of the targeted system, (e) and (f) are the frequency response of the targeted system, H(z), correspondingly.

As a 2-D example, the targeted log-magnitude diagram is presented in Fig. 4.6(a). As seen, the assumed log-magnitude is in the form of concentric circles with different steps. As mentioned before, the magnitude and phase of the minimum-phase filter are related to each other by the DHT. Fig. 4.6(b) illustrates the impulse response. As seen, the signal is a one-sided asymmetric half-plane. Also, one may notice that as the quantized structure has been used in the spectral domain (the concentric circles with different steps), some higher-order harmonics appeared in a spatial domain, which are circulating around the peak value of the impulse; this result agrees with our theory of quantization. The result for the approximated minimum-phase 2-D impulse response is presented in Fig. 4.6(c), and the corresponding magnitude of a transfer function (in dB) is shown in Fig. 4.6(d). Almost half of the truncated impulse response in Fig. 4.6(c) has a non-zero entry.

Next, we have to prove that the filter designed is minimum-phase. As already has been shown, the system is one-sided; thus, the causality condition is insured. Also, the designed digital filter is FIR; thus, the filter is stable. Thus, if we prove the inverse system is stable, the system would be minimum-phase. To do that, we use Huang's theorem. Note that our system is half-plane. However, we can always use a successive right-shear operator to convert a half-plane system to a first-quadrant system. If the resultant system is stable by Huang's theorem, so would be the original system. The root-loci diagrams of the quarter-plane system for $|z_1| = 1$ and $|z_2| = 1$ are illustrated in Fig. 4.6(e) and Fig. 4.6(f), respectively. As seen, all the calculated z_2 and z_1 points remain inside the unit circle, which shows that the filter designed is minimum-phase by Huang's theorem.

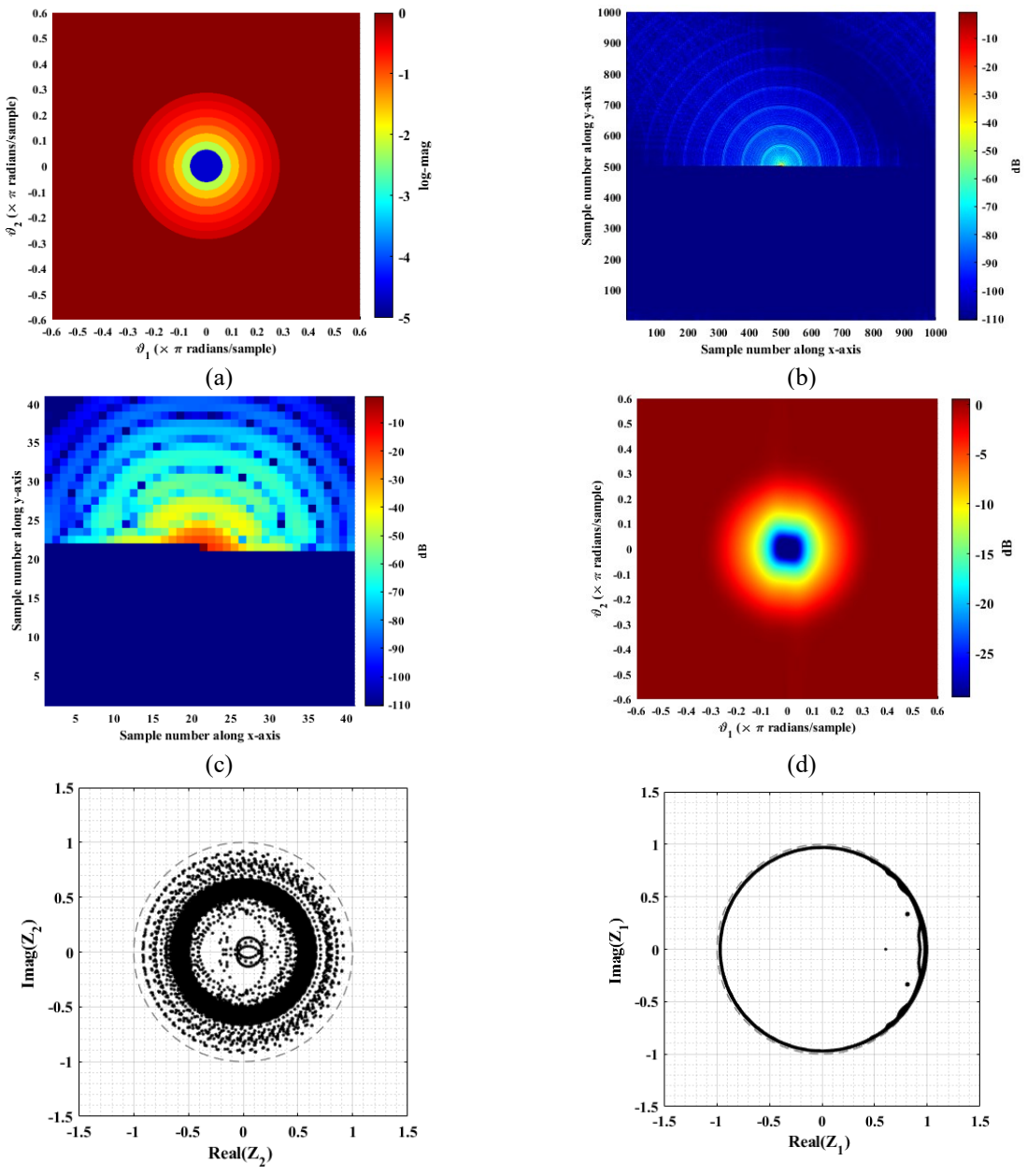

Fig. 4. 6. An Exemplar 2D minimum-phase filter. (a) and (b) illustrate the z-plane of the two filters transfer functions, $\widehat{H}(z)$, with different cut-off frequencies, (c) and (d) are the revised impulse responses of the targeted system, (e) and (f) are the frequency response of the targeted system, H(z), correspondingly.

Chapter 5
Noise shaping for PA design

5.1 Fundamental implications

We define the normalized spatial frequencies as $\boldsymbol{\vartheta} = [\vartheta_1,\ \vartheta_2]$, which is simply the digital frequency vector normalized to π. Another vector is the antenna direction cosines $\boldsymbol{P} = [U, V]$, normalized wave number. These two vectors can be related to each other by $\boldsymbol{\vartheta} = \delta \boldsymbol{P}$. The scalar factor of $\delta = d/\lambda$, where d is a constant (it is not the element spacing), converting the normalized lattice to the physical one, and λ is the wavelength. For the Nyquist design, $d = \lambda$ and the normalized spatial frequency and wave number vectors become equal. Evidently, for a dense array $\delta < 1$, while for the sparse one $\delta > 1$.

Considering that $U = sin\theta cos\varphi$ and $V = sin\theta sin\varphi$, the visible region is defined as the region confined by $U^2 + V^2 \leq 1$. This is simply because $|sin\theta| \leq 1$ and that, out of this region (called the invisible or imaginary region), the EM wave decays or says it does not contribute to a coherent wavefront, plane wave propagation. Thus, the visible region is of unit radii in $\boldsymbol{P}$ (or *U*-*V*) plane and of α radius in $\boldsymbol{\vartheta}$ plane. One may consider the excitation of the antenna array as a 2-D discrete signal; thus, based on the sampling theorem, the array factor is periodic. In this regard, the shape of one fundamental period of the array factor is not unique. This is because the lattice matrix is not unique.

If one considers ρ as the normalized array pitch for $\|\boldsymbol{b_1}\|_2 = \|\boldsymbol{b_2}\|_2 = \rho$, then it should be respectively taken as 0.5 and $\frac{1}{\sqrt{3}} \approx 0.58$ for the Nyquist design of the square and the so-called hexagonal lattice.

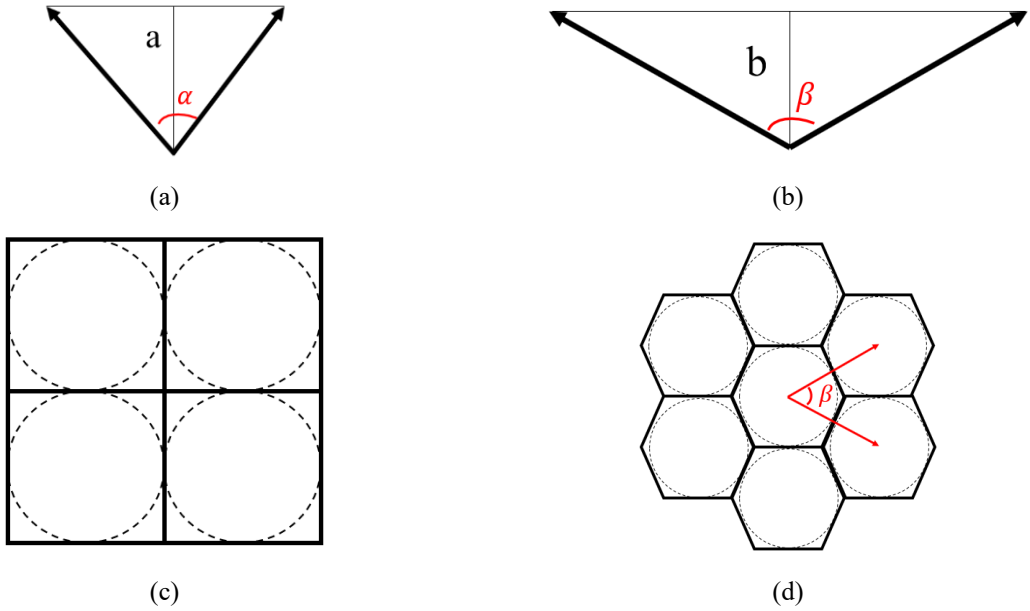

Fig. 5. 1. Element location lattices and reciprocal lattice periods. (a) two equal length basis vectors of Element location lattice, (b) two basis vectors of the reciprocal lattice. Schematic of the reciprocal domain period for (c) square lattice and (d) hexagonal one.

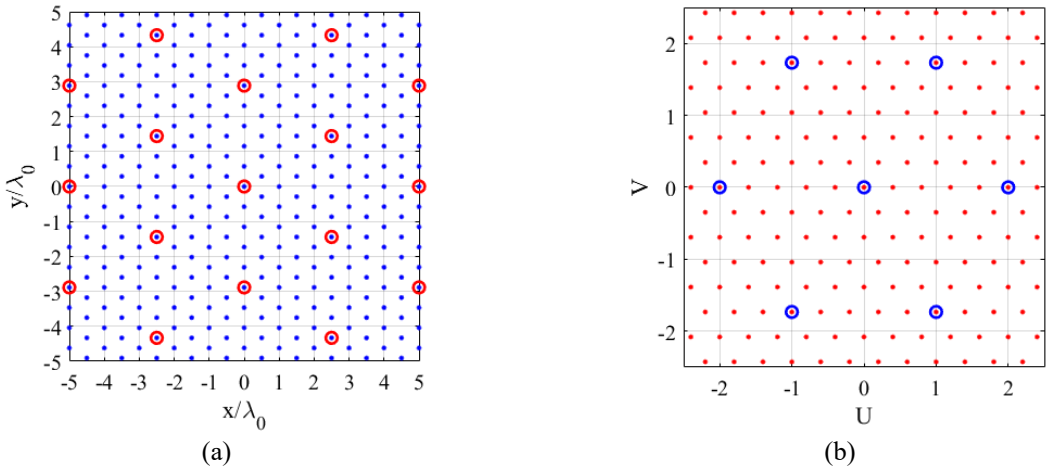

Fig. 5. 2. Example of hexagonal Element location lattice and reciprocal lattices. (a) Element location lattice and reciprocal steering lattice and (b) periodicity lattice and steering lattice.

That comes from algebra. If two base vectors were of equal length, so would the reciprocal lattice basis vectors. Besides, the product of the stem lengths is 0.5, ab = 0.5, as shown in Figs. 5.1(a)-(b). Also, $\alpha + \beta = 180°$. The schematic of the fundamental period for square and hexagonal lattices is shown in Figs. 5.1 (c)-(d). Dashed circles show the visible region. For example, for a hexagonal lattice, to avoid the grating lobe appearance for any steered array factor, the distance between the center of two adjacent periods should be at least 2 on the *U-V* plane. In Fig. 5.1(d),

$\beta = 60°$ and that, the stem b is $\sqrt{3}$ and so that a = $\frac{1}{2\sqrt{3}}$ which contributes to normalized element spacing of $\rho = \frac{1}{\sqrt{3}}$.

The Nyquist hexagonal lattice generates the densest PL without the appearance of grating lobes for any steered array factor or, equivalently, the sparsest ELL among regular lattices constituted by regular *polyhedral* prototile [100]-[101]. In simple words, decreasing element density per unit area makes the antenna cheaper, at least from the number of elements used perspective. However, the preceding statement is controversial, as pointed out later. In Fig. 5.2(a), a hexagonal ELL with a Nyquist design is shown by blue dots. Its reciprocal lattice is shown with the same color in Fig. 5.2(b), which is PL. As seen, the distance between the two elements of PL is 2; this lattice is orthogonal to the lattice shown in Fig. 5.1(d). The SL in Fig. 5.2(b) and its reciprocal lattice are shown in red color. Here, $\boldsymbol{T} = 5\,\boldsymbol{I}$; thus, the steering lattice is 25 times denser than PL. That means the beam can only be defined in 25 directions. The SL elements are precisely the samples of the beamspace domain, and thereby, the reciprocal domain becomes periodic, which explains that the lattice in Fig. 5.2(a), shown by the red hollow circles, is, in fact, the SL periodicity lattice in the reciprocal domain which is 25 times sparser than ELL.

5.2 Real-valued noise shaping

For the real-valued noise shaping (RV-NS), the RCDF should be utilized whose frequency response is conjugate symmetric. For now, we use the RV-NS to address the phase-only synthesis of the array. That means that the filter should be designed so that the shifted spectrum of the PDA error would be in the visible region.

As an example, for a 1-D case, let us consider the targeted beam point at U_0, as shown in Fig. 5.3. The borders of the visible window (or area of interest) are supposed to be off U_v range. In this

case, if one designs a CCDF at the center spatial frequency of -U_0 with the band's rejection of U_v, the in-band quantization error of excitation would be pushed out from the visible window at the center frequency of *O* with the band rejection of U_v. However, in the case of the real-valued filter, the digital filter might be designed for the band rejection of $U_v + U_0$, which means that a part of the PDA noise would be pushed out excessively, and that might be considered as the limitation of the phase-only synthesis since.

A visual representation of the proposed method for the 2-D case is illustrated in Fig. 5.4 for the planar array. Besides, we considered $\boldsymbol{\vartheta} = [\vartheta_1, \vartheta_2]$ as a 2-D normalized frequency in Fig. 5.4(a), the targeted beam point, *T*, is rotated 180° with respect to the origin, finding the center of the shifted stopband (SB). The frequency response magnitude is symmetric with respect to the origin.

Therefore, every point on one side of the border of symmetry (BOS) has a mirrored copy on the other side. That generates an intersection region between the SB and its mirrored copy which is truncated in Fig. 5.4(b), yields the truncated shifted stopband (TSSB). In practice, since some QLs may appear there, the filter design should consider the intersection region. Overall, the real-valued digital filter is realizable with an even stopband (ESB), as depicted in Fig. 5.4(c). Having performed the RV-NS, the realized band rejection (RBR) will be like the one schematically shown in Fig. 5.4(d). As seen, the same as the 1-D counterpart, a part of the stopband is out of the visible region, which is the disadvantage of the RV-NS since it inserts excessive noise. This excessive stopband corresponds to the beam pointing angle and the array pitch size.

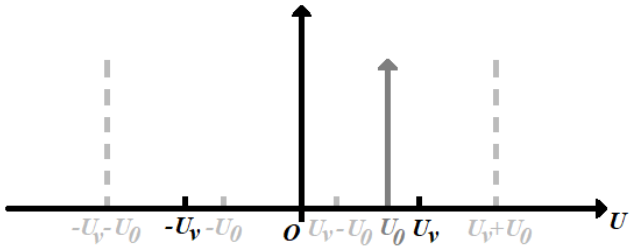

Fig. 5. 3. A schematic view of the digital filter spectrum and the targeted beam point at U_0.

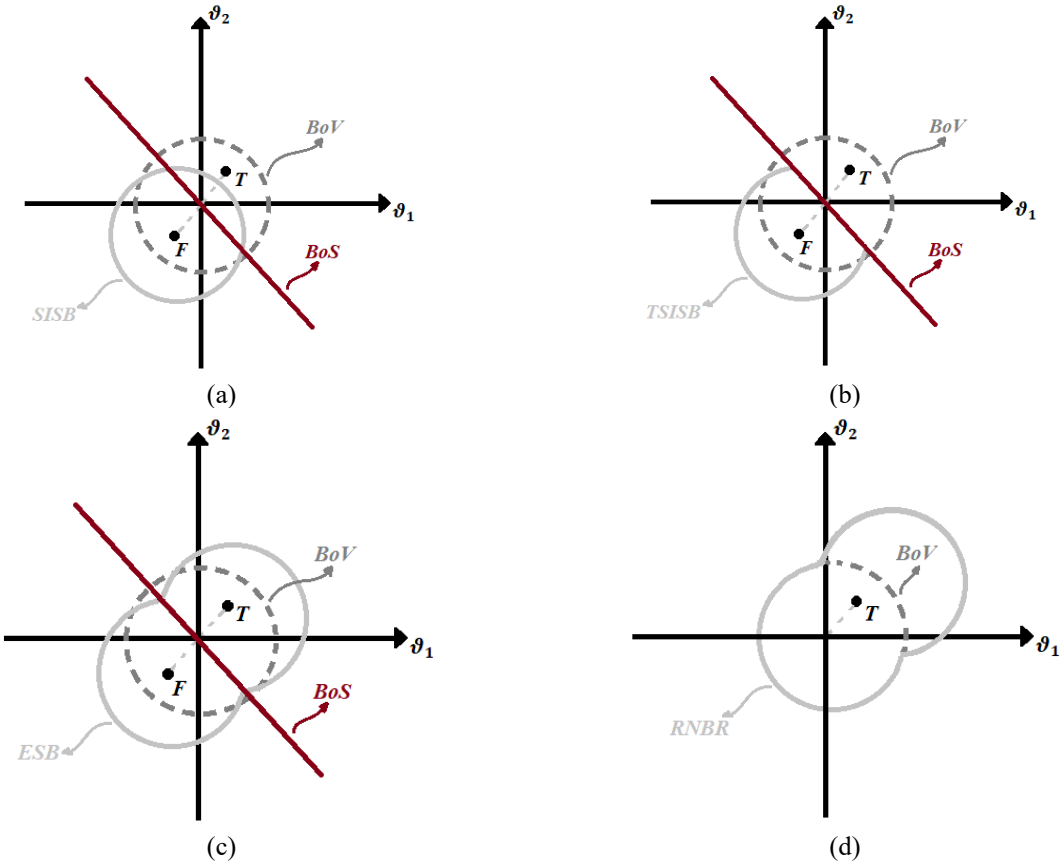

Fig. 5. 4. Design of filter layout for phase-only synthesis. Schematic view of the (a) shifted stopband, (b) truncated shifted stopband, (c) even stopband, and (d) realized band rejection region.

5. 3. RVNS for square lattice PA beamforming

Let us reconsider the exemplar PA of Fig. 5.5(a). The constituent element is an aperture-coupled patch operating at a 10 GHz center frequency. The patch is designed and matched in a periodic boundary condition (PBC). The antenna is backed by a reflector, increasing the antenna's front-to-back ratio. Other specifications are the same as mentioned in Fig. 3.9. The revised system and the resultant PDA are shown in Figs. 5.5(a) and 5.5(b), respectively. The targeted filter frequency

response includes two major constituents comprising the spots (deep nulls) corresponding to the QLs and the circular shape background associated with the visible region. Of course, they are shifted according to the beam point direction and subsequently symmetrized. The reason for using spots or (notches) is that the error spectrum is not flat. The exact solutions, by FDTD, to radiation patterns of antennas are illustrated in Figs. 5.5(d). Both patterns are normalized to the maximum gain of the one designed by RV-NS. As seen, near the extreme of the visible window, there is a sharp roll-off for full-wave results that can primarily be attributed to the edge diffraction. The constituting element is *y*-polarized. The element factor is considered in Fig. 5.5(d) for the computed result, making about 3-4 dB roll-off close to the extreme of the visible window on the E-plane. Note that we approximately eliminated the coupling factor in the element factor by using the PBC. As seen, the RV-NS method compensates for the gain loss incurred by the quantization to some extent. Compared to the one with high precision PDA, the RV-NS cost for antenna gain degradation is about 0.1 dB, cf. Fig. 3.9. However, the non-quantized PDA is not realizable; thus, the antenna designed based on the noise shaping approach has the highest gain of practical systems. Evidently, the amount of gain compensation depends on the filter specifications. Note that the excessive stopband region and/or depth of band rejection can increase the gain loss. The above example also shows that the noise shaping method outperforms the dithering. The exact solution for the PA designed using NSD-RPDF showed 0.27 dB gain loss compared to the RV-NS.

However, the RV-NS fails to shift the QLs into the invisible region for some commanded beam directions. That, in particular, happens for $\rho \geq 0.5$. It follows that the RCDF frequency response is conjugate symmetric, and the filter is designed based on the shifted error pattern. For an antenna with $\rho \geq 0.5$, this may prohibitively yield a vast bandstop region for some beam directions covering the whole fundamental period of the array factor.

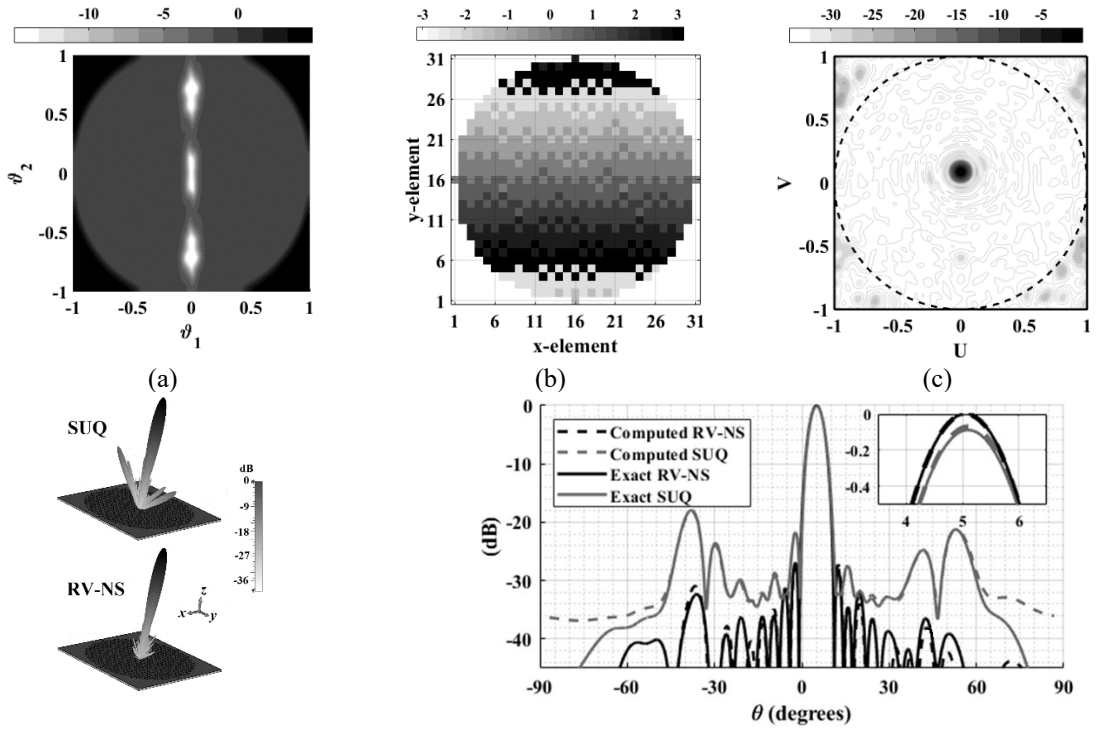

Fig. 5. 5. Planar phased array based on RV-NS compared with the one compared with simple uniform quantization (SUQ). (a) Frequency response of the revised digital filter, (b) the phase delay arrangement, (c) array factor designed by RV-NS. (d), compared with analytical results, the 3D exact solution of patterns for an antenna designed based on SUQ and RV-NS (e) exact patterns on the plane.

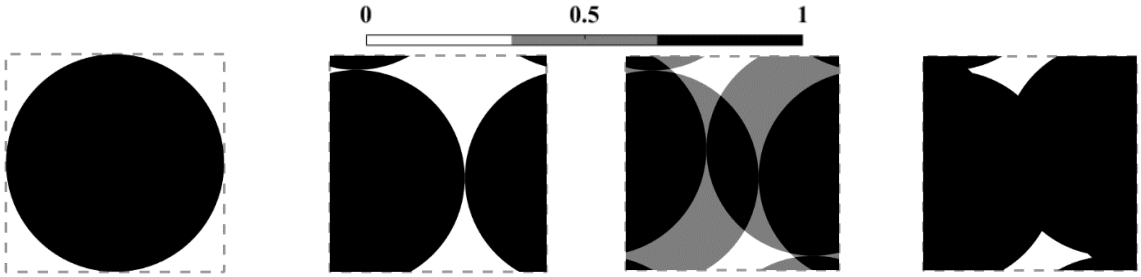

Fig. 5. 6. Schematics of filter layout background for $\rho = 0.5$ and $[\theta, \varphi] = [50°, 10°]$, (a) disk associated to the visibility region, (b) shifted layout to beam point, (c) intersection pattern of symmetric copies, (d) unweighted filter layout background.

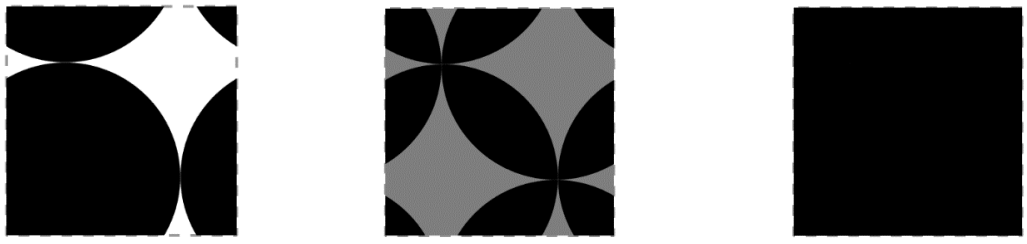

Fig. 5. 7. Schematics of filter layout background for $\rho = 0.5$ and $[\theta, \varphi] = [45°, 45°]$, (a) shifted layout, (b) intersection pattern of symmetric copies, and (c) unweighted filter layout background.

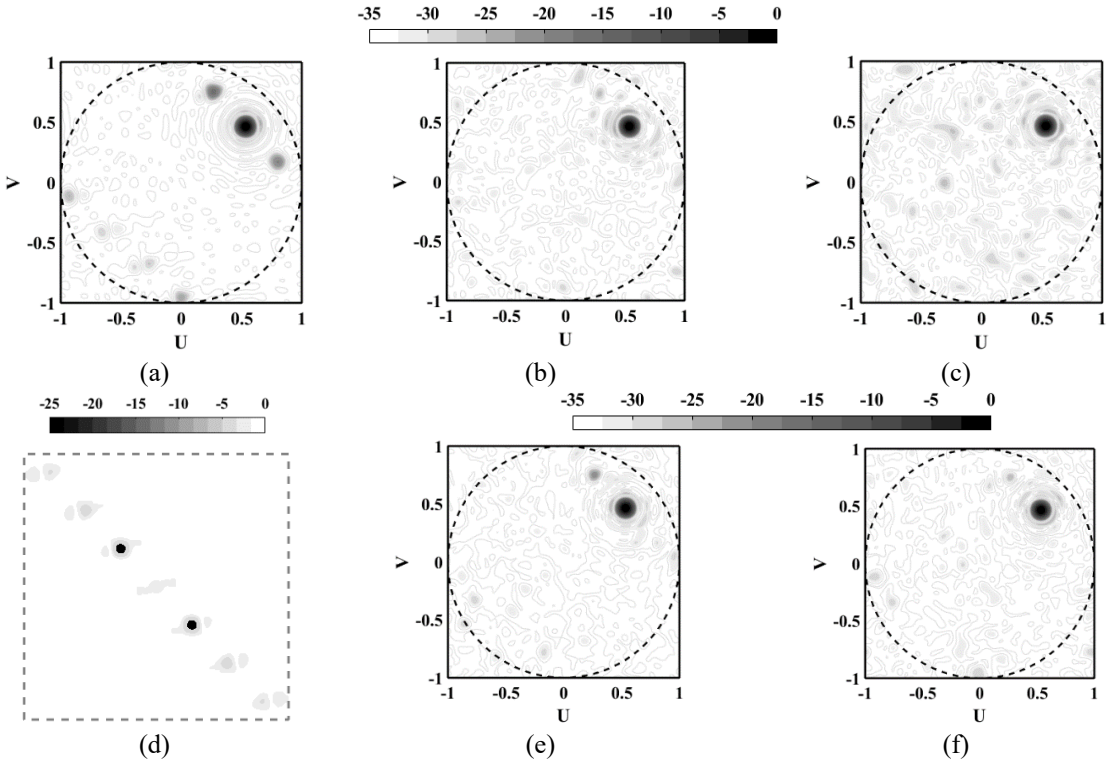

Fig. 5. 8. Comparison of random dither and RV-NS based on spaced notches. (a) steered array factor, $[\theta, \varphi]$ = [45°, 41°], computed for (a) simple quantization, (b) RPDF and (c) TPDF systems. (d) filter layout example of RV-NS type II, decibel array factor for (e) RV-NS type I, and (f) RV-NS type II.

TABLE 5.1
NORMALIZED DIRECTIVITY AND SLL IN DB FOR ARRAY FACTORS OF FIG. 5.8.

	SUQ	RV-NS type I	RV-NS type II	RPDF	TPDF
SLL	-16	-20.9	-25.6	-25.3	-23.6
$D_n(\boldsymbol{\vartheta_0})$	0	-0.02	-0.07	-0.17	-0.27

For Nyquist design, the method can "see" some portion of the invisible region, particularly for beam steering along the principal axes or close to them. Besides, the fundamental period becomes visible for some critically large array pitches. Fig. 5.6 schematically illustrates how this is so.

The black circular disk is associated with the visible region, and the gray dashed line illustrates the fundamental period boundary. After shifting and symmetrizing, Figs. 5.6(b)-5.6(c), the resultant unweighted filter layout background (FLB) would be in the form shown in Fig. 5.6(d); actually, one can compute that directly.

On the other hand, the method does not "see" the free spectrum for those steering angles along $\varphi = \mp 45°$ or close to that. This is simply because the shifted invisible region is covered by the mirrored copy of the black disk, which has been shown in Fig. 5.7 for the commanded beam at $[\theta, \varphi] = [45°, 45°]$.

In cases where the invisible region is not reachable, our strategy is to define the RCDF only as some spaced notches. Those correspond to the QLs inside the visible region and their mirrored copies. In Figs. 5.8(a)-(c), array factors of excitation signals quantized to 3 bits by SUQ, RPDF, and TPDF are depicted, respectively. The RV-NS approach also addresses this problem based on spaced notches strategy. Two RCDFs are used with different depths of notches. Let us call them RV-NS type I and type II. The minimum null depths in their filter layout are correspondingly -10 dB and -22 dB. For example, the filter layout for type II is shown in Fig. 5.8(d). There are two symmetric deep nulls and some seemingly very shallow ones. Indeed, the deep nulls are intended for main QLs with higher peaks. However, there are also other QLs have smaller peak amounts, cf. Fig. 5.8(a). Without considering the shallow notches associated with those minor QLs, those regions would be out-of-band; thus, the noise shaper amplifies those region error magnitudes and may become malignant. The results of array factors for two systems are shown in Figs. 5.8 (e) and 5.8 (f). Also, the SLL and the normalized directivities for all cases are tabulated in Table 5.1. As can be seen, the RPDF and RV-NS type II QL peak level performances are almost the same. However, the RV-NS type II incurs less directivity loss. This is ironic since although the RPDF inserts the least amount of dither power among all systems that comply (2), Table 5.1 proves that RV-NS designed based on the spaced-notches strategy is optimal. The preceding statement is in addition to the fact that, generally, the RV-NS is a spectrally inefficient method, imposing excessive noise power on the system.

5.4 Rationale behind the gain compensation

In the example of Fig. 5.5, the antenna directivity increased after noise shaping. Here we explain the reason. The imaginary region has no physical reality in EM propagating mode but contributes to evanescent wave components [102]. Referring to the discrete form of Parseval's equation,

$$\sum_{\boldsymbol{i}\in\mathbb{Z}^2} |s[\boldsymbol{i}]|^2 = \int_{\boxtimes} |S(\boldsymbol{\vartheta})|^2 d\boldsymbol{\vartheta} \tag{5.6}$$

where $\boxtimes$ is a stenography for any shape of the beamspace fundamental period. The power pumped into the terminal of a physical antenna is associated with the equation left side, but the radiated power only contributes to the visible region of the beamspace domain. In this regard, if one succeeds in pushing the QLs out of the visible region, the antenna directivity may increase. However, in such a "thought experiment," the cost of QL suppression should be clarified. Note that this compensation is a portion of the gain loss due to the QLs suppression, not the gain loss due to the inserted noise. In this regard, one may write the following in a hemispherical sense:

$$D(\boldsymbol{\vartheta_0}) \propto P(\boldsymbol{\vartheta_0}) \left[\int_{\otimes} P(\boldsymbol{\vartheta}) d\boldsymbol{\vartheta} \right]^{-1} \tag{5.7}$$

where $\otimes$ signifies the visible region of the beamspace domain and $P(\boldsymbol{\vartheta})$ might be considered as a power pattern, then $D(\boldsymbol{\vartheta_0})$ corresponds to the antenna directivity at the specified DOA, $\boldsymbol{\vartheta_0}$. Could one only displace the QLs from the visible region to the imaginary one, $P(\boldsymbol{\vartheta_0})$ would almost remain constant, referring to (5.6). That contributes to an increase in antenna directivity since, in (5.7), the integration inside the bracket decreases. However, in practice, it might not be possible to push all the in-band noise out-of-band. Besides, the system imposes some overloads, meaning that it inserts some portion of noise; thus, $P(\boldsymbol{\vartheta_0})$ drops, which degrades the antenna directivity, corresponding to the inserted noise power. As stated before, MPS can better satisfy such a request

among all systems with the same magnitude spectrum.

5.5 Complex-valued noise shaping

If the underlying signal is the complex-valued excitation, the phasor $jA_i e^{j\Phi_i}$, no shift for the filter response is required, in contrast to the RV-NS approach. We may call that complex-valued noise shaping (CV-NS) or simply CV. In this case, both RCDF and CCDF are possibly to be utilized. The advantage of CCDF over RCDF is that its frequency response is one-sided; thus, it may contribute to more spectrally efficient noise shaping. For the CV method, minor lobe performance is examined for ρ equal to 0.5 (709 elements) and 0.4 (1129-element). All filters are designed using the DHT method with a truncated impulse response of 20×30 under the Han window. Also, the performance of the RV method for the 3-*bit* system is compared with those of the CV one. The excitation amplitude is quantized to 3 bits for the RV-NS approach. The 3-*bit* amplitude quantization does not incur considerable distortion on the radiation pattern.

The method of minor lobe performance for a 4-*bit* system can be seen in Fig. 5.9. Comparing with the SUQ, and CV-NS has almost eliminated all QLs in the visible region; almost no minor lobe with more than -35 dB has appeared in the visible region. As expected, decreasing the number of bits to three, QLs of much higher levels show up.

It can be seen in Fig. 5.10 for a 3-bit system that although both methods can acceptably suppress the QLs, the CV method outperforms the RV one. Besides, in Figs. 5.10(b) and 5.10(c), no effective portion of the invisible region is reachable by the RV-NS; thus, RCDFs are designed based on the spaced-notches strategy. However, even in Fig. 5.10(a), both methods can push the QLs to the invisible region, the RV-NS still has inferior performance. The frequency responses of revised systems are shown in Figs. 5.11(a) and 5.11(b).

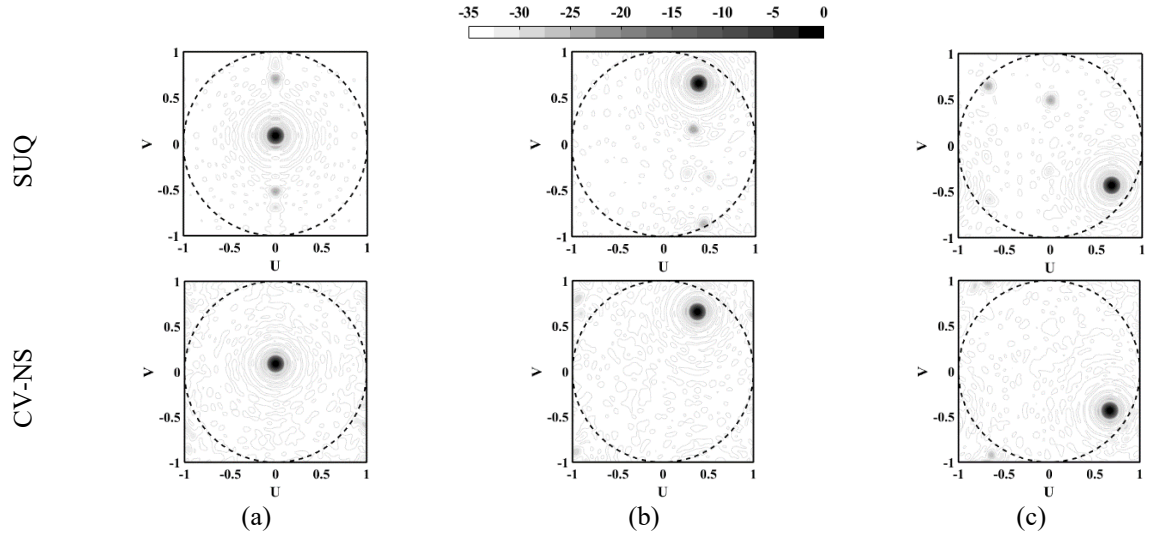

Fig. 5. 9. Decibel array-factor for 0.5 normalized pitch, excitation magnitude and phase are quantized to 4 bits and the main beam is commanded at (a) $[\theta, \varphi]$ = [5°, 90°], (b) $[\theta, \varphi]$ = [49.2°,60°], and (c) $[\theta, \varphi]$ = [52.6°, -33°].

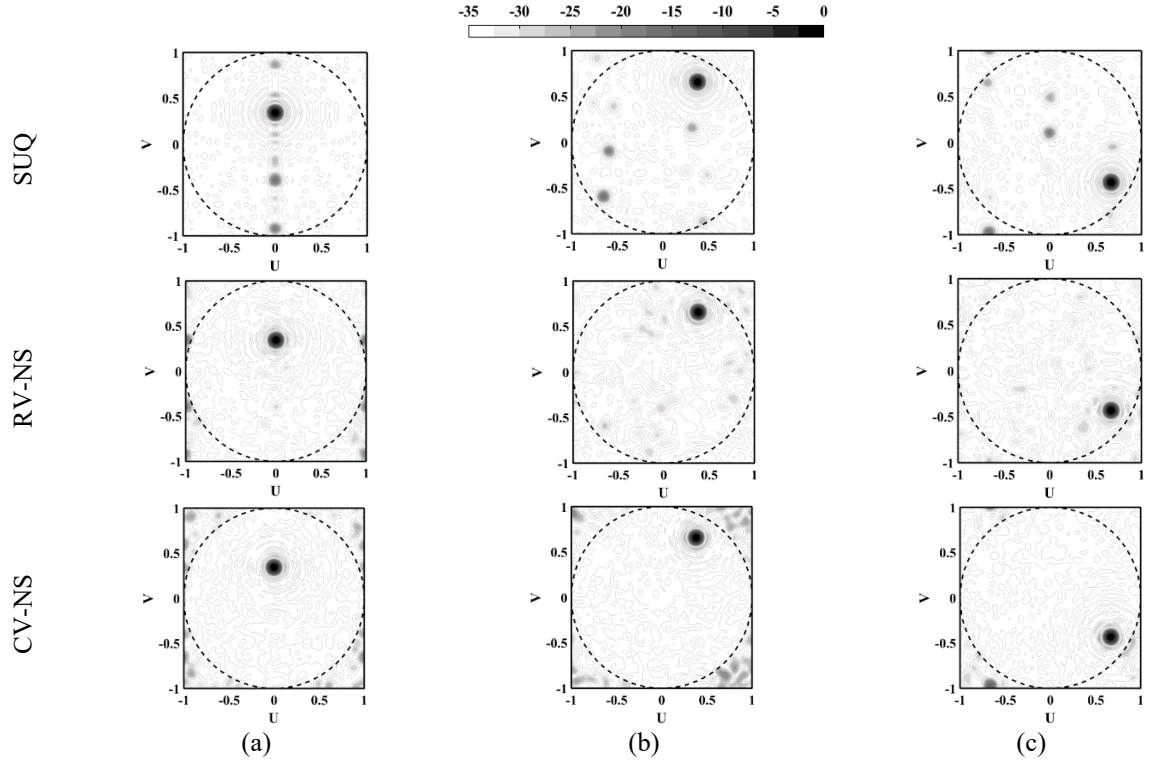

Fig. 5. 10. Decibel array-factor for 0.5 normalized pitch, excitation magnitude and phase are quantized to 3 bits and the main beam is commanded at (a) $[\theta, \varphi]$ = [20°, 90°], (b) $[\theta, \varphi]$ = [49.2°,60°], and (c) $[\theta, \varphi]$ = [52.6°, -33°].

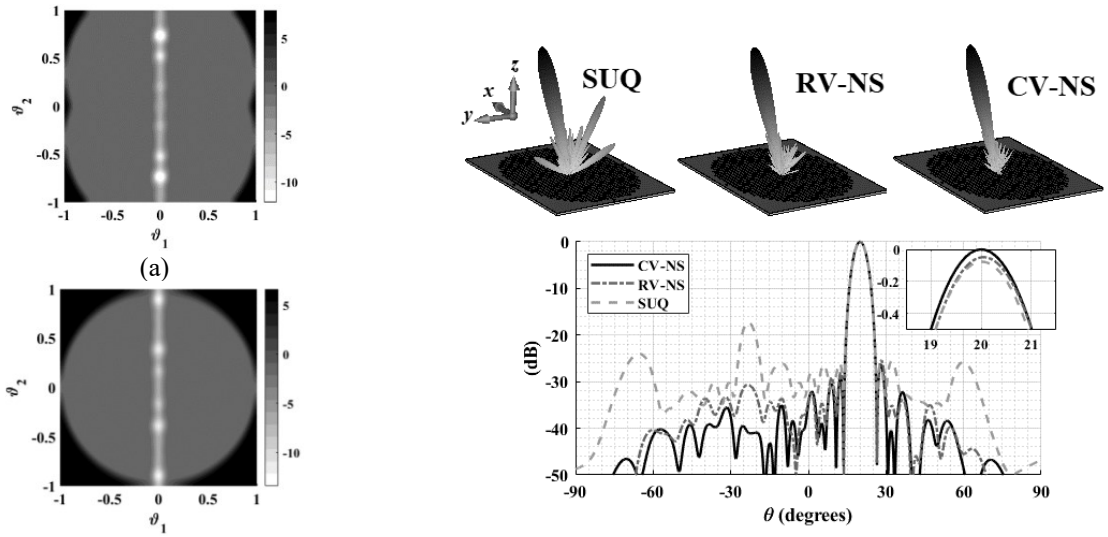

(a) (b) (c)

Fig. 5. 11. Design of phased array based on RV- and CV-NS methods for 0.5 normalized array pitch. Computed frequency response of revised (a) real-valued, (b) complex-valued digital filter, and (c) the corresponding exact solutions of radiation patterns.

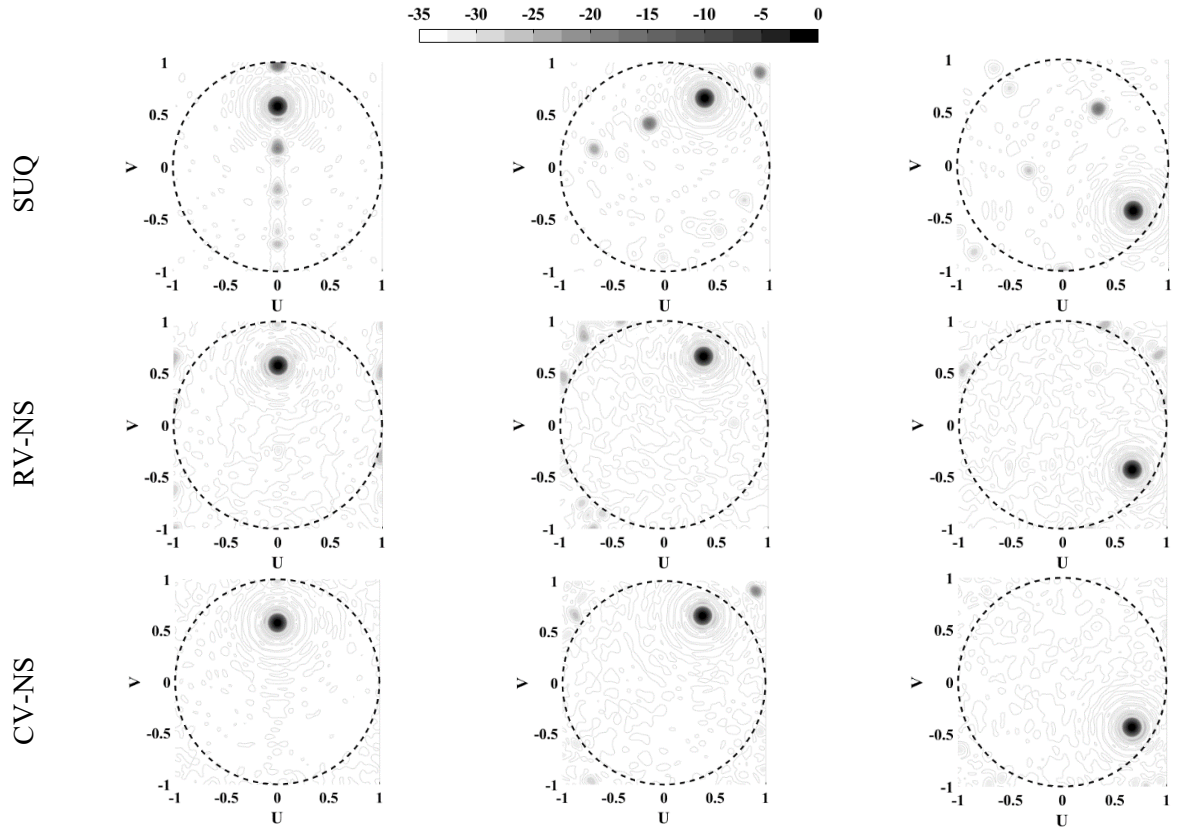

(a) (b) (c)

Fig. 5. 12. Decibel array-factor for 0.4 normalized pitch, excitation magnitude, and phase are quantized to 3 bits. The main beam is commanded at (a) $[\theta, \varphi]$ = [35°, 90°], (b) $[\theta, \varphi]$ = [49.2°,60°], and (c) $[\theta, \varphi]$ = [52.6°, -33°].

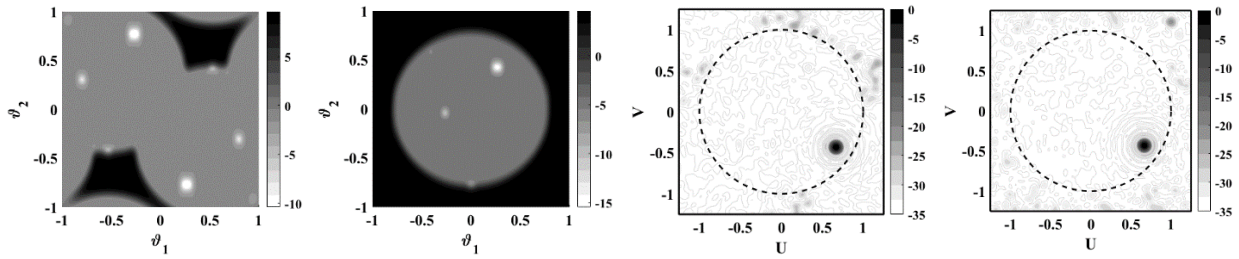

Fig. 5. 13. Design of phased array based on RV- and CV-NS methods for 0.4 normalized array pitch. (a) Computed frequency response of the revised (a) real-valued, (b) complex-valued digital filter, and corresponding decibel array-factors on one fundamental period of the beamspace domain in (c)-(d).

The corresponding full-wave solutions for the radiation patterns are illustrated in Fig. 5.11(c). As expected, the antenna designed based on the CV-NS has a negligible amount of more gain and less minor lobe level in comparison to the others; the mean excitation power is almost the same for all antennas. Thus, the better performance of the one designed by the CV approach is more related to more efficient noise shaping.

Generally speaking, decreasing the antenna pitch can dramatically decrease the quantization distortion. The original signal is almost bandlimited, while the power of quantization noise distributes in a broader region of the beam space domain, and the maximum QL level drops.

In addition, some QLs are alias versions of the original ones; as such, antennas with smaller pitches received less severe QL levels. Besides, it may lead to more QLs appearing at high spatial frequencies inside the so-called invisible region; thus, there would be no need to address them in the filter design. In Fig. 5.12, the simulation results of the array example with $\rho = 0.4$ are illustrated using a 3-*bit* system. In addition to less quantization distortion than the one with $\rho = 0.5$, the noise shaper also works more effectively for this case. Furthermore, for the RV method, there is enough free spectrum for all beam directions; hence, the error can be conveniently pushed to the invisible region. Overall, both RV and CV methods work much more effectively than those of Fig. 5.10. Again, note that the system performance is not unique and depends on the filter applied. In Fig. 5.13, the performance of both methods is presented on one fundamental period of

steered array-factor, $[\theta, \varphi]$ = [52.6°, -33°]. Specifically, Figs 5.13(a) and 5.13(b) show the frequency responses of the system used. As seen, though the RV-NS imposes excessive bandstop, it "sees" enough portion of the invisible region. The distortion due to the amplitude quantization is somehow different from the phase quantization, and it depends more on the tapering approach used. Furthermore, the phase quantization error manifests itself by preventing the received signals from being combined coherently; hence, phase quantization is more problematic than amplitude quantization.

Quantizing the high precision amplitude to 3-4 bits work acceptably well with almost no considerable distortion, although such a judgment depends on the application. However, using 2-*bit* amplitude quantization yields an increase of considerable distortion. See the contours faintly illustrated for SUQ in Fig. 5.14 that the QLs, due to amplitude quantization, seemingly circulate the main beam. Although the amplitude and phase quantization errors are much more severe for the 2-*bit* system than those of the 3-*bit* ones, e.g., in Fig. 5.14(a), SLL for SUQ is about 9.6 dB; still, CV-NS works promising and suppresses the in-band QLs.

Thus, although a smaller array pitch adds to the costs due to the more control elements needed, those costs might be compensated back to some extent since the pattern receives less severe distortion and the noise shaper works more efficiently; thereby, the system can be designed with cheaper devices. Further of importance is the lattice used.

Finally, such implementation should be done for wideband systems' upper end of the signal temporal-frequency band, ensuring that the error pushed to the invisible region remains safe. Thus, the radius of the visible disc should be assumed to be unity for the upper-frequency band.

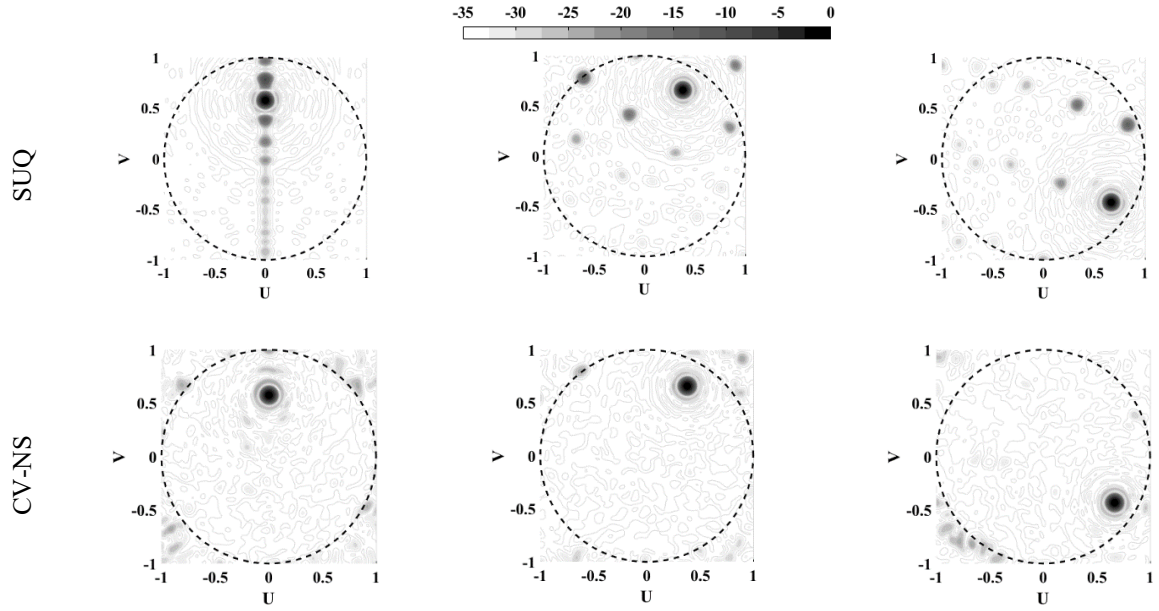

Fig. 5. 14. Decibel array-factor for 0.5 normalized pitch, excitation magnitude, and phase are quantized to 2 bits. The main beam is commanded at (a) $[\theta, \varphi]$ = [35°, 90°], (b) $[\theta, \varphi]$ = [49.2°,60°], and (c) $[\theta, \varphi]$ = [52.6°, -33°].

5.6 Hexagonal lattice PA

5.6.1. Fundamentals

The suboptimality of classic square lattice is well-known. That requires a denser basic lattice comparison to, for example, the hexagonal one. However, one should recognize that the classic square lattice, $\rho = 0.5$, provides a freer spectrum by which the noise shaping process can be carried out with greater fidelity, particularly for the RV-NS method.

Consider an almost circular-aperture hexagonal lattice PA with a diameter of $16\lambda_0$. Fig. 5.15(a) shows the uniform phase distribution array factor on more than one fundamental period. Fig. 5.15(b) shows almost one period of the steered array factors in which 3-*bit* SUQ is assumed. As seen, the quantization yields the appearance of QLs.

Phase quantization hinders the input signals from being combined coherently, which typically causes more severe distortion than amplitude quantization. We observed that the QLs show up periodically with respect to the azimuth angle. For the square- and the so-called hexagonal lattice that is respectively $\Delta\varphi_s$ = 90° and $\Delta\varphi_h$ = 60°. It is because the QLs of a planar array are the intersection of those of the linear arrays located on the principle axes of the coordinate system. Fig. 5.15(c) illustrates another array factor example with an offset angle of 3×60°. The QL patterns are just rotated along the center, respecting the offset azimuth angle. This concept might be exploited in designing filter layout spots for different angles. In Fig. 5.16, the wavefront traversal is schematically illustrated for a hexagonal lattice array. The filter impulse is of size 20×10. In Fig. 5.16(a), the axes are in terms of sample number, while Fig. 5.16(b) illustrates the ELL layout and the physical positions of active elements normalized to the wavelength. Note that in the case of a square lattice, the two figures would show up in the same fashion.

This non-linear mapping between the two domains is one of the discrepancies between square lattice noise shaping and its hexagonal counterpart. Evidently, the same happens in a reciprocal domain for array factor and filter frequency response, which will be discussed later in the particular RV-NS approach section.

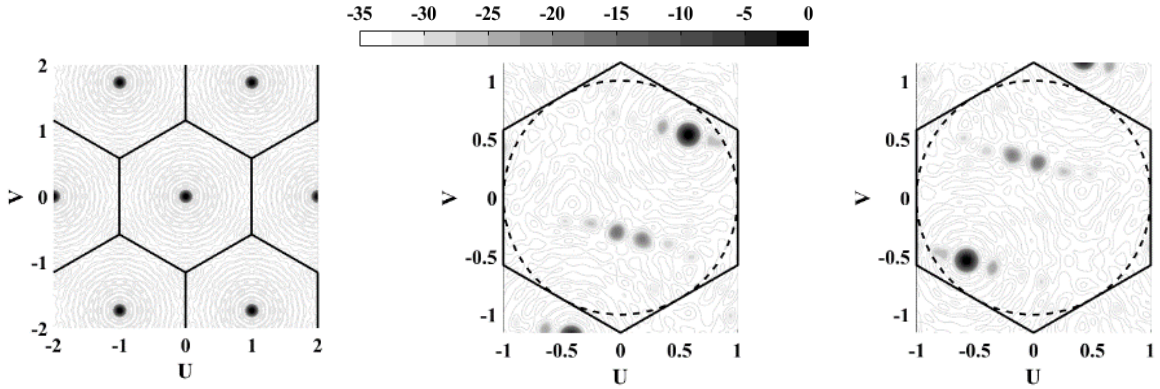

Fig. 5. 15. Exemplar hexagonal array with 3-bit digital phase shifter. (a) Array factor of excitation with uniform phase distribution and magnitude Taylor weighting of 37 dB SLL. Decibel array-factor of excitation signal quantized by 3-bit simple quantization system for the beam point direction at θ = 52° with (b) φ = 43° and (c) φ = 223°.

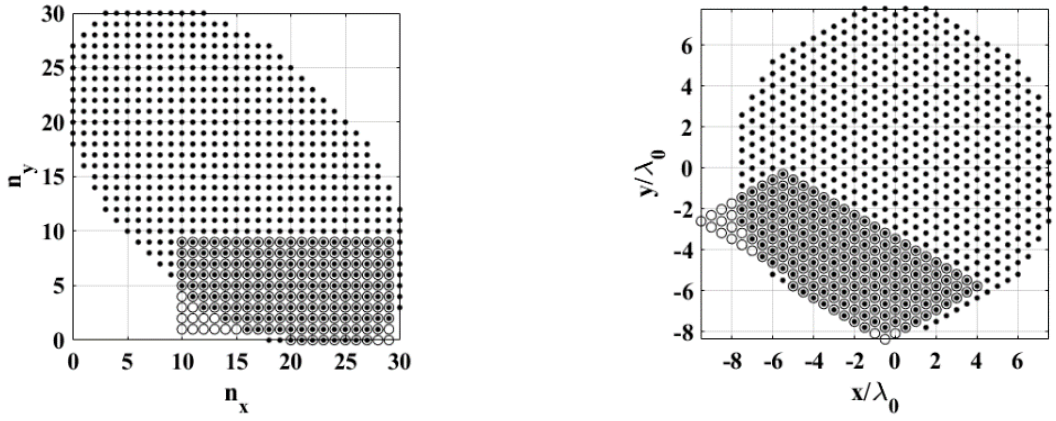

Fig. 5. 16. Schematic of noise shaper wavefront. (a) Impulse response samples, hollow circles, are schematically overlaid on the samples associated with the antenna active elements in which the noise shaper wavefront is assumingly striking to the sample $[n_x, n_y]$ = [19, 0], and (b) corresponding element location lattice layout.

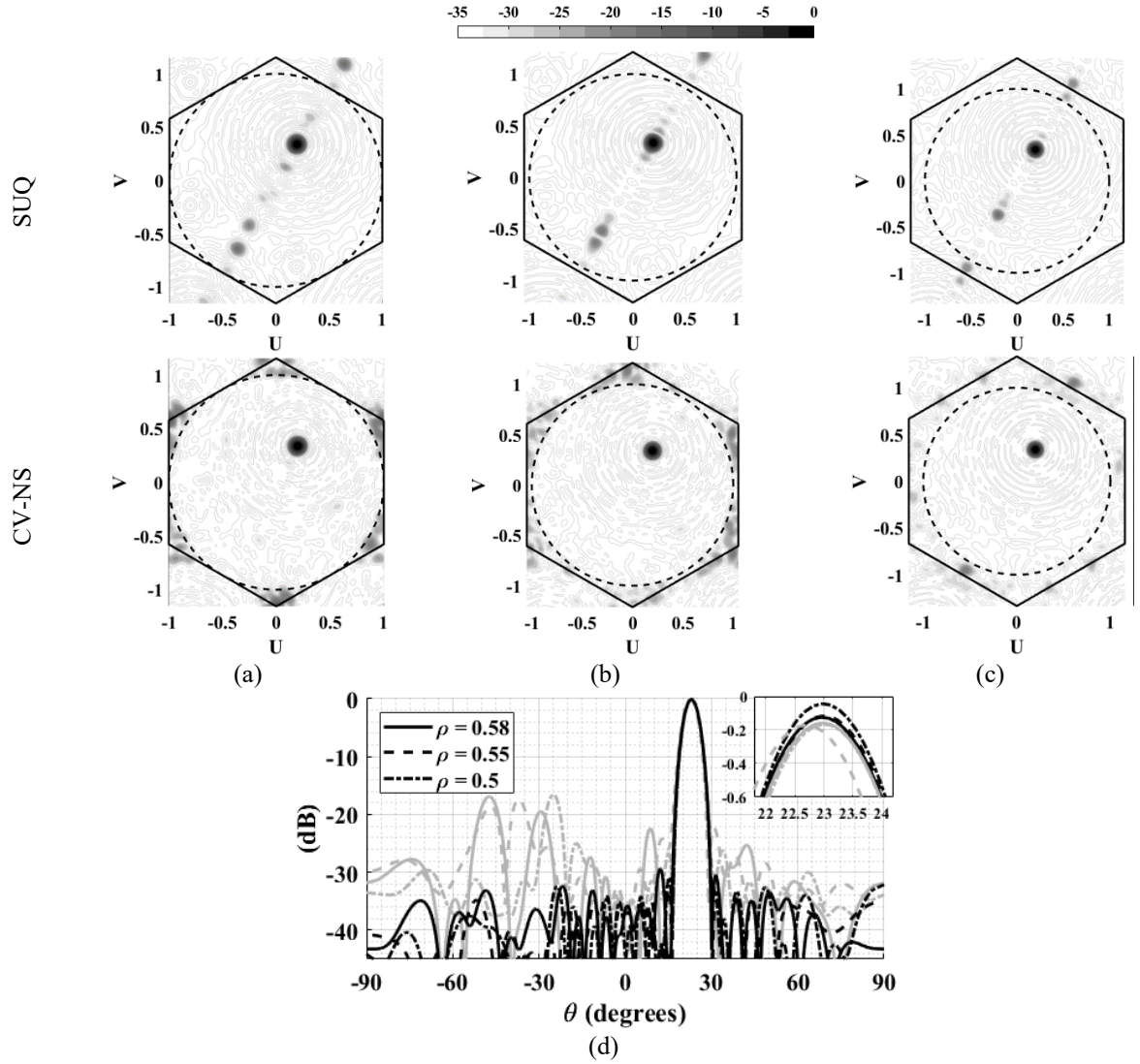

Fig. 5. 17. Decibel array factors in which different 3-bit systems quantize the complex beamforming coefficients. The normalized array pitches are respectively (a) 0.58, (b) 0.55, (c) 0.5. (d) Normalized array-factors on φ = 60° plane.

5.6.2 CV-NS

In Fig. 5.17, the beam is commanded at $[\theta, \varphi]$ = [23°, 60°]. The CBW is quantized into 3 bits for both phase and amplitude. The array factors designed based on SUQ and CV-NS systems are shown for normalized array pitches of ≈ 0.58, 0.55, and 0.5. Those correspondingly lead to 685, 769, and 931, constituting elements on array aperture.

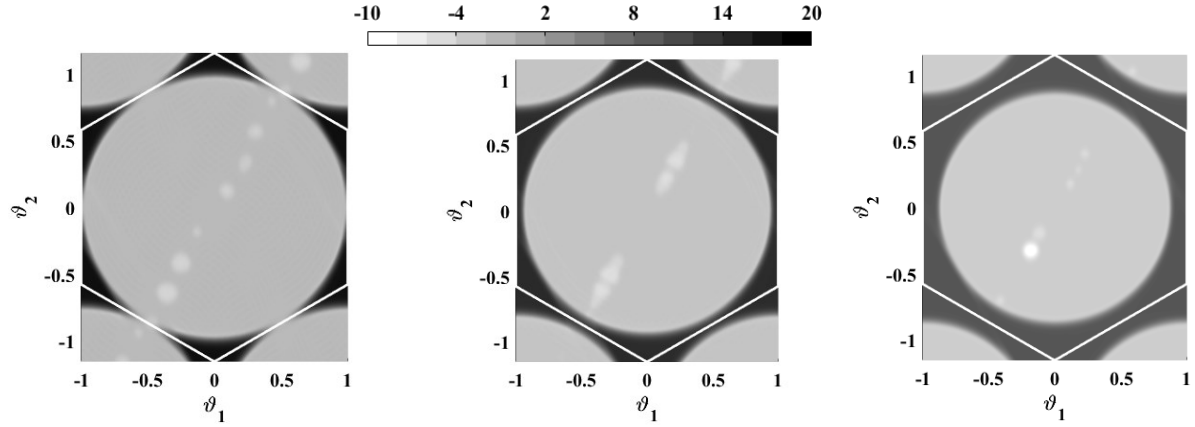

(a) (b) (c)

Fig. 5. 18. The revised systems for different pitches. Normalized pitch, ρ, equal to (a) 0.58, (b) 0.55, (c) 0.5.

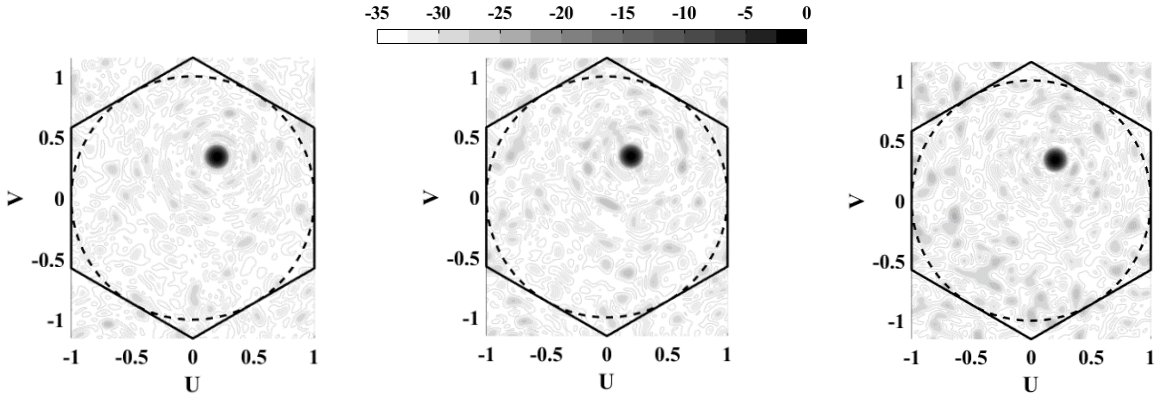

(a) (b) (c)

Fig. 5. 19. Array factors for different dithering. (a) RPDF, (b) TPDF, (c) GPDF.

TABLE 5.2
DIRECTIVITY LOSS WITH RESPECT TO HIGH PRECISION SYSTEM.

	SUQ	**CV-NS**	**RPDF**	**TPDF**	**GPDF**
Loss	0.15 dB	0.18 dB	0.31dB	0.48 dB	0.68 dB
SLL	16.77 dB	29.6 dB	26 dB	24.7 dB	24.2 dB

As seen in Fig. 5.17(a), the method is feasible in QL suppression. Nevertheless, the filter stopband region is quite broad [see Fig 5.18(a)]. Hence, the system imposes a significant portion of noise which is detrimental to the antenna gain. The array factors for CV-NS systems on $\varphi = 60°$ plane are shown in Fig. 5.17(d). Those for SUQ systems are also sketched faintly for comparison. All diagrams are normalized to the high-precision system array factor peak. As seen, all array factors designed based on the CV method have more gain values than those designed by the SUQ system. That is true because effective QL suppression pushes the error into the invisible region.

That does not happen in dithering, which typically imposes further gain degradation than the SUQ system. Moreover, note the results for $\rho = 0.55$, in which the beam for SUQ has about 0.4 degrees deviation. That has happened due to distortion beneath the main beam; see the notches in Fig. 5.17(b) associated with the QLs in the array factor. Thus, the results show that noise shaping can realign the beam point deviation by digging out the distortion beneath the main beam.

Sometimes power leaks through the minor lobes, here in terms of QLs in the visible region, yields considerable antenna gain loss and rise of interference, but some other times, it manifests itself as distortion inside the invisible region, which according to the Parseval equation yields small gain loss amount. Indeed, the distortion inside the invisible region does not contribute to the interference. As stated, it decreases the antenna directivity to some extent. That explains why the results for $\rho = 0.58$ show lower directivity than the one for $\rho = 0.5$ ($\alpha \approx 0.86$), which contributes to a smaller visible region in one fundamental period of array factor. This is because, as much as the filter stopband region becomes smaller, the noise shaper inserts a smaller amount of noise and yields smaller antenna gain loss.

In Figs 5.18(a)-5.18(c), the maximum out-of-band amplifications are 18.1 dB, 12.83 dB, and 5.91 dB, respectively. We also observed some results for the dithered systems shown in Figs. 5.19 with rectangular, triangular, and Gaussian (with zero mean and standard deviation of about half of the LSB) probability density functions, respectively written as RPDF, TPDF, and GPDF. The amount of gain loss and minor lobe level is Tabulated in Table 5.2.

Let's terminate this section with some full-wave solutions. Like the previous section, an almost circular aperture with a $16\lambda_0$ diameter is assumed with different normalized array pitches, including ≈ 0.58, 0.55, and 0.5. Furthermore, the beam is assumed to point at $[\theta, \varphi] = [23°, 0°]$. The constituting array element is assumed to be an aperture-coupled patch. The simulation results

are compared in Fig. 5.20 for SUQ [(a), (b), and (c)] and CV-NS [(d), (e), and (f)]. As expected, the CV-NS successfully suppresses the in-band quantization distortion. The SUQ results are sketched faintly in Fig. 5.20(g), while the black lines show CV-NS system results. The maximum antenna gains of those with ρ = 0.5 are more than other systems. That might be attributed to less distortion than the array factor with a smaller received pitch, which is expected by the dubious white noise assumption. However, that is incorrect for the second case, ρ = 0.55. Its maximum gain is less than that belonging to ρ = 0.58 with a considerable point deviation of about 0.4°. This might be attributed to a relatively huge impulse-shaped QL that happens beneath the main beam. It can be seen for the deep notch considered for the filter design in Fig. 5.18(b). Based on what was stated before, the QLs of the SUQ systems of Figs. 5.18 and 5.20 examples are of the same shape with different offset rotation angles, $\Delta\varphi_h$ = 60°. Note that the noise shaper does not work the same since the filters used are different. This is a good example of harmonic distortion that differs from the classic white noise premise.

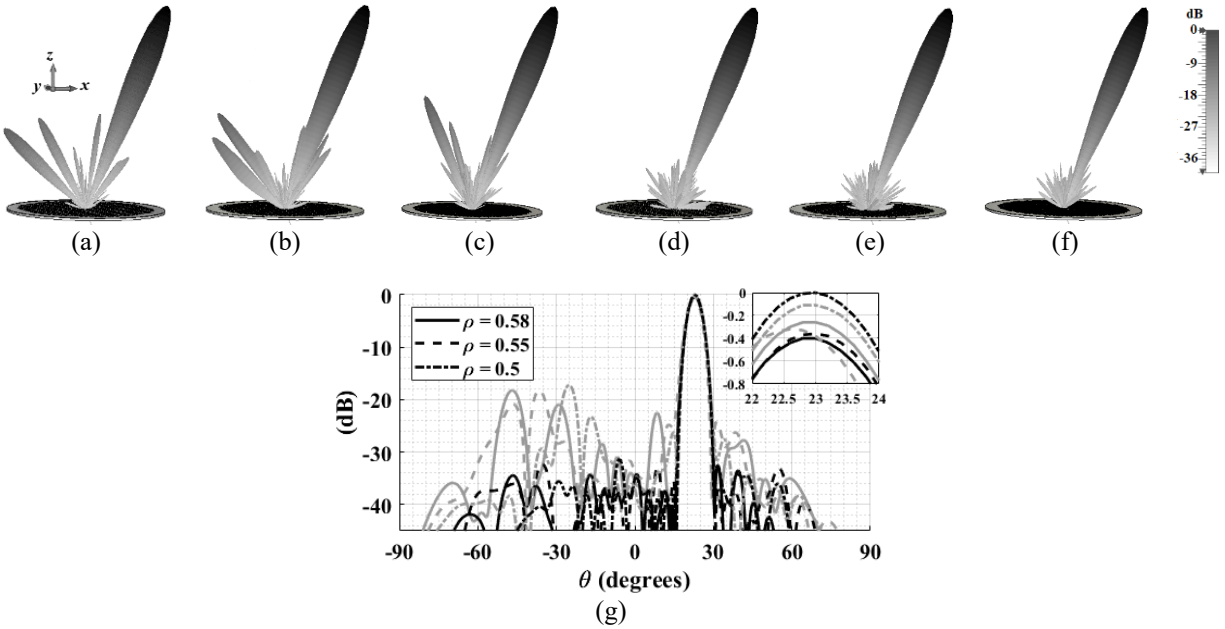

Fig. 5. 20. Full-wave simulations of 3D radiation patterns, $[\theta, \varphi]$ = [23°, 0°]. Normalized array pitch of (a) 0.58, (b) 0.55, (c) 0.5 for simple quantization system. Normalized array pitch of (d) 0.58, (e) 0.55, (f) 0.5 for CV-NS. (g) Full-wave simulations of radiation patterns on H-plane.

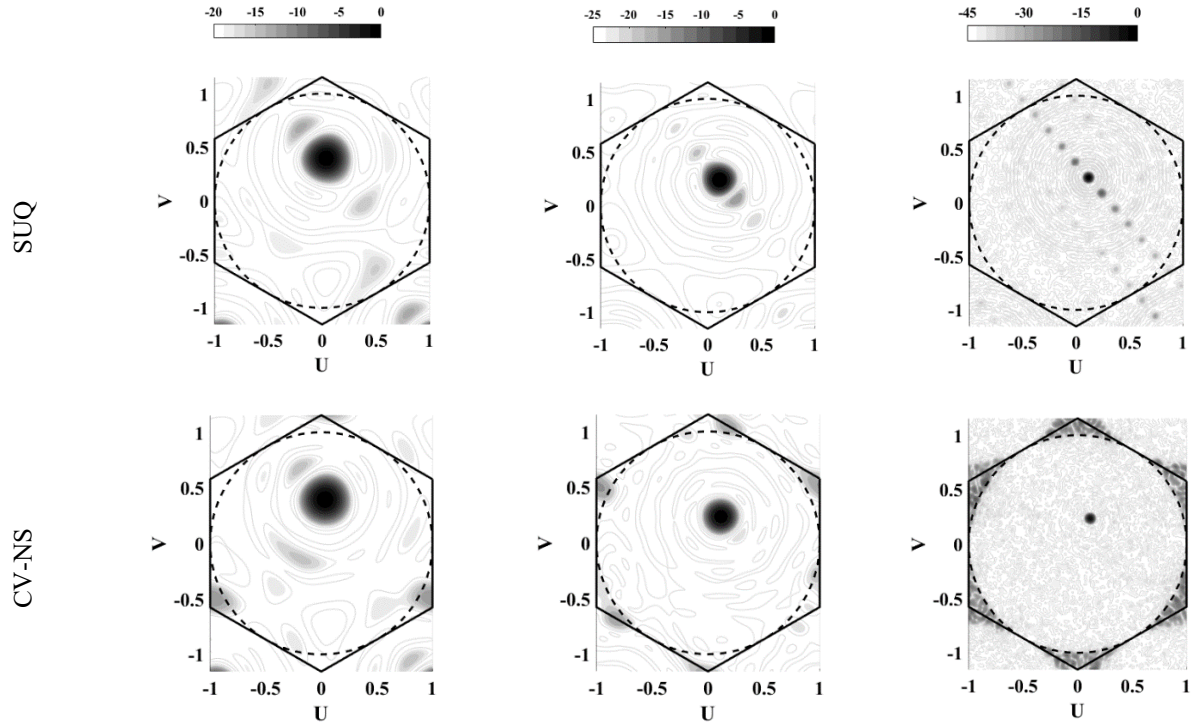

Fig. 5. 21. Decibel array factor for phased array with different diameters. The phased array diameter of (a) 5λ, (b) 7λ, and (c) 33λ. All systems are quantized into 3 bits.

5.6.3 Array size and number of elements

Influential factors in noise shaping include lattice type, array pitch, number of bits, maximum tolerable SLL, the digital filter used, and array size/number of elements. Generally speaking, noise shaping is not an effective approach for very small-scale size PAs. We observed that the system performance deviates from the predefined spectral shape for less than a specific number of elements. Strictly speaking, the noise shaping performance is a function of the number of elements, not the array size.

In Fig. 5.21, some steered array factors are shown for different aperture diameters, including 5λ (61 elements), 7λ (151 elements), and 33λ (3319 elements), respectively, designed for 20 dB, 25 dB, and 45 dB SLL Taylor weightings. For all of them, the phase and amplitude of CBWs are quantized to 3 bits. It is witnessed that the result would not be acceptably compatible with the

predefined spectral shape for smaller array sizes, e.g., In Fig. 5.21(a), the noise shaper does not work acceptably for the current array pitch and SLL.

Besides, it might be evident that the antenna gain loss compensation is a function of predefined SLL since that determines the depth of the filter stopband, which controls the total power of noise inserted. Moreover, we observed that the distortion could be acceptably shaped for relatively small array diameters, e.g., 5λ, but with a smaller array pitch of $\rho = 0.5$, contributing to 91 elements not shown here for brevity. That might be because a wider invisible region makes the noise shaper pump more effective for such a case, and actually smaller array pitch increases the total number of elements.

5.6.4 RV-NS

A schema of a circular disk corresponding to the visible region is shown in Fig. 5.22(a). The gray dashed parallelogram is an indication of the fundamental period. The design procedure of filter layout for the RV method is schematically shown in Fig. 5.22. The same as the square case in Fig. 5.6, the area in which the two copies have no intersection is the "reachable" free spectrum; the method can "see" those out-of-band areas corresponding to the invisible region. That is precisely the white color area in Fig. 5.22(d) and the resultant filter layout shown in Fig. 5.22(e), considering the notches associated with the QLs inside the visible region.

In Fig. 5.23(a), the frequency response of the targeted or revised system is shown. Also, that is shifted respecting the beam position to show how the noise shaper works in the beamspace domain [see Fig. 5.23(b)]. As seen in Fig. 5.23(c), the array factor for the 3-*bit* system is spectrally shaped with respect to Fig. 5.23(b).

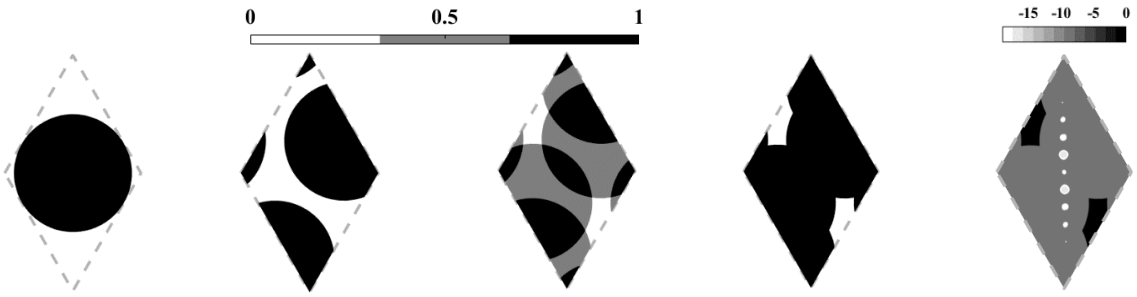

(a) (b) (c) (d) (e)

Fig. 5. 22. Schematics of filter layout constituents for $\rho = 0.5$ and $[\theta, \varphi] = [52°, 223°]$. (a) circular disk corresponding to the visibility region, (b) shifted layout to the image of beam point, (c) intersection pattern of symmetric copies, (d) unweighted filter layout background, and (e) filter layout.

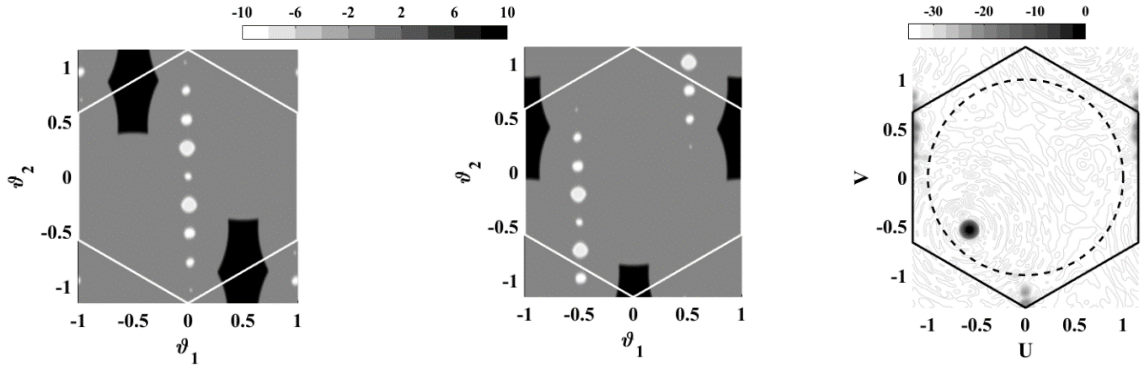

(a) (b) (c)

Fig. 5. 23. Design of Hexagonal phased array based on real-valued method and 0.4 normalized pitch. (a) Revised transfer function, (b) shifted copy of (a) with respect to the beam position, and (c) decibel array factor of a spectrally shaped system by the real-valued method.

In some cases, there may be non or not enough out-of-band regions that the method can see. Two examples are shown in Figs. 5.24 for normalized array pitches of 0.55 and 0.58. The beam point is commanded at $[\theta, \varphi]$ = [52°, 223°]. A very small portion of the invisible region is achievable, almost nothing for the one with $\rho \approx 0.58$. Even for the case of $\rho = 0.55$, the very small region achievable does not help very much. That is because a vast stopband yields a huge up-shift of digital filter frequency response. Note that the filter impulse response should be normalized to its reference sample to be used in noise shaping. The normalization causes an upshift. That means the system would not have enough in-band attenuation, and the noise shaper would not effectively work.

For such situations, one may only use spaced-notches corresponding to the QLs inside the visible region.

Comparing the square and hexagonal lattices for the case at hand might be beneficial. It is almost always possible to see enough of the invisible region for the array factor steered along the Nyquist square lattice principle axis. However, this is not the case for its Nyquist hexagonal counterpart. Such a discrepancy might be realized by looking at the element domain in Fig. 5.16.

Note that in a square lattice, the lattice matrix is an identity matrix but in the hexagonal one is not. Almost the same mapping happens in the reciprocal domain if one uses an N-time identity matrix as the tiling matrix. Indeed, it is possible to change the fashion of the steering lattice by changing the steering lattice matrix, but that does not help since the intersection of the two copies is related to the lattice matrix and the beam point direction.

Thereby, for Nyquist hexagonal lattice, except for some very narrow steering angles, $< 5°$, there is almost always not enough achievable free spectrum for the RV approach. Nevertheless, that might be an unfair comparison between hexagonal and square lattices. Hexagonal lattice provides a freer spectrum with the same array pitch size. For the Nyquist square lattice, the method does not "see" free spectrum for those steering angles along $\varphi = \mp 45°$, while enough free spectrum can be seen for all steering angles for the hexagonal lattice with half-wavelength array pitch. These remarks are schematically shown for square and hexagonal lattices in Figs. 5.25.

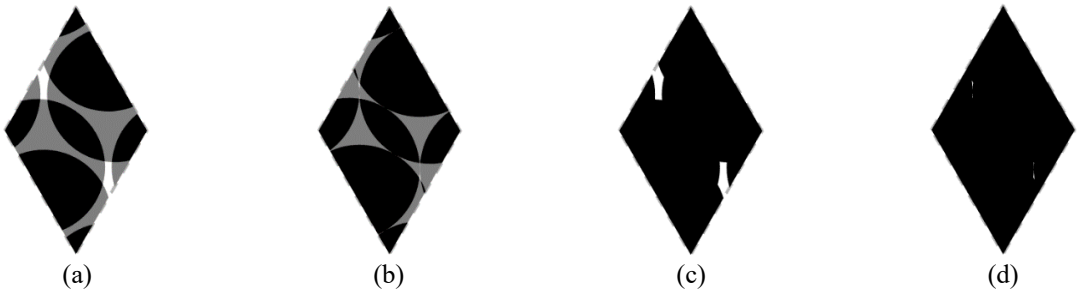

(a) (b) (c) (d)

Fig. 5. 24. The schema of intersection pattern of symmetric copies for an array with different array pitch. (a) $\rho = 0.55$ (b) $\rho \approx 0.58$ and the resultant unweighted filter layout is shown respectively in (c) and (d).

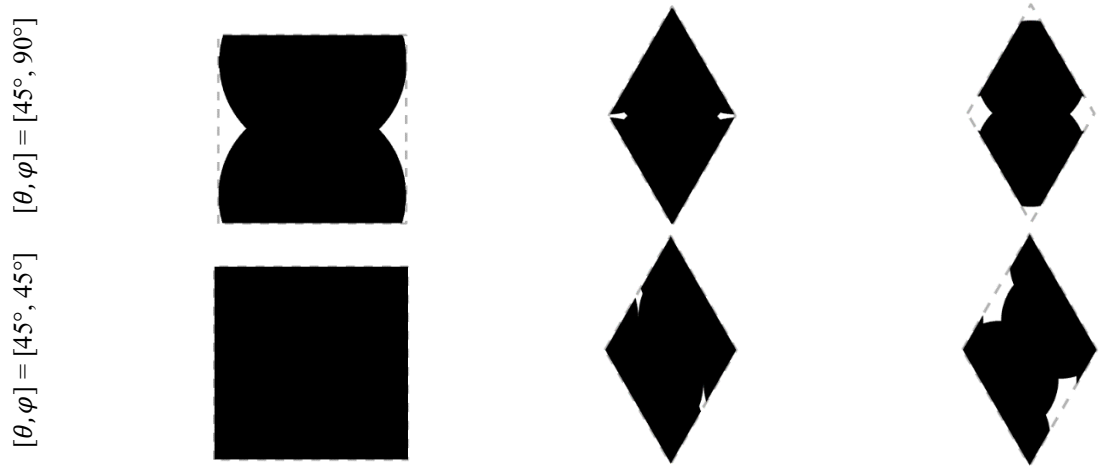

(a) (b) (c)

Fig. 5. 25. Unweighted filter layout. For (a) Nyquist square and hexagonal lattices with array pitch of (b) $\rho \approx 0.58$, and (c) $\rho = 0.5$.

5.7 Null restoration

The interfering signal is unfortunate because it contaminates the original signal typically coming through the main beam. If the interference comes from any direction except the main beam, it can be addressed by embedding a null in the radiation pattern of receiving antenna to improve the overall reception performance. Let us call that jammer null (JN).

Another superiority of noise shaping over conventional random methods can be realized on this account. The randomization-based methods contribute to a flat noise; they fill up the nulls and worsen the problem in such cases. On the other hand, the underlying problem can be treated with the spectrally shaped dither. The JN(s) in the radiation pattern should be addressed in the digital

filter design; thus, the quantization error can be pumped out of those areas, and the nulls can be restored to some extent.

Fig. 4.26 illustrates an example of a hexagonal lattice array in which a JN is assumed at about $[\theta_n, \varphi_n]$ = [25°, 180°], and the main beam at $[\theta, \varphi]$ = [19°, 0°], the color bar is set for [-60, 0] to better reveal the JN in array factor. The Figs. 5.26(a) and 5.26(b) show the array factors of high-precision (HP) and the 3-*bit* SUQ systems. It can be seen in Fig. 5.26(b) that the QLs have appeared, and the JN is wiped out. Note that the JN is still in its position but is buried beneath the distortion incurred by the quantization. Fig. 5.26(c) shows the result for RPDF dither. As expected, it just suppresses the QLs with the cost of minor lobe level mean value increase. The array factors along the $V = 0$ are shown in Fig. 5.26(d).

One should note the discrepancy between QL suppression and null restoration. The problem due to QLs in conventional PA is more related to error periodicity, which can trivially be addressed by inserting noise with specific statistical properties. However, restoring JNs is much more complicated as it cannot simply be treated by interrupting the periodicity of error as the problem cannot be solved by dithering.

The noise shaping might treat the underlying problem. The JN(s) in the radiation pattern should be addressed in the digital filter design; thus, the quantization error can be pumped out of those areas, and the nulls can be restored to some extent. However, we will show that much more attenuation is needed for this case compared to QL suppression and the filter design is more challenging and trickier.

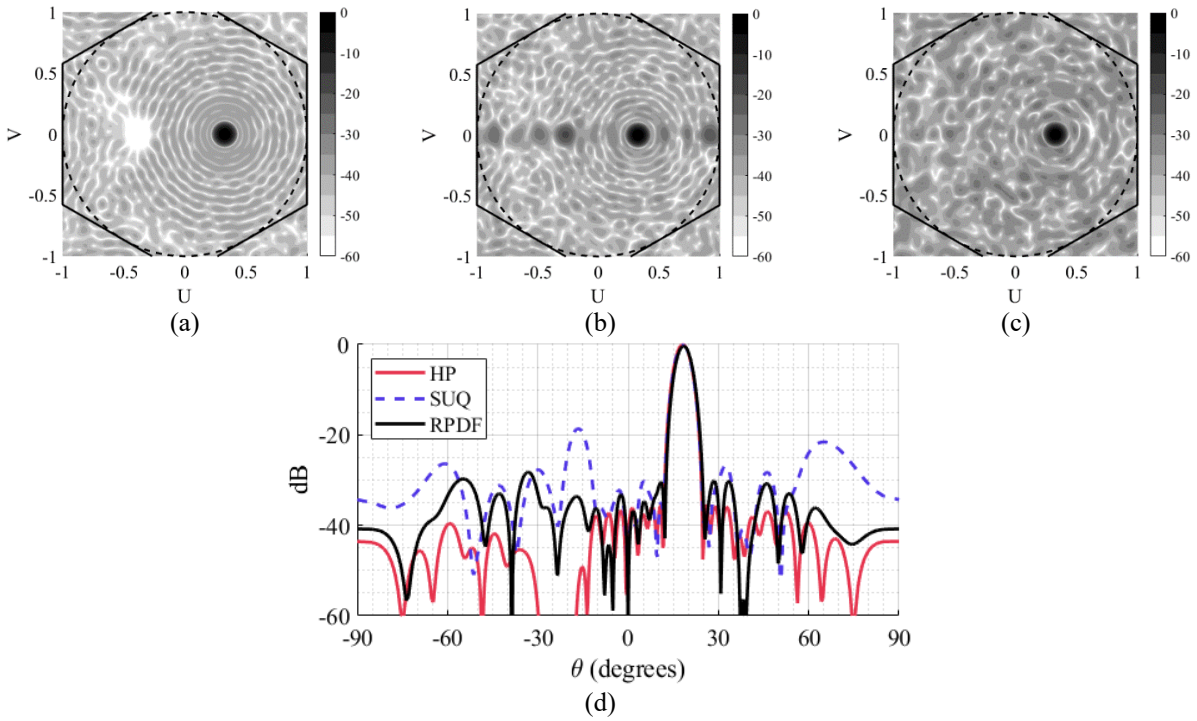

Fig. 5. 26. Array factor with imbedded null. For (a) high precision (HP), (b) 3-bit simple uniform quantization (SUQ), (c) 3-bit RPDF. and (d) Array factors along V = 0.

Consider the examples of Fig. 5.27. One filter frequency response is shown in Fig. 5.27(a). As seen, the background disk is again considered, corresponding to the visible region along with some small notches and a big one associated with the QLs and the JN to cancel out the hypothetical jamming signal. Let us call the notch(s) embedded in the digital filter associated with the JN as restoring notch (RN). The maximum depth of notches for the largest QL and the RN is considered almost equal. To better see that, the filter responses along the principle axes are shown in Fig. 5.27(b). The wide RN has almost the same depth as the notch considered at $\vartheta = 0.9$ for addressing the associated QL. The result of the array factor is shown in Fig. 5.27(c). It can be seen that the QLs are suppressed to some extent, but the JN has not been restored. This is because dealing with harmonic distortion and QLs is much easier than digging out 60 dB quantization residue; thus, the system failed to restore the JN.

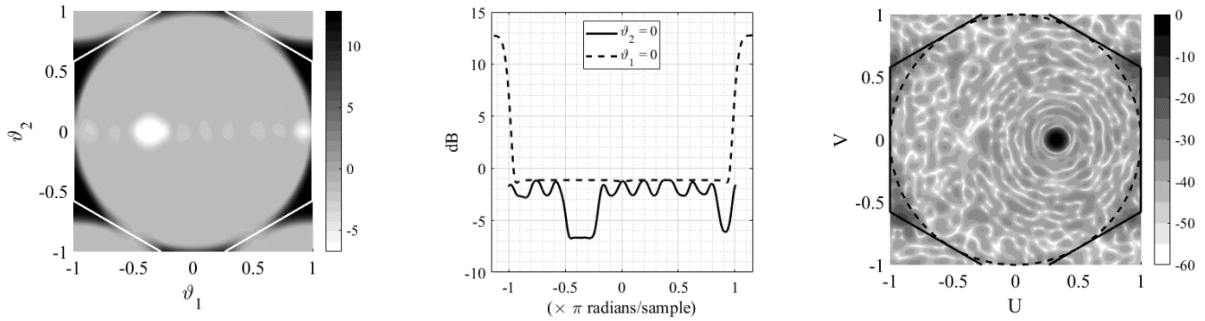

(a) (b) (c)

Fig. 5. 27. Array factor with imbedded null designed based on complex-valued method (a) Frequency response of the targeted system with a small restoring notch depth, (b) frequency response along the principal axes, and (c) the associated array factor.

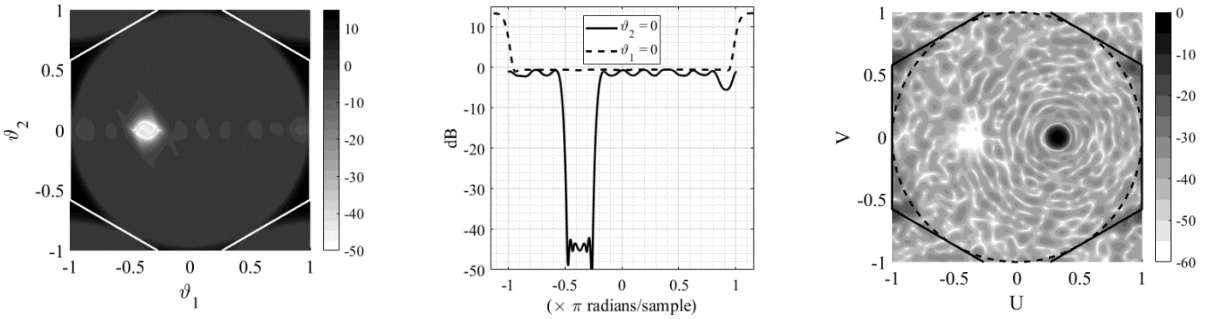

(a) (b) (c)

Fig. 5. 28. Array factor with imbedded null designed based on complex-valued method with deep restoring notch. (a) Frequency response of the targeted system, (b) frequency response along the principal axes, and (c) the associated array factor.

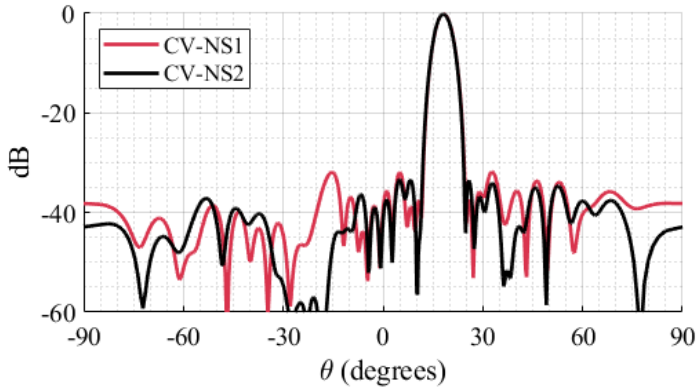

Fig. 5. 29. Array factors along the V = 0 for Fig. 4.26(c) is called CV-NS1, and Fig. 4.27(c) is regarded as CV-NS2.

In Fig. 5.28(a), the RN depth is increased up to 45 dB; see Fig. 5.28(b) for the 1-D diagram. The result of the array factor is shown in Fig. 5.28(c). In this case, the JN is acceptably restored, and QLs are also suppressed. One can better compare the two examples of Figs. 5.27 and 5.28 along the $V = 0$ in Fig. 5.29. Thus, the filter design for spectrally shaping the array factor error is

more challenging when the null is embedded in the radiation pattern. Note that noise shaping is a unique approach to address such a problem; the traditional randomization methods fail to address the underlying problem. However, it is worth noting that RNs are "expensive." Since it is required to consider very deep attenuation, the number of JNs embedded in the radiation pattern of the antenna is a limitation. This is because increasing the number of RNs increases the upshift in the frequency response of the filter and that, the attenuation imposed by the circular disk background may turn to a very small amount or even an in-band amplification and so that the side lobe level increases in the visible region. In such a case, the system should be designed with more bits. Overall, the success of noise shaping in such scenarios can be measured by the amount of gain degradation, minor lobe suppression, and efficacy of null restoration.

In Fig. 5.30, the results of 4-*bit* systems are compared with HP one for two JNs embedded in the array factor steered at $[\theta, \varphi] = [15°, 90°]$. The method is potent in restoring 60 dB JNs to some extent. To predict the viability of this approach in practice, let's double-check the result with exact solutions. The full-wave simulation results are presented in Fig. 5.31. It can be seen that the results are somehow compatible with the computed ones in Fig. 5.30. However, the full-wave result shows a little inferior performance for null retrieval. There are some artifacts with about -52 dB magnitude inside the JNs. That can be attributed to the mutual coupling between the elements. Note that the microstrip patches were impedance matched in an infinite periodicity assumption, which can explain the minor deviation between the computation and full-wave simulation results.

Some more computation results are shown in Fig. 5.32 and 5.33 for 4- and 5-*bit* systems with different numbers of JNs. As shown in Fig. 5.32(b), much less distortion is realized compared to a 3-*bit* system, but most of the JNs are still deformed or are filled up by the quantization residue. Nevertheless, as seen in Figs. 5.32(c), the CV method can acceptably restore all JNs, 3 to 4 ones

with about 60 dB depth, and QLs are also suppressed. Systems with more than five bits are typically good enough for general applications. However, the quantization due to even 6 bits DAs and DPSs can relatively fill the nulls. In this regard, it is recommended to ameliorate the radiation pattern by using noise shaping because it can simply restore such nulls for 5 to 6-bit accuracy. As shown in Fig. 5.33 for 5-*bit* quantization, the CV method acceptably approaches the in-band response of the HP system for a relatively high number of JNs. The results along $V = 0$ are shown in Figs. 5.34 proves it is beneficial to use such an approach, even for 5 bits and more. For a relatively high number of bits, e.g., 5-6 bits, that the system does not contribute to considerable QLs level, it might even be possible to cause some small amplification in the visible region except those areas that correspond to JNs, to restore a significant number of JNs, if the minor lobe level would comply with the application at hand.

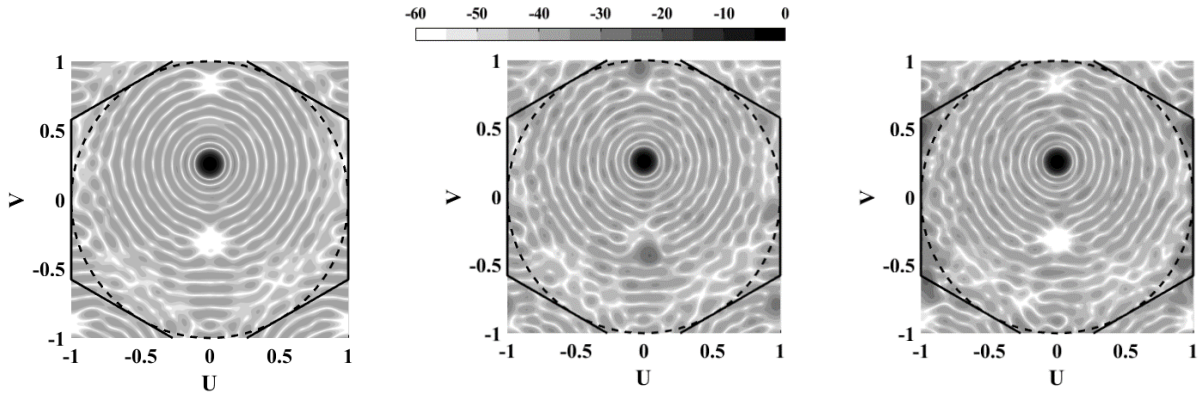

(a) (b) (c)

Fig. 5. 30. Array factor with 2 imbedded nulls. For (a) high-precision, (b) 4-bit simple quantization, and (c) 4-bit CV-NS.

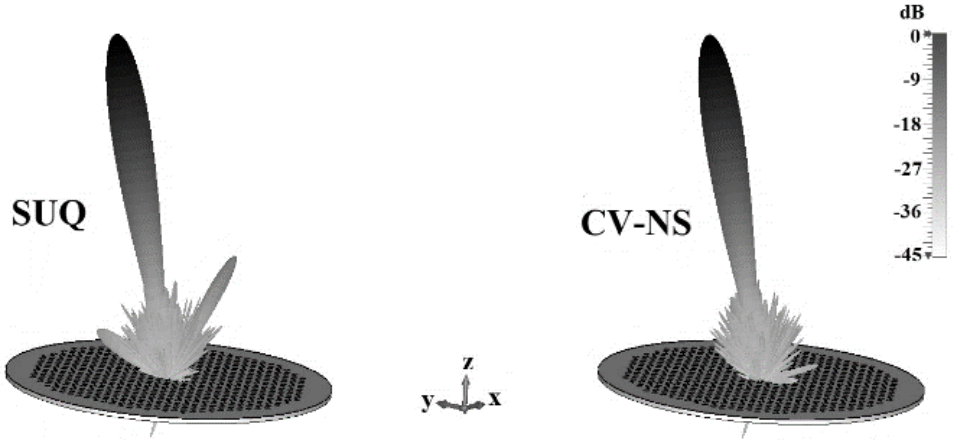

(a)

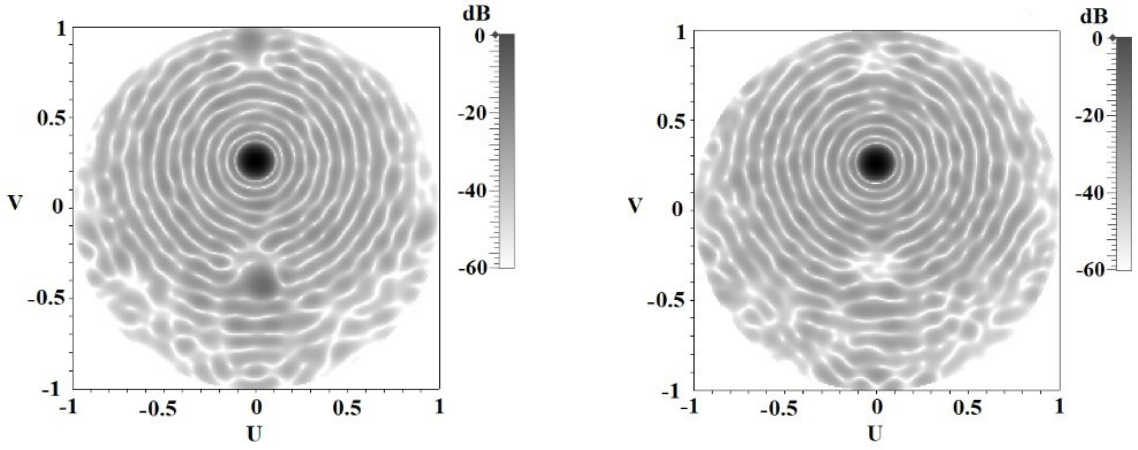

(b) (c)

Fig. 5. 31. Full-wave simulation results for 4-bit systems. (a) 3D patterns in the angular domain. Orthographic projection for (b) simple uniform quantization (SUQ) and (c) CV-NS.

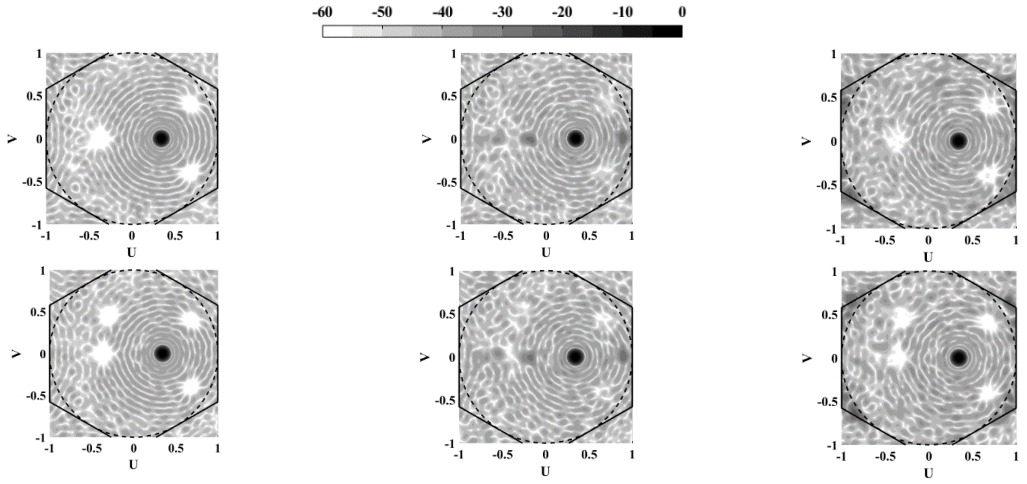

(a) (b) (c)

Fig. 5. 32. Decibel array factors with multiple imbedded nulls and 4bit systems. For (a) high precision, (b) simple quantization, and (c) CV-NS.

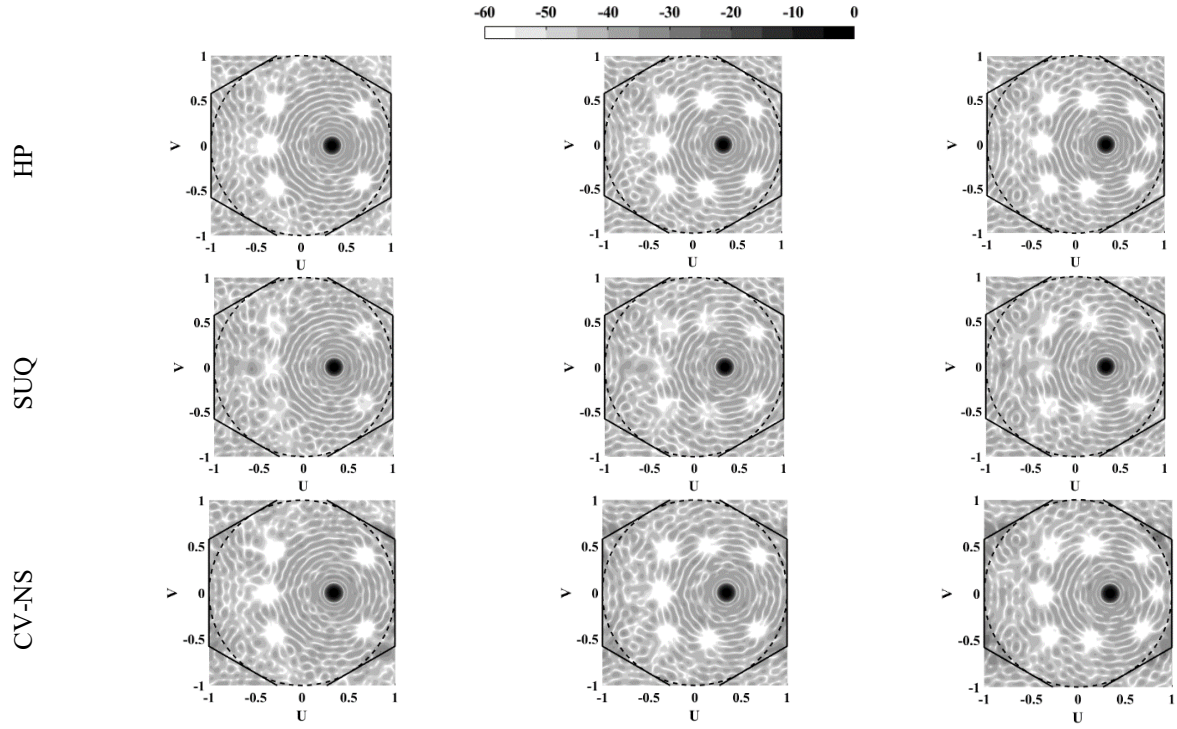

(a) (b) (c)

Fig. 5. 33. Decibel array factors for 5bit systems. (a) 5, (b) 7, and (c) 8 nulls.

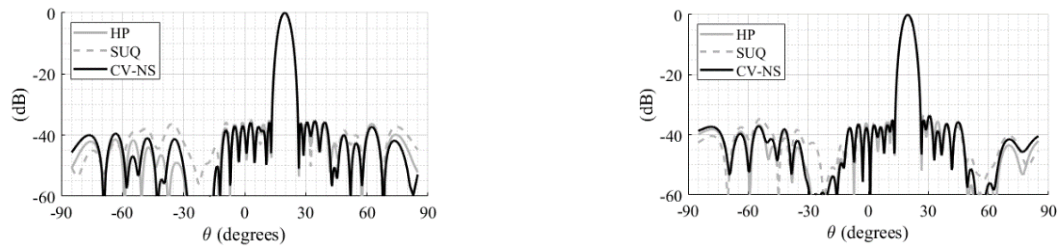

(a) (b)

Fig. 5. 34. Decibel array factors in Fig 5.33 along V = 0 for (a) 7, (b) 8 nulls.

5.8 Shaped beam

It has been stated in previous sections that if the error signal would be a complex value, one may use the CV method to shape that spectrally, but if the error is a real-valued quantity, one may exploit the RV method by assuming the real signal would be the excitation phase. That was precisely due to the importance of phase error. The product of such a process is a spectrally shaped PDA error. However, we might only be interested in spectrally shaped amplitude error in some scenarios. This mainly happens in beam shaping. Consider the example of Fig. 5.35, in which a flat-top beam is designed using the Fourier synthesis method. As might be evident, the excitation phase can be realized using a 1-bit system with no error. For amplitude, we have used 3-*bit* SUQ. The computed radiation pattern is shown in Fig 5.35(a) for an array of a square lattice. The beam is in a broadside direction, which means that RCDF can be used for noise shaping since the array factor is symmetric with respect to the origin. As either the error signal or filter impulse sequence are real quantities, the noise shaping procedure yields a spectrally shaped amplitude error even if one uses the CV approach. Its array factor is shown in Fig. 5.35(b). This is an example of real-valued noise shaping but for amplitude. Note that it is possible to do the noise shaping for a complex signal as two separate real-valued procedures of phase and amplitude. However, as stated before, CV-NS is spectrally more efficient and might be more beneficial for steered array factors at least.

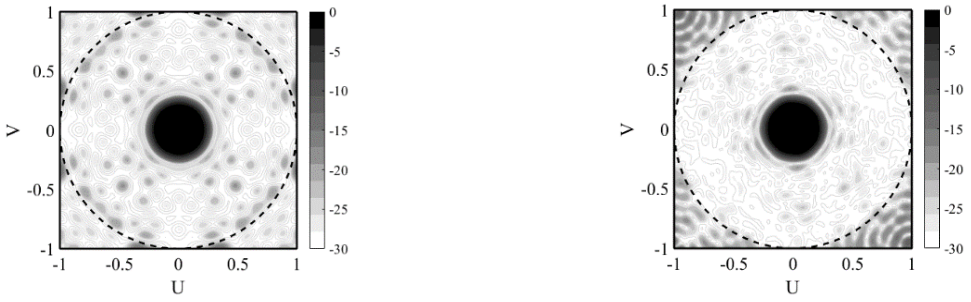

(a) (b)

Fig. 5. 35. Decibel array factor for shaped beam. (a) simple quantization, (b) spectrally shaped error.

As another example, consider the special case of a geosynchronous orbit (GEO) satellite since the earth's angular size from GEO is relatively small, about 2×8.69°. Here, contoured beam coverage is considered and is designed to be compatible with geographical and political boundaries (GPB) and population density. The circular-aperture square lattice PA is assumed to have about 50λ diameter at 11.7 GHz with $\rho = 0.9$ normalized array pitch, contributing to 2121 radiating elements. The GEO satellite is assumed at 0°N latitude and 107°W longitude.

The whole antenna system is rotated about 7.58° along the x-axis in the satellite coordinate system, and its z-axis is aimed at a sub-satellite point on the earth's equator. The antenna is aimed at [52.45°N, 107°W] on earth.

The HP excitation components are shown in Figs. 5.36(a) and 5.36(b). Also, the 20-dB contour pattern in the satellite coordinate system is sketched in Fig. 5.36(c), in which the projected GPB is plotted in the background. Since the antenna has several radiating elements, as a cheap solution, let's use 2-*bit* DAs and DPSs. The array factor is shown in Fig 5.37(a). As before, the dashed circle represents the boundary of the visible region. The solid square shows the fundamental period of the array factor, and the circle plotted faintly signifies the earth region, which is visible to the satellite. For this example, there is no invisible region to push the distortion there, and element spacing is large enough; thus, the square lattice is utilized for simplicity.

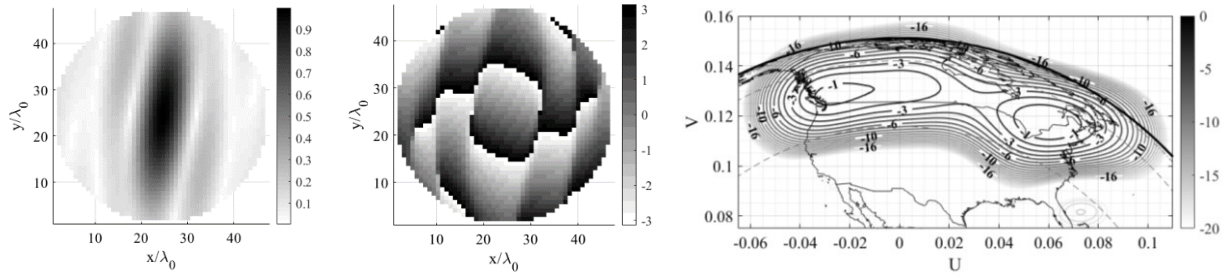

(a) (b) (c)

Fig. 5. 36. HP contour beam. Excitation (a) magnitude, (b) phase, (c) 20 dB contour coverage.

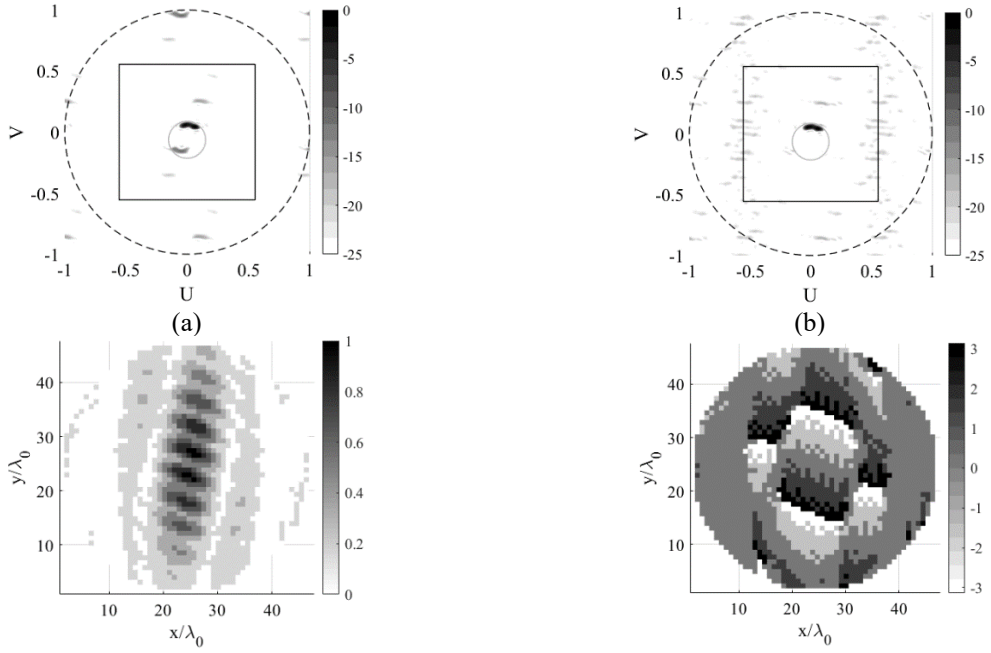

(a) (b)

(c) (d)

Fig. 5. 37. Contour beam with quantized beamforming weights. Array factor for (a) simple quantization, (b) spectrally shaped noise, (c) and (d) amplitude and phase of the spectrally shaped noise system.

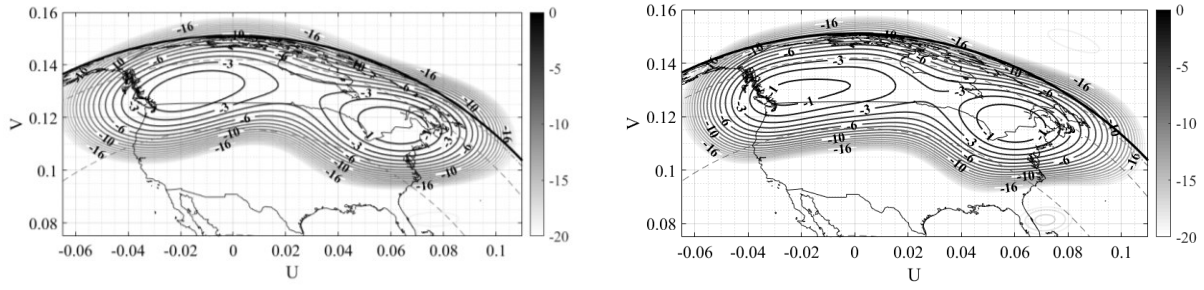

(a) (b)

Fig. 5. 38. 20 dB contour coverage. For (a) simple quantization and (b) CV-NS.

Because of 2-*bit* coarse quantization, an 11 dB QL appeared inside the earth region. It might be interesting to note that The QL is less likely to show up in the earth region for a greater number of bits. This is simply because decreasing the quantization step decreases the error periodicity, and the QL shows up at higher spatial frequencies, which may go beyond the earth region. Also, it can be seen that the QL imitates the main beam shape, which is an indication of the coherent error.

We may only be interested in the earth region. On this account, one may use noise shaping to exile the QL from the region of interest, as shown in Fig. 5.37(b). As seen, the QL is dismissed from the earth region and spills over to the space region. The resultant excitation components are shown in Figs. 5.37(c) - 5.37(d). Note the discrepancies of amplitude component with the ideal case one. If the antenna was designed for a static beam, many elements, about 800, would become zero magnitudes; thus, they would turn into dummies to save costs.

It is not just a matter of QL suppression. The noise shaper can redecorate the beam shape. This has been shown in Fig. 5.38, in which it can be seen that the SUQ system contour pattern deviates from the ideal case illustrated in Fig. 5.36, but the one with spectrally shaped noise resembles more to the ideal pattern.

It is possible to increase the array pitch further to decrease the number of elements. That contributes to a smaller array factor fundamental period; some grating lobes appear inside the visible region. Although those are the leakage of RF power, they might still be acceptable as far as they do not reach the earth region. Indeed, the noise shaper can exile the QLs from the earth region and somehow redecorate the beam shape; however, that leads to more distortion inside the visible region since the out-of-band region becomes smaller and more amplification happens to lead to more antenna gain loss.

Chapter 6
Noise shaping at sub-array layer

6.1 Contiguous sub-array view angle

At least three influential factors limit the antenna view angle for the contiguous sub-array. The First is the SAF windowing effect, which incurs directivity loss during beam steering. The second is the overlap efficiency, which determines the periodicity of UL-AF and fidelity of grating lobe suppression by SAF. The third is the antenna beamwidth, which is determined by the aperture size and ultimate layer beamforming coefficients. However, the influential factors are more than the three points mentioned above, which will be discussed later.

Consider a linear array of two-layer sub-array overlapping in which three elements constitute the overlapped sub-array. The central element is not overlapped, see Fig. 6.1, while the two other ones are shared between the two adjacent sub-arrays located on two opposite sides of the center element. This is almost the simplest overlapped sub-array system. In this configuration, the second layer is twice sparser than the first. For now, consider the first layer is of Nyquist design (the array pitch is half-wavelength); thus, there would be no invisible region for this case. The first layer elements are shown by solid black circles in Fig. 6.1, while hollow circles illustrate the second layer. For the case at hand, the SAF is associated with two zeros located on the unit radii of the root-loci diagram. The array is designed for 25 dB SLL. This should consider both layers. In this regard, the SAF should have enough attenuation for the SL-AF grating lobe(s); we may call it an image beam hereafter. The required SLL determines the position of the two conjugate symmetric zeros shown in Fig. 6.2(a). As seen, the sidelobe at $\vartheta = \pm 1$ ($\theta = \pm 90°$) is 25 dB below the maximum directivity.

Referring to Fig. 6.2(b), If one steers the beam, the image beam, whose spatial angular frequency is represented by a solid red circle, goes to a very small level first (at zero position) and shows up again at -25 dB normalized value at $\vartheta = 0.212$ which for the Nyquist case is associated with $\theta = 12.218°$. The array factors are shown in Fig. 6.2(c). Note that the value of the image beam shown in the root-loci diagram is not precisely the sidelobe level in the overall array factor (O-AF) since the main beam has a specific beamwidth. In other words, for two antennas with the same sub-array configuration, the narrower beam antenna has a wider view angle than the one with a broader beam. In the current example, the main beam (represented by a solid black circle) would suffer from about 1 dB directivity loss due to the windowing effect, as shown in Fig. 6.2(b). On the other hand, the second layer array weighting may also be designed for 25 dB SLL.

For this example, the second layer array is assumed to have 23 elements; thus, the antenna has 47 radiating elements with a half-wavelength array pitch. Some computed array factors are shown in Fig. 6.2(d). As our convention, we show the SAF by black dot-dashed. Indeed, such an array has a narrow view angle due to the contiguous sub-array. One may compromise the design by considering another influential factor: the array pitch. Consider the same sub-array arrangement and coefficients but with 0.4 normalized array pitch. The root-loci diagram is shown in Fig. 6.3(a) for the un-steered array factor. Everything is the same as Fig. 6.2(a) except the shaded region associated with the invisible/imaginary region. This means that the SAF would not have sidelobe in this case since the conjugate symmetric zeros are located inside the invisible region, which does not contribute to a coherent wavefront.

Fig. 6. 1. A schematic of the proposed 2-layer linear array of a 3-element sub-array in which two out of three elements overlap.

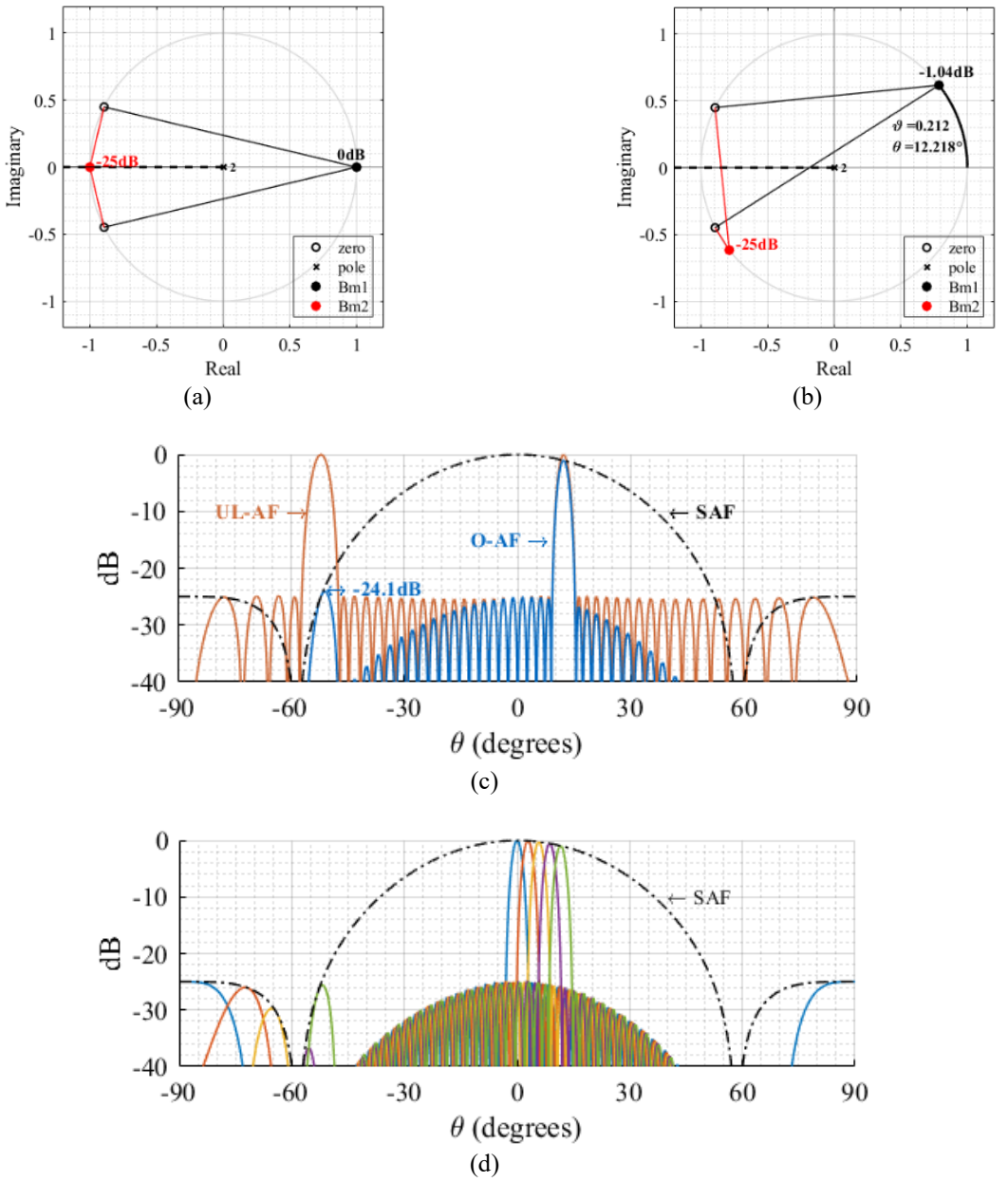

Fig. 6. 2. Design of linear array with 3-element sub-array overlapping and 0.5 normalized pitch. The root-loci diagram for (a) un-steered, (b) steered array of Nyquist design, (c) array factor for the beam at 12.218°, and (d) array factors for different steering angles.

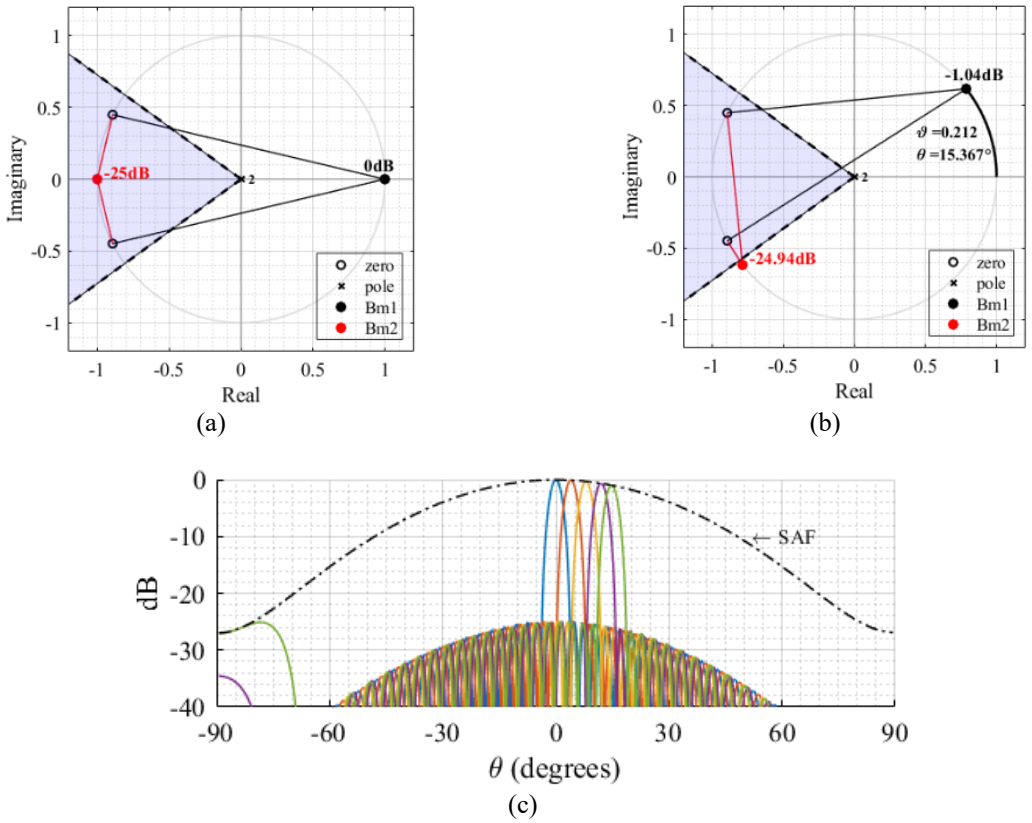

Fig. 6. 3. Design of linear array with 3-element sub-array overlapping and 0.4 normalized pitch. The root-loci diagram for (a) un-steered, (b) steered array, and (c) the decibel array factors for different steering angles.

As the positions of zeros are not changed, the array factor is not changed in one fundamental period. However, the visible region becomes smaller, which increases the antenna view angle. Let again steer the beam at $\vartheta = 0.212$, which is associated with θ =15.36°; the root loci diagram is shown in Fig. 6.3(b). Thus, the 1dB antenna directivity loss happens at a larger scan angle. This result justifies that the SAF is less directive than the previous case because the element spacing has decreased; thus, the sub-array is physically smaller. That should not be surprising since a denser array means a greater number of elements on both layers, which means that a greater number of phase shifters/data converters on the second layer is needed. Nevertheless, understanding the benefits of the dense array provides flexibility in design. Some array factors are shown in Fig. 6.3(c) for the underlying example. As expected, the SAF is much less directive than the previous example, with no sidelobe.

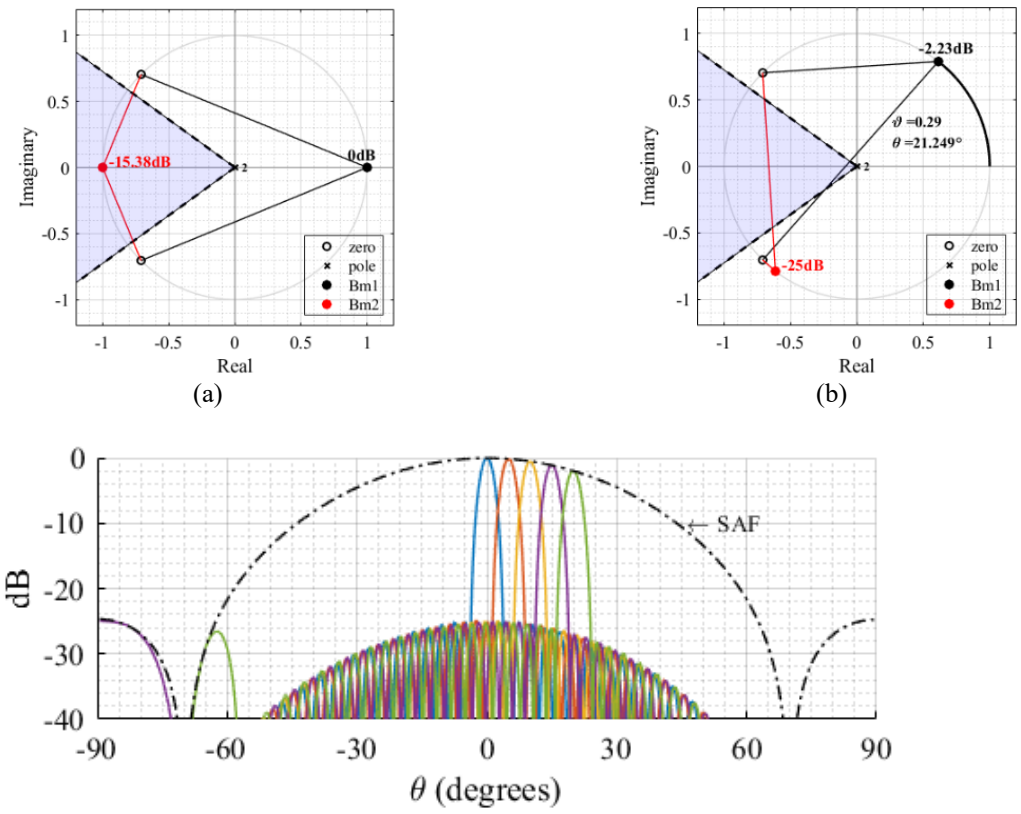

Fig. 6. 4. Wide view angle design of linear array with 3-element sub-array overlapping and 0.4 normalized pitch. The root-loci diagram for (a) un-steered, (b) steered array factor of 0.4 normalized pitch and wide view angle design, and (c) the decibel array factors for different steering angles.

Depending on tolerable directivity loss and bandwidth, the array can be designed for a wider view angle. In the previous case, we considered the sub-array coefficients, or equivalently the positions of the zeros, the same as the first example of Nyquist design. However, one may move the two conjugate symmetric zeros toward the zero frequency, broadside beam position, which means that the SAF becomes more directive, and sidelobe appears when the zeros appear out of the visible region. For the underlying design, the SLL may violate the 25-dB norm but not inside the visible region; hence, the multiplication of normalized distances of the frequency of invisible region boundary, the location that the dashed line cuts the unit radii, from the two zeros should be -25 dB. The root-loci diagram is shown in Fig. 6.4(a). As seen, the two zeros are inside the visible region. Also, the maximum SLL is about 15 dB inside the invisible region. In this case, the array

has about 21 degrees view angle with respect to the 25 dB SLL norm. However, due to the windowing effect of directive SAF, it suffers from 2.23 dB directivity loss; note Figs. 6.4(b) and 6.4(c). If less directivity loss is required, the SAF should be designed less directive.

As stated, the array is designed denser than the example of Fig. 6.2; thus, more elements are needed on both layers, which means that more phase shifters for the analog array should be used compared to the Nyquist design. For example, 29 elements for the second layer are considered in the current design, which is 6 elements more than the Nyquist design. Also, such a design should be carried out for the upper end of the temporal-frequency band for wideband solutions. Furthermore, if one assumes the phase shifters would have a flat frequency response, there would be beam squint as the visible region size changes by changing the temporal frequency; this point is irrelevant to dense or Nyquist design.

In Fig. 6.5 (a), such an array is realized using an aperture coupled patch as the radiating elements at the center frequency of 10 GHz. The element spacing is about 0.4λ, with 19 elements for the second layer. The proposed feed network has a peculiar configuration. As seen, the center element power is equally divided into two, and each is subsequently combined with half power coming from the adjacent elements, which are subsequently combined and introduced to the second layer. Two unbalanced power dividers are used for each sub-array to realize the computed sub-array coefficients. The array is designed for a 20° steering angle with sidelobes less than the 25-dB norm; this is almost the same as the design in Fig. 6.4 but with a smaller number of elements. The simulated results of 3-D radiation patterns are shown in Figs. 6.5(b)-(c). Also, the 1-D pattern on the azimuth plane, H-plane, is shown in Fig. 6.5(d). The simulated beam on the extreme has 0.23 dB more directivity than the computed one, which was to have 2 dB gain scan loss; note that these values are different for 3D radiation patterns owing to the edge diffraction effect. Also, SLL due

to the image beam at 61.5° is about -25.56, a 0.9 dB higher than what is predicted by computation. These two observations show that the SAF has realized negligibly less directive than what is designed for, which can be attributed to a minor error in power dividers. Also, for the extreme beam, the sidelobe level in the passband of SAF is 1.5 dB more than what was to be.

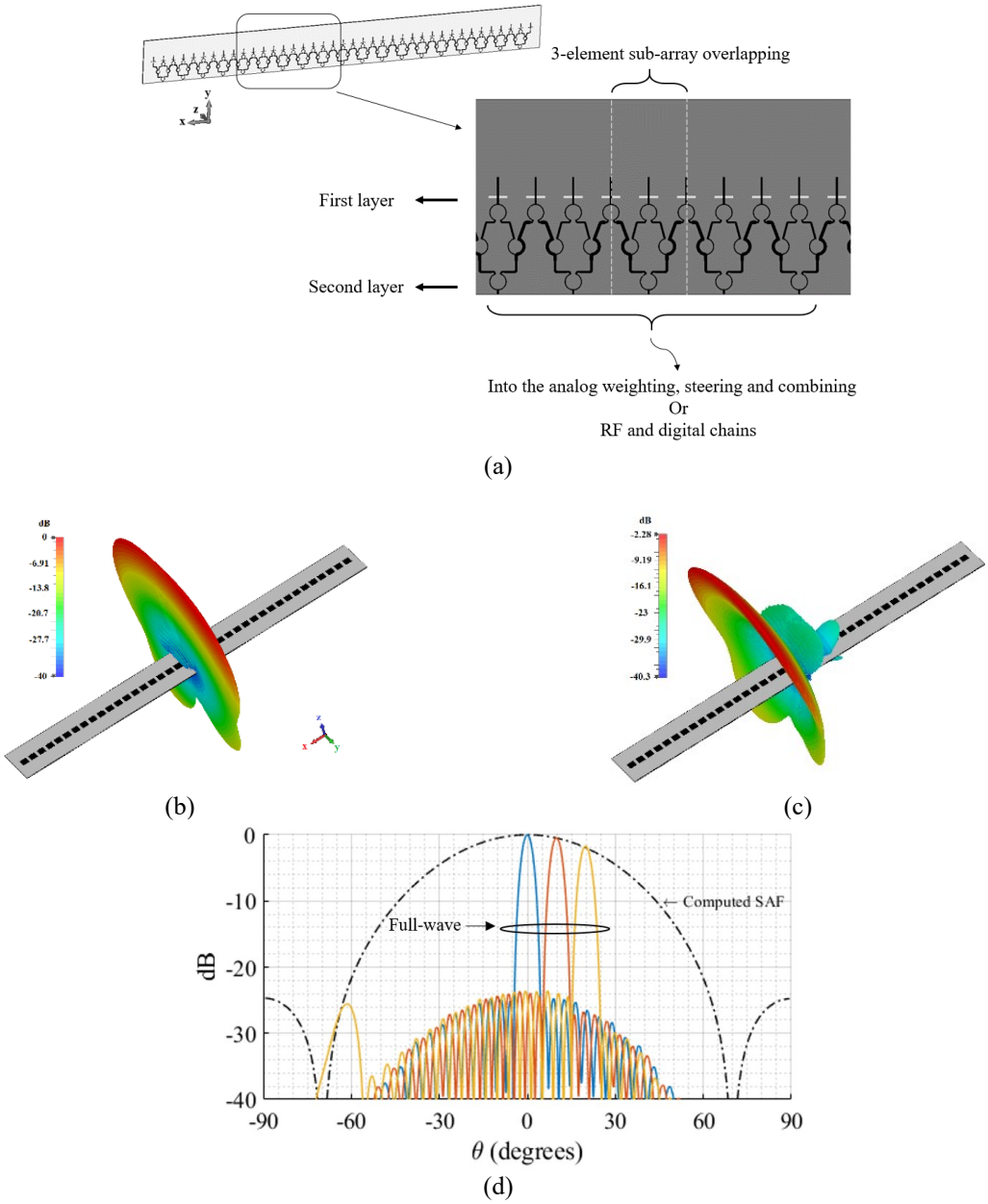

Fig. 6. 5. Feed network realization of linear array with 3-element sub-array overlapping and 0.4 normalized pitch (a) the proposed array configuration, 3D radiation pattern at 10 GHz for beam steered at (b) 10°, (c) 30°, (d) full-wave simulation results of 1-D patterns shown by solid black lines compared with commutated ones illustrated faintly.

This can be attributed to the mutual coupling effect. The sub-array might be realized in a more complicated form for superior performance or a smaller number of phase shifters or RF chains and ADCs. Of course, it is possible to use larger sub-arrays that lead to more feeding network complications.

Increasing the number of sub-array elements increases the number of transfer function zeros, and the SAF can be more conveniently formed. Also, the overlapped efficiency is of great importance. As much as more elements overlap, the reciprocal domain period would be sparser; hence, one can easier suppress the image beams. Nevertheless, in practice, increasing the number of overlapping elements in just one layer terminates in a bulky and complicated network, and in some cases, it becomes impractical.

Another possibility is to use a greater number of sub-array layers, which may facilitate generating more zeros for spatial FIR filtering. For example, consider a three-layer array schematically shown in Fig. 6.6(a). As seen, each first layer element is overlapped by two sub-arrays. This simple configuration does not change the density of element spacing but generates a real transmission zero. For equal power division, it happens at $\vartheta = \pm 1$. The second layer is also tiled to a third layer. Each second-layer sub-array includes four elements that are overlapped by two adjacent sub-arrays. The third layer is twice sparser than the second and the first layers. Hence, there are two sub-array factors: the first-layer sub-array factor (FL-SAF) and the second-layer sub-array factor (SL-SAF). The UL-AF, which belongs to the third layer, would be tapered in the overall array factor (O-AF) by the envelope composite sub-array factor (C-SAF).

The array configuration designed based on microstrip technology is shown in Figs. 6.6(b), 6.6(c) and 6.6(d). As stated, the first layer sub-array is just a simple power division contributing to a transmission zero, as shown. The crossover is used based on back-to-back branch-line couplers

for the second-layer sub-array. However, this design is based on symmetric sub-array coefficients, which means $a = d$ and $b = c$. The disadvantage of this approach is the gain scan loss seen in Fig. 6.7(d).

One method to solve the gain scan loss is to use transmission zero(s) in the proximity of zero frequency on the root-loci diagram. As stated, the first layer sub-array is just a matter of equal power division contributing to a transmission zero, as shown in Fig. 6.8(a). The same element spacing of 0.4λ is considered for this case, either. The rest of the three transmission zeros can be realized on the second layer by using the four-element sub-array, as shown in Fig. 6.8(b). Thus, the root loci of the C-SAF would have four zeros precisely at the prescribed locations, as shown in Fig. 6.8(c). All sub-array factors are illustrated in Fig. 6.8(d). The second layer sub-array coefficients are computed about $[a, b, c, d]$ = [-0.4, 0.45, 0.97, 1]. The layout of the array feeding network is shown in Fig. 6.8(e). The closed view of the second-layer sub-array is shown in Fig. 6.8(f), respectively. Note that a is a negative coefficient; thus, its associated arm is longer in Fig. 6.8(f). Fig. 6.8(g) shows some full-wave simulations on H-plane. The computed C-SAF is overlaid to show the accuracy of system implementation.

It may be judged that the array coefficients are acceptably realized since the overall radiation patterns follow the C-SAF envelope with minor deviation. The tiny discrepancies can be attributed to an error in power dividers and slight mismatches in different components such as radiators, crossovers, *etc*., which incurs minor inaccuracies in realizing array coefficients. This array can steer up to 20 degrees with SLL below 25 dB and gain less than 0.4 dB.

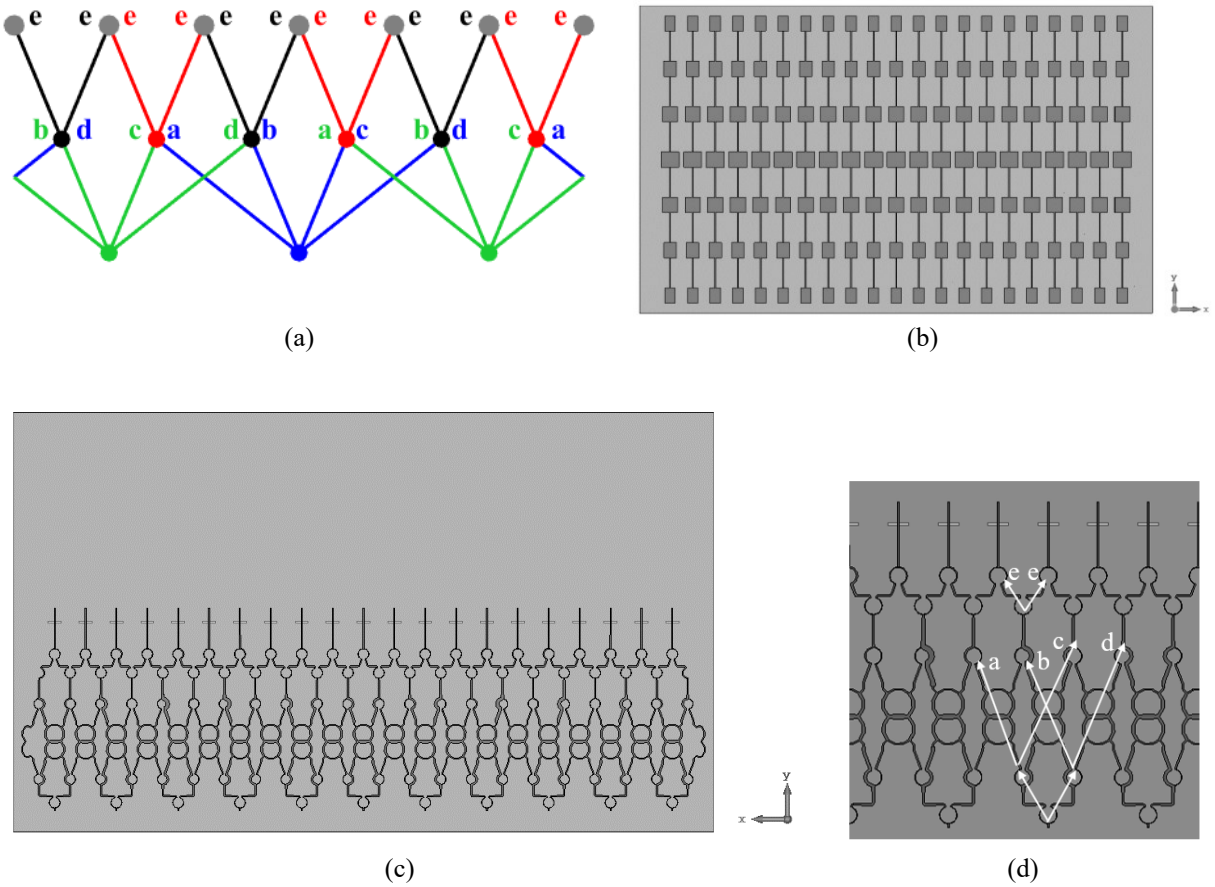

(a) (b)

(c) (d)

Fig. 6. 6. Three-layer sub-array overlapping feeding network. (a) Schema of the proposed sub-array system, (b) top view of the antenna, (c) whole array feeding network, and (d) closed view of multi-layer sub-array.

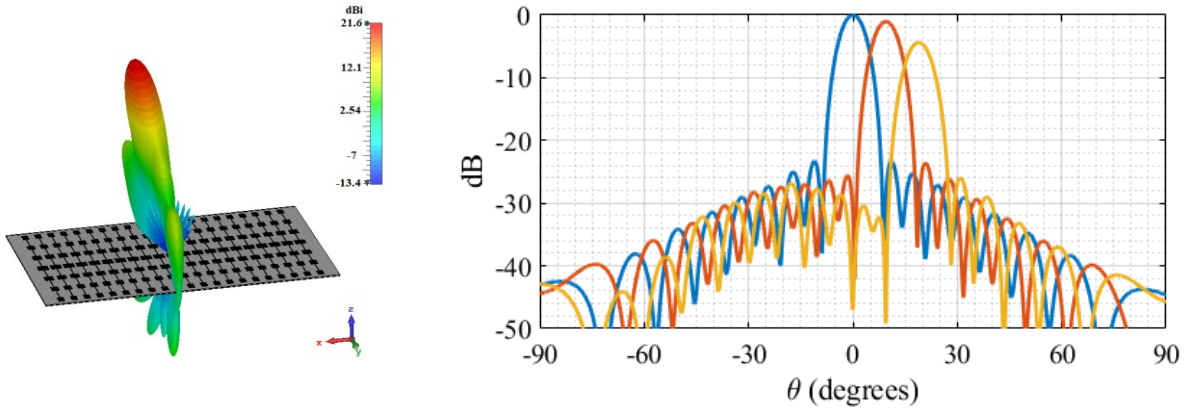

(a) (b)

Fig. 6. 7. Full-wave simulation results of pattern for the three-layer sub-array overlapping. (a) 3D gain pattern, the beam steered at about 10 degrees, (b) radiation pattern on H-plane.

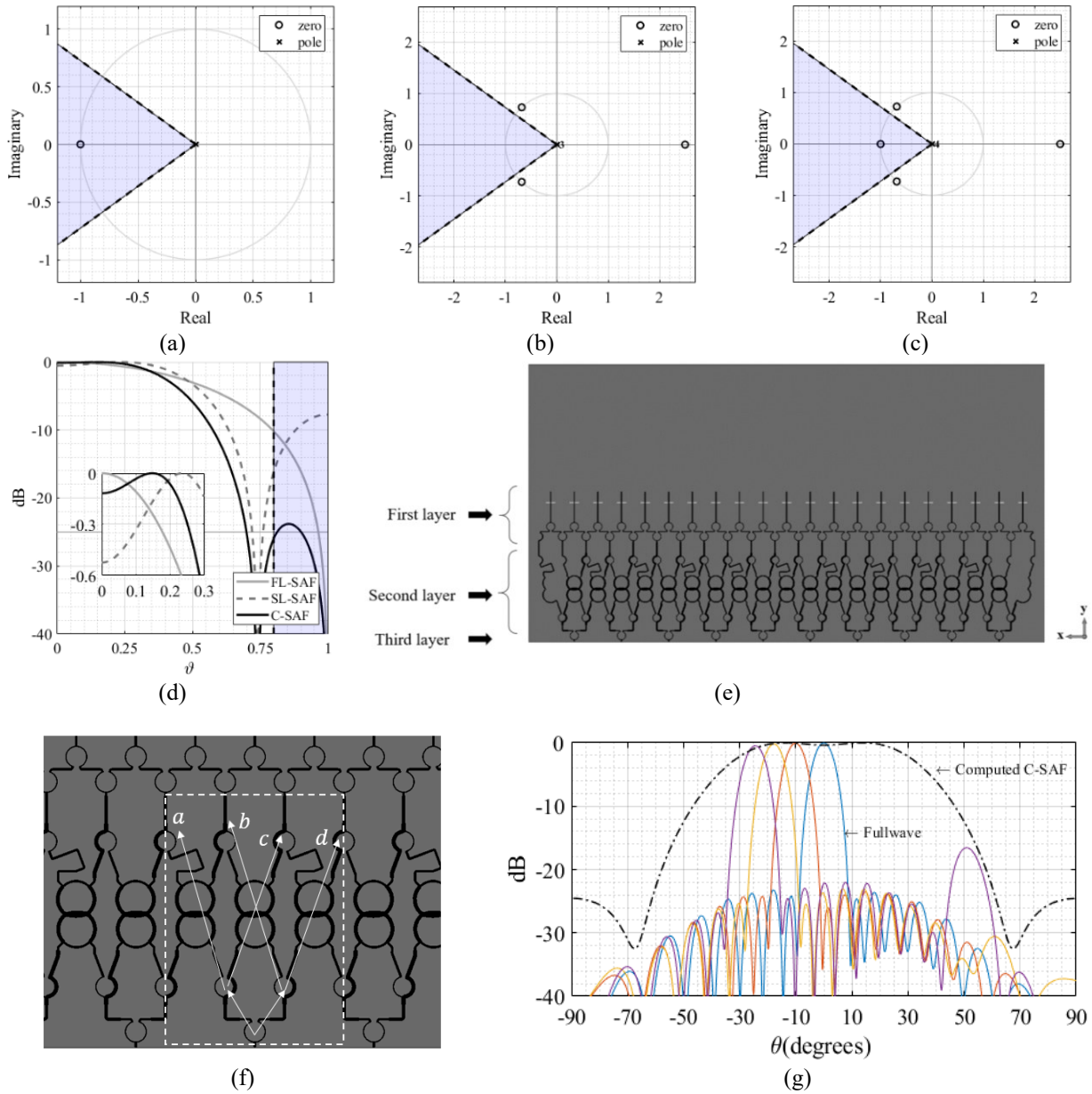

Fig. 6. 8. Wideband design of three-layer sub-array overlapping feeding network based on flat-top beam. The root-loci diagram for (a) first-layer sub-array factor (FL-SAF), (b) second-layer sub-array factor (SL-SAF), (c) composite sub-array factor (C-SAF). (d) sub-array factor versus normalized spatial frequency. (e) the whole array feeding network, (f) closed view, and (g) full-wave simulations on H-plane.

The array can also be realized in a 2D manner. For example, it is designed to scan along the azimuth direction with a minor lob level below -25 dB. Three layers are considered in which the two first layers are contiguous, which might be implemented in the analog domain. The first layer lattice (FL-L) is hexagonal. The first layer sub-array includes seven elements, as shown in Fig. 6.9(a). The rest of the six surrounding elements overlap except for the center element. The tiling

matrix realizes the third layer $\boldsymbol{T_{SL2}} = \begin{bmatrix} 1 & 0 \\ 0 & 2 \end{bmatrix}$. This means that three elements in one column of SL-L contribute to one element of the third layer in which two out of three overlap with adjacent sub-arrays along the *y*-direction. The lattices are shown in Fig. 6.9. In Fig. 6.9(c), the FL-L elements are shown by the black dots, while smaller and larger loops illustrate the second and the third layer elements. Regarding the overlap, note that along the y-direction, only elements on the apices overlap on the first layer. Also, on the second layer, only the center element, one out of three, does not overlap.

The FL-SAF, SL-SAF, C-SAF, and UL-AF are correspondingly shown in Fig. 6.10. As seen for an un-steered UL-AF, there are two copies of the main beam along the $V = 0$, showing up on two opposite sides of the hexagonal period boundary. That can easily be understood from how the first-layer sub-arrays overlap. The UL-AF and two O-AFs are shown in Fig. 6.11. As can be seen, the C-SAF has filtered out all grating lobes of UL-AF. However, as stated before, the contiguous sub-array has a narrow range of beam scans. In this case, the grating lobe along the $V = 0$ starts to show up as a sidelobe after 10 degrees steering angle.

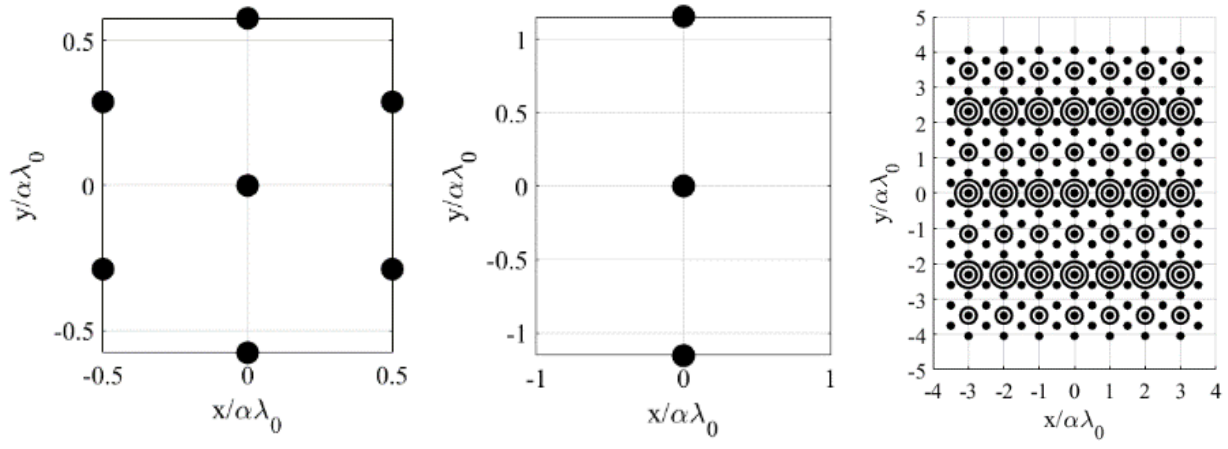

(a) (b) (c)

Fig. 6. 9. Schematic of multilayer planar phased-array. (a) first layer sub-array, (b) second layer sub-array, and (c) all three lattices overlaid.

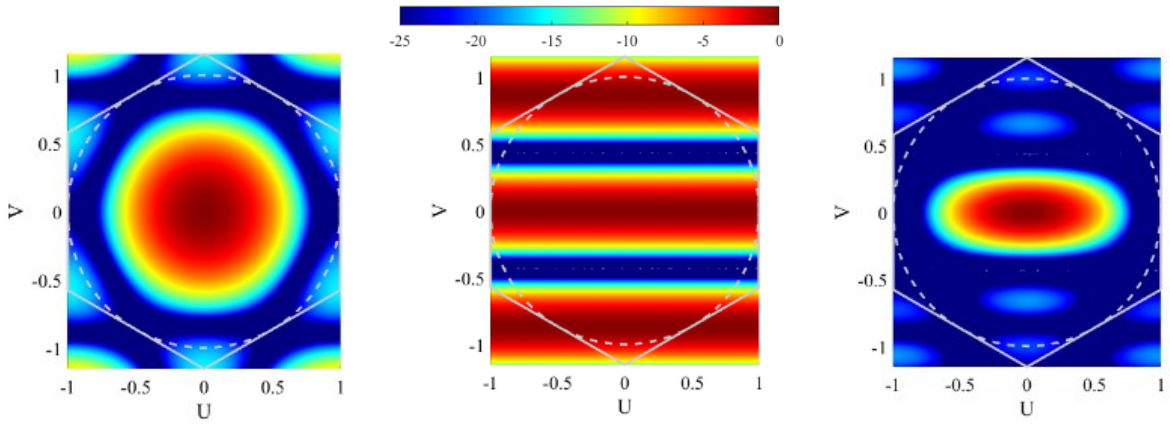

(a) (b) (c)

Fig. 6. 10. Sub-array factors of multilayer planar phased array. (a) first-layer sub-array factor, (b) second-layer sub-array factor, (c) composite sub-array factor.

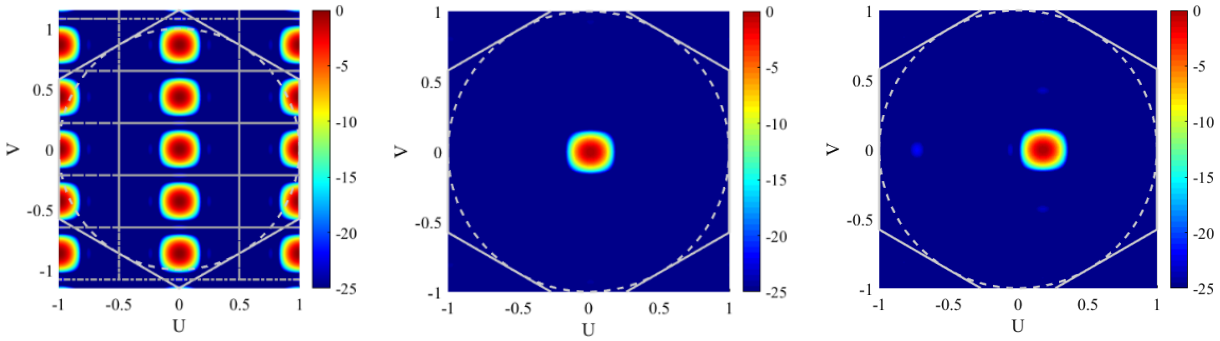

(a) (b) (c)

Fig. 6. 11. Array factors of multilayer planar phased array. (a) ultimate-layer array factor, (b) un-steered overall array factor (O-AF), (c) steered O-AF to 10 degrees.

6.2 Noise shaping at sub-array layer

The sub-array might be steered instead of the contiguous one in the preceding section. This is traditionally more the case for HBF, but in principle, it can also be used for ABF and DBF. The same as the previous section, the sub-array configurations are assumed to have two and/or multiple layers, here up to three layers; therefore, we may talk about different lattice layers. The first-layer lattice, $\boldsymbol{L}_1\mathbb{Z}^2$**,** the lattice that the radiators are positioned on can be regularly tiled in an infinite number of fashions; thus, theoretically, there is an uncountable number of ways to realize sub-array. The sub-array schemes may include several layers in which each can be realized in an analog or digital domain, though some might not be practical or convenient to implement in the analog

domain at least. For the analog implementation of sub-array, it helps to decrease the number of RF chains per radiator (in HBF), but in any beamforming scheme, it is an effective approach for minor lobe suppression. One other application of the resampling matrix is to make a sub-array.

In Figs. 6.12(a) and 6.12(b), the classic hexagonal lattice is tiled by, respectively, sub-array tiling matrices of, $\boldsymbol{T_{sub1}} = \begin{bmatrix} 1 & -2 \\ 1 & 2 \end{bmatrix}$ and $\boldsymbol{T_{sub2}} = \begin{bmatrix} 2 & 0 \\ -1 & 2 \end{bmatrix}$, where the solid circles show the first-layer lattice (FL-L) elements, whereas the hollow ones illustrate the second-layer lattice (SL-L), the lattice that the sub-array outputs are positioned on, $\boldsymbol{L_1 T_{sub}} \mathbb{Z}^2 = \boldsymbol{L}_2 \mathbb{Z}^2$. Those tiling matrices contribute to the nearly square SL-L. Both lattices are the same but 60° rotated with respect to the other. Here, $\boldsymbol{L}_2$ is four times sparser than $\boldsymbol{L}_1$**.** One can see four elements of FL-L inside a nearly square tile on SL-L, including one center element (which has a hollow circle) and three other elements. Then, there are several options for choosing the sub-array type. Just as a "thought experiment" example, let us assume a 3×3 parallelogram-shaped sub-array in which eight out of nine elements overlap in two ways. The gray dashed lines in Figs. 6.12(c) and 6.12(d) signify the boundaries of the sub-arrays, while the thin black lines visualize the element connections to the second layers' inputs. Two adjacent sub-arrays overlap two out of eight sub-array elements. For example, the element located at $\boldsymbol{L}\begin{bmatrix} -1 \\ 1 \end{bmatrix} = (0, \frac{1}{\sqrt{3}})$ in Fig. 6.12(c) and $\boldsymbol{L}\begin{bmatrix} 0 \\ 1 \end{bmatrix} = (\frac{1}{2}, \frac{1}{2\sqrt{3}})$ in Fig. 6.12(d) are shared between two neighboring sub-arrays. Also, six out of eight are shared among three sub-arrays, cf. Figs. 6.12(c) and 6.12(d). As seen, the elements located at $\boldsymbol{L}\begin{bmatrix} 1 \\ 0 \end{bmatrix} = (\frac{1}{2}, \frac{-1}{2\sqrt{3}})$, are connected to two second-layer near-neighboring inputs, $\rho_n = \frac{1}{\sqrt{3}}$, and the far-neighboring ones, $\rho_f = 1$.

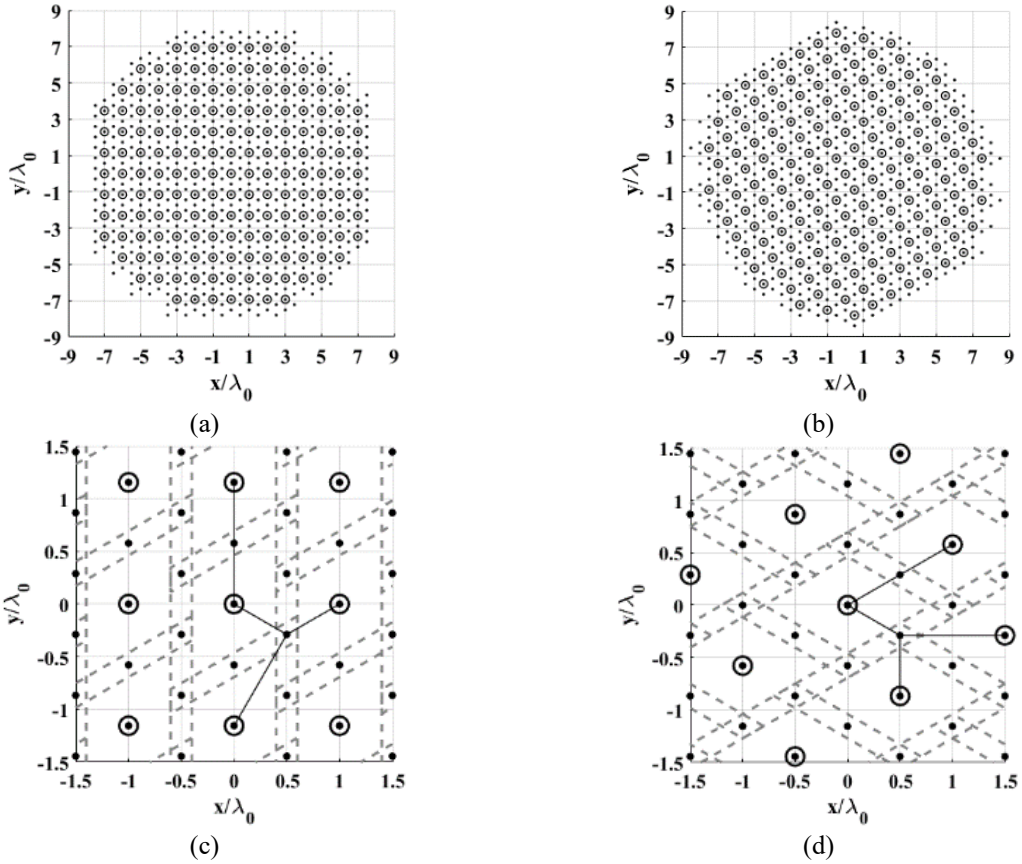

Fig. 6. 12. Two sub-array overlapping schema. Sub-array realized by (a) $\boldsymbol{T_{sub1}}$, (b) $\boldsymbol{T_{sub2}}$, and the corresponding close view of (c) lattices in (a) and (d) lattices in (b).

Indeed, the "element sharing" can be physically implemented using power combiners/dividers if the sub-array is implemented in the analog domain.

For now, we assume a hypothetical scenario that all layers of the array are implemented in the analog domain, and sub-arrays would be phase-steered. In each layer, the magnitude and phase of output signals should be controlled by exploiting the gain control units, such as DAs, and time/phase delay units, such as DPSs. Henceforth, let us continue with the one shown in Fig. 6.12(b). Its decibel SAF and the second-layer array factor (SL-AF), $[\theta, \varphi] = [43°, 199°]$, are respectively illustrated in Figs 6.13(a) and 6.13(b). The second-layer input signal is quantized to 4 bits. The error pattern is shown in Fig. 6.13(c).

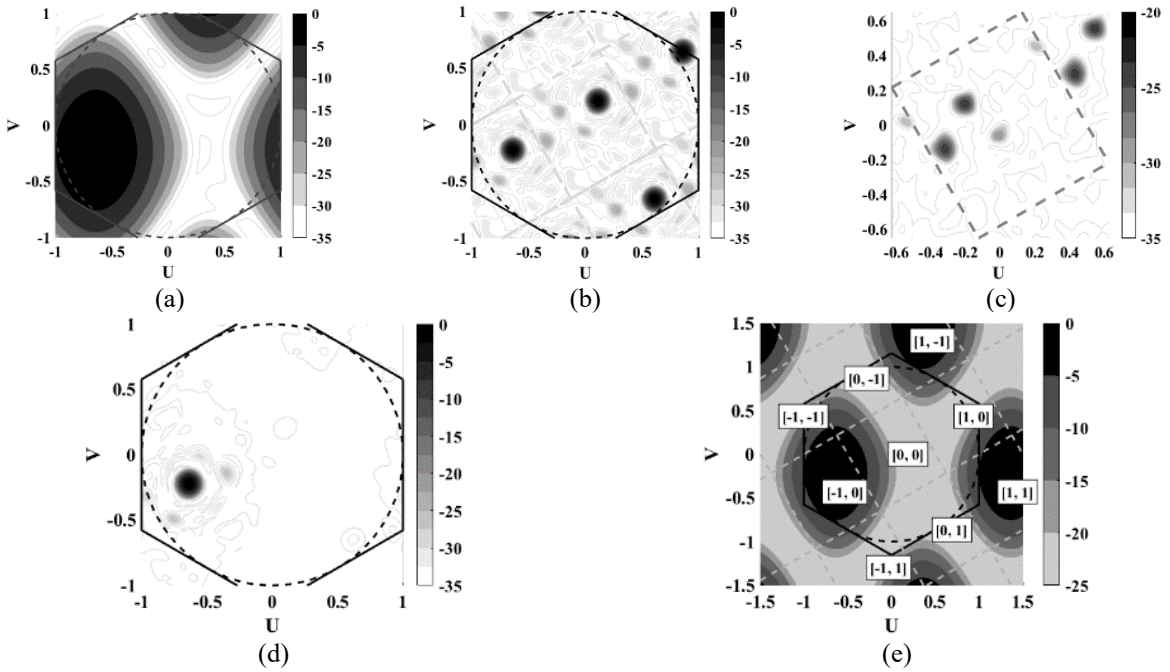

Fig. 6. 13. Computed sub-array factor and array factor for array of Fig. 6.12(b). (a) sub-array factor and (b) the second-layer array factor, (c) normalized second-layer error pattern, (d) the overall array factor, and (e) the sub-array factor tiled by the second-layer array factor periodicity.

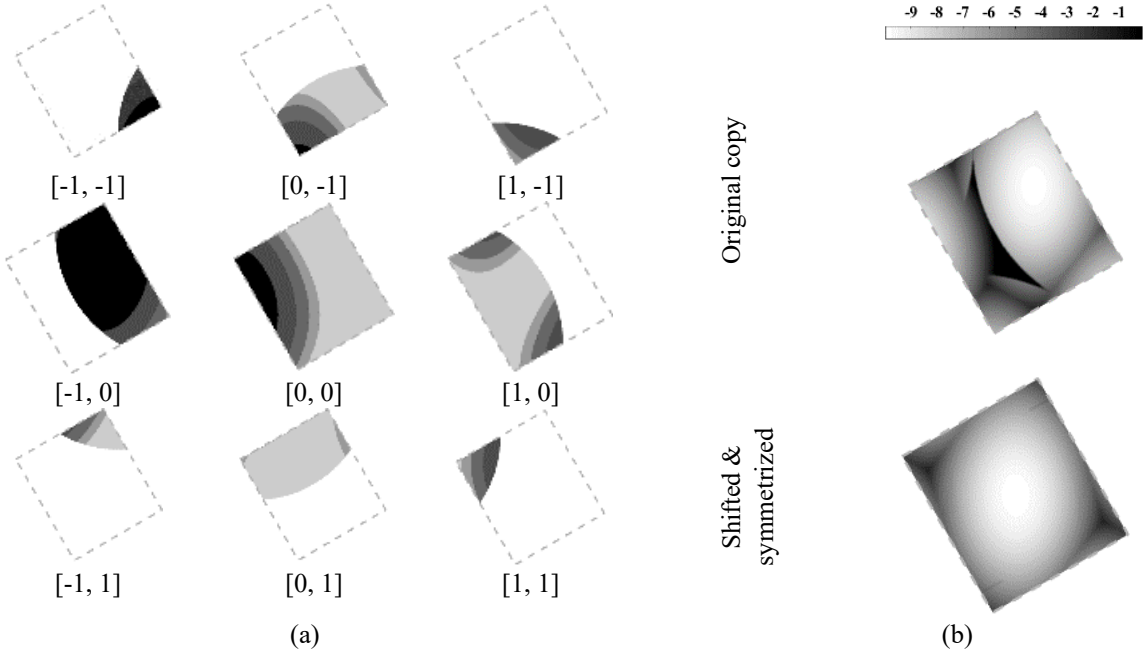

Fig. 6. 14. Filter layout design for noise shaping at sub-array layer. (a) nine tiles cropped by the visibility window and (b) exemplar filter layout background and the shifted & symmetrized copy.

As mentioned, the SL-L is of a nearly square lattice that contributes to a nearly square reciprocal one; such a fundamental period is faintly sketched in Fig. 6.13(b) and 6.13(c). As seen, we can tile the whole beamspace domain with such a prototile that is smaller than the visible region. There

must be precisely four complete periods of SL-AF in one fundamental period of the SAF, $|\boldsymbol{T_{sub2}}| = 4$. Indeed, the SAF suppresses all (grating) lobes of the SL-AF except the one contributing to the main beam in the overall array factor of Fig. 6.13(d). On this account, QLs of the SL-AF, particularly those happening in the vicinity of the main beam, show up inside the overall array factor. For example, in Figs. 6.13(b) and 6.13(d), the QL peak levels are about 23 dB and 26.5 dB, respectively. Accordingly, the second-layer error pattern might be spectrally shaped, corresponding to the SAF. As stated in the study, the quantization distortion is supposed to be pushed to the area where other layers' sub-array factors have high attenuation. That proves the importance of an MPS because it contributes to less out-of-band noise amplification. In contrast to the preceding sections, increasing too much out-of-band noise power is impossible since it should correspond to the SAF attenuation.

One may intuitively wish to push the SL-AF distortion to the "farther area" from where the main beam is intended since that is precisely SAF maximum, and pushing the distortion to the "farther area" is supposed to alleviate the QL level in the overall array factor. Such a strategy sometimes works if the circular symmetric SAF is directive enough. However, the idea needs a minor revision. The preceding idea can be easily undermined since the SL-AF is periodic with a smaller period size than the SAF. Thus, the adjacent copies' distortion pushed to that "farther area" may become visible in the overall array factor if they happen in the region where the SAF does not have enough attenuation. This has been elaborated on and addressed in the following paragraphs.

Consider the decibel SAF tiled by the SL-AF periodicity in Fig. 6.13(e). Each of those tiles overlaps with the visible region of the SAF and receives an integer vector tag. There are precisely nine tiles of which five of them are repetitive, including two sets of three tiles, one set of two tiles, and one set of one tile, e.g., consider the set {[-1, 0], [1, -1], [1, 1]}. The unique tile is the reference

one [0, 0] which has no duplication among the nine tiles. Now, if one succeeds in pushing the SL-AF distortion farther from the main beam located in the tile [-1, 0] with no discrimination in direction, that may lead to an increase of QL level in the overall array factor since other adjacent copies simultaneously push the distortion toward the passband of the SAF, cf. Figs. 6.13(b) and 6.13(e). We propose to design the digital filter with respect to all tiles overlapping with the visible region. Although some tiles are duplicate copies, their intersections with the visible region become unique, as shown in Fig. 6.14(a), where we have cropped each tile's content by the visible region boundary. We assume the area out of the visible region as a pure free spectrum. However, the overall filter layout background is designed based on all tiles' intersection, which is reversed and accompanied by some further trivial manipulations; see the "original copy" in Fig. 6.14(b).

The original copy can be used if the CV-NS is intended. On the other hand, if only the phase of the second-layer excitation signal is controllable, the RV-NS might be utilized. That would be specific to an array with all layers implemented in the analog domain. In such a case, both filter layout constituents involving the background and the notches should be shifted and symmetrized with respect to the reference sample of the SL-AF. However, as in the previous sections, a big portion of the precious free spectrum is wasted due to symmetry. Note that the method's success in QL suppression is a function of SAF shape and overlap efficiency, in addition to "now-classic" influential parameters, including array pitch, *etc*.

In Fig. 6.15(a), frequency responses of the (revised) CCDF and RCDF are illustrated. The gray dashed lines show the fundamental period. Note that the noise shaping has been done on the array of the second layer.

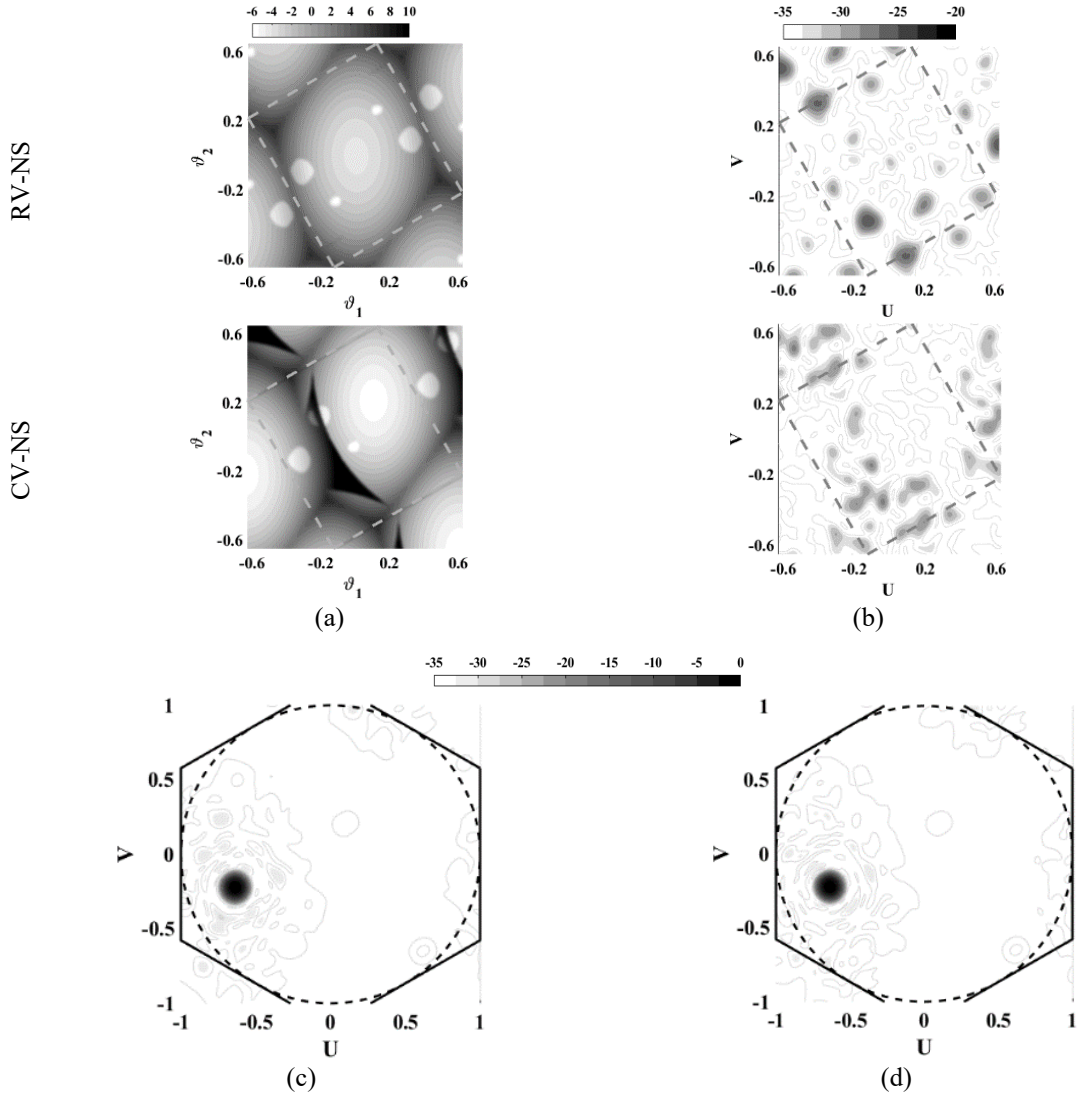

Fig. 6. 15. Phased array designed based on RV- and CV- methods. (a) Frequency response of the revised filters, (b) error patterns, and (c) decibel overall array factors for the targeted point at $[\theta, \varphi] = [43°, 199°]$.

It might be evident that with the same attenuation considered for the filter layout background and notches, RV-NS incurs more out-of-band amplification, as it is spectrally less efficient since its stopband is wider. In Fig. 6.15(a), the stopband attenuation of RCDF is considered less than that of the CCDF, but it might be evident in Fig. 6.15(b) that the RV method generates more out-of-band amplification than the CV one does. The overall array factors in Figs. 6.15(c) and 6.15(d) show improvement compared to that shown in Fig. 6.13(d).

It might be erroneously assumed that the more directive SAF provides a freer spectrum, which is not necessarily correct since the larger sub-array makes the SL-AF periodicity smaller. In this regard, the overlap efficiency is of great importance, implying a more directive sub-array factor with a possible greater array periodicity area. In addition, the sub-array realization would be more complicated.

Now, assume the sub-arrays outputs are introduced to a digital platform that contributes to the HBF. The identical sub-arrays are arranged in a hexagonal fashion of seven elements. One possibility for a tiling matrix is $\boldsymbol{T}_s = \begin{bmatrix} 1 & -1 \\ 1 & 2 \end{bmatrix}$, which contributes to an SL-L that is three times sparser than the FL-L. The schematic is shown in Fig. 6.16(a). Each pair of adjacent sub-arrays precisely overlap two FL-L elements; thus, each element is intersected by three sub-arrays except sub-array centers. Also, we assume that the identical analog sub-arrays are phase-steered with high precision. In this regard, the weighting coefficients of the seven-element sub-arrays should be computed so that the SAF would suppress the six grating lobes. Such an antenna may be utilized for a radar system in which the transmit signal is radiated through a wide-shaped beam, whereas the radar listens to echoes through the multiple simultaneous beams (beam cluster). The underlying design concerns the beam cluster's minor lobe level below -35 dB. Note that the SL-AF might be steered with respect to SAF to generate a beam cluster. The overall array factor, G, can be written as

$$G(\boldsymbol{f}\boldsymbol{R}^{-1}\boldsymbol{L}^{-1}) = G_1((\boldsymbol{f}+\boldsymbol{f}_1)\boldsymbol{R}^{-1}\boldsymbol{L}^{-1})G_2((\boldsymbol{f}+\boldsymbol{f}_1+\boldsymbol{f}_2)\boldsymbol{R}^{-1}\boldsymbol{L}^{-1}\boldsymbol{T})$$

where G_1 and G_2 are respectively SAF and SL-AF, and $\boldsymbol{T}$ is the tiling matrix generating the sub-array, and $\boldsymbol{R}$ is another resampling matrix that simply resamples the ELL generating the reciprocal lattice $\check{\boldsymbol{L}}$. In the above equations, $\boldsymbol{f}_1$ steers the beam cluster while $\boldsymbol{f}_2$ steers the individual beam

with respect to the cluster center. G_1 is fixed for all beams while G_2 should be specifically designed for each beam.

The SAF should acceptably suppress all six "grating lobe clusters" up to about -35 dB. The two-layer array is considered as a circular aperture of about 40λ. The steered SAF is shown in Fig 6.16(b), $[\theta, \varphi]$ = [20°, 80°]. Also, for the current exemplar design, we considered 19 beams arranged in a hexagonal fashion to constitute the beam cluster, and thereby, the transmit beam is hypothetically shaped in a hexagonal form. Fig. 6.16(b) shows the SAF and Figs. 6.17(a) and 6.17(d) illustrate the O-AF. The windowing effect of SAF can be easily seen; specifically, the six grating lobes are suppressed by SAF.

Then, the CBW is quantified by 4 bits based on the definition $\mathbb{Q}_2$ in (3.5). As seen in Fig. 6.17(b) and 6.17(e), some distortions show up in the overall array factor, and the minor lobe level even violates 30 dB. Like the previous case, one may spectrally shape the error to push it toward the available regions on the SL-AF that SAF has enough attenuation there and can be acceptably suppressed in the overall array factor. The revised system in Fig. 6.18 is designed for SL-L based on the tiling approach introduced before. It can be seen in Figs. 6.17(c) and 6.17(f), that the distortion is pushed out toward the region where the SAF has more attenuation, and the sidelobe level is effectively suppressed.

The disadvantage of the directive sub-array factor is its realization complexity. On this account, the array may be designed more optimally for minor lobe suppression by using more sub-array layers. Besides, that can simplify the sub-array complexity with the cost of more layers, as shown in the contiguous sub-array section. In Fig. 6.19, a schema of a three-layer sub-array system is shown. Seven elements constitute each first-layer sub-array.

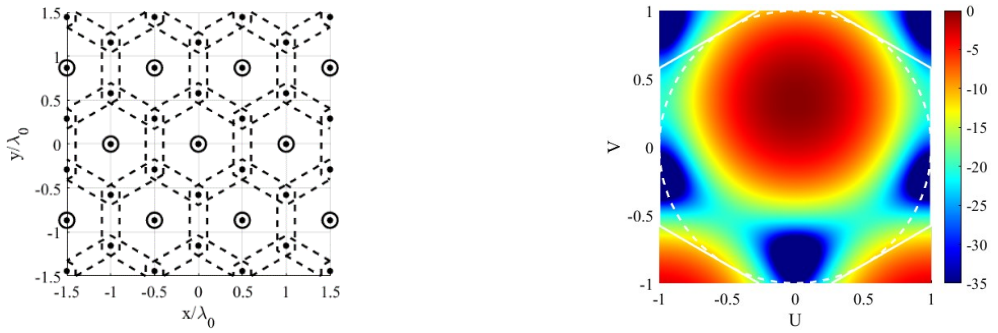

Fig. 6. 16. Planar array with two-layer sub-array overlapping. (a) Schematic of lattices and sub-arrays and (b) sub-array factor.

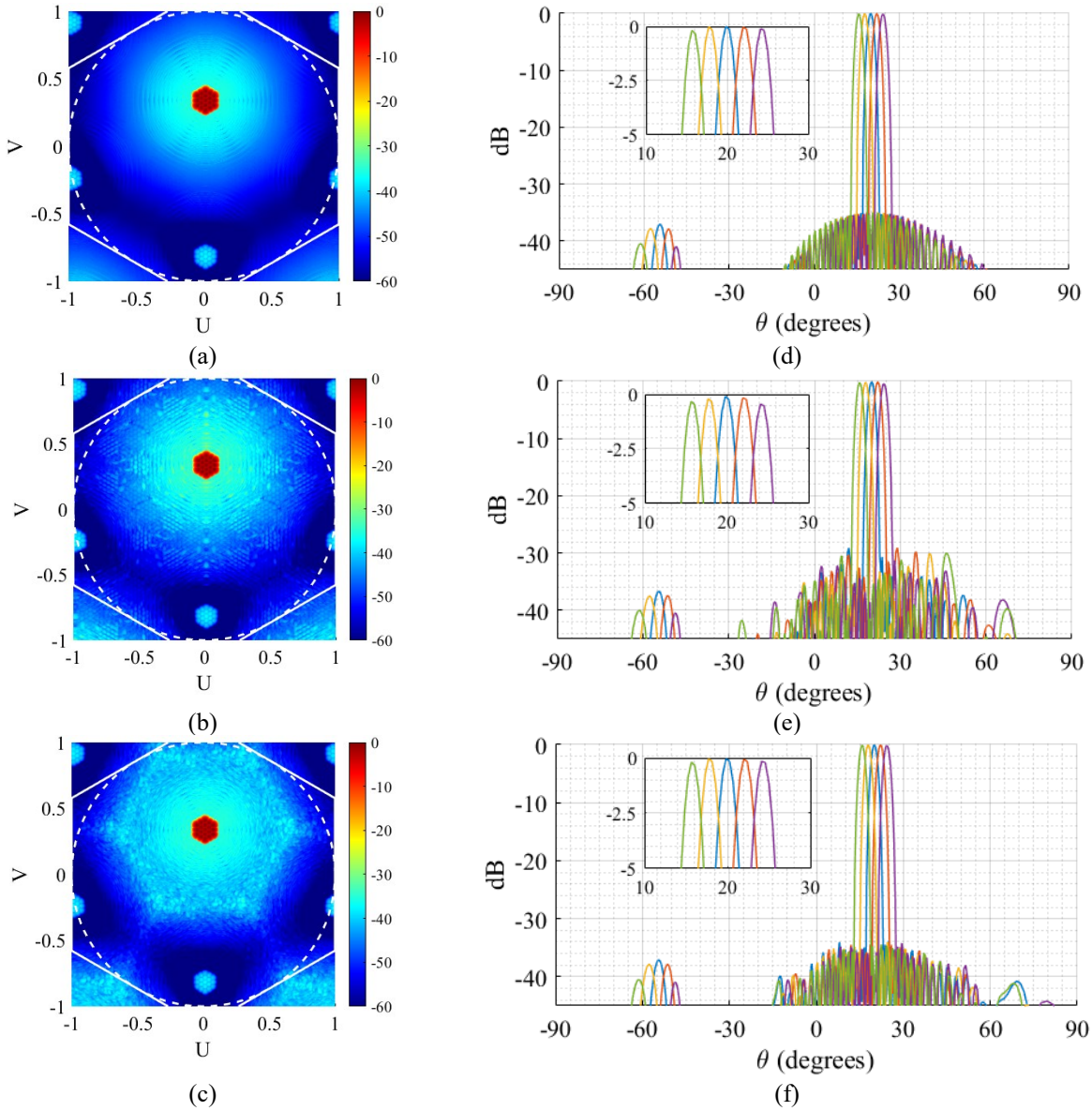

Fig. 6. 17. Computed array factor plotted against the direction cosines. For (a) high precision, (b) 4-bit, and (c) CV-NS. Computed array factor along the U = 0 for (d) high precision, (e) 4-bit, and (f) CV-NS.

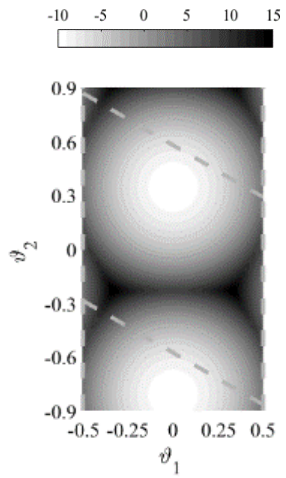

Fig. 6. 18. Revised filter frequency response used for noise shaping in the example of Fig. 6.17.

In this case, there are two layers of sub-arrays, including the first- and the second-layer ones. Nevertheless, let us define the tiling matrix as $\boldsymbol{T}_{s1} = \begin{bmatrix} 2 & -1 \\ -1 & 2 \end{bmatrix}$, which contributes to SL-L. Note that the generating and tiling matrices are not unique, but the period area is. Each second-layer sub-array is assumed to contain 19 elements, shown in Fig. 6.19(a). In Figs. 6.19, the SL-L elements are sketched with solid black circles, while the black hollow ones show the third-layer lattice (TL-L) elements; hence, as an example, the hollow circle in Fig 6.19(a) are the solid ones in Fig. 6.16(a). It might be evident that the TL-L is just an enlarged version of SL-L by a factor of two. In other words, $\boldsymbol{T}_{s2} = 2\boldsymbol{I}$ and that the composite tiling matrix $\boldsymbol{T}_c = \boldsymbol{T}_{s1}\boldsymbol{T}_{s2} = \begin{bmatrix} 4 & -2 \\ -2 & 4 \end{bmatrix}$. Fig. 6.19(a) shows the SL-L elements of one exemplar sub-array; the rest are sketched faintly. There are three SL-L element types, including those in sub-array centers, those located on the first tier of the sub-array center, and those on the second tier of each sub-array but are not a sub-array center. Evidently, the sub-array centers are intersected by six included sub-arrays. As depicted in Fig. 6.19(b), the SL-L elements located on the first tier of each sub-array are overlapped by three other included sub-arrays.

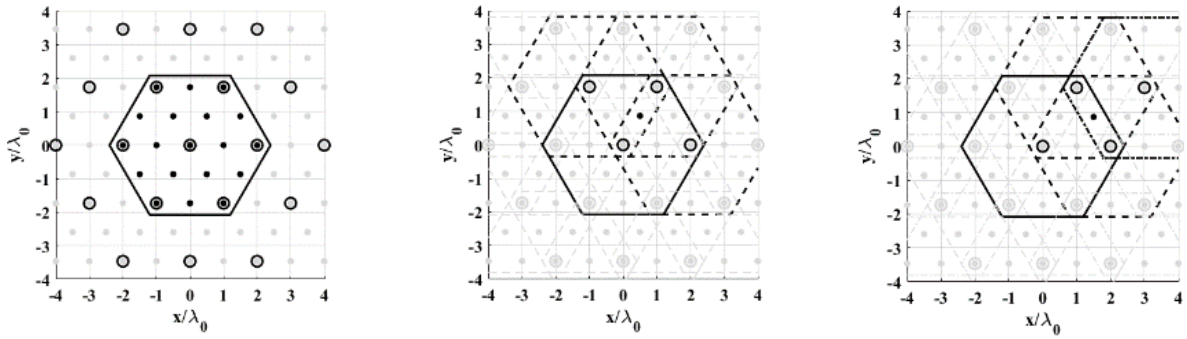

(a) (b) (c)

Fig. 6. 19. Schema of three-layer sub-array overlapping. (a) second layer lattice, third layer lattice, and the boundary of the second-layer sub-array, (b) three included sub-arrays intersect with the first-tier element of the underlying sub-array, (c) Two included and one non-included sub-arrays intersect with a second-tier element.

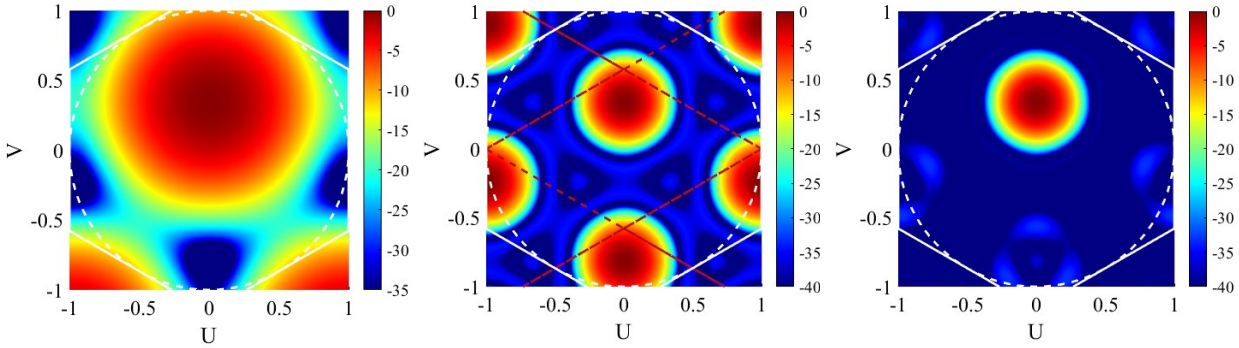

(a) (b) (c)

Fig. 6. 20. Computed sub-array and array factors of three-layer sub-array overlapping. (a) first-layer sub-array factor, (b) second-layer sub-array factor, (c) composite sub-array factor.

Furthermore, those SL-L elements on the second tier of each sub-array which are not sub-array centers, are overlapped by two other included sub-arrays and a non-included one, as visualized in Fig. 6.19(c). Therefore, all SL-L elements are overlapped by four sub-arrays except the sub-array centers, which are overlapped by seven sub-arrays.

The FL-SAF and SL-SAF are shown in Fig. 6.20(a) and 6.20(b). The periodicity of SL-SAF is shown with the dashed red line. The C-SAF is illustrated in Fig. 6.20(c). As seen, all beam copies of SL-SAF are partially suppressed by the FL-SAF except the one that contributes to the main beam in C-SAF. The beam cluster is shown in Fig. 6.21(a) for the HP system. It can be seen in Fig. 6.21(a) that C-SAF suppresses all grating lobes to some extent. The array factors along the $U = 0$ are illustrated in Fig. 6.21(d).

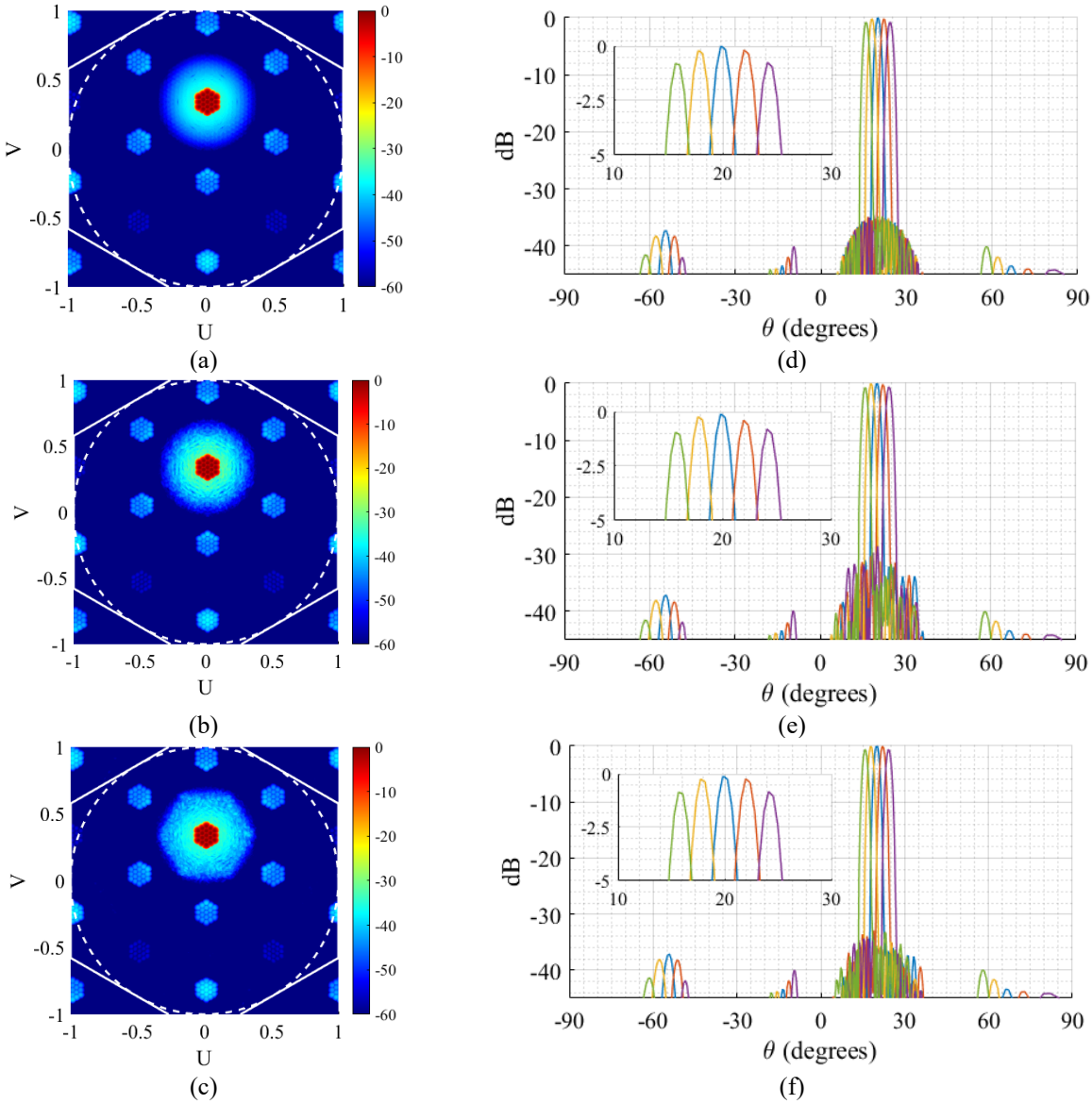

Fig. 6. 21. Computed array factor plotted against the direction cosines. For (a) high precision, (b) 4-bit, and (c) CV-NS. Computed array factor along the $U = 0$ for (d) high precision, (e) 4-bit, and (f) CV-NS.

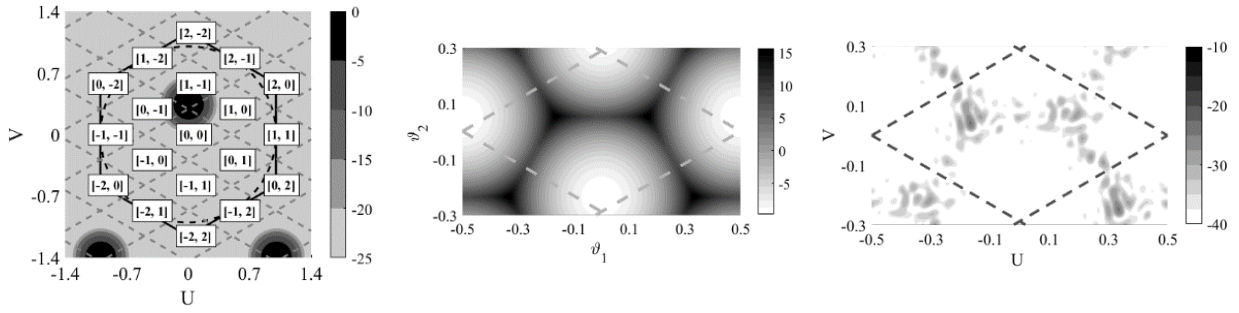

Fig. 6. 22. Design of digital filter for noise shaping for the phased array of Fig. 6.21. (a) composite sub-array factor tilled by the third-layer lattice periodicity, (b) frequency response of the revised system, and (c) error pattern, the overlaid overall array factors along $U = 0$ for 4-bit representation of complex beamforming weights.

Strictly speaking, the six near-neighboring beam clusters are more suppressed by the SL-SAF and the six far-neighbor ones by the FL-SAF; those are regions in Fig. 6.20(c) where the FL-SAF severely suppresses the grating lobes. The six remaining far-neighbor "grating beam clusters" are more suppressed by SL-SAF, though the FL-SAF also has considerable attenuation. The current configuration can better suppress the sidelobes in comparison to the example of Fig. 6.17 since the C-SAF is much more directive than the SAF of Fig. 6.16. However, some distortion can still appear in the overall array factor in the vicinity of the main beam.

The in-band UL-AF distortion should be spectrally shaped to minimize its manifestation in O-AF. The results of the array factor for the 4-bit system and the spectrally shaped one are shown in Fig. 6.21. The filter layout should be designed based on the C-SAF tiled by the periodicity of the ultimate layer array factor, which in this case, is the third layer. As seen in Fig. 6.22(a), almost 19 tiles overlap with the visible region, among which except four ones, {[0, 0], [0, -1], [1, -1], [1, 0]}, the rest of them have no significant contributions to the filter layout shape since the C-SAF has enough attenuation there. Accordingly, the filter layout is designed, and the filter's frequency response based on the DHT approach is computed. The impulse response is normalized to the reference sample to find the targeted system with the frequency response shown in Fig. 6.22(b). As seen, it has been realized by the four tiles' contributions. The distortion will be pushed to the region where the revised (targeted) system has amplification, which is precisely the available spectrum where the C-SAF has enough attenuation. The resultant error array factor is shown in Fig. 6.22(c), following the filter shape.

Chapter 7
Optimization

7.1 Fundamentals

Optimization is a mapping from parameter space (PS) to objective space (OS), $\mathbb{R}^m \longrightarrow \mathbb{R}^k$, which can be written

$$\min \qquad \boldsymbol{f}(\mathbf{x}) = [f_1(\mathbf{x}), f_2(\mathbf{x}), \dots, f_k(\mathbf{x})] \tag{7.1}$$

where $\mathbf{x} \in \mathbb{R}^m$ is the decision variable vector inside the PS, subject to m constraints, and $\boldsymbol{f}$ is a vector of k objectives. From the number of objective perspectives, the problem might be single-objective, $k = 1$, multi-objective, $1 < k \leq 4$, or many-objective $k \geq 4$.

Several search methods include point- and population-based methods, including particle swarm optimization (PSO) and genetic algorithm (GA). Brainstorm optimization (BSO) is a simple and relatively new swarm intelligence with a random method mimicking the problem-solving of human beings in a brainstorming process [104]. There are three main operators in BSO comprising clustering, solution generation, and selection. The block diagram of BSO is illustrated in Fig. 7.1. In its original version, clustering in PS is used, in which the solution population is separated into several clusters. The effectiveness of this implementation is investigated in [105] for several antennas. However, the clustering strategy is a time-consuming process. In particular, the algorithm can be inefficient and quite time-consuming for PA and RA, with high dimensional decision variables. One solution to this problem is clustering in OS (BSO-OS) which typically has less dimension than PS.

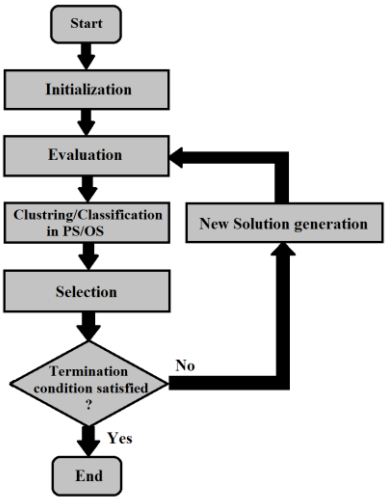

Fig. 7. 1. Block diagram of brain storm optimization.

When solutions inside PS are clustered, it means solutions are categorized according to their similarities (similarity of individuals' ideas in the brainstorming process) but clustering inside OS is, in fact, a kind of classification according to the goodness of the feasible solution, so elitism is enhanced.

7.2 Multi-objective optimization

Multi- and many-objective problems (MOPs) map a tuple of *m* decision variable from PS to a tuple of *k* objectives in OS. Unlike single-objective optimization, judging which individual is excellent in MOP is difficult since objectives are conflicting. In Pareto-based optimization, a solution with vector objective $y^{(1)} \in \mathbf{Y} \subset \mathbb{R}^k$ is said dominates $y^{(2)} \in \mathbf{Y}$, (symbolically written as $y^{(1)} \prec y^{(2)}$), if and only if:

$$\begin{cases} \forall i \in \{1,2,\dots,k\} : y_i^{(1)} \leq y_i^{(2)} \\ \text{and} \\ \exists j \in \{1,2,\dots,k\} : y_j^{(1)} < y_j^{(2)} \end{cases} \tag{7.2}$$

A vector solution **x** is called non-dominated (Pareto optimal/efficient) if there is no improvement in one objective without degrading in value of other objectives.

The set of all non-dominated solutions is called the Pareto set, and the set of all Pareto objective vectors is called the Pareto front [104]. However, the realization of the Pareto front is not an easy task. Since without specific maintenance of solution diversity, the strict search of non-dominated regions prematurely excludes some feasible answers, and Pareto curve/surface will not get fully expanded. Hence, in MOP, there are two goals, one is to find the Pareto front, and the other is to maintain the diversity of solutions.

There are some efforts in the literature to extend brainstorming algorithms for MOPs. The first version of multi-objective brainstorm optimization (MOBSO) is presented in [106], In which the population (in OS) is clustered into *c* clusters based on each objective. Individuals satisfying most objectives are survived. The global archive is updated in each iteration according to the best solution. In [107], the crowded comparison approach, originally used in non-dominated sorting genetic algorithm II (NSGA-II), ensures the diversity of the solution. Crowding distance is a method to estimate the intensity of solutions around a specific solution. The less crowded solution will survive. Thus, a diversity of solutions can be acceptably exercised during the optimization procedure. Also, in [108], the decomposition method is used to realize MOBSO with modified search efficiency and a very acceptable distribution of the solution.

Here, we keep the diversity of solutions by using the virtue of group information. If two solutions (new solution and old one) were mutually non-dominating, we choose the one based on the "diversity approach," in which the distance between the centroid (mean value) of all clusters is considered as a simple norm of the solution expansion in OS. The population is clustered into *c* clusters, and the distances between centroids are calculated and compared to their old counterpart. The solution belonged to the one with more value who would survive. Besides, some solutions in each iteration are selected randomly to ensure the solutions' diversity further.

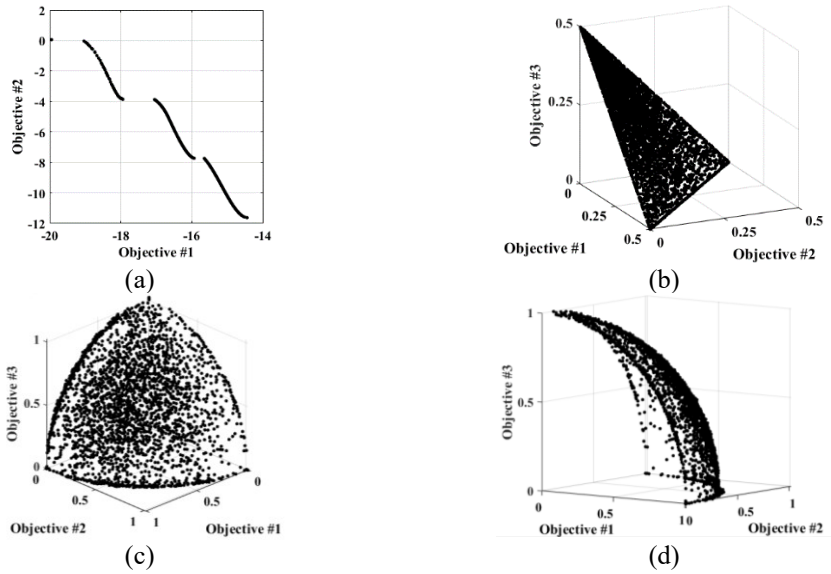

Fig. 7. 2. The estimated Pareto front for some test functions. (a) Kursawe function, (b) DTLZ1, (c) and (d) DTLZ4.

Fig. 7.2 shows the results for some test functions, including the Kursawe function, examples of the dual-objective problem, DTLZ1, and DTLZ4, which are tri-objective problems. As seen, the algorithm can acceptably converge to Pareto fronts.

7.3 Reflectarray optimization

Optimizing a sizeable planar antenna with several hundred to thousands of elements is difficult as the PS is of high dimensions. It is computationally expensive and time-consuming. Sometimes, it becomes impossible for the algorithm to converge. Accordingly, it might be beneficial to decrease the number of unknown parameters, though it may somehow localize the algorithm. One method introduces a kind of perturbation, defined by a polynomial, to the aperture phase. Zernike polynomial can be used for such a purpose [109], which can be defined as even and odd polynomial along the azimuth direction, as follows:

$$\begin{cases} Z_l^n(\rho,\varphi) = R_l^n(\rho)\cos(n\varphi) & Even \\ Z_l^{-n}(\rho,\varphi) = R_l^n(\rho)\sin(n\varphi) & Odd \end{cases} \tag{7.3}$$

where $0 \le \rho \le 1$ is the radial distance and $R_l^k(\rho)$ is the polynomial radial term is defined

$$R_l^k(\rho) = \sum_{k=0}^{\frac{l-n}{2}} \frac{(-1)^k (l-k)!}{k!\left(\frac{l+n}{2}\right)!\left(\frac{l-n}{2}-k\right)!} \rho^{l-2k}$$

For the case of RA with pencil beam, this is the radial term that is more important. Specifically for symmetric problems. However, the azimuth term can also be used as it provides more variety of solutions.

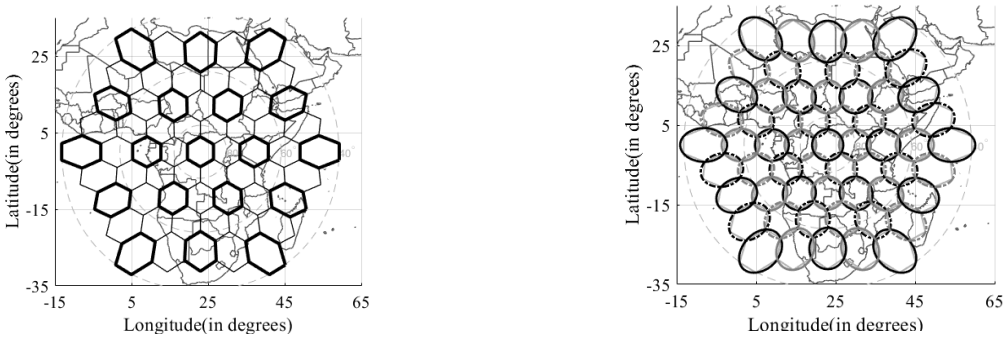

(a) (b)

Fig. 7. 3. An exemplar layout of multi-spot medium earth orbit coverage (a) ideal radio cells and (b) associated 4-cell reuse scheme with ideal radiating spots.

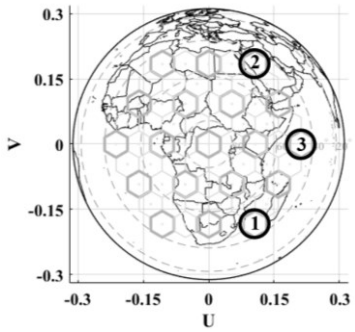

Fig. 7. 4. Three objective beams are shown by the black loops.

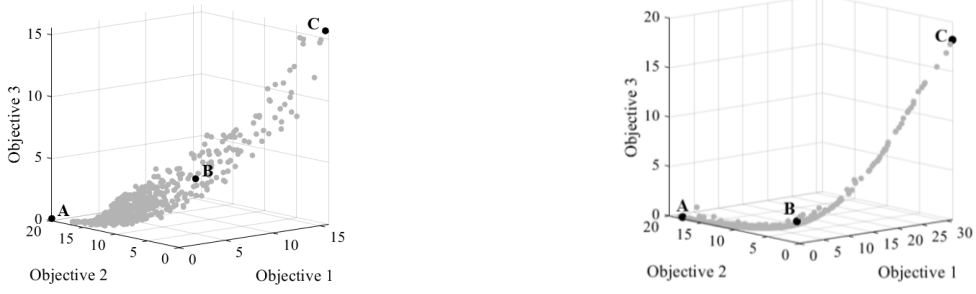

(a) (b)

Fig. 7. 5. Estimated Pareto fronts. The coordinate of Solution A, B and C are respectively at (a) [x, y, z] = [0, 20, 0.16], [4.61, 4.21, 4.56] and [15.87,0.47,15.61], (b) [x, y, z] = [0.49, 18.35, 0.06], [5.01, 3.69, 1.86] and [30.71, 0, 17.81].

Note that there are other options, including the Jacobi polynomial, which belongs to the class of orthogonal polynomials, and many other polynomials, such as Chebyshev, Legendre, Zernike, *etc*. are special cases of Jacobi polynomial. For $\alpha, \beta > -1$, and x belongs to [-1, 1], the Jacobi polynomial of order N at point x (real value) can be defined as:

$$J_N^{(\alpha,\beta)}(x) = \sum_{k=0}^{N} \binom{N+\alpha}{N-k}\binom{N+\beta}{k}\left(\frac{x-1}{2}\right)^k \left(\frac{x+1}{2}\right)^{N-k}$$

In the above equation, the Jacobi term can be used for the radial term in (6).

The RA aperture phase is optimized as in the following procedure. First, the aperture phase distribution for each focus is calculated, and a perturbation according to the aggregation of Zernik/Jacobi terms with different coefficients is introduced to each phase distribution. Then, perturbed aperture phases corresponding to each focus are added by a weighting factor providing a full reflective matrix. The coefficients multiplied by every Jacobi term and the weighting factor are considered the decision variables of the MOBSO. The error between the i*th* mask and the radiation pattern corresponding to the i*th* feed position is considered the i*th* objective (y_i). The vector objective $\mathbf{Y} = [y_1, y_2, \ldots, y_n]$ is optimized in a multi-objective scheme based on Pareto dominance.

Let us consider an example of a medium earth orbit (MEO) satellite with multi-spot coverage. The satellite is assumed to be 14,065 Km above the equator. The z-axis of the satellite coordinate system is aimed at the sub-satellite point (SSP). As common, the ideal radio cells are considered hexagonal. Note that the current design is based on the constant beam approach, which is more practical; the projected radio cells appear in different sizes and shapes on earth. An example of radio cell arrangement is shown in Fig. 7.4. For simplicity, we only consider one set of co-channel cells to be covered by one aperture antenna.

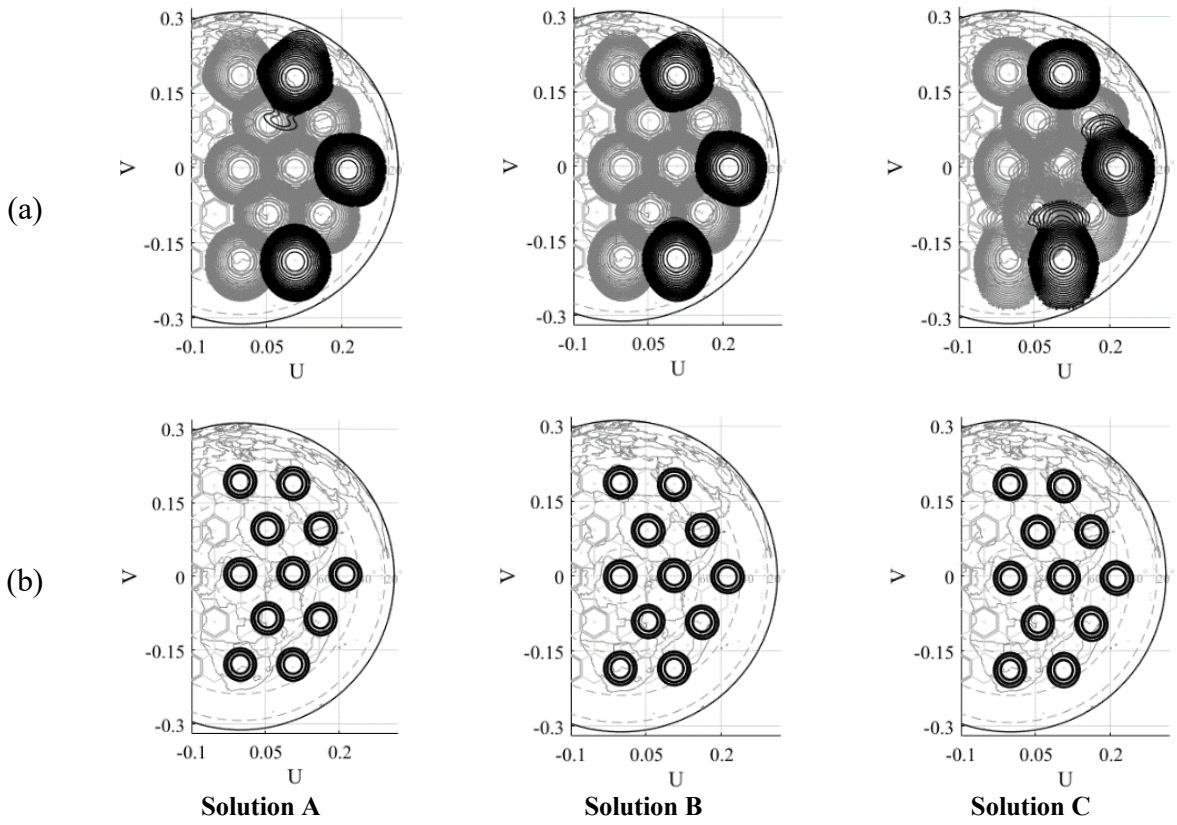

Fig. 7. 6. Three exemplar solutions of estimated Pareto front. (a) 20 dB contour, (b) 4 dB spots.

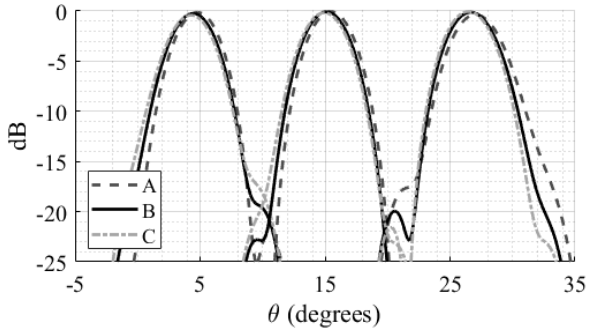

Fig. 7. 7. Computed patterns along $U = 0$.

Fig. 7.4 shows the radio cells of interest with the hexagons plotted by bold lines. Note that we could choose an orthogonal radio-cell arrangement. However, the current scheme might be easier to realize for an offset-fed RA. The diameter of the antenna is assumed to be 185.5 mm, which at 30 GHz contributes to 18.55λ. The lattice is assumed to be a square with a pitch, ρ, of 3.5 mm, and the antenna F/D is about 1.25. The aperture is considered symmetric with respect to the y-axis. We used a tri-objective optimization based on the approach explained in the previous section. Three

constant feed positions are assumed to correspond with three objective beams. This has been illustrated in Fig. 7.4. It is evident that there are other possibilities for the objective beams. We found that the current arrangement may yield better results by trial and error. Actually, those three beams are more challenging to comply with the requirements; thus, they have been chosen as the objectives. We have considered two optimization setups. In one whose estimated Pareto front is shown in Fig. 7.5(a), both radial and azimuth polynomial terms are used, while for Fig. 7.5(b) is used only radial terms are utilized. As seen, the Pareto front is better expanded for Fig. 7.5(a). Note that the number of polynomial terms is also a decisive approach, which controls the amount of algorithm localization. Here, nine terms are used. The estimated Pareto fronts shown in Figs. 7.5 are realized after 500 iterations. Specifically, 150 agents were recruited for each iteration, and the external archive size was about 1000, comprising the non-dominating solutions found. The optimization yields high-precision PDAs. The associated 20 dB and 4 dB spots are shown in Figs. 7.6 for Solutions A, B, and C in Fig. 7.5(a).

For Solution A, the two beams along the $V = 0.184$ interfere with the radio cell located at [U, V] = [0.055, 0.092]; hence, they do not comply with the 20-dB co-channel norm. That is simply because Solution A is located at the end of estimated Pareto fronts along the "objective 2" axis; see Fig. 7.6(a). Also, Solution C is located on the largest objective 1 and 3 values but is of minimum value for objective 2. It can be seen in Fig. 7.6(a) for Solution C that all beams located in the vicinity of objective beams 1 and 3 interfere with other radio cells and that Solution C also fails to comply with the predefined requirements. Not that objective beam 2 for Solution C is much better than Solution A for both results.

Solution B might be assumed as "balanced solutions," which means that all beams show up in an acceptable fashion; see Fig. 7.6(a) for Solution B. Also, Fig. 7.6(b) shows that the 4 dB spots

are somehow located in the predefined locations with acceptable spot widths. For the sake of further clarification, the beams along the $U = 0$ are shown in Fig. 7.7. As seen, Solution A shows a small misalignment specifically for the beam commanded at about $\theta = 26.4°$, which is close to the objective Beam 2 and shows 0.3 dB gain loss in comparison to the other solutions. This is almost applied to the beam located at about 4.4° for Solution C, close to the objective Beam 1. Overall, the algorithm is potent for finding a range of solutions based on a predefined feed position. Based on the estimated Pareto front, one may choose a balanced solution that is good enough for all objectives to pass the system requirements.

7.4 Optimized filter for noise shaping of sparse element spacing

In general, when the visible region is not accessible, there might be at least two approaches to deal with that. The first one is to use a spaced-notches filter. That is how we dealt with the QLs when the RV method did not achieve the invisible region in the preceding chapters. In fact, that can also be used when the array pitch violates the Nyquist design. Fig. 7.8(a) illustrates a computed array factor. The hexagonal lattice PA aperture is almost circular with a diameter of about 17λ. The normalized array pitch is about $\rho = 0.635$ contributing to 733 radiating elements. Also, the antenna is designed for 30 dB SLL Taylor weighting, and the beam is commanded at $[\theta, \varphi] = [30°, 45°]$. Both phase and amplitude are quantized to 3 bits. As can be seen in Fig. 7.8, one period is smaller than the visible region, although a very tiny invisible region exists. Such an array can steer up to about 48° without the grating lobe appearance. The RPDF result is shown in Fig. 7.8(b). It has decreased the QL level to about 23 dB, see Table 7.1. However, as stated before, the random dither is quite sub-optimal compared to the spectrally shaped dither.

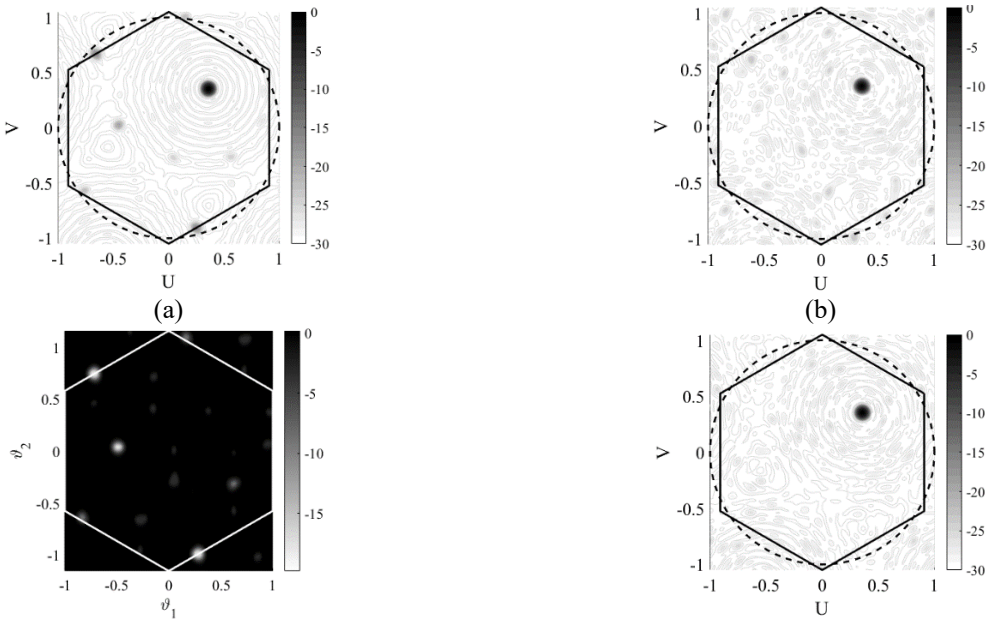

Fig. 7. 8. Steered array factor for array pitch $\rho = 0.635$. (a) simple quantization, (b) RPDF. (c) Spaced-notches filter, (d) array factor realized by CV-NS based on spaced-notches filter.

TABLE 7.1
GAIN LOSS WITH RESPECT TO HIGH PRECISION SYSTEM IN FIG. 7.8.

	SUQ	**RPDF**	**Spaced-notches**
Gain loss	0.275 dB	0.92 dB	0.38 dB
SLL	16.72 dB	23.1 dB	25.2 dB

In Fig. 7.8(c), the frequency response of a spaced-notches filter is shown, and the result of the array factor is in Fig. 7.8(d). This method simply attenuates the QLs and spans their energy on the whole fundamental period of the array factor. It is even possible to suppress some of the QLs collectively. As seen, its performance is much better than dithering. The QL level in Fig. 7.8(d) is decreased to about 25.2 dB. The normalized gain loss is also shown in Table 7.1.

The second approach only removes the distortion from the field of interest. Consider an example of low earth orbit (LEO) satellite located at 550 Km above the equator. As shown in Fig. 7.9(a), that yields a maximum satellite view angle of about $\theta_S = 2\times67°$, which associates with the elevation of $\theta_e = 0°$ viewed by the observer on earth. Such satellites typically carry several PAs (e.g., four PAs), each generating multiple simultaneous beams, but here for simplicity, only one

spot beam is considered. The edge of coverage (EoC) is defined as an elevation of about $\theta_{EoC} = 36°$, which is shown in Fig. 7.9(b). That requires the antenna to have a maximum steering angle of $\theta \approx 48°$. In Fig. 7.9(c), the beam is commanded at $[\theta, \varphi] = [48°, 120°]$. The geographical and political boundaries are shown in the background. The 3-dB spot radius is about 1.985°. A black contour shows its corresponding projection on earth in Fig. 7.9(d). As stated, the in-band is the region of interest that might be considered in two ways for the case. One is the region circumscribed by the EoC. The other one might be the whole region on earth visible from the satellite viewpoint. Anyway, the main goal for this example is to push considerable distortion to the region where the antenna radiation would spill over to space or the tiny invisible region.

That is precisely the area close to the apices of the hexagonal shape period in Fig. 7.9(c). However, one should recognize the discrepancy between this case and those in the previous chapters when enough invisible region was available as out-of-band. This is because the out-of-band distortion turns to minor lobes inside the visible region, significantly decreasing antenna directivity.

The main challenge in noise shaping is to choose the most optimal filter. The noise shaping solution is unique with respect to the filter used, wavefront traversal, and quantizer specifications. However, choosing an optimal filter is challenging since there are typically several options and various possible solutions. For example, the amount of attenuation considered for each notch, background disc level(s), and the impulse response size. For the current example, we may give more priority to the region circumscribed by the EoC; thus, it has been defined as in-band. In Fig. 7.10, a filter is designed for such a simple scenario. Only the circular disk corresponds to the EoC region, and notches associated with the QLs are not considered.

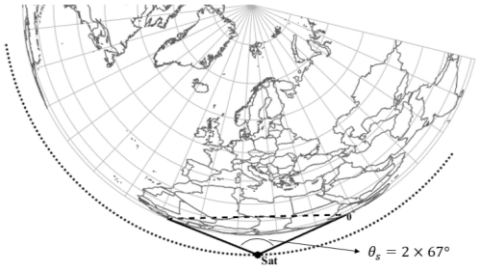

(a)

(b)

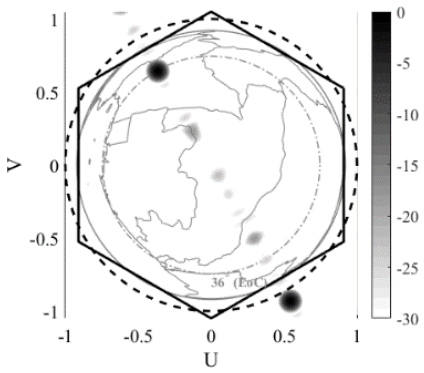

(c)

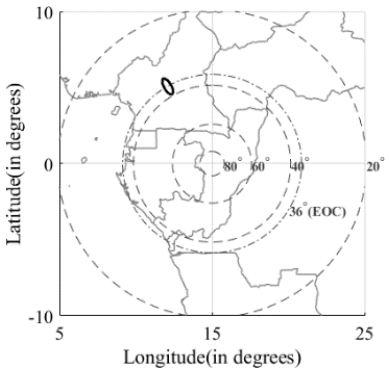

(d)

Fig. 7. 9. Exemplar low-earth orbit satellite position, antenna pattern, and projection on earth. (a) a schema of satellite position and its field of view. (b) edge of the coverage (EoC), 36°, and other elevations. (c) array factor for 3-bit simple uniform quantization, (d) a contour of 3 dB spot on earth.

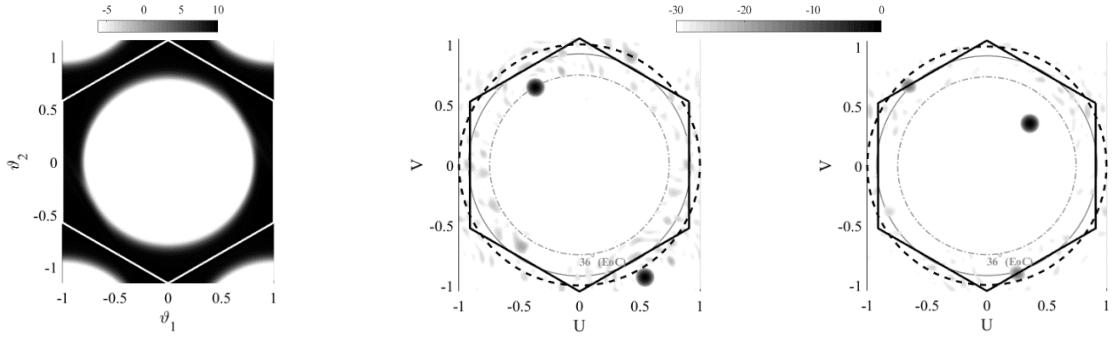

(a) (b) (c)

Fig. 7. 10. CV-NS results based on digital filter with stopband corresponding to EoC. (a) Revised system frequency response, computed array factor steered at (b) $[\theta, \varphi] = [48°, 120°]$, (c) $[\theta, \varphi] = [30°, 45°]$.

TABLE 7.2
GAIN LOSS AND SLL IN FIG. 7.10.

	SLL	Gain loss
Fig. 7.10(b)	19.9 dB	0.59 dB
Fig. 7.10(c)	15 dB	0.46 dB

However, as might be expected, the filter does not work exactly the same for all steering angles as the SLL, and gain loss slightly varies; consider Table 7.2. On the other hand, we may prefer the distortion only spillover over to space and invisible region. The filter in Fig. 7.11 is designed for such a purpose. However, as the stopband is quite broad, it incurs a huge upshift in the frequency response of the revised system in Fig. 7.11(a). As a result, some artifacts appear inside EoC with about 29 dB magnitude. Besides, the filter imposed more antenna gain loss than Fig. 7.10, See Table 7.3. In this regard, we may more optimally control the out-of-band distortion in terms of location and level. This is significant for the amount of antenna gain loss. In Fig. 7.12, two levels opt for filter layouts instead of one level. This is because we prioritized the region inside the EoC but still wished to control the amount of SLL inside the region between the EoC and elevation zero. Also, the notches corresponding to the QLs are also considered this time. To optimally design the filters, particle swarm optimization (PSO) is recruited. We have considered a vector of five elements as the decision variable vector; thus, in PSO, each particle position is characterized by five dimensions. Two elements are associated with the two levels of filter background, and three corresponding to three possible levels of notches. The optimizations are carried out by using 100 iterations and 150 swarm populations. The convergence diagrams are shown in Fig. 7.13, in which the steering angle 1 and 2 are, respectively, associated to $[\theta, \varphi] = [48°, 120°]$ and $[\theta, \varphi] = [30°, 45°]$. It can be seen in Table 7.4 that antenna gain loss and SLL are promoted in comparison with Fig. 7.11.

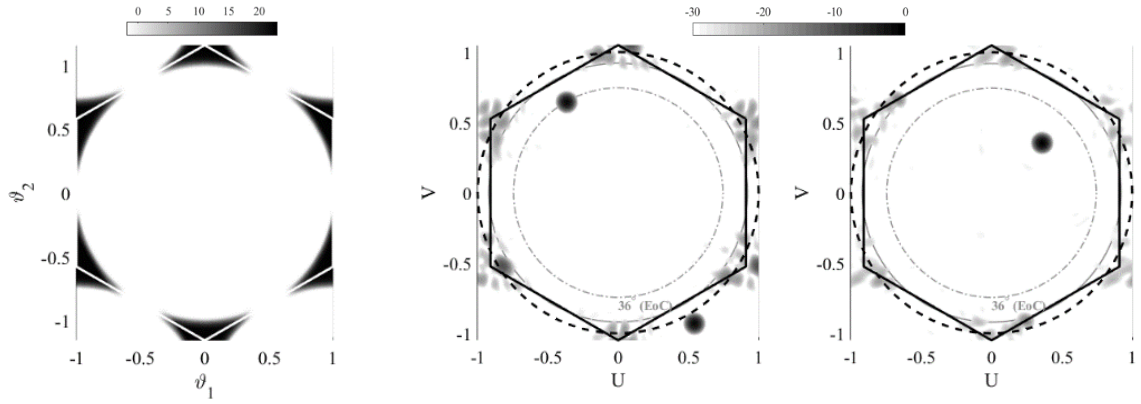

Fig. 7. 11. CV-NS results based on digital filter with stopband corresponding to elevation zero. (a) the revised system frequency response, computed array factor steered at (b) $[\theta, \varphi] = [48°, 120°]$, (c) $[\theta, \varphi] = [30°, 45°]$.

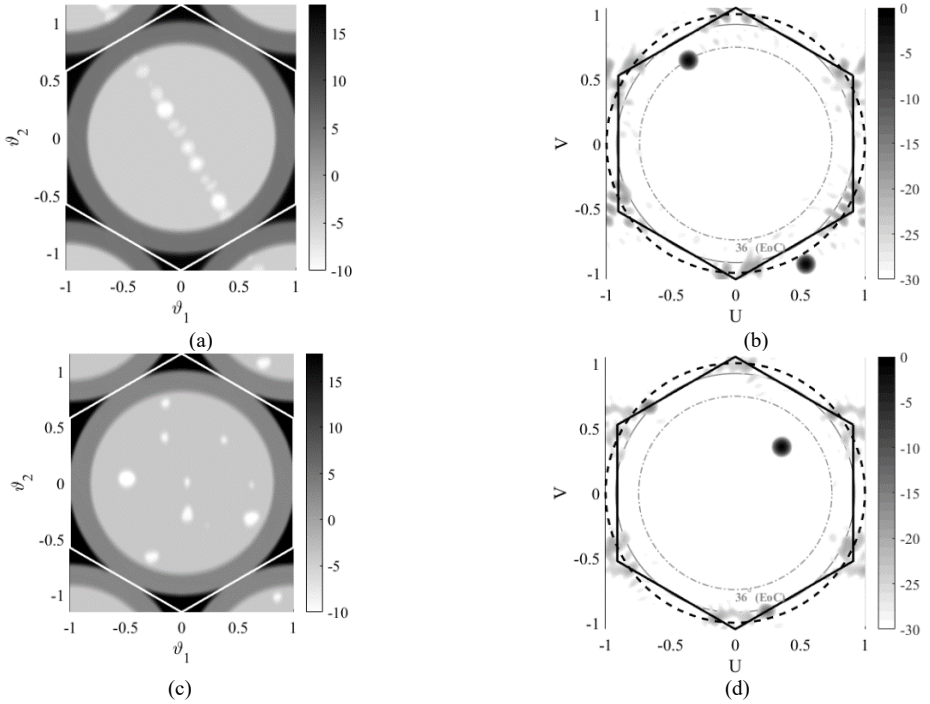

Fig. 7. 12. CV-NS results based on digital filter with filter layout designed by particle swarm optimization. (a) the revised system frequency response, computed array factor steered at (b) $[\theta, \varphi] = [48°, 120°]$, (c) $[\theta, \varphi] = [30°, 45°]$.

TABLE 7.3
GAIN LOSS AND SLL IN FIG. 7.11.

	SLL	Gain loss
Fig. 6.10(b)	9.7 dB	1.73 dB
Fig. 6.10(c)	16.1 dB	1.05 dB

TABLE 7.4
GAIN LOSS AND SLL IN FIG. 7.12.

	SLL	Gain loss
Fig. 6.11(b)	18.6 dB	1.081 dB
Fig. 6.11(c)	16.13 dB	0.837 dB

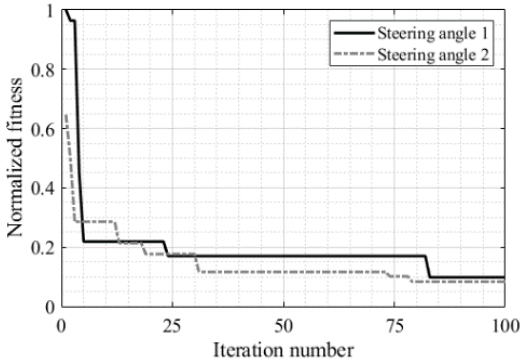

Fig. 7. 13. Fitness versus iteration number.

Chapter 8
Noise shaping for Reflectarray

8.1. Quantization error and signal statistics

The PDA quantization due to pixel frequency response downgrades the RA radiation performance. As the quantization error is generally a function of the original signal, it may yield a harmonic error that behaves differently than a spectrally flat one. Nevertheless, as stated before, the quantization error can theoretically be an independent signal from the original one.

Fig. 8.1(a) shows the PA active elements. The black dots may also be assumed as the center of each RA pixel. The lattice is assumed triangular, the so-called hexagonal, with normalized pitch, ρ, of about $\frac{1}{\sqrt{3}} \approx 0.58$. For these preliminary models, we assumed $3bit$ SUQ. For a fair comparison, the magnitude of the field on the RA aperture is also assumed for the PA. The RA is prime-focused with an *F/D* of 1.4, which yields about 11-12 dB edge-tapering for the case at hand. The decibel array factor and the field spectra for respectively PA and RA are illustrated in Figs. 8.1(b) and 8.1(c). As seen, the SD nature of RA helps to dissolve the QLs in beamspace, while they appear in harmonized form with a considerable peak level, about 19 dB, in the PA array factor.

In contrast to the simple mathematical model assumed in the preceding paragraph, the pixel frequency response is a function of EM wave incidence angle; thereby, the PTC is a function of incidence angle. Besides, the quantization is usually non-uniform for linearly polarized (LP) ones, whereas at least in a specific frequency range, it shows up in an acceptably uniform fashion for circularly polarized ones designed based on variable rotation technique (VRT) [110].

The aperture-coupled patch is schematically illustrated in Fig. 8.2(a). The frequency responses are for hexagonal infinite-periodicity; seven elements on the hexagonal lattice are depicted in Fig. 8.2(b). The full-wave simulation results of phase delay are shown in Fig. 8.2(c) for normal incidence. Pixel_1 to Pixel_8 implies the frequency responses of a pixel due to different delay lines, which are not explicitly shown here for brevity. Such an arrangement of frequency responses leads to PDA non-uniform quantization, specifically at lower and higher extremes of the frequency band of interest, which incurs distortion and limits the antenna bandwidth. This has been shown in the example Fig. 8.3, where the beam is aimed at $[\theta,\ \varphi] = [20°, 60°]$ for an offset-fed aperture in which the feed is rotated 20 degrees along the x-axis in RA coordinate system. As seen, the weighted PDA error spectrum is shifted to the beam position in the error pattern and subsequently shows up in the overall pattern. Note that some quantization distortions happen out of the visible band, which is an advantage of the relatively small pixel used, ρ = 0.42. The distortion manifestation in beamspace is related to the PDA, field magnitude on aperture (feed pattern and position), and the pixel response. In a "soft" PDA, the phase varies gently on aperture and is usually more favorable since it contributes to more antenna bandwidth. One may intuitively expect the distortion shows up at lower (spatial-frequency) bands for acceptably soft PDA; thus, it is more likely to appear inside the visible region. However, that is not precisely correct.

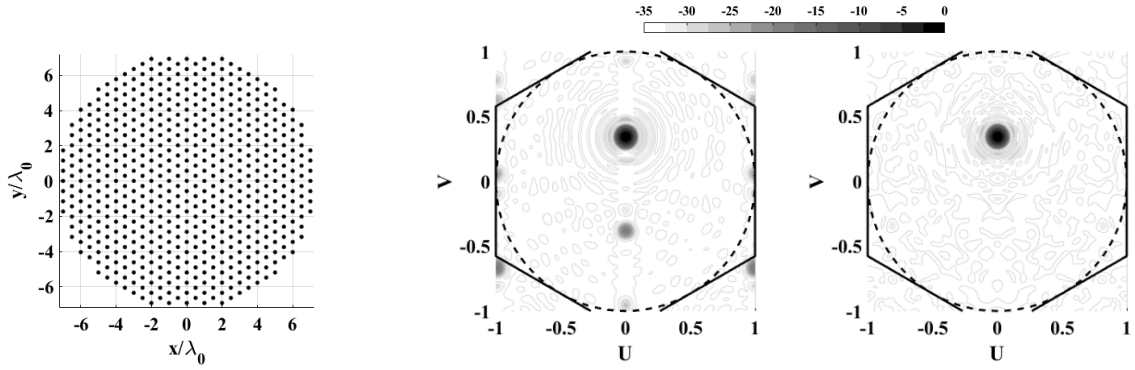

(a) (b) (c)

Fig. 8. 1. Comparison of quantization lobe for phased array and reflectarray. (a) Active elements in lattice assumed, decibel (b) phased array factor, and (c) reflectarray field spectra.

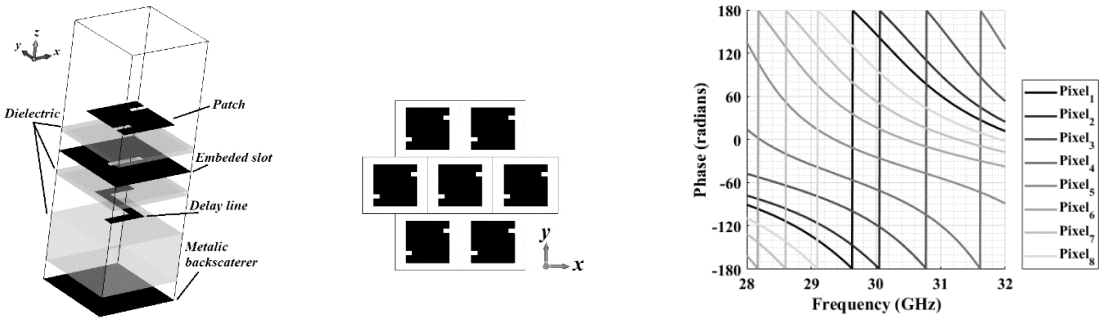

(a) (b) (c)

Fig. 8. 2. Aperture coupled patch unit cell. (a) Exploded visual representation of pixel with periodic boundary condition, (b) seven elements on a hexagonal lattice, and (c) eight pixels frequency responses phase.

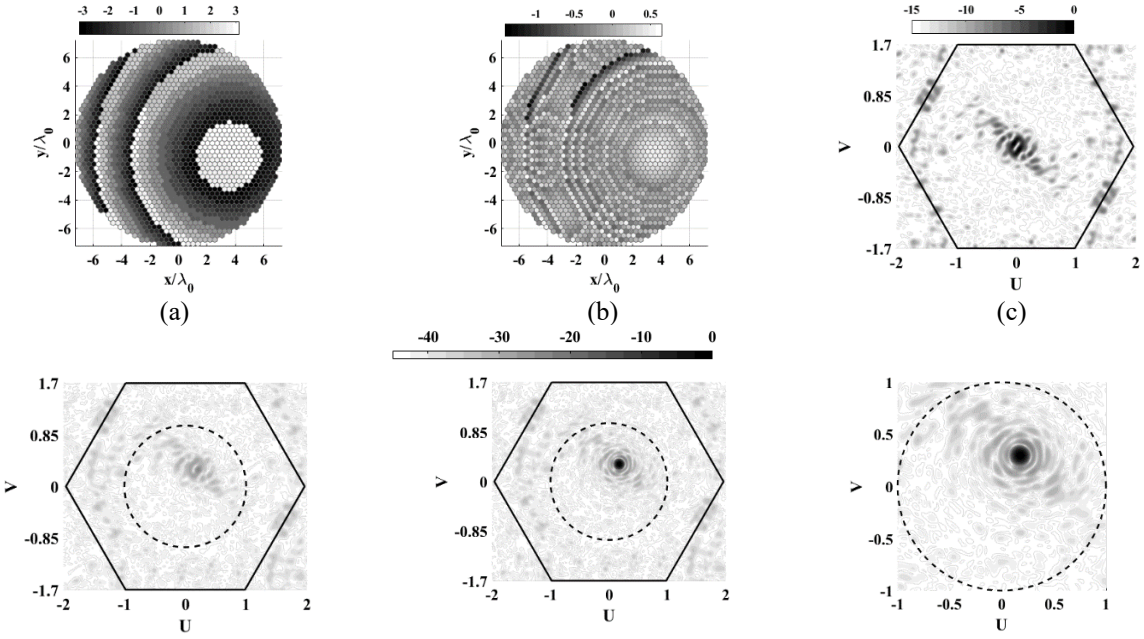

(a) (b) (c)

(d) (e) (f)

Fig. 8. 3. Exemplar reflectarray with unit cell shown in Fig. 8.2. (a) phase delay arrangement, (b) weighted phase delay arrangement error, (c) phase delay arrangement error spectra, (d) error pattern, (e) field spectra on one fundamental period, (f) field spectra on visibility region.

A practical pixel frequency response contributes to non-uniform quantization, at least for LP antenna, and thereby, even in the case of sharp phase variation, a considerable portion of distortion may happen in-band. Besides, it does not directly obey the PDA; instead, the complex exponent of PDA error is weighted by field intensity on the aperture. In this regard, an acceptable and optimal design might be acquired using signal statistics. We define the "weighted histogram," in which the intensity of the electric field weights the replication of the phase.

Therefore, that becomes the task of assigning the optimal reference phase, the reference distance between the defined port and pixel, according to the high phase priority region for maximum fidelity. The PDAs and weighted histograms, with five degrees resolution, at 29 GHz, 30 GHz, and 31GHz are illustrated in Fig. 8.4. Sweeping the frequency, the high priority phase state region travels from about -3.14 radians to -2 radians at 29 GHz to about 1 radian to 2 radians at 31 GHz. Therefore, each frequency point has its phase priority region. Fig. 8.5 shows the PDA error, TC diagram, and field spectra at 30 GHz for two different pixel reference phases. As seen, the TC is a function of the incidence angle; for example, each specific delay line of the pixel yields some close quantization steps associated with different incidence angles. More importantly, the antenna pattern of Case I is much more distorted than that of Case II. That is because the high-priority phase range of 2 to 3 radians, see Fig. 8.4(b), is covered by almost one quantization step for Case I.

The underlying phase range is highly prioritized since it happens in the region beneath the FPC on the aperture surface, where the phase varies gently, see Figs. 8.5(a). Thus, it contributes to low-frequency harmonics, and consequently, some corresponding distortions happen at low spatial frequencies of PDA spectra and subsequently shift to the beam position in the antenna pattern, see Fig. 8.5(c) for Case I. Nevertheless, though signal statistics is a useful method, it might not always be possible to use it conveniently. Besides, it just helps to minimize the damage to the resulting antenna pattern, which in some cases might be considerable.

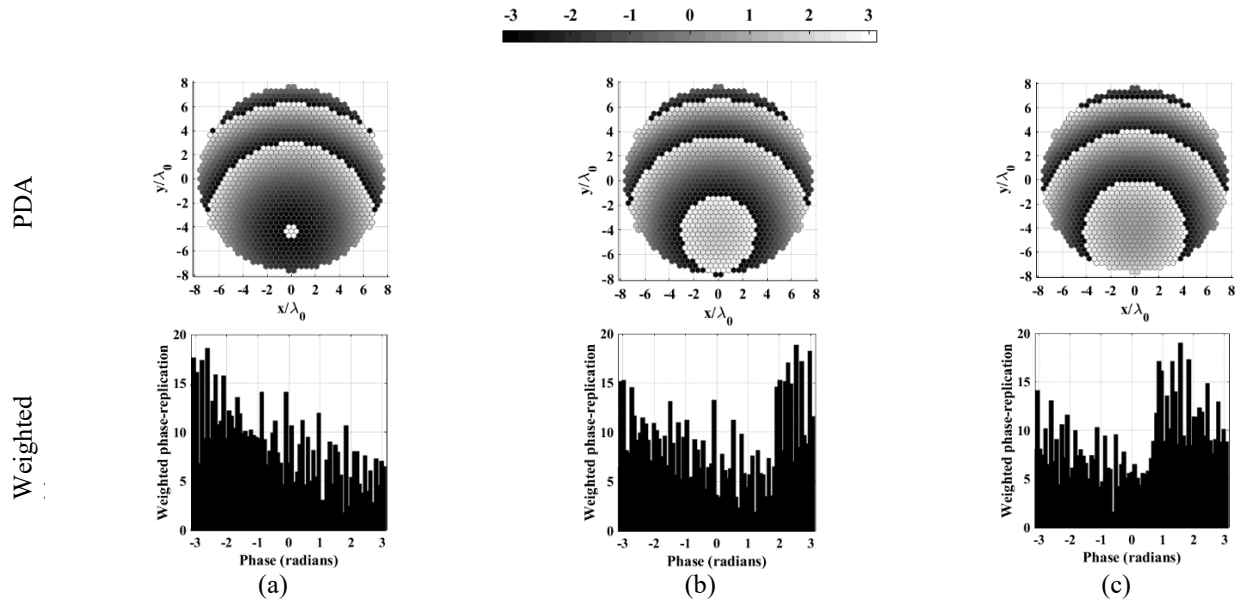

Fig. 8. 4. High-precision phase delay arrangement (PDA) and weighted histogram. (a) 29 GHz, (b) 30 GHz (c) 31 GHz.

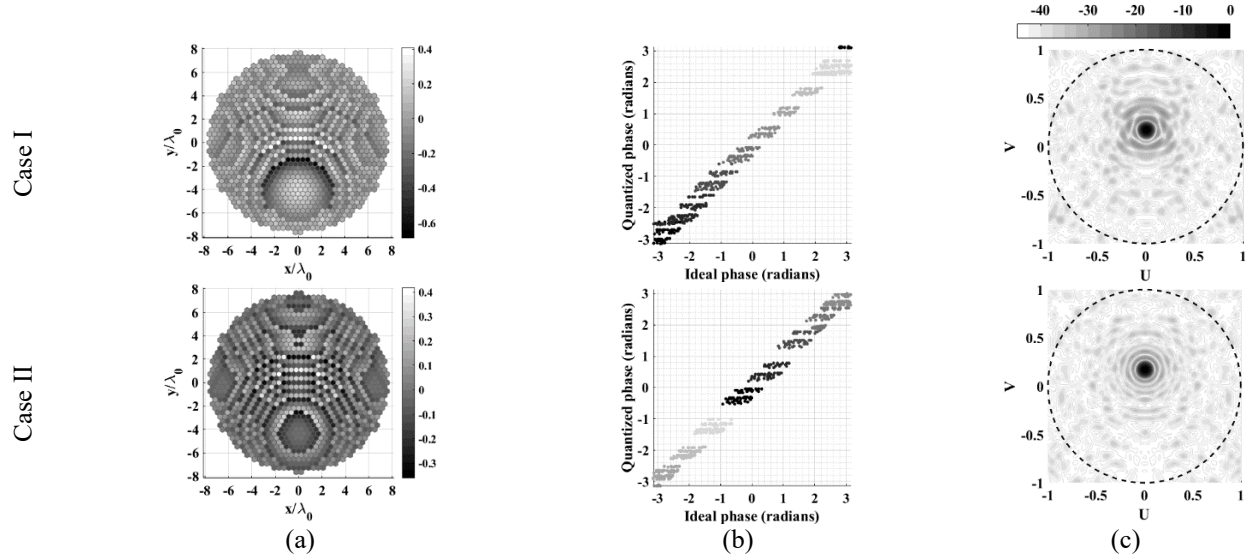

Fig. 8. 5. Two phase delay arrangements errors with different phase references. (a) weighted phase delay arrangements error, (b) transfer characteristics diagram, (c) field spectra at 30 GHz, and the main beam are intended at $[\theta, \varphi]$ = [90°, 20°].

8.2. Noise shaping

Although the space-fed antenna is a naturally SD system, it might still be tempting to check whether dithering can address the distortion in the radiation pattern of the space-fed antenna or not.

For the case at hand, the feed imposes the aperture field. Hence, the design is a phase-only

synthesis, and we use RV-NS to address the quantization error. As stated before, to spectrally shape the PDA error, one should note that the PDA error is steered to the point direction in the reflected field error spectrum; thus, we should shift the targeted frequency band of the filter in reverse with respect to the beam direction. However, as the RCDF is of (conjugate) symmetric frequency response, we could shift it to the beam direction.

Generally speaking, noise shaping is independent of antenna polarization type since it is carried out on the *field spectra*, the same as array-factor in PA antenna. However, the final distortion pattern is a function of polarization that might be considered in the filter layout in the designer's favor. Besides, the field projection on the aperture is a function of polarization also. In other words, following the radiation from the aperture, one can realize that some multiplying trigonometric functions taper the resultant radiation pattern. As an example, for the *x*-polarized incident field, the co-polar component of the E-field is in relation

$$E_{co} \propto \mathbb{E}_{xx} \left(sin^2 \varphi + cos^2 \varphi \, cos \, \theta\right)$$

where $\mathbb{E}_{xx}$ indicates the spectra of the *x*-polarized reflected field due to *x*-polarized impinging one. The term inside the parenthesis generates a sharper roll-off along the *V* direction, which resembles the effect of element and coupling factors in the PA antenna.

The noise shaping approach can theoretically alleviate the distortion due to the large quantization width. However, that might be too good to be true. By way of further explanation, it is irrelevant to and can do nothing for the local periodicity assumption (LPA) issue and may further add to problems by inserting the noise into the PDA. This comes from the approximate nature of discretized space-fed antenna design, which is based on LPA. If the individual pixel values vary sharply, there would be higher-order modes of field close to the boundaries of the pixels due to the discontinuity. If one models the pixel by surface impedance, such evanescent modes can be altered

by reactive lumped elements as they are localized stored energies; that means that the effective value of the surface impedance can severely deviate from the one assumed in an infinite periodicity assumption.

A part of each pixel information exists in, or better to say, depending on, the neighboring pixels, and that is precisely a significant discrepancy between an antenna and, for example, an image from noise shaping perspective. That is to say, ideally, the quantizer should take a look around the current underlying element and attributes a realizable complex value to that, then diffuses the quantization error to the neighboring elements; thereby, during the subsequent wavefront traversal of those neighboring elements, the quantizer assigns realizable values to them as well, which also have mutual impacts on the current underlying sample complex values and that, the amount of initial diffused error would be inaccurate or wrong. We may call this a "wavefront interruption problem" (WIP). Such an issue more or less happens for all antenna types but is not always that malignant. For example, for those space-fed antennas designed by manipulating the surface impedance and those having highly miniaturized elements, WIP might be more problematic.

Regarding the dubious white noise premise, the noise shaper may work less effective or less predictable for coarse quantization. That is more the case with reconfigurable antennas and highly miniaturized pixels with limited phase states. For the traditional design of the MF-RA, the PDA might be intuitively written as

$$\varphi_{\boldsymbol{i}} = \left(\sum_{n=0}^{M-1} \alpha_n\right)^{-1} \sum_{n=0}^{M-1} \alpha_n \left(k\left\|\acute{\boldsymbol{r}}_{d_n,\boldsymbol{i}}\right\|_2 + \xi_{d_n,\boldsymbol{i}}\right) \tag{8.1}$$

where α_n is an arbitrary weighting, the subscript d_n signifies the n*th* design element, *e.g.,* assume $\boldsymbol{f}_{d_n}$ is the vector of the nth feed position associated with the nth beam direction, $\boldsymbol{p}_{d_n}$ In the SF-RA sense, then $\acute{\boldsymbol{r}}_{d_n,\boldsymbol{i}} = \alpha \boldsymbol{L}\boldsymbol{i} - \boldsymbol{f}_{d_n}$, where $\boldsymbol{L}$ is the lattice matrix, α is the weighting factor, and $\boldsymbol{i}$ is an

integer column vector. Besides, $\xi_{d_n,\boldsymbol{i}} = -k\left(\boldsymbol{r_i} \odot \boldsymbol{p}_{d_n}\right)$. Accordingly, one may write

$$\Psi_{\boldsymbol{i}} = \langle \xi_{d_n,i} \rangle_n + k\left[\langle \left\| \acute{\boldsymbol{r}}_{d_n,\boldsymbol{i}} \right\|_2 \rangle_n - \left\| \acute{\boldsymbol{r}}_{s,\boldsymbol{i}} \right\|_2\right] \tag{8.2}$$

where $\acute{\boldsymbol{r}}_{s,\boldsymbol{i}} = \boldsymbol{r_i} - \boldsymbol{f}_s$ and $\boldsymbol{f}_s$ is an arbitrary feed position. Thus, the PDA error spectrum steers based on in the beamspace domain for an MF-RA. Ideally, in mechanical steering, the PDA is frizzed, but the feed displacement manipulates the spatial frequencies; thus, care should be devoted to that in the design of the filter layout. For example, if one designs the filter corresponding to the central beam position, the feed assigned to the extreme beam transfers some "out-of-band" artifacts, amplified by the RV-NS process, to the visible region of the beamspace domain.

This is a challenge for mechanical steering since it asks for a filter with a wide stopband that weakens the noise shaper "pump." Also, as a correction to the point mentioned above, the PDA is not exactly frizzed in mechanical steering since the pixel frequency response is a function of the angle of incidence.

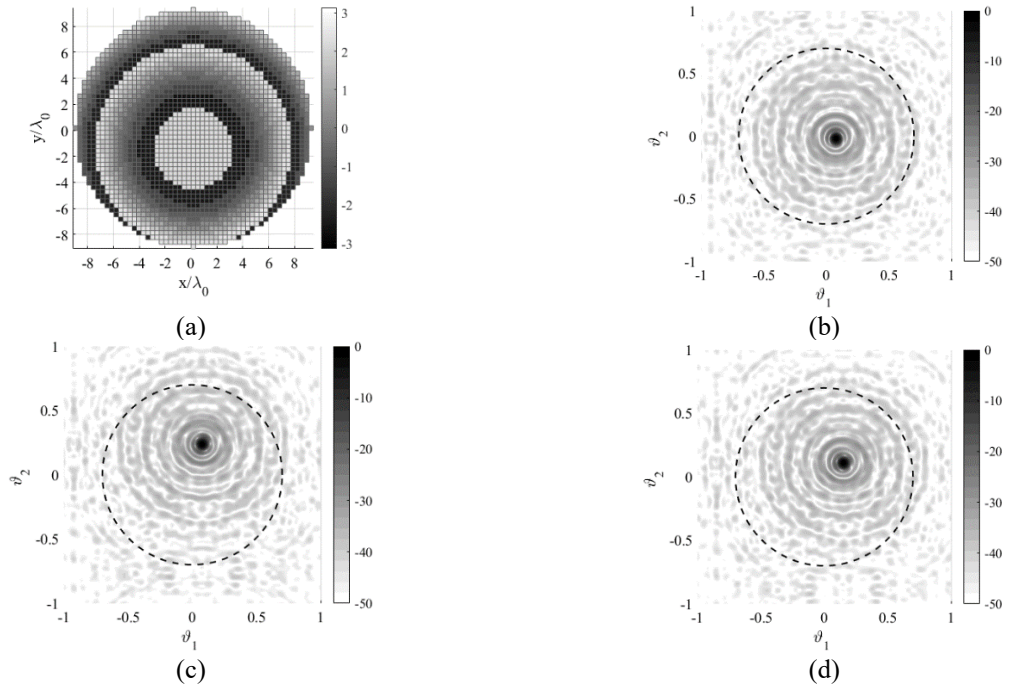

Fig. 8. 6. Results of simple quantization for different steering angles. (a) phase delay arrangement, computed pattern for beam steered at (b) $[\theta, \varphi] = [3.37°, -13°]$, (c) $[\theta, \varphi] = [21.24°, 72.62°]$, (d) $[\theta, \varphi] = [15.42°, 36.26°]$.

It might be beneficial to note that if one uses (8.1) to design the Multi-focal PDA for specific focuses and associated beam directions, the feed positions would not precisely be under control and should be specified for each vector $\boldsymbol{\alpha}$ chosen. This can be problematic for design, e.g., a feed position might not be practical due to the blockage it may cause. The optimization approach introduced in Chapter 7 provides results for predefined feeds' positions and associated beam directions, clarifying its superiority.

In Fig. 8.6(a), the PDA for Solution B in Fig. 7.6 is shown, which is here quantized to 8 "prime steps" generated by a practical pixel, the "prime steps" because the pixel frequency response is a function of angle of incidence. Furthermore, the pixel arrangement has been carried out with respect to the median feed position, rotated 13 degrees along the *x*-axis. The results of computed radiation patterns for three objective beams are illustrated in Figs. 8.6(b)-8.6(d). The quantization incurs in-band distortion, which means an increase in sidelobe level in the visible region.

In Fig. 8.7(a), a revised RCDF is shown designed with respect to the beam at $[\theta, \varphi] = [3.37°, -13°]$. The associated spectrally shaped PDA is plotted in Fig. 8.7(b) and the radiation pattern in Fig. 8.7(c). Compared with Fig. 8.6(b), one can see that the in-band distortion is acceptably pushed out of the visible region.

There is an excessive stopband inherent with the RV-NS method. The effect of this excessive stopband can be seen in Fig. 8.7(c), a small area on the right outside of the visible region. Then, the feed is rotated to steer the beam at $[\theta, \varphi] = [21.24°, 72.62°]$, the computed radiation pattern is shown in Fig. 8.7(d). As seen, the distortion is entered into the visible region; since the filter was not designed for this direction.

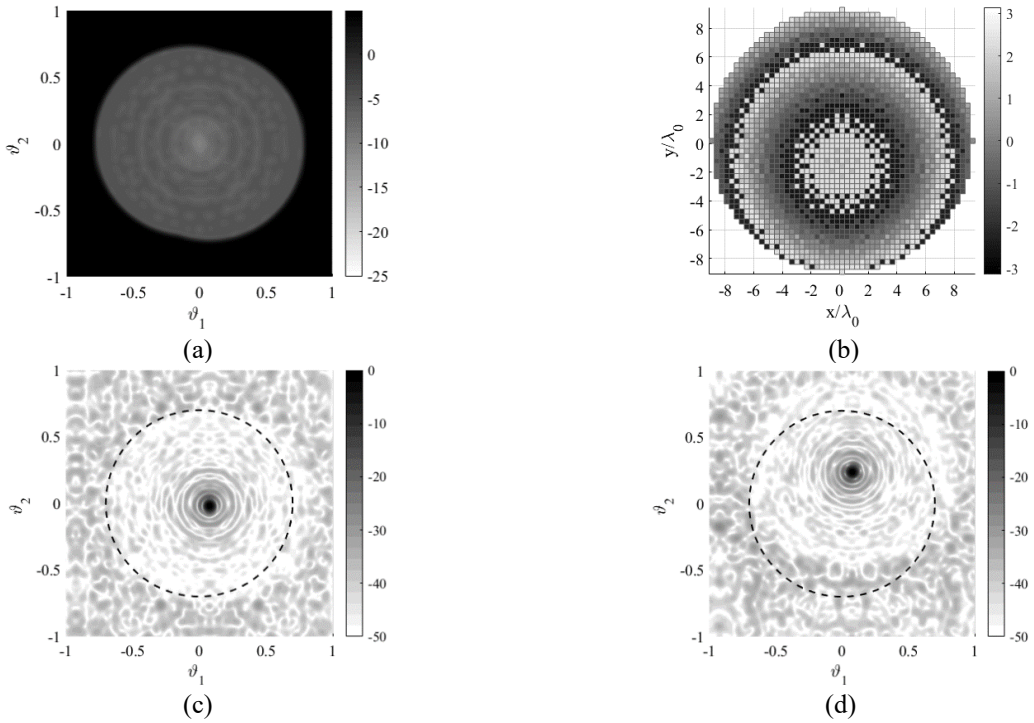

Fig. 8. 7. Results of noise shaping for different steering angles. The filter is designed with respect to one steering angle. (a) The revised digital filter design with respect to one beam only, (b) phase delay arrangement, computed pattern for beam steered at (c) $[\theta, \varphi] = [3.37°, -13°]$, (d) $[\theta, \varphi] = [21.24°, 72.62°]$.

Besides, the distortion is almost not exactly shifted version of Fig. 8.7(c) due to the different pixel responses with respect to the angle of incidence. Thus, as stated before, the filter should be designed with respect to the extreme beams. Moreover, the visible region size is a function of temporal frequency; hence, the bandstop filter should be designed for the highest frequency of antenna bandwidth. Finally, the filter in Fig. 8.7(a) inserts considerable noise into the PDA.

Specifically, it would be worsened if the design considers all extreme beams and the visible boundary is considered for the upper end of the frequency band; since both contribute to a wider bandstop region; in fact, these are the limitations of the approach narrowing the antenna view angle for mechanical steering. As stated before, such a design may lead to a catastrophe in practice since it would be against the LPA design. Thus, one may compromise the bandstop filter depth; to ensure that the inserted noise would be small enough.

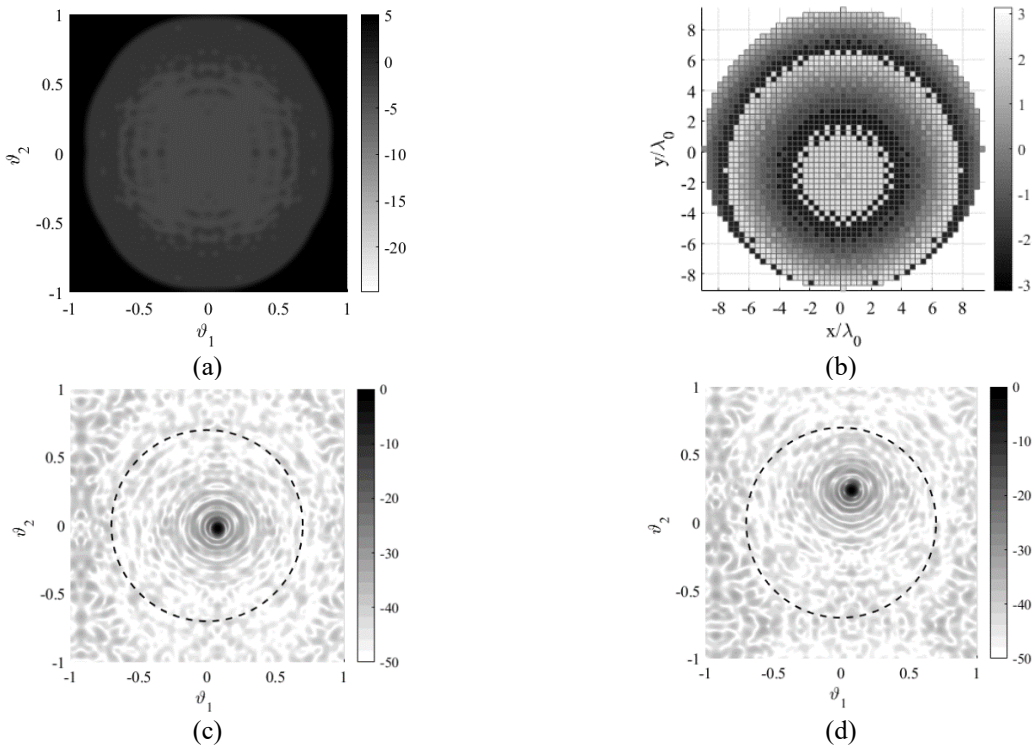

Fig. 8. 8. Results of noise shaping for different steering angles. The filter is designed with respect to extreme beams. (a) Revised digital filter designed with respect to extreme beams, (b) phase delay arrangement, computed pattern for beam steered at (c) $[\theta, \varphi] = [3.37°, -13°]$, (d) $[\theta, \varphi] = [21.24°, 72.62°]$.

In some cases, the distortion may only move from the area of interest inside the visible region; thus, the filter can be designed with a smaller stopband.

In Fig. 8.8(a), the filter is designed for extreme beams (and their image ones with respect to the y-axis). As seen, the filter stopband became wider than that shown in Fig. 8.7(a). Also, the filter layout background has been considered with 5 dB less attenuation. The results of spectrally shaped PDA and two exemplar beams are shown in Figs. 8.8(c)-8.8(d). Note that we could design the filter with more attenuation, leading to a cleaner in-band response, but the design is compromised for LPA. Overall, comparing the results of Fig. 8.6, one can see that still, the method is theoretically capable of cleaning the in-band distortion to some extent.

A smaller pixel size would lead to less in-band distortion since the quantization is wideband, and a smaller portion of the fundamental period becomes visible. Secondly, the noise shaper works more efficiently, and the results would be even better. The other possibility is the lattice used.

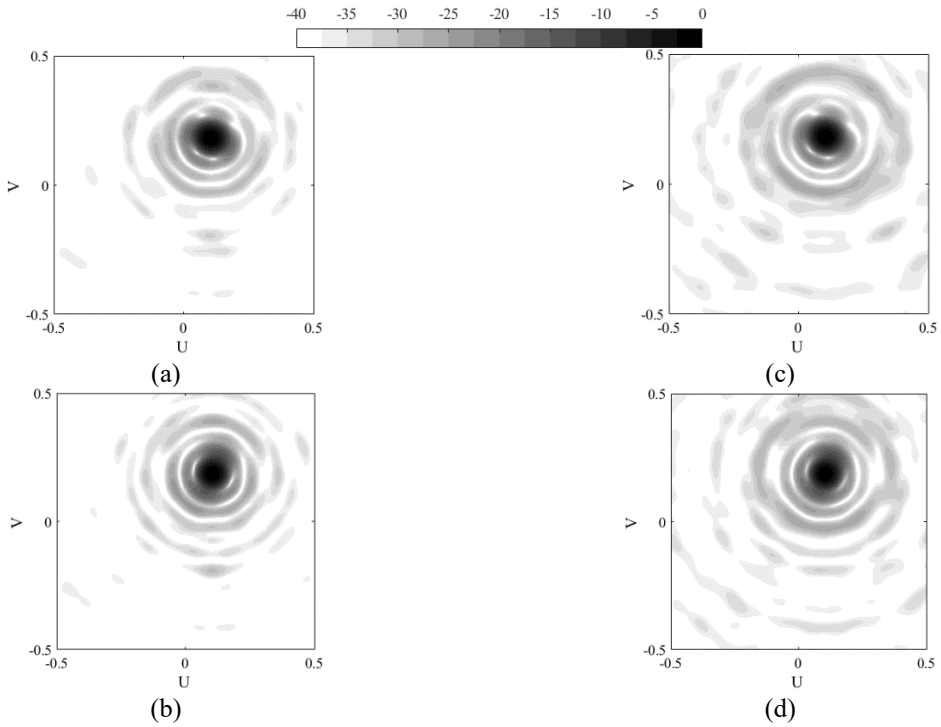

Fig. 8. 9. Computed patterns for noise shaping system. (a) -0.075 (b) +0.075 *F/D* misalignment error. Computed patterns for simple quantization system and (c) -0.075 (d) +0.075 *F/D* misalignment error.

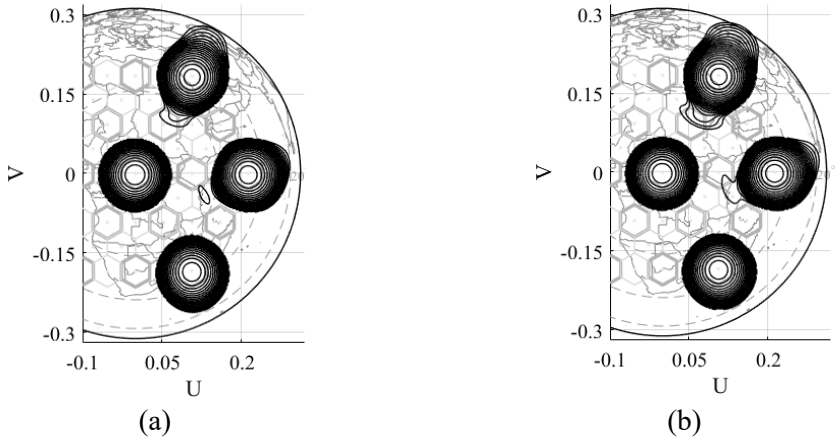

Fig. 8. 10. Computed 20 dB roll-off for four beams. The 20-dB roll-off for (a) noise shaping, (b) simple quantization.

As a general rule, the hexagonal lattice provides a freer spectrum for the same element spacing; thus, noise shaping would be more successful.

8.3. Practical considerations

In practice, there are several types of errors, including PCB material and fabrication errors and feed misalignments in terms of angle and focal distance. Also, the feed horn behavior changes in front of the reflector in terms of feed phase center, impedance matching, and radiation pattern.

Nevertheless, the computation results demonstrate some level of immunities for the spectrally shaped PDA (NS system) in comparison to the conventional design (SQ system). Fig. 8.9 illustrates the beam performance for 1.175 and 1.325 *F/D* (±0.075 misalignment error). It can be seen that the misalignment errors fill up the nulls and increase the sidelobe more for the conventional design than the spectrally shaped one. Also, the spectrally shaped PDA 20 dB roll-of performance in Fig. 8.10 shows slight superiority for the extreme beams of NS.

8.4. Experimental verification

For experimental verification, two RAs are fabricated. The configuration of prototypes is shown in Fig .8.11(a). The prepregs used to laminate the layers are not shown in this figure. The two prototypes are precisely the same except in their delay line layer. An exemplar array of slot and patch layers are shown in Figs. 8.11(b) and 8.11(c), respectively. One prototype is designed based on simple quantization (SQ), whose PDA is shown in Fig. 8.6(a), while the other is based on noise shaping (NS) design in Fig. 8.8(b). The photographs of the two fabricated delay line layers are shown in Fig. 8.11(d) and 8.11(e). In Fig. 8.11(a), the dielectric substrates (1)-(3) are RO5880NS with 1.575 mm, 0.252 mm, and 0.252 mm thick, respectively. All copper cladding is 0.18 microns. Also, all layers are laminated together using prepreg which is RO4450f bondply with a permittivity of 3.52. The pixels frequency responses are simulated for 0-55 degrees of angle of incidences for eight quantization steps realized by manipulating the delay lines. Accordingly, the PDA is quantized with respect to the feed rotation vector of $[R_x, R_y, R_z] = [13°, 0°, 0°]$ and pixels frequency responses at 30 GHz.

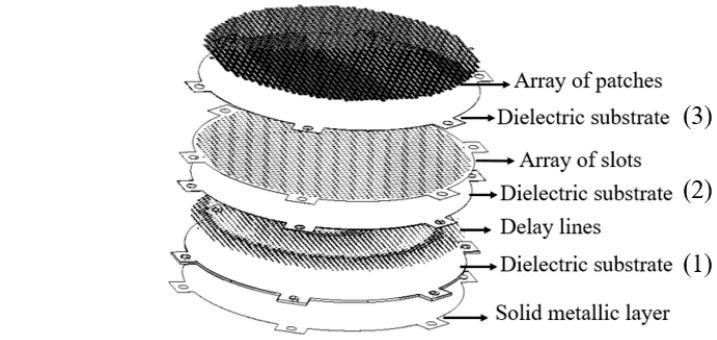

(a)

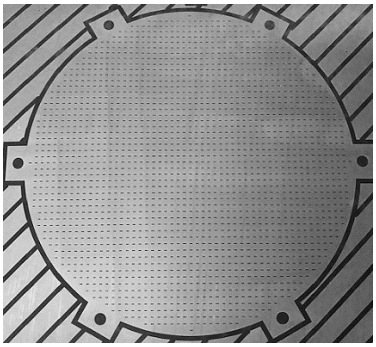

(b)

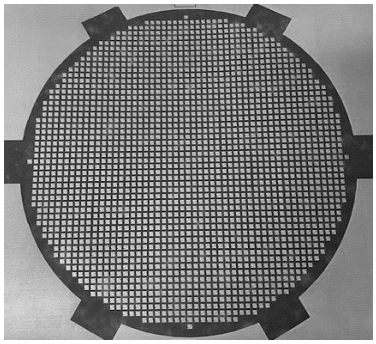

(c)

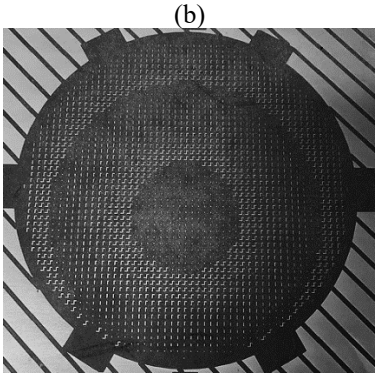

(d)

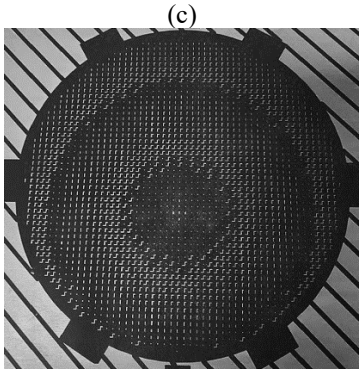

(e)

Fig. 8. 11. Reflectarray different layers and pictures of fabricated layers. (a) Schematic of reflectarray configuration. Photo of fabricated (b) slot layer, (c) patch layer, (d) delay-line layer for simple quantization, and (e) delay-line layer for noise shaping.

The RA diameter is 18.55 cm (18.55λ at 30 GHz). A standard WR-34 pyramidal horn (SAR-1725-34KF-E2) available in our lab is used, which operates in the 22-33 GHz band.

The RA *F/D* is about 1.25, ensuring the edge tapering of 10-11 dB. A photograph of the feed horn in front of the RA is shown in Fig. 8.12(a). The horn aperture is 24mm × 32.9mm and has about 17.8 dBi gain at 30 GHz. The measured radiation pattern of the horn at 30 GHz is shown in Fig. 8.12(b).

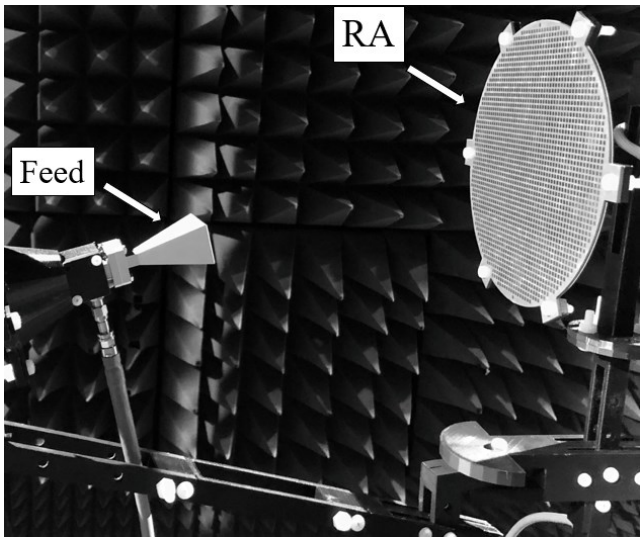

(a)

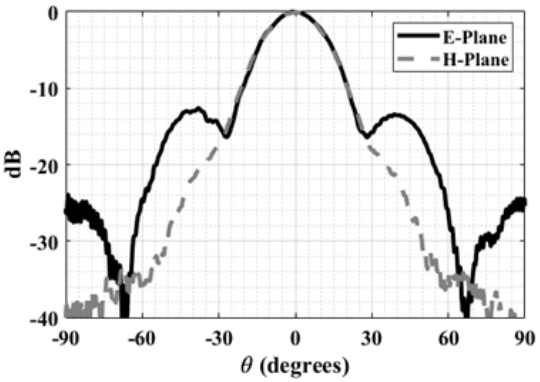

(b)

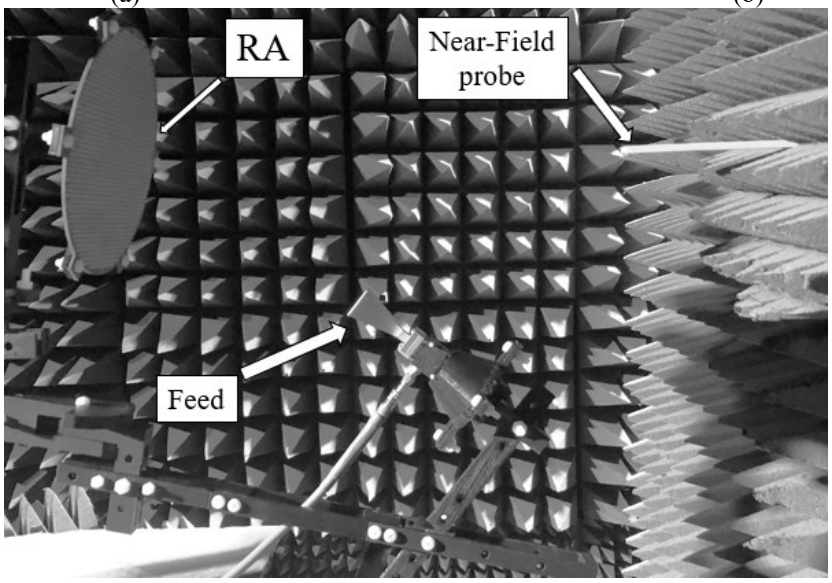

(c)

Fig. 8. 12. Pictures of feed horn and measured radiation pattern. Fabricated reflectarray and measurement setup. (a) Feed horn in front of the reflectarray. (b) Feed horn measured radiation pattern at 30 GHz, and (c) near-field measurement setup.

The experiment is carried out in an anechoic chamber. The antenna system, including the RA, feed, and struts, are placed in front of the NSI planar near-field scanner, see Fig. 8.12(c). The near-field radiation of the antenna was sampled with an open-ended WR28 waveguide probe. The extracted data was subsequently transformed into far-field radiation patterns using Fourier transform to obtain experimental results.

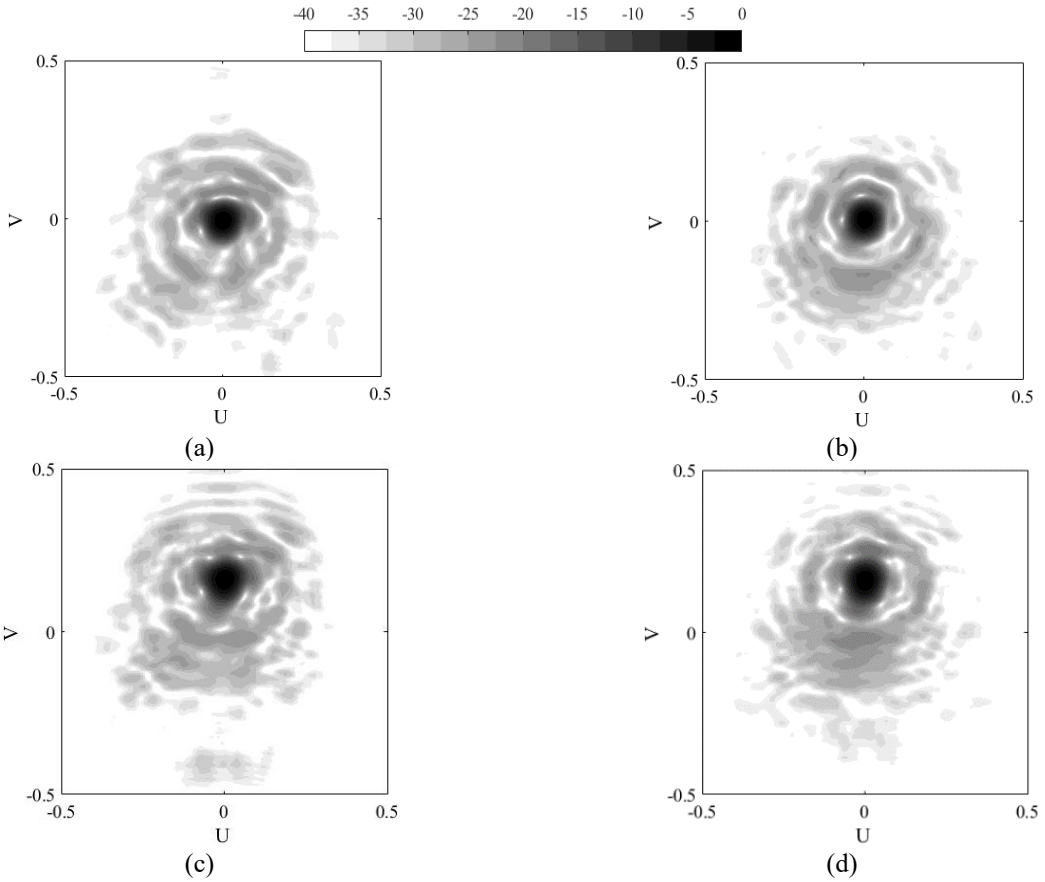

Fig. 8. 13. Measured radiation pattern for feed rotation vectors of $[13°, 0°, 0°]$ at 30 GHz. (a) noise shaping, (b) simple quantization. Measured radiation pattern for feed rotation vectors of $[24.75°,\ 0°,\ 0°]$ at 30 GHz for (c) noise shaping, (d) simple quantization.

The measured patterns at 30 GHz are shown in Fig. 8. 13 for two feed positions. The results represent slightly superior side lobe performance for the NS system. The co- and cross-polarizations of radiation patterns on the E-plane are shown in Fig. 8. 14 for a better comparison at different frequencies.

The co-polar contents are plotted with solid lines, whereas dashed lines show the cross-polarizations. For each antenna, all patterns are normalized with respect to the one shown in Fig. 8.14(a) with a feed rotation vector of $[13°, 0°, 0°]$. This shows the approach's feasibility in side lobe suppression, specifically in the presence of error discussed in Fig. 8.10. It can be seen that the one designed based on noise shaping shows less side lobe level.

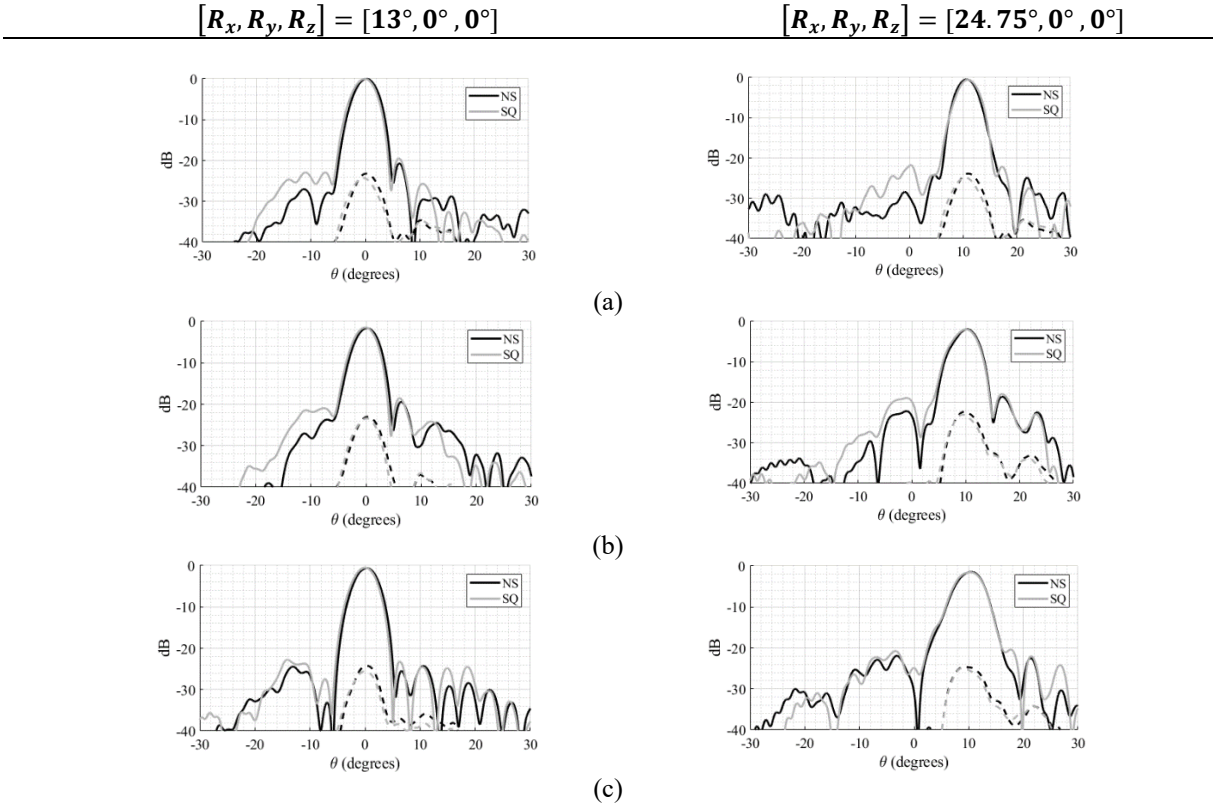

Fig. 8. 14. E-plane measured radiation patterns for feed rotation vectors of [13°, 0°, 0°] and [24.75°, 0°, 0°]. At (a) 30 GHz, (b) 30.5 GHz, and (c) 29.5 GHz. (Solid lines are co-polar and dashed lines for cross-polarizations).

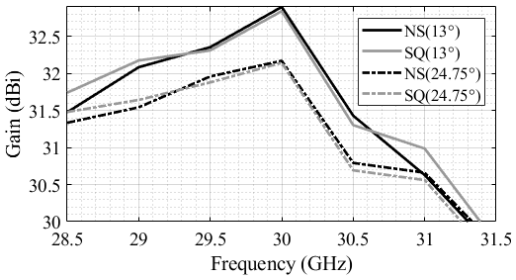

Fig. 8. 15. Measured gain versus frequency.

The cross-polarization level is a function of the field projection on aperture, pixel cross-polarization content, and feed cross-polar content. In the case of offset feeding, the field projection dominates others. The cross-polar contents remain close to 21-24 dB in the direction of the main beams for all cases. The antenna gain (for NS) is measured at about 32.9 dBi at 30 GHz for the feed rotation angle of [13°, 0°, 0°], corresponding to 57.72% aperture efficiency. For the feed

rotation angle of 24.75° the aperture efficiency is about 49.1% (0.7 dB gain scan loss). The measured antenna gains over the frequency are shown in Fig. 8.15. The two antenna works almost the same over the frequency range of 28-32 GHz. The negligible more gain realized by NS might be attributed to its smaller sidelobe level. However, this characteristic does not remain correct for all frequencies. This might be attributed to an increase in phase error due to frequency-dependent pixel response (and feed horn pattern). Note that the noise shaping design is carried out at 30 GHz, and the quantization is with respect to the feed rotation vector of $[13°, 0°, 0°]$. Thus, although the antenna is designed for different feed positions, the quantization is carried out with respect to one feed position associated with one steering angle. In other words, the pixel is sensitive to the incident angle, which changes by changing the feed rotation, and the antenna has superior behavior at one angle. This is somehow an issue for MF-RA design since the PDA quantization is associated with one feed position; thus, the pixel arrangement on the reflective surface needs to be revised by rotating the feed, which is impossible.

The NS prototype beam roll-off performance for some 2D scan angles is shown in Fig. 8.16. The antenna fails to comply with the 20 dB CCI norm for some of the beams measured. In particular, the beams along the V = 0 remain acceptably the same as the one predicted by theory, but the other's performance is downgraded. This can be attributed to the practical pixel sensitivity to the incident angle and misalignment errors. The beam at [U, V] = [0.1, 0.18] has about 1.2 dB and 1.4 gain scan loss with respect to that at the center for NS and SQ, respectively. Such a gain scan loss might be acceptable for many applications; however, the roll-off for the extreme beams does not comply with the CCI norms. Nevertheless, as predicted by theory, the NS performance is slightly superior to SQ, specifically for extreme beams. It should also be pointed out that we have used a resonant type element, which has a narrow bandwidth and is sensitive to the incident angle,

which clarifies the narrowband behavior of the antenna in Fig. 8.15 and the inferior efficiency for extreme beams in Fig. 8.16. If a larger *F/D* is used, extreme beams can be ameliorated since the quadratic phase shift approaches the linear progressive phase, as stated in Section II, and the EM incident angle decreases, promoting pixel performance. Also, pixels whose frequency response is less sensitive to the angle of incidence can promote that.

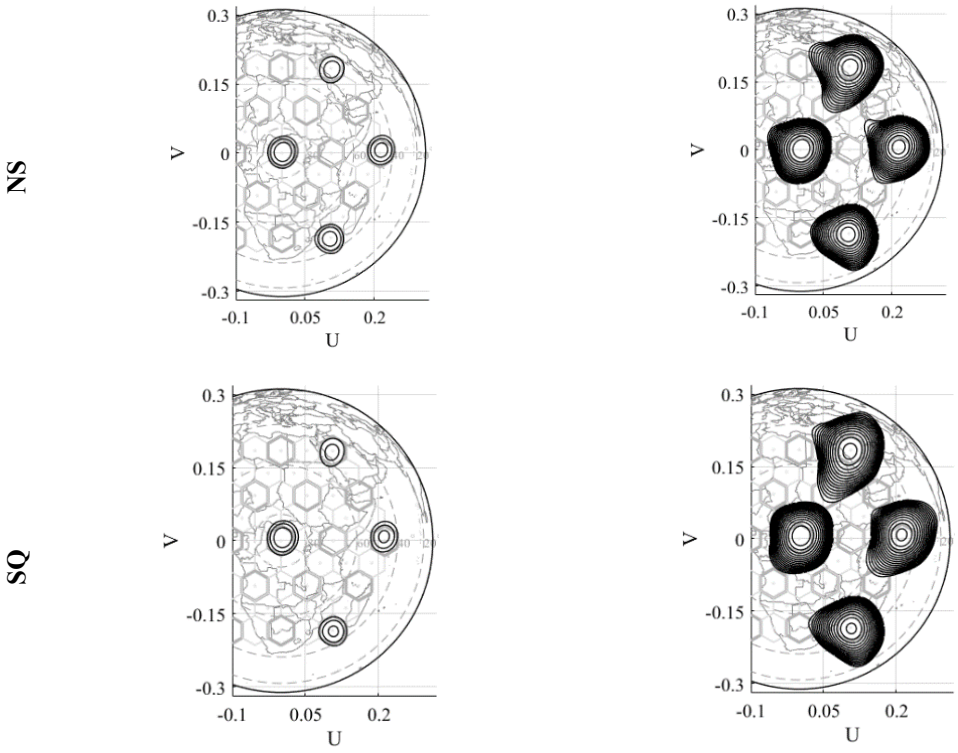

Fig. 8. 16. Measured four different beams. (a) 4 dB spot, (b) 20 dB roll-off.

Chapter 9
Conclusions and future works

9.1. Conclusions

There are two methods to deal with the quantized beamforming weights. The former method directly synthesizes the pattern based on available quantized weights. In principle, it requires a discrete search engine. In this regard, the metaheuristic techniques do not offer an exact solution; thus, if they converge, an acceptable solution might be provided. Thus, they are computationally expensive and time-consuming, with no repeatable solutions. Moreover, for large 2D/3D arrays, because of high dimensional parameter space, the algorithm may fail to converge.

The latter approach synthesizes the pattern for a high-precision system and subsequently addresses the quantization issue as a post-synthesis procedure. One post-synthesis approach is deliberately inserting a portion of noise before the quantization process to break up the error coherency. Such a method is called dithering. The dithering can make the error *benign,* ideally independent of the original signal. However, it has been shown in this thesis that the random dither is a sub-optimal solution in terms of antenna gain loss and quantization lobe suppression. Furthermore, it does not generally provide a repeatable beam. On this account, the second type of dither, the spectrally shaped one, is more attractive as it sounds more optimal from many perspectives. The method is called noise shaping. The advantage of noise shaping as a post-synthesis method lets the designer choose any desired method for syntheses, such as fast analytical ones (like the Fourier synthesis method), point search, or population-based algorithms. Also, noise shaping is a non-iterative method; thus, it is computationally cheap, and its response is unique and repeatable since only one solution is associated with a specific filter design. Those exceptional

properties make the approach more attractive than dithering, in which its solution is not repeatable and suboptimal in terms of quantization lobe suppression and gain loss.

In this thesis, noise shaping is used to address the distortion due to the quantization in analog, digital and hybrid beamforming of square and hexagonal lattices. The effectiveness of the approach seems quite promising. It is observed that successfulness is a function of several subjective factors, in which the key points are the number of available quantization states, the minimum-phase system, filter layout design related to the region of interest in the beamspace domain, and of course, the array pitch. The method can compensate for some portions of antenna gain loss due to the quantization, in contrast to the white noise process that further decreases the antenna gain.

In particular, the noise shaping approach and design of filters for several different examples and scenarios have been exhaustively investigated. It has been shown that although the classic hexagonal lattice provides a very small invisible region in comparison to the classic square, the method can still push the distortion to the invisible region. However, it has been witnessed that the antenna has received relatively more gain degradation than a classic square lattice, which is particularly challenging for phase-only synthesis as the invisible region is not reachable for most steering angles. However, the method used in phase-only synthesis can “see” a freer spectrum for the hexagonal one than its square counterpart for the same array pitch size. Also, it has been shown that noise shaping is superior to the randomization-based (dithering) method in null steering. At the same time, the dithering approaches are ineffective for null restoration. The noise shaper was exploited to excavate the distortion in those regions of beamspace where nulls are embedded. Therefore, the array factor nulls can be preserved. Moreover, the noise shaper has been used with two strategies for those cases with large element spacing. One was based on spaced notches filter

design which spans the quantization lobes on the beamspace domain and yields negligible antenna gain loss. The second was based on removing the distortion from the region of interest. A brute-force search has been used to minimize the side lobe level and gain loss for the optimal filter design. Also, it has been shown that the noise shaper can revise the distorted shaped-beam.

Contiguous sub-array overlapping is investigated for linear and planar array optimal design with respect to antenna view angle. It is shown that an optimal design of a spatially oversampled array yields a wide view angle with a smaller number of elements. The structures are implemented in two and three layers with different array pitches. The Full-wave simulations are acceptably compatible with design computations.

A novel method is proposed for spectrally shaping the beamforming weights quantization error at the sub-array layer in which the in-band distortion is intended to move into the position where the sub-array factor has high attenuation. To do that, the sub-array factor or the composite sub-array factor is tiled by the periodicity of the ultimate-layer array factor. Then the digital filter layout is designed based on the superposition of all tiles overlapping with the visible region of the sub-array factor, and the ultimate layer array factor is spectrally shaped to minimize the number of bits quantifying the beamforming weights. The method is investigated for analog, digital, and hybrid array beamforming with multi-layer overlapped sub-array systems of different sizes and shapes. In all cases, its performance is promising and potent in alleviating the overall array factor distortion.

Moreover, Reflectarray was designed using the sequential approach, where the radiation pattern was synthesized for a high-precision system. The noise-shaping approach has addressed the phase quantization arrangement of the practical pixel response. It is found that although the element spacing can be significantly reduced in a space-fed antenna in comparison to the phased array, the

local periodicity assumption and feed rotation angle limit the method's performance. In particular, the local periodicity assumption limits the depth of the digital filter stopband, and the beam steering, by feed rotation, increases the in-band region. Both of which downgrade the noise shaper performance. Besides, it is shown that a space-fed antenna is naturally a subtractive dither system that somehow mitigates the quantization lobe level by itself. Nevertheless, the method is still feasible for accurate design and fabrication, specifically at higher frequencies when the quantization noise increases due to the limited number of phase steps. The measurements showed slight promotion in side lobe level and beam roll-off. A resonant type element based on a delay line has been used, which might be more suitable for the case at hand since inserting noise might be more detrimental for sub-wavelength unit cells. However, the pixel used downgraded the antenna view angle due to the pixel's sensitivity to the incident angle, which might be promoted by a larger F/D or a pixel less sensitive to the incidence angle.

9. 2. Future works

Hybrid beamforming based on multi-layer sub-array overlapping can be further investigated for the planar array. Thus, there would be three objectives: i) to study and design analog beamforming, (ii) to develop a digital beamforming, and (iii) to integrate both analog and digital sections to come up with a novel hybrid beamforming.

Regarding the analog section, the optimal design and shape of a sub-array with enough elements should be chosen, and the associated feeding network should be realized. The shape of the sub-array determines the fashion of the array factor's fundamental period, and the overlapping is important for grating lobe cancellation. The greater the number of sub-array elements, the more transmission zeros for sub-array beamforming, which facilitates the beam steering at the sub-array layer since the sub-array factor can be better shaped. However, a sizeable physical sub-array

decreases the period of the reciprocal domain[7], which increases the number of grating lobes. To facilitate the cancelation of grating lobes, a more significant number of elements should be overlapped, complicating the feeding network. Most articles published in the literature theoretically investigated this array configuration's features without clarifying the feeding network implementation. Therefore, the method used in this thesis might be expanded to 2D planar array to realize the large and complicated sub-array overlapping system[8].

In regard to the digital section, the method based on noise shaping can decrease the gate delay, as it is the main issue of digital beamforming. It is specifically important for high data rates and multiple beams. Also, the choice of digital platforms and configurations significantly decreases the delay and power consumption.

[7] The period of sub-array factor in comparison to fundamental period of the overall array factor.
[8] Also, one should note that the complicated feeding network incurs other problems such as noise figure deterioration which should be addressed for a practical system by using suitable LNAs.

Bibliography

[1] J. K. Hunton and A. G. Ryals, "Microwave variable attenuators and modulators using PIN diodes," *IEEE Trans. Microw. Theory Tech.,* vol. MTT-10, pp. 262–273, 1962.

[2] B.-W. Min and G. M. Rebeiz, "A 10-50-GHz CMOS distributed step attenuator with low loss and low phase imbalance," *IEEE J. Solid-State Circuits,* vol. 42, no. 11, pp. 2547–2554, 2007.

[3] H. Dogan, R. G. Meyer, and A. M. Niknejad*,* "Analysis and design of RF CMOS attenuators," *IEEE J. Solid-State Circuits,* vol. 43, pp. 2269–2283, 2008.

[4] B. H. Ku and S. Hong, "6-bit CMOS digital attenuators with low phase variations for X-Band phased-array systems," *IEEE Trans. Microw. Theory Tech*., vol. 58, pp. 1651–1664, 2010.

[5] K. Park, S. Lee, and S. Jeon, "A new compact CMOS distributed digital attenuator," *IEEE Trans. Microw. Theory Tech.,* vol. 68, pp. 4631–4641, 2020.

[6] A. Natarajan et al., "A fully-integrated 16-element phased-array receiver in SiGe BiCMOS for 60-GHz communications," *IEEE J. Solid-State Circuits,* vol. 46, pp. 1059–1075, May 2011.

[7] H. Jeon and K. W. Kobayashi*, "* A High Linearity +44.5-dBm IP3 C-Band 6-Bit Digital Phase Shifter Using SOI Technology for Phased Array Applications*," IEEE Microwave and Wireless Components Lets.,* vol. 29, 2019.

[8] B. C. Brock, "The Application of Taylor weighting, digital phase shifters, and digital attenuators to phased-array antennas," Sandia National Laboratories, Albuquerque, 2008.

[9] B. Ning, Z. Chen, X. Wang, and W. Mei, "Codebook-Based Hybrid Beamforming Design for MISOME Wiretap Channel," *IEEE Trans. on Antenna and Propag.,* vol. 8*,* 2019.

[10] M. Weber, J. Cho, J. Flavin, J. Herd, and M. Vai, *"*Multi-Function phased array radar for U.S. civil-sector surveillance needs*,"* 32nd Conference on radar meteorology, 2005.

[11] M. N. Kulkarni, A. Ghosh, and J. G. Andrews, "A comparison of MIMO techniques in downlink millimeter wave cellular networks with hybrid beamforming, " *IEEE Trans. on Antenna and Propag*., vol. 64, 2016.

[12] C. T. Lin and H. Ly, "Sidelobe reduction through subarray overlapping for wideband arrays," *Proceed. of the IEEE Radar Conf., 2001.*

[13] S. Han, C-Lin I, Z Xu, and S Wangn "Reference Signals design for hybrid analog and digital beamforming," *IEEE comm. Lett.*, vol. 18, 2014.

[14] A. Abbaspour-Tamijani and K. Sarabandi, "An affordable millimeter-wave beam-steerable antenna using interleaved planar subarrays*,*" *IEEE Trans. Antennas Propag.*, Vol. 51, pp. 2193–2203, 2003.

[15] J. S. Lim and A. V. Oppenheim, editor. *Advanced topics in signal processing*. Signal processing series, New Jersey: Prentice-Hall, 1988.

[16] S. Sheikh and A. Kishk, "Multifocal reflectarray with optimized aperture phase," *IEEE Antennas Propag. Soc. Int. Symp*. 2020.

[17] A. B. Sripad and D. L. Snyder, "A necessary and sufficient condition for quantization errors to be uniform and white," *IEEE Trans. Acoustics, Speech and Signal Process.*, vol. 25, pp. 442-448, October 1977.

[18] A. V. Oppenheim, R.W. Schafer, and J. R. Buck, *Discrete-Time Signal Processing*, New Jersey: Prentice-Hall, 1999.

[19] R. A.Wannamaker, S. P. Lipshitz, and J. Vanderkooy, "Quantization and dither: A theoretical survey," *J. of the Audio Engin. Soci.*, vol. 40, pp. 355-375, May 1992.

[20] L. Schuchman, "Dither signals and their effect on quantization noise," *IEEE Trans. Communication Technology*, pp. 162-165, December 1964.

[21] B. Widrow and I. Kollar, *Quantization Noise: Roundoff Error in Digital Computation, Signal Processing, Control, and Communications*, New York: Cambridge University Press, 2008.

[22] M.R. Schroeder, "Images from computers," *IEEE Spectrum*, vol. 6, pp. 66-78, March 1969.

[23] C. J. Miller, "Minimizing the effects of phase quantization errors in an electronically scanned array," in *Symp. on Electronically Scanned Phased Arrays and Applications*, 1964.

[24] F. A. Aronov, "New method of phasing for phased array using digital phase shifters," in *Radio Engin. and Electronic Physics,* vol. 11, pp.1035–1040, 1966.

[25] W. F. Hayes, "*Digital Simulation*," US Patent #3,643,075, February 15, 1972.

[26] M. Smith and Y. Guo, "A comparison of methods for randomizing phase quantization errors in phased arrays,*" IEEE Trans. Antennas Propag.*, vol. 31, pp. 821–828, 1983.

[27] *R.C. Hansen and G. G. Charlton*, "Subarray quantization lobe decollimation," *in IEEE Trans. Antennas Propag.*, vol. 47, pp. 1237–1239, 1999.

[28] W. Jiang, Y. Guo, T. Liu, W. Shen, Wei Cao, "Comparison of random phasing methods for reducing beam pointing errors in phased array*," IEEE Trans. Antennas Propag.*, vol. 51, pp. 782–787, 2003.

[29] W. P. M. N. Keizer, "Low sidelobe phased array pattern synthesis with compensation for errors due to quantized tapering," *IEEE Trans. Antennas Propag.*, vol. 59, pp. 4520–4524, 2011.

[30] C. Hemmi, M. H. McCullough, B. L. Ball, "Two-Dimensional Quantization Method for Phased-Array Scanning," in *Antennas and Propag. Magazine IEEE*, vol. 56, pp. 43-59, 2014.

[31] Y. Zhang, H. Sun, and Q. H. Liu, "Integer linear programming roundoff method for arbitrary planar phased-array scanning," *IEEE Trans. Antennas Propag.*, vol. 67, pp. 3040–3047, 2019.

[32] R. J. Mailloux, *Phased array antenna handbook*, Artech House, Inc: Norwood, 2005.

[33] H. A. Spang and P. M. Schultheiss, "Reduction of quantizing noise by use of feedback," in *IRE Trans. on Communications Systems*, vol. 10, pp.373-380, 1962.

[34] R.W. Floyd and L. Steinberg, "An adaptive algorithm for spatial greyscale," *Proceeding of the S.I.D*, Vol. 17, pp.75-77, 1976.

[35] P. W. Wong, "Adaptive error diffusion and its application in multiresolution rendering," *IEEE Trans. Image Proc.*, vol. 5, pp. 1184-1196, 1996.

[36] T. C. Chang and J. P. Allebach, "Quantization of accumulated diffused errors in error diffusion," *IEEE Trans. Image Proc.*, vol. 14, pp. 1960-1976, 2005.

[37] Y. H. Fung and Y. H. Chan, "Optimizing the error diffusion filter for blue noise halftoning with multiscale error diffusion," *IEEE Trans. on Image Proc.*, vol. 22, pp. 413-417, 2012.

[38] S. Pavan, R. Schreier, and G. Themes, *Understanding delta-sigma data converters.* Wiley, New Jersey, 2017.

[39] R. Paknys, Applied Frequency-Domain Electromagnetics. New Jersey: John Wiley & Sons, 2016.

[40] T. N. Ross, G Cormiert, K Hettak, and J. S. Wight, "High-power X-band GaN switched-filter phase shifter," *2014 IEEE MTT-S International Microwave Symposium (IMS2014).*

[41] *Analog Device,* GaAs MMIC 5-bit digital phase shifter, 15 - 18.5 GHz, HMC644ALC5, 2016. [Online]. available: https://www.analog.com/media/en/technical-documentation/data-sheets/hmc644alc5.pdf.

[42] *Macom,* Digital phase shifter 4-bit, 8.0 - 12.0 GHz, MAPS-010146, 2002. [Online]. Available: https://cdn.macom.com/datasheets/MAPS-010146.pdf

[43] *Analog Device,* GaAs MMIC *0.5dB LSB GaAs MMIC 6-bit digital attenuator, DC - 13 GHz*, HMC424LP3, 2016. [Online]. available: https://www.analog.com/media/en/technical-documentation/data-sheets/hmc424lp3.pdf.

[44] R. Valkonen, "Compact 28-GHz phased array antenna for 5G access," *IEEE/MTT-S International Microwave Symposium*, 2018.

[45] A. H. Aljuhani, *et al*. "*A Scalable Dual-Polarized 256-Element Ku-Band Phased-Array SATCOM Receiver with ±70° Beam Scanning," IEEE/MTT-S International Microwave Symposium*, 2018.

[46] A. K. Bhattacharyya, "Floquet modal based analysis of overlapped and interlaced subarrays," *IEEE Trans. on Antennas and Propagation, vol. 60, pp. 1814-1820, April 2012.*

[47] D. Petrolati, P. Angeletti, and G. Toso, "A Lossless Beam-Forming Network for Linear Arrays Based on Overlapped Sub-Arrays," *IEEE Trans. on Antennas and Propagation, vol. 62, pp. 1769-1778, 2014.*

[48] C. A. Balanis, Antenna Theory. Hoboken, NJ, USA: Wiley, 4th ed., 2016.

[49] "IEEE standard for definitions of terms for antennas," IEEE Std 145-2013 (Revision of IEEE Std 145-1993), pp. 1–50, 2014. DOI: 10.1109/IEEESTD.2014.6758443.

[50] E. Carrasco, M. Barba, J. A. Encinar, "Reflectarray element based on aperture-coupled patches with slots and lines of variable length," *IEEE Trans. Antennas Propag.*, vol. 55, pp. 820-825, March. 2007.

[51] [E. Carrasco, J. A. Encinar, M. Barba, "Bandwidth Improvement in Large Reflectarrays by Using True-Time Delay," in *IEEE Trans. Antennas Propag.*, vol. 9, pp. 1139–1142, Nov. 2010.

[52] P. Nayeri, F. Yang, A. Elsherbeni, "Broadband reflectarray antennas using double-layer subwavelength patch elements," in *IEEE Trans. Antennas Propag.*, vol. 9, pp. 1139–1142, Nov. 2010.

[53] S. Sheikh and A. Kishk, "Dual polarization reflectarray antenna based on interdigitated surface," in *IEEE Antennas Propag. Soc. Int. Symp*.2020.

[54] S. Sheikh, "Miniaturized-element frequency selective surface based on the transparent element to specific polarization," in *IEEE. AWPL*, vol. 15, pp. 1661–1664, 2016.

[55] J. A. Encinar et al., "Dual-polarization dual-coverage reflectarray for space applications," in *IEEE Trans. Antennas Propag.*, vol. 54, pp. 2827–2837, Oct. 2006.

[56] M. M. Tahseen and A. Kishk, "Bandwidth enhancement in Ka-Band circularly polarized reflectarray using stacked cross-bowtie elements," in *17th International Symposium on Antenna Technology and Applied Electromagnetics* (*ANTEM*), 2016.

[57] D M-D-Rioja, E Martinez-De-Rioja, et al., "Reflectarray to Generate Four Adjacent Beams per Feed for Multispot Satellite Antennas," *IEEE Transactions on Antennas and Propagation*, vol. 67, Issue: 2, Feb. 2019.

[58] E Martinez-de-Rioja, D Martinez-de-Rioja, *et al*., "Advanced Multibeam Antenna Configurations Based on Reflectarrays: Providing multispot coverage with a smaller number of apertures for satellite communications in the K and Ka bands," *IEEE Antennas and Propagation Magazine*, vol: 61, Issue: 5, Oct. 2019.

[59] D.M. Pozar, S. D. Targonski, and R. Pokuls, "A shaped beam microstrip patch reflectarray," in *IEEE Trans. Antennas Propag.*, vol. 47, pp. 1167–1173, Jul. 1999.

[60] L. Liang and S. V. Hum, "Design of UWB reflectarray as an impedance surface using Bessel filter," in *IEEE Trans. Antennas Propag.*, vol. 64, pp. 4242–4255, 2016.

[61] H. Yang, F. Yang, S. Xu, M. Li, X, Cao, and J. Gao, "A 1-Bit multipolarization reflectarray element for reconfigurable large-aperture antennas," in *IEEE Antennas and Wireless Propagation Letters*, vol. 16, pp. 581–584, 2016.

[62] R. Pereira, R. Gillard, R. Sauleau, P. Potier, T. Dousset and X. Delestre, "Dual linearly-polarized unit-cells with nearly 2-bit resolution for reflectarray applications in X-band," *IEEE Trans. Antennas Propag.*, vol. 60, pp. 6042–6048, 2012.

[63] D. Berry, R. Malech, and W. Kennedy. "The Reflectarray Antenna," *IEEE Trans. Antennas Propag.,* vol. 11, No. 6, 645-651, June 1963.

[64] T. Metzler and D. Schaubert, “Scattering from a stub loaded microstrip antenna,” in Proc. Antennas Propag. Soc. Int. Symp. Dig., June 1989.

[65] D. C Chang and M.-C Huang, "Microstrip reflectarray antenna with offset feed," *Electron. Lett*., vol. 28, No. 16, 1489 – 1491, July 1992.

[66] E. Carrasco, M. Barba, and J. Encinar, "Encinar reflectarray element based on aperture-coupled patches with slots and lines of variable length," in *IEEE Trans. Antennas Propag.,* vol. 55, pp. 820-826, 2007.

[67] E. Carrasco, M. Barba, B. Reig, C. Dieppedale, and J. A. Encinar. "Characterization of a Reflectarray Gathered Element with Electronic Control using Ohmic RF MEMS and Patches Aperture-Coupled to a Delay Line." *IEEE Trans. Antennas Propag.,* Vol. 60, No. 9, 4190-4201, Sept. 2012.

[68] E. Carrasco, M. Barba, and J. A. Encinar. "X-Band Reflectarray Antenna with Switching-Beam using PIN Diodes and Gathered Elements." in *IEEE Trans. Antennas Propag.,* Vol 60, No. 12, 5700-5708, Dec. 2012.

[69] F. Venneri, S. Costanzo, and G. D. Massa. "Reconfigurable Aperture-Coupled Reflectarray Element Tuned by Single Varactor Diode." *Electronics Letters* Vol. 48, No. 2, 68-69, 2012.

[70] E. Carrasco, M. Barba, and J. A. Encinar. "Design and Validation of Gathered Elements for Steerable-Beam Reflectarrays Based on Patches Aperture-Coupled to Delay Lines." in *IEEE Trans. Antennas Propag.,* Vol. 59, No. 5, 1756-1761, May 2011.

[71] M. Abd-Elhady, W. Hong, and Y. Zhang. "A Ka-Band Reflectarray Implemented with a Single-Layer Perforated Dielectric Substrate." *IEEE Antennas and Wireless Propagation Lett.,* Vol. 11, 600-603, 2012.

[72] M. A. Moharram and A. Kishk, "Optically Transparent Reflectarray Antenna Design Integrated with Solar Cells," in *IEEE Trans. Antennas Propag.,* Vol. 64, 1700-1713, 2016.

[73] S. M. A. M. Hasan Abadi, K. Ghaemi, and N. Behdad, "Ultra-wideband, true-time-delay reflectarray antennas using ground-plane-backed, miniaturized-element frequency selective surfaces," *IEEE Trans. Antennas Propag*., vol. 63, no. 2, pp. 534–542, Feb. 2015.

[74] L. Liang, S. V. Hum, "An Impedance Surface-Based Method for Designing Wideband Reflectarrays," *IEEE Antennas and Propagation Society International Symposium*, 2015.

[75] R. E. Hodges, D. J. Hoppe, M. J. Radway, N. E. Chahat, "Novel Deployable Reflectarray Antennas for CubeSat Communications," *International Microwave Symp*., Phoenix, USA, 17-22 May 2015.

[76] Mars Cube One, Accessed on: https://en.wikipedia.org/wiki/Mars_Cube_One.

[77] C. Tienda, J.A. Encinar, M. Arrebola, M. Barba, E. Carrasco, "Design, Manufacturing and Test of a Dual-Reflectarray Antenna with Improved Bandwidth and Reduced Cross-Polarization," *IEEE Trans. on Antennas and Propagat.* Vol.61, No. 3, 1180-1190, March 2013.

[78] Eduardo Martinez-de-Rioja, Daniel Martinez-de-Rioja, *et al*., "Advanced Multibeam Antenna Configurations Based on Reflectarrays: Providing multispot coverage with a smaller number of apertures for satellite communications in the K and Ka bands," *IEEE Antennas and Propagation Magazine*, Volume: 61, Issue: 5, Oct. 2019.

[79] D. Martinez-de-Rioja, R. Florencio, J. A. Encinar, E. Carrasco, and R. R. Boix, "Dual-Frequency reflectarray cell to provide opposite phase shift in dual circular polarization with application in multibeam satellite antennas" *IEEE Antennas and Wireless Propag. Letters*, vol. 18, 2019.

[80] J. Huang and R. J. Pogorzelski, "A Ka-band microstrip reflectarray with elements having variable rotation angles," *IEEE Trans. Antennas Propag*., vol. 46, no. 5, pp. 650–656, May 1998.

[81] A. Mahmoud, A. Kishk, Z. Hao, and W. Hong, "Ka-Band Circularly Polarized Reflectarray," *IEEE Antenna and Propag. Magazine*, Vol 58, 2016.

[82] D. M. Pozar, Microwave Engineering, New York: John Wiley & Sons, 2012.

[83] L. Schuchman, "Dither signals and their effect on quantization noise," *IEEE Trans. Communication Technology*, pp. 162-165, December 1964.

[84] R. A.Wannamaker, S. P. Lipshitz, and J. Vanderkooy, "Quantization and dither: A theoretical survey," *J. of the Audio Engin. Soci.*, vol. 40, pp.

[85] Gray, R.M., and T.G. Stockham, "Dithered Quantizers," *IEEE Trans. Inform. Theory*, vol. 39, pp. 805–811, 1993.

[86] J. S. Lim and A. V. Oppenheim, editor. *Advanced topics in signal processing*. Signal processing series, New Jersey: Prentice-Hall, 1988.

[87] N. A. D'Andrea, F. Guglielmi, U. Mengali, A. Spalvieri, "Design of transmit and receive digital filters for data communications," *IEEE Trans. Communications*, vol. 42, pp. 357-359, 1994.

[88] H. Samueli, "On the design of optimal equiripple FIR digital filters for data transmission applications," *IEEE Transactions on Circuits and Systems*, vol. 35, pp. 1542-1546, 1988.

[89] M. Sobaszek, "Self-Tuned class-D audio amplifier with post-filter digital feedback implemented on digital signal controller," *IEEE Transactions on Circuits and Systems I: Regular Papers*, Vol. 67, pp. 797-805, 2020.

[90] A. Belyaev, P. Fayolle, "Adaptive Curvature-Guided Image Filtering for Structure + Texture Image Decomposition," *IEEE Transactions on Image Processing,* Vol. 27, pp. 5192-5203, 2018.

[91] B. A. Shenoi, *Introduction to digital signal processing and filter design.* New York: John Wiley & Sons, 2005.

[92] T. C. Chang and J. P. Allebach, "Quantization of accumulated diffused errors in error diffusion," *IEEE Trans. on Image Processing*, Vol. 14, pp. 1960-1976, 2005.

[93] Y. H. Fung and Y. H. Chan, "Optimizing the error diffusion filter for blue noise halftoning with multiscale error diffusion," *IEEE Trans. on Image Proc.*, Vol. 22, pp. 413-417, 2012.

[94] S. Pavan, R. Schreier, and G. Themes, *Understanding delta-sigma data converters.* Wiley, New Jersey, 2017.

[95] J. D. Krieger, C. Yeang and G. W. Wornell, "Dense delta-sigma phased arrays," *IEEE Trans. Antennas Propag.*, vol. 61, pp. 1825–1837, 2013.

[96] R. R. Read and S. Treitel, "The stabilization of two-dimensional recursive filters via the discrete Hilbert transform," *IEEE Trans. on Geoscience Electronics*, vol. 11, pp.153-160, 1973.

[97] S. Chakrabarti and S. K. Mitra, "Design of two-dimensional digital filters via spectral transformations," in *Proc. of the IEEE*, vol. 65, pp. 905-914, 1977.

[98] J. W. Wood, "Multidimensional signal, image and video processing and coding," NewYork, Elsevier, 2012

[99] B. A. Shenoi, *Introduction to digital signal processing and filter design.* New York: John Wiley & Sons, 2005.

[100] S. L. Hahn, *Hilbert transforms in signal processing*. Norwood, Massachusetts: Artech House, 1996.

[101] J. W. Wood, "Multidimensional signal, image and video processing and coding," NewYork, Elsevier, 2012.

[102] L. Middleton and J. Sivaswamy, "Hexagonal image processing: A practical approach," London, Springer, 2005

[103] T. S. Rappaport et al., "Wireless communications and applications above 100 GHz: opportunities and challenges for 6G and beyond," *IEEE Access*, *vol. 7, pp. 78729-78757, 2019.*

[104] S. Cheng, Y. Shi, "Brain storm optimization algorithm," Switzerland, Springer, 2018.

[105] A. Aldhafeeri and Y. Rahmat-Samii, "Brain storm optimization for electromagnetic applications: continuous and discrete," *IEEE Trans. on Antenna and Propag.* , vol. 67, pp.2710-2723, 2019.

[106] Y. Shi, J. Xue, and Y. Wu, "Multi-objective optimization based on brain storm optimization algorithm," in *International Swarm. Int. Research*, July 2013.

[107] Y. Gao, B. Song, H. Zhao, X. Hu, Y. Qian, X. Chen, "An Improved selection method based on crowded comparison for multi-objective optimization problems in intelligent computing," *mobile networks apps.,* 2019. [online]: DOI 10.1007/s11036-019-01403-7.

[108] C. Dai, X, Lei, *"A multiobjective brain storm optimization algorithm based on decomposition," Hindawi Complexity,* vol.43, 2019.

[109] D. M. Pozar, S. D. Targonski, and R. Pokuls, "A shaped beam microstrip patch reflectarray," in *IEEE Trans. Antennas Propag*., vol. 47, pp. 1167–1173, Jul. 1999.

[110] D. Martinez-de-Rioja, R. Florencio, J. A. Encinar, E. Carrasco, and R. R. Boix, "Dual-Frequency reflectarray cell to provide opposite phase shift in dual circular polarization with application in multibeam satellite antennas" *IEEE Antennas and Wireless Propag. Letters*, vol. 18, 2019.